TECHNISCHE UNIVERSITÄT MÜNCHEN

Lehrstuhl E23 für Technische Physik

Walther-Meißner-Institut für Tieftemperaturforschung
der Bayerischen Akademie der Wissenschaften

Spin Transport in Insulating Ferrimagnets

Kathrin Marlène Ganzhorn

Vollständiger Abdruck der von der Fakultät für Physik der Technischen
Universität München zur Erlangung des akademischen Grades eines

Doktors der Naturwissenschaften

genehmigten Dissertation.

Vorsitzender: Prof. Dr. Andreas Weiler

Prüfer der Dissertation:
1. Prof. Dr. Sebastian T. B. Goennenwein
2. Prof. Dr. Alexander Holleitner

Die Dissertation wurde am 25.10.2017 bei der Technischen Universität München
eingereicht und durch die Fakultät für Physik am 05.10.2018 angenommen.

Abstract

In this thesis, we discuss proof of principle experiments for the read-out and transfer of information via spin currents in a ferrimagnetic insulator (FMI). First, we focus on the read-out of magnetic states, i.e. the sublattice magnetic moment configuration in a FMI. To this end, we exploit the spin Hall magnetoresistance (SMR) in heterostructures consisting of a FMI and a platinum (Pt) layer. We expand the well established macrospin-based SMR picture to a microscopic model based on the orientation of the individual sublattice magnetic moments. The latter can straightforwardly be applied to a variety of non-collinear magnetically ordered systems and even antiferromagnets. We verify our theoretical predictions experimentally in the canted magnetic phase of the FMI gadolinium iron garnet (GdIG) and find that for a non-collinear magnetic configuration the SMR response cannot be described by the net magnetization, but is indeed determined by the orientation of the individual magnetic moments, in agreement with our theoretical model. These results show that SMR measurements allow for an all-electrical mapping of magnetic phases in insulators and give important details on their magnetic structure and sublattice configurations.

We then turn to the transfer of information via spin wave excitations (magnons) which can propagate in a FMI. In particular, we study the magnon mediated magnetoresistance (MMR) effect, i.e. the transport of non-equilibrium magnons, which are injected and detected electrically using two parallel Pt strips deposited on top of the ferrimagnet. A systematic study of the MMR in yttrium iron garnet (YIG) as a function of the injector-detector distance, temperature and magnetic field gives first important insights into the microscopic origin of the MMR. Based on these results, we present a proof-of-principle device performing logic operations via the incoherent superposition of non-equilibrium magnons. We also study the thermal injection of magnons, which gives rise to an additional voltage at the detector via the non-local spin Seebeck effect (SSE). Our experimental results suggest that the non-local SSE depends on a complex interplay of both interfacial transparency and magnon transport properties. Finally, we investigate the MMR effect in the collinear magnetic phase of GdIG and find a distinct temperature and magnetic field dependence of the MMR signal, that is qualitatively different from the one observed in YIG/Pt. This complex behavior can partially be attributed to the magnetic field dependence of the magnon transport properties in GdIG.

This thesis gives new insights into fundamental properties of insulating, magnetically ordered materials, such as their magnetic structure and magnon transport properties.

Furthermore, our results are of interest for future spintronics applications, namely for magnetic sensing and read-out, as well as for information transfer and processing.

Zusammenfassung

In dieser Dissertation werden Grundlagenexperimente für das Auslesen und die Übertragung von Informationen mithilfe von Spinströmen in ferrimagnetischen Isolatoren (FMI) durchgeführt. Zunächst behandeln wir das Auslesen der magnetischen Untergitterkonfiguration in einem FMI. Hierzu wird der Spin Hall Magnetwiderstandseffekt (SMR) in Heterostrukturen aus einem FMI und einer Platinschicht (Pt) untersucht. Wir erweitern das etablierte, Makrospin-basierte SMR Modell und schlagen ein neues mikroskopisches Modell vor, das auf der Orientierung der einzelnen magnetischen Untergittermomente basiert. Letzteres kann ohne Weiteres auf eine Vielzahl von magnetisch geordneten, nicht-kollinearen und sogar antiferromagnetischen Systemen angewandt werden. Die theoretischen Vorhersagen werden experimentell in der magnetisch verkanteten Phase des FMI Gadolinium-Eisen-Granat (GdIG) überprüft. Unsere Messungen bestätigen, dass der SMR Effekt dann nicht mehr durch die Nettomagnetisierung gegeben ist, sondern - im Einklang mit dem vorgeschlagenen Modell - durch die Orientierung der einzelnen magnetischen Momente bestimmt wird. Diese Ergebnisse zeigen, dass SMR-Messungen eine rein elektrische Charakterisierung von magnetischen Phasen in Isolatoren ermöglichen und Aufschluss über deren magnetische Struktur und Untergitterkonfigurationen geben können.

Im zweiten Teil dieser Arbeit wird die Übertragung von Informationen in Form von Spinwellen (Magnonen), die durch einen FMI propagieren, behandelt. Insbesondere wird der Transport von Nichtgleichgewichtsmagnonen untersucht, die mithilfe von zwei auf dem FMI aufgebrachten Pt Streifen elektrisch injiziert und detektiert werden. Eine systematische Untersuchung dieses sogenannten magnonenvermittelten Magnetwiderstandseffektes (MMR) in Yttrium-Eisen-Granat (YIG) als Funktion des Injektor-Detektor Abstandes, der Temperatur und des Magnetfeldes, gibt Aufschluss über den mikroskopischen Ursprung des MMR. Basierend auf diesen Erkenntnissen wird ein Bauelement implementiert, das Logikoperationen mittels inkohärenter Superposition von Nichtgleichgewichtsmagnonen ausführt. Des Weiteren wird der Transport von thermisch injizierten Magnonen in YIG/Pt untersucht, die eine zusätzliche Spannung am Detektor verursachen. Der beobachtete Effekt wird als nichtlokaler Spin Seebeck Effekt (SSE) bezeichnet. Die experimentellen Daten deuten darauf hin, dass der nichtlokale SSE von einem komplexen Zwischenspiel der Grenzflächentransparenz und der Magnonentransporteigenschaften abhängt. Abschließend wird der MMR Effekt in der kollinearen Phase von GdIG untersucht. Die gemessene Temperatur- und Magnetfeldabhängigkeit des MMR Effektes in GdIG unterscheidet sich qualitativ von den Beobachtungen in YIG. Dieses komplexe Verhalten kann zum Teil auf eine starke Magnetfeldabhängigkeit der Magnonentransporteigenschaften in GdIG zurückgeführt werden.

Diese Dissertation gibt neue Einblicke in fundamentale Eigenschaften von isolierenden, magnetisch geordneten Materialien, z.B. deren magnetische Struktur und Magnonentransporteigenschaften. Zudem sind die Erkenntnisse von Interesse für zukünftige Spinelektronikanwendungen, insbesondere für magnetische Sensoren und zur Informationsübertragung und -verarbeitung.

Contents

Chapter 1

Introduction

“Those of us who have come later will never be able to experience [...] the enormous and enthusiastic astonishment at the fact that [a] small, hardly detectable electrical spark [...] has suddenly acquired the demonic power to leap across countries, mountains, and entire continents.”

These words were written by the Austrian author Stefan Zweig in his work ”Decisive moments in history” [1], where he describes the great technical accomplishment of laying a telegraphic cable across the Atlantic ocean in the 1860s, reducing the (one-way) communication time between America and Europe from two or three weeks (for a letter carried by steamship) to several minutes for a short message. While at that time successfully developing and handling a 4000 km long undersea cable to enable transatlantic messaging was considered a groundbreaking achievement, nowadays the main focus in communication technology lies in making microscopic electronic devices faster and more energy efficient. The general approach of encoding a message in what Zweig called a “hardly detectable electrical spark” is still applicable today, as information is usually carried by the charge of electrons. However, beside their charge, electrons also exhibit a spin. This additional degree of freedom has gained much interest in recent years, giving rise to the research field of spintronics, which in more general terms comprises different concepts of information transfer via angular momentum currents. These can be for instance electrical spin (polarized) currents in ferromagnetic metals or spin-wave excitations in magnetically ordered insulators. While the spin diffusion length in a ferromagnetic metal is typically very short of the order of nm [2], spin waves in ferromagnetic insulators (FMI) can propagate over much larger distances on the µm scale. In this context, a new effect called magnon mediated magnetoresistance (MMR) was recently observed in bilayers consisting of the FMI yttrium iron garnet ($Y_3Fe_5O_{12}$, YIG) and two parallel, electrically isolated Pt strips deposited on top of the YIG [3, 4]. Driving an electrical charge current through one of the strips (injector), gives rise to a transverse electrical spin current via the spin Hall effect (SHE) [5, 6]. Since the electron spin current cannot cross the Pt/FMI interface, a spin accumulation builds up there. The latter is converted into non-equilibrium magnons, the quanta of spin-wave excitations, which diffuse across the insulator away from the injector.

The non-equilibrium magnons are detected via the inverse effect in the second Pt strip, giving rise to a non-local voltage which can be measured in open-circuit conditions. This combination of electron spin and magnon currents in a FMI/Pt bilayer represents an important step towards transferring information over several 10 µm through a magnetic insulator. In order to exploit this effect for applications, i.e. information transfer and processing within a magnonic system, a more thorough understanding of the microscopic origin of the MMR is required, which is one of the main aims of this thesis.

In addition to investigating the transfer of information through a magnetic insulator, we address another important aspect of spintronics, i.e. magnetic data storage. In particular, we focus on the associated read-out processes. The concept of magnetic recording was already proposed in 1888 by O. Smith [7] followed by the first magnetic tape recorders in the 1930s. Although technology has greatly evolved in the meantime, the basic approach of encoding logical bits as a magnetic state which can be read out afterwards is still similar today. In general, a common strategy for the read-out of magnetic states is to make use of magnetoresistive effects, i.e. the dependence of a materials electrical resistivity on the magnetization orientation. One well established magnetoresistive effect in metals, which is currently used for sensor applications (linear or angular position sensors), is the anisotropic magnetoresistance (AMR) [8, 9]. A similar effect called spin Hall magnetoresistance (SMR) [10–12] was recently discovered in FMI/normal metal (NM) bilayers. The SMR is mediated by a spin current flow across the FMI/NM interface, leading to a resistivity change in the NM depending on the magnetization orientation in the insulating ferrimagnet.

Promising materials for next generation data storage technologies are antiferromagnets, where the net magnetization is compensated due to the antiparallel alignment of neighboring magnetic moments. Antiferromagnets therefore exhibit no magnetic stray fields, eliminating disruptive cross-talk between adjacent bits and allowing for high density storage devices. Furthermore, the lack of net magnetization makes antiferromagnets robust against external magnetic fields, preventing accidental switching and memory loss. However, this property also makes the read-out of the antiferromagnetic states challenging. Recent measurements in antiferromagnetic metals give evidence that the AMR is not sensitive to the net magnetization but probes the sublattice specific moment orientation, allowing to determine the encoded magnetic state [13, 14]. The question arises whether the same applies for magnetoresistive measurements in FMI/NM bilayers. In this thesis we therefore investigate the sensitivity of the SMR effect to the orientation of individual sublattice magnetic moments in an insulating magnet. Since the manipulation of the magnetic state of an antiferromagnet via an external magnetic field can be challenging, we choose the three-sublattice ferrimagnet gadolinium iron garnet ($Gd_3Fe_5O_{12}$, GdIG) which has a net magnetization at finite external magnetic field. In addition to a collinear ferrimagnetic phase, GdIG exhibits a canted magnetic phase, where the sublattice moments are non-collinear and the corresponding canting angles with respect to the applied field depend on the temperature and magnetic field magnitude. SMR measurements as a function of temperature and magnetic field in GdIG/Pt bilayers therefore allow for a systematic study of the SMR response as a function of the sublattice magnetic moment orientation.

This thesis is organized in two main parts: in Part I we expand the current macrospin-based SMR model to a microscopic description based on the orientation of individual magnetic moments residing on different sublattices (Chap. 2). Chapter 3 introduces the material systems investigated in this thesis and gives a short overview over the experimental methods. We verify our theoretical predictions experimentally in Chap. 4 and present the first SMR measurements conducted in the non-collinear magnetic phase of the insulator GdIG using Pt as the normal metal. Our experimental results give strong evidence that indeed the SMR is not determined by the net magnetization of the FMI but rather depends on the orientation of the individual magnetic moments. We conclude that the SMR is a promising candidate for the all-electrical read-out of magnetic states in antiferromagnetic insulators and more generally can be used to probe non-collinear magnetic structures in insulators, such as conical or frustrated magnetic states.

In Part II we turn to the transport of non-equilibrium magnons in a non-local FMI/Pt nanostructure. Chapter 5 gives an overview over the current theoretical understanding of magnon injection and transport in a ferrimagnetic insulator. In Chap. 6, we study the MMR effect, i.e. the diffusion of electrically injected magnons through the ferrimagnetic insulator YIG as a function of temperature, magnetic field and injector-detector distance. These measurements allow for a better understanding of the dominating magnon contributions and the microscopic origin of the MMR. Following these results, we present the first proof-of-principle device implementing a magnon-majority gate based on the incoherent superposition of magnons in the YIG film (Chap. 7). Potential switching frequencies of a few GHz and straightforward downscaling make this device promising for future spintronics applications. In addition to the electrical injection of magnons, the latter can also be excited thermally at the injector, giving rise to the non-local spin Seebeck effect (SSE), which can also be detected in the second Pt strip. Our temperature dependent investigation of the non-local SSE in YIG/Pt presented in Chap. 8 indicates that the latter is governed by a complex interplay of interface and transport properties. After an extensive study of the magnon transport in YIG/Pt, we turn to the diffusion of electrically injected magnons in a GdIG/Pt non-local nanostructure in Chap. 9. In contrast to YIG, where only the fundamental magnon mode is thermally populated at room temperature and expected to contribute to the MMR, GdIG has a more complex magnon spectrum with an additional thermally populated high energy mode. By comparing the experimental results to calculations of the GdIG magnon spectrum we can therefore study the influence of multiple magnon modes on the MMR effect. The key findings on magnon injection and transport in ferrimagnetic insulators are compiled in Chap. 10.

Finally, the most important results obtained within this thesis are summarized in Chap. 11. We furthermore propose future experiments which may allow to resolve some of the open questions concerning both the spin Hall magnetoresistance in non-collinear magnetic structures as well as magnon transport in a non-local configuration.

Part I

Spin Hall magnetoresistance in FMI/Pt bilayers

Magnetically ordered materials are often characterized in terms of their net magnetization, a quantity which can be experimentally determined using a magnetometer. In the simplest case, this is achieved by moving the sample through a pick up coil and measuring the induced voltage. For a theoretical description of the magnetic properties, a macrospin approximation can be applied using the net magnetization vector $\mathbf{M} = n\boldsymbol{\mu}_i$, where n is the number of magnetic moments per volume. This macrospin model is based on the assumption that all individual atomic magnetic moments $\boldsymbol{\mu}_i$ are aligned along the same direction. While this assumption is valid in collinear magnets, many material systems with long-range magnetic order have a more complex magnetic structure, forming e.g. canted, spiral or topological [15, 16] phases, such that the macrospin approximation can no longer be applied straightforwardly. Some materials furthermore exhibit rich magnetic phase diagrams such as the one found for example in Cu_2OSeO_3 (CSO) [17–19], depicted in Fig. 1.1 (Figure taken from Ref. [17]). Here, both collinear (ferrimagnetic) and non-collinear (conical, skyrmionic) phases are observed, such that CSO cannot be described in a macrospin model throughout the whole phase diagram. On a similar note, a large number of magnetically ordered materials are antiferromagnetic (AFM) and can also not be described in terms of a macrospin. This is due to the fact that all atomic magnetic moments compensate each other and the net magnetization of the AFM is zero. Antiferromagnets are steadily gaining interest for future applications since their long range magnetic order can be used for data storage [13, 14, 20–22], while the magnetic structure is mostly unaffected by external magnetic fields. Considering this large variety of magnetically ordered phases, a simple characterization method for the microscopic magnetic structure of different materials is of great importance.

In general, the presence of different magnetic phases, and in particular also of phase transitions, can be deduced from magnetization and susceptibility measurements - e.g. superconducting quantum interference device (SQUID) magnetometry - as a function of magnetic field magnitude, magnetic field orientation and temperature (see Fig. 1.1). However, since conventional magnetometry is sensitive only to the total (net) magnetic moment, such experiments do not allow for a direct mapping of the microscopic magnetic structure in non-collinear or antiferromagnetic phases. The experimental investigation of the latter therefore usually requires more complex methods, such as x-ray magnetic circular dichroism (XMCD), spin polarized neutron scattering or Lorentz transmission electron microscopy. In conductive materials, magnetoresistance measurements can be exploited for the electrical detection of the magnetic properties. It was recently shown that the anisotropic magnetoresistance (AMR) effect allows to determine the orientation of the sublattice moments in an antiferromagnet [13, 14]. In the case of magnetically ordered insulators on the other hand, the magnetic properties can be probed by placing a normal metal layer on top and investigating spin torques at the magnet/metal interface [23–25]. More specifically, in a bilayer consisting of a (collinear) ferrimagnetic insulator and a normal metal with strong spin orbit coupling such as Pt, the resistance of the normal

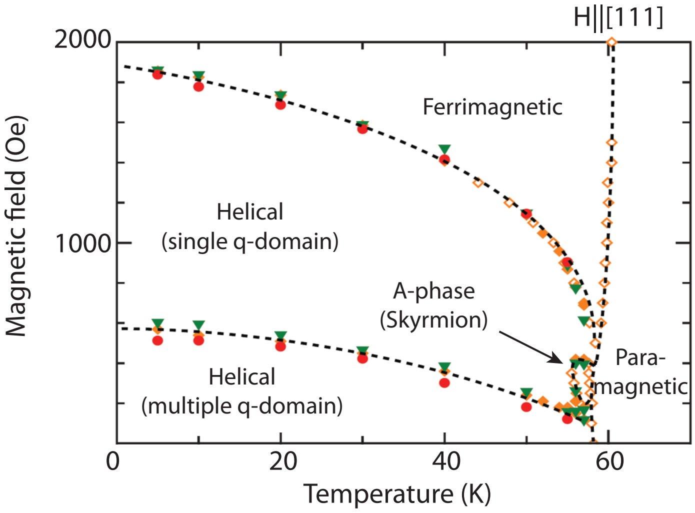

Figure 1.1: Magnetic phase diagram of a Cu_2OSeO_3 (CSO) bulk sample determined via magnetization (red dots), electric polarization (green triangles) and ac susceptibility (orange) measurements. Below the ordering temperature $T_c \approx 60\,\mathrm{K}$, the magnetic moments in CSO arrange in non-collinear conical or skyrmionic configurations or exhibit a collinear ferrimagnetic order, depending on the applied magnetic field magnitude. Figure taken from Ref. [17].

metal depends on the orientation of the (net) magnetization in the ferrimagnet. This effect is called spin Hall magnetoresistance (SMR) [10–12, 26, 27] and is based on spin torque, i.e. a flow of angular momentum across the magnet/metal interface. The latter is well established for collinear magnets, which can be described by a macrospin approximation [28, 29]. However, the spin torques acting on non-collinear magnetic structures are still subject to current investigations.

In the first part of this thesis, we therefore propose a microscopic theoretical description of the SMR effect in complex magnetic structures, taking into account the orientation of all individual magnetic moments. We verify the proposed model experimentally in the insulating ferrimagnet gadolinium iron garnet ($Gd_3Fe_5O_{12}$, GdIG), which can assume a collinear as well as a canted magnetic phase and can easily be manipulated by an external magnetic field. Our experimental results show that indeed the SMR effect in GdIG/Pt is sensitive to the orientation of magnetic moments residing on different magnetic sublattices and is not simply determined by the orientation of the net magnetization $\mathbf{M}$ (as described in the macrospin approximation). In particular, we observe a 90° shift of the SMR angular dependence (also parametrized as a SMR sign inversion) in the magnetic canting phase compared to the collinear phase. This observation can be rationalized within the proposed microscopic model and is further confirmed by XMCD measurements and atomistic spin simulations. The spin Hall magnetoresistance therefore represents a powerful tool for the electrical mapping of magnetic structures in insulators.

Part I of this thesis is structured as follows: in Chap. 2, we start with a compact overview of the relevant theoretical concepts including the generation and detection of spin currents as well as the theory of SMR in the macrospin approximation. We then expand the latter to a microscopic description of the SMR in canted ferrimagnets based on the assumption that each magnetic moment contributes individually to the SMR. The two material systems investigated in this part, i.e. the collinear ferrimagnet yttrium iron garnet ($Y_3Fe_5O_{12}$, YIG) and the compensated ferrimagnet GdIG, are both introduced in Chap. 3, followed by a description of the experimental setup. In Chap. 4, we present our experimental SMR results in YIG/Pt and GdIG/Pt. The latter were published in Phys. Rev. B **94**, 094401 (2016) [30].

Chapter 2

Spin Hall magnetoresistance: theoretical overview and modeling

2.1 Spin current generation and detection

In addition to their charge, electrons also carry angular momentum or spin. In metallic systems, two independent transport channels are typically considered for spin up and down electrons, based on the two current model proposed by Mott [31]. The total electron charge current density is then given by

$$\mathbf{J}_c = (\mathbf{J}_\uparrow + \mathbf{J}_\downarrow) \tag{2.1}$$

where $\mathbf{J}_{\uparrow,\downarrow}$ is the current density of spin up and spin down electrons, respectively. Here, we use the technical current direction for the electron charge current density, i.e. $\mathbf{J}_c$ has units of $\mathrm{A/m^2}$. The corresponding spin (polarized) current density is defined as

$$\mathbf{J}_s = \frac{\hbar}{-2e} (\mathbf{J}_\uparrow - \mathbf{J}_\downarrow) \tag{2.2}$$

with $-e < 0$ the electron charge. A spin current is a flow of angular momentum and therefore has a flow direction $\mathbf{J}_s$ and a polarization direction (the spin orientation). The factor $\frac{\hbar}{-2e}$ accounts for the different dimensionalities of the charge and spin currents, as $\mathbf{J}_s$ is an angular momentum (particle) current in units of $\mathrm{J/m^2}$. Note that in the following discussions, we are mainly interested in the current directions and therefore often denote J as a current (instead of current density) for simplification.

In order to exploit spin currents for applications, a conversion process from electron charge to spin current and vice versa is required. A well established concept for this conversion is using a metal without long-range magnetic order, typically called “normal metal” (NM) in literature, which exhibits large spin orbit coupling: driving a charge current through the NM gives rise to a transverse electron spin current via the so-called spin Hall effect (SHE) [5, 6]. The origin of the SHE is an asymmetric scattering of spin up and down electrons, due to either intrinsic (Berry curvature [32, 33]) or extrinsic (skew scattering [34–36], side jump scattering [37]) mechanisms. The generated spin current is given by [38]

$$\mathbf{J}_{\mathrm{s}}^{\mathrm{SHE}} = \Theta_{\mathrm{SH}} \frac{\hbar}{2e} \mathbf{J}_{\mathrm{c}} \times \boldsymbol{\sigma} \tag{2.3}$$

where $\boldsymbol{\sigma}$ is the electron spin polarization in the metal and Θ_{SH} the spin Hall angle, i.e. the conversion efficiency between charge and spin current. The inverse spin Hall effect (ISHE) described by [38]

$$\mathbf{J}_{\mathrm{c}}^{\mathrm{ISHE}} = \Theta_{\mathrm{SH}} \frac{2e}{\hbar} \mathbf{J}_{\mathrm{s}} \times \boldsymbol{\sigma} \tag{2.4}$$

in turn can be used for the electrical detection of a spin current. The spin Hall angle can be positive (Pt, Au, Ag) or negative (Ta, W) and its amplitude depends on the strength of the spin orbit coupling and is therefore material specific [39]. In the present work we use Pt as the NM, due to its comparatively large spin Hall angle, making it a good candidate for charge-transport based (electrical) spin current generation and detection. More specifically, values in the range $\Theta_{\mathrm{SH}} = 3\% - 12\%$ were experimentally extracted by different groups [10, 26, 27, 40, 41]. These differences are typically attributed to the sensitivity of Θ_{SH} to the deposition method (electron beam evaporation or sputtering) and to the concentration and type of impurities in the Pt [42].

2.2 Spin Hall magnetoresistance in the macrospin model

In the first part of this thesis, we study the spin Hall magnetoresistance (SMR) [10–12] in bilayers consisting of a ferrimagnetic insulator (FMI) and the normal metal Pt. The SMR effect corresponds to a modulation of the Pt resistance as a function of the magnetization orientation in the FMI and is mediated by a spin current, i.e. a flow of angular momentum, across the Pt/FMI interface. This process is sketched in Fig. 2.1 (Figure adapted from Ref. [30]): a charge current $\mathbf{J}_c \parallel \mathbf{j}$ driven through the Pt induces an electron spin current in the metal with flow direction $\mathbf{J}_s \parallel -\mathbf{n}$ and polarization $\boldsymbol{\sigma} \parallel -\mathbf{t}$ due to the SHE according to Eq. (2.3). The SMR is usually described in a macrospin model in terms of a magnetization $\mathbf{M} = \boldsymbol{\mu}/V = \sum \boldsymbol{\mu}_i/V$, where $\boldsymbol{\mu}$ is the total magnetic moment and $\boldsymbol{\mu}_i$ are all the individual atomic moments in the volume V. When $\boldsymbol{\sigma}$ is perpendicular to the magnetization direction $\mathbf{m} = \mathbf{M}/M$ in the FMI (see Fig. 2.1 (a)), a spin transfer torque can be exerted on the magnetization [10, 12, 43]. The ability to exert a torque can be identified as an absorption of $\mathbf{J}_s$ which in turn manifests itself as an additional dissipation channel for charge transport in the Pt layer, such that the metal resistivity ρ increases. However, for $\boldsymbol{\sigma} \parallel \mathbf{m}$, no torque can be exerted and the spins accumulate at the Pt/FMI interface. This leads to a back flow of the spin current ($\mathbf{J}_{\mathrm{s,back}}$) away from the interface which (partly) counteracts the original spin current (see Fig. 2.1 (b)). $\mathbf{J}_{\mathrm{s,back}}$ is converted back into a charge current and in this configuration the Pt resistivity reaches a minimum. In Part II of this thesis, the spin accumulation at the Pt/FMI interface

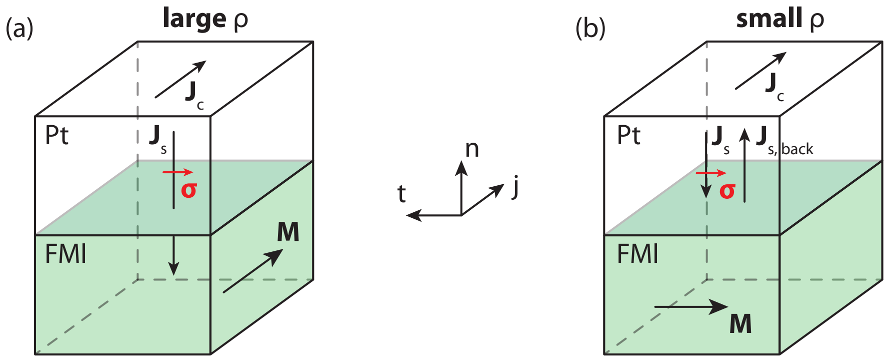

Figure 2.1: Spin Hall magnetoresistance response of a FMI/Pt bilayer. (a) A charge current $\mathbf{J}_c$ applied to the Pt layer generates a transverse spin current $\mathbf{J}_s$ via the SHE. When the electron spin polarization $\boldsymbol{\sigma}$ is perpendicular to the magnetization direction $\mathbf{M}$ in the FMI, a torque can be exerted on the magnetization, such that the spin current is partly absorbed by the ferrimagnet and the resistivity ρ of the metal is increased. (b) When $\mathbf{M} \parallel \boldsymbol{\sigma}$, $\mathbf{J}_s$ cannot cross the interface and spins accumulate there, giving rise to a spin back flow $\mathbf{J}_{\text{s,back}}$. The latter is converted back into a spin current via the ISHE, leading to a smaller Pt resistivity ρ. Figure adapted from Ref. [30].

obtained for $\boldsymbol{\sigma} \parallel \mathbf{m}$ will be discussed in more detail, since the electron spin accumulation can be converted into a magnon accumulation in the FMI. This effect however is usually neglected in the description of the SMR and will not be taken into account here.

Quantitatively, the longitudinal resistivity of the Pt follows [12]

$$\rho_{\text{long}} = \rho + \rho' + \rho_1 \left(1 - m_t^2\right) = \rho + \rho' + \rho_1 \left(1 - (\mathbf{m} \cdot \mathbf{t})^2\right) \tag{2.5}$$

where m_t is the projection of the magnetization unit vector $\mathbf{m}$ onto the transverse direction $\mathbf{t} \parallel \boldsymbol{\sigma}$ and ρ is the intrinsic electric resistivity of the bulk normal metal. ρ' and ρ_1 are defined as [12]

$$\frac{\rho'}{\rho} = -\Theta_{\text{SH}}^2 \frac{2\lambda}{d_{\text{NM}}} \tanh\left(\frac{d_{\text{NM}}}{2\lambda}\right) \tag{2.6}$$

$$\frac{\rho_1}{\rho} = \Theta_{\text{SH}}^2 \frac{\lambda}{d_{\text{NM}}} \text{Re} \frac{2\lambda G_{\uparrow\downarrow} \tanh^2\left(\frac{d_{\text{NM}}}{2\lambda}\right)}{\sigma_{\text{NM}} + 2\lambda G_{\uparrow\downarrow} \coth\left(\frac{d_{\text{NM}}}{\lambda}\right)} \approx \Theta_{\text{SH}}^2 \frac{\lambda}{d_{\text{NM}}} \frac{2\lambda G_r \tanh^2\left(\frac{d_{\text{NM}}}{2\lambda}\right)}{\sigma_{\text{NM}} + 2\lambda G_r \coth\left(\frac{d_{\text{NM}}}{\lambda}\right)} \tag{2.7}$$

with Θ_{SH} the spin Hall angle (see Sect. 2.1), λ the spin diffusion length in the NM, d_{NM} the thickness of the NM layer and σ_{NM} the electrical conductivity of the NM. $G_{\uparrow\downarrow} = G_r + iG_i$ is the complex spin mixing interface conductance per unit area [44] and gives a measure for the efficiency of the angular momentum transfer across the interface. As customary in literature, we assume that the imaginary part G_i of the spin mixing conductance is smaller than the real part G_r [45], such that we can neglect G_i and can simplify Eq. (2.7).

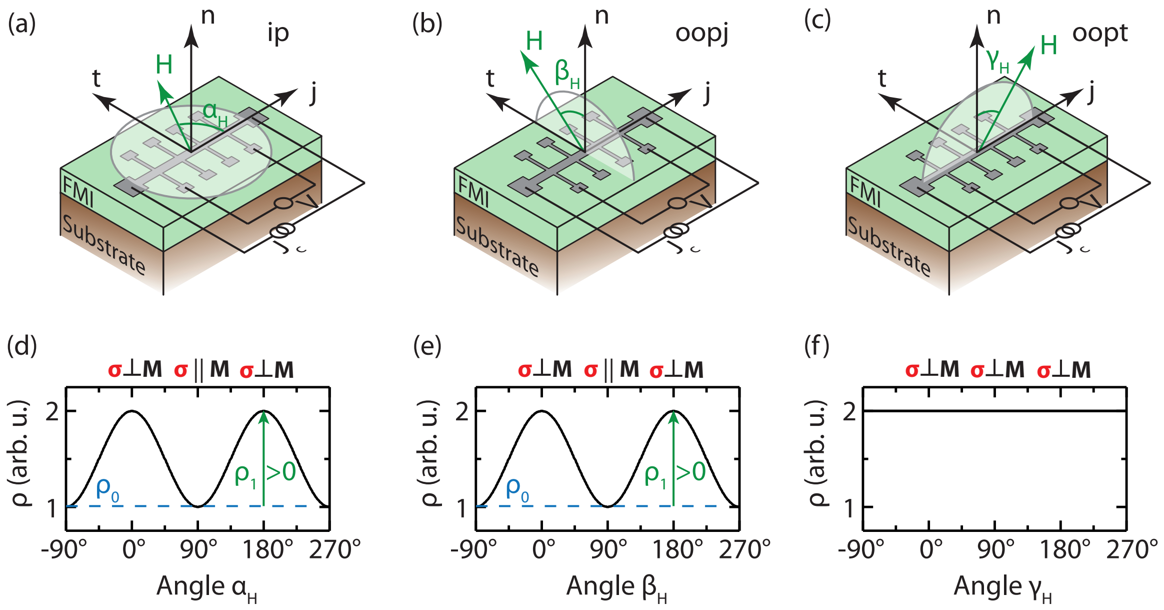

Figure 2.2: Typical SMR measurement configuration in a FMI/Pt Hall bar structure, where the external magnetic field is rotated (a) in the **j**-**t**-plane (ip), (b) in the **n**-**t**-plane (oopj) and (c) in the **n**-**j**-plane (oopt). The wiring for a 4 point resistance measurements is shown in black. The expected modulation of the resistivity ρ as a function of the external magnetic field orientation $\mathbf{H}$ for all three rotation planes is displayed in panels (d)-(f). For the ip (oopj) rotation a $\cos^2(\alpha_\mathrm{H})$ ($\cos^2(\beta_\mathrm{H})$) dependence on the magnetic field orientation is expected, with ρ_0 the resistivity for $\boldsymbol{\sigma} \parallel \mathbf{M}$ and $\rho_1 > 0$ the amplitude of the resistivity modulation. During the oopt rotation, $\mathbf{M}$ is always perpendicular to $\boldsymbol{\sigma}$, such that a constant resistivity $\rho_0 + \rho_1$ is expected.

In the experiments presented in Chap. 4, the Pt resistivity ρ is measured as a function of the magnetization orientation for a fixed magnetic field magnitude (see Fig. 2.2 (a)). We therefore focus on the angle dependent resistivity modulation with amplitude ρ_1 and describe the SMR response in a simplified form as

$$\rho_\mathrm{long} = \rho_0 + \rho_1 \left(1 - (\mathbf{m} \cdot \mathbf{t})^2\right) \tag{2.8}$$

where $\rho_0 = \rho + \rho'$ corresponds to a constant offset which is independent of the magnetization orientation. Assuming that the magnetization of the FMI is always parallel to the external magnetic field[1], when the latter is rotated in the sample plane (see Fig. 2.2 (a)) the resistivity reads

$$\rho_\mathrm{long} = \rho_0 + \rho_1 \cos^2\left(\alpha_\mathrm{H}\right) \tag{2.9}$$

---

[1] This assumption is valid for a magnetic field large enough to overcome all anisotropy and demagnetization fields, and as long as the ferrimagnet is in a collinear magnetic state.

with α_H the in-plane angle between the external magnetic field direction $\mathbf{H}$ and the charge current direction $\mathbf{j}$. The expected angular dependence of the Pt resistivity for an in-plane magnetic field rotation is depicted in Fig. 2.2 (d). The SMR ratio is defined as [10]

$$\mathrm{SMR} = \frac{\rho_1}{\rho_0}. \tag{2.10}$$

Based on Eq. (2.8), we can also discuss the SMR response for an out of plane rotation of the external magnetic field. When the magnetization is rotated in the **n**-**t**-plane, i.e. with respect to the **j**-axis (oopj rotation) as sketched in Fig. 2.2 (b), the projection m_t of the magnetization on the **t**-direction depends on the magnetic field orientation and the resistivity therefore follows

$$\rho_\mathrm{long} = \rho_0 + \rho_1 \cos^2\left(\beta_\mathrm{H}\right) \tag{2.11}$$

where β_H is the angle between the external field and the **n**-axis. The expected $\cos^2\left(\beta_\mathrm{H}\right)$ resistivity angular dependence for an oopj rotation is shown in Fig. 2.2 (e) [10]. In contrast, for a magnetic field rotation with respect to the **t**-direction (oopt rotation), i.e. in the **j**-**n**-plane in Fig. 2.2 (c), the projection m_t is constant and independent of the angle γ_H between $\mathbf{H}$ and $\mathbf{n}$. No resistivity modulation is therefore expected for the oopt rotation, as sketched in Fig. 2.2 (f). The characteristic SMR angular dependencies sketched in Fig. 2.2 are indeed consistent with experimental observations in FMI/Pt bilayers [10].

We would like to emphasize that the angular dependence of the SMR in the oop rotation planes is qualitatively different from the one observed for the anisotropic magnetoresistance (AMR) in electrically conductive ferromagnets, where the resistivity depends on the relative orientation of the magnetization $\mathbf{m}$ with respect to the charge current direction $\mathbf{j}$ [9]. The metal resistivity ρ is therefore determined by the projection m_j, such that a finite modulation of ρ is observed for an oopt rotation, while ρ is constant in the oopj rotation plane [10]. For an in-plane magnetic field rotation both AMR and SMR effect give rise to a resistivity modulation, such that in general both contributions should be considered.

However, in a FMI/Pt bilayer we expect no AMR contribution [10], since the FMI is not conductive and the Pt has no long range magnetic order. While a SMR model including a possible AMR contribution from induced magnetic moments in the Pt layer was also proposed [46], x-ray magnetic circular dichroism (XMCD) measurements demonstrated that AMR contributions from the latter can be neglected in our typical FMI/Pt samples (fabricated as described in Sect. 3.2) [47]. In Chap. 4, we therefore focus on magnetoresistance measurements conducted as a function of the in-plane magnetic field orientation and attribute the experimentally observed resistivity modulation to the SMR effect.

After discussing the characteristic SMR signature, we now give a short overview of the parameters which influence the amplitude of the SMR effect as described in the macrospin model. Most SMR measurements have been conducted in FMI/Pt bilayers with yttrium iron garnet (YIG, see Sect. 3.1.1) as the ferrimagnetic insulator and typical

SMR amplitudes of the order of $\rho_1/\rho_0 \approx 10^{-4} - 10^{-3}$ were found [10, 11, 27, 40, 48]. According to Eq. (2.7), the amplitude of the resistivity modulation ρ_1 depends on the spin diffusion length λ in the NM, the spin Hall angle Θ_{SH} and the real part of the spin mixing conductance G_r, i.e. parameters related to the normal metal layer and the interface. In particular, ρ_1 reaches a maximum for $d_{\mathrm{NM}} = 2\lambda$. In Pt $\lambda \approx 1.5\,\mathrm{nm}$, such that a maximum SMR ratio is observed for a Pt thickness $d_{\mathrm{NM}} = 3\,\mathrm{nm}$ [10]. While λ and G_r are mostly temperature independent, Θ_{SH} was found to decrease with decreasing temperature leading to a smaller SMR effect at low temperatures [40] (see Sect. 4.1).

Furthermore, the method used for the fabrication of the FMI/NM bilayer has a strong impact on the interface properties and spin Hall angle and consequently on the amplitude of the SMR effect. In particular, when the NM film is not deposited *in-situ* (without breaking the vacuum) onto the FMI, but on top of a FMI previously exposed to the environment (air, humidity, dirt, etc.), the interface quality can be affected. In order to ensure satisfying interface properties, the FMI surface can be treated for instance via chemical etching and/or laser annealing. A systematic study of the influence of the surface treatment for *ex-situ* NM layers on the SMR effect can be found in Ref. [48].

We now turn to the impact of the FMI properties on the SMR effect amplitude. In particular, first measurements of the SMR as a function of the FMI thickness in YIG/Pt bilayers were conducted recently [43]. The observed SMR ratio is independent of the YIG thickness, consistent with the theoretical model (Eq. (2.8)) where only the orientation of the magnetization is relevant for the SMR, but the magnetic volume or total magnetic moment in the FMI do not enter the model. Only for a YIG thickness of the order of one monolayer ($\approx 1-2\,\mathrm{nm}$ depending on the crystalline orientation) or less the SMR amplitude decreases [43]. In order to understand this behavior, a more detailed investigation of ultra-thin YIG films, in particular their magnetic properties, is required. However, these observations indicate that the SMR is not dominated by bulk effects and underline the importance of the topmost FMI layer (close to the interface) for spin transfer torque. Another example highlighting the relevance of the surface FMI layer will be discussed in Sect. 9.2.

In addition to measurements in YIG/Pt, the SMR effect has also been studied in other FMI/Pt bilayers with collinear ferrimagnets, such as $\mathrm{Fe_3O_4}$/Pt, $\mathrm{NiFe_2O_4}$/Pt, [10], $\mathrm{CoFe_2O_4}$/Pt [49], exhibiting similar SMR amplitudes of the order of $\rho_1/\rho_0 \approx 10^{-4}$. Note however, that a detailed quantitative comparison of the SMR amplitude in different material systems requires a systematic study of samples with similar properties (Pt thickness, fabrication method, etc.).

2.3 Microscopic modeling of the spin Hall magnetoresistance

2.3.1 Multi-sublattice ferrimagnet

As discussed in the previous section, the SMR was up to now mostly investigated in bilayers consisting of a collinear ferrimagnet, which can in general be described in a macrospin model [12]. However, the influence of different sublattices and non-collinear magnetic structures has not been studied in detail up to now. According to Eq. (2.7), the SMR amplitude depends on the spin mixing conductance, which is affected by the local magnetic moments in the FMI at the interface [45]. In this section, we therefore expand the current macrospin description to a microscopic model and assert that the SMR should be described in terms of individual contributions from magnetic moments residing on different sublattices. In particular, we no longer describe the resistivity modulation based on the orientation of the net magnetization $\mathbf{m} = \mathbf{M}/M$ as stated in Eq. (2.8) [12], but put forward a more general expression which takes into account the orientation of individual magnetic sublattice moments

$$\rho = \rho_0 + \sum_X \rho_{1,X} \left(1 - \langle (\mathbf{m}_{X,i} \cdot \mathbf{t})^2 \rangle_i \right) . \tag{2.12}$$

Here, $\rho_{1,X}$ is the sublattice specific SMR amplitude and $\mathbf{m}_{X,i} = \boldsymbol{\mu}_{X,i}/|\boldsymbol{\mu}_{X,i}|$ is the orientation of the individual magnetic moment $\boldsymbol{\mu}_{X,i}$. $\langle \cdots \rangle_i$ denotes the average over all moments i on sublattice X and allows to include non-collinear magnetic moment configurations or orientation fluctuations within one sublattice.

For simplicity we start our discussion based on a ferrimagnet consisting of two magnetic sublattices A and B with magnetic moments $\boldsymbol{\mu}_A$ and $\boldsymbol{\mu}_B$ tilted by the angles ξ_A and ξ_B with respect to the external magnetic field (see Fig. 2.3). This can be for example an antiferromagnet (or ferrimagnet) at high magnetic fields (spin flop phase) or a compensated ferrimagnet close to the compensation temperature T_{comp} (see Sect. 3.1.2 and 4.2). We first focus on the limit of a 2D system, in which the magnetic moments are confined to the **j**-**t** plane. The extension to three dimensions will be discussed in Sect. 2.3.4. Furthermore, we assume that all individual magnetic moments i within one sublattice X are collinear. Equation (2.12) then reads

$$\rho = \rho_0 + \sum_X \rho_{1,X} \left(1 - (\mathbf{m}_X \cdot \mathbf{t})^2\right). \tag{2.13}$$

When the sublattice moments are all collinear, Eq. (2.13) is equivalent to Eq. (2.8) for $\rho_1 = \sum_X \rho_{1,X}$, i.e. both macrospin and microscopic model yield the same SMR response. In particular, there is no easy way to distinguish ferromagnetic (single sublattice) and ferrimagnetic (multiple sublattice) collinear order in SMR experiments. This is due to the fact that the SMR is 180° symmetric and does not differentiate between parallel or antiparallel sublattice magnetization orientation with respect to the external field. For magnets with a non-collinear spin structure however, the microscopic and macrospin-based models yield qualitatively different SMR responses, as we will see in the following.

We discuss Eq. (2.13) based on the sublattice configuration depicted in Fig. 2.3. For comparison, the SMR response expected from a macrospin model, where the angular dependence of the resistivity ρ is given by the orientation of the net magnetic moment $\boldsymbol{\mu}$ (Eq. (2.8)), is displayed in Fig. 2.3 (a) and follows a $\cos^2(\alpha_\mathrm{H})$ dependence. The individual resistivity response for sublattices A and B, however, is plotted in Fig. 2.3 (b) and (c) for $\xi_A = 30°$ and $\xi_B = -56°$, respectively[2]. For each sublattice, the resistivity follows a $\cos^2(\alpha_\mathrm{H})$ dependence shifted by the sublattice moment canting angle, i.e. $\cos^2(\alpha_\mathrm{H} + \xi_{A,B})$. Using Eq. (2.13) and assuming for now that both sublattices contribute equally to the SMR, i.e. $\rho_{1,A} = \rho_{1,B} = \rho_1$, the total resistivity reads (see Appendix B for details on the calculations)

$$\begin{aligned}\rho &= \rho_0 + \rho_{1,A}\left(1 - (\mathbf{m}_A \cdot \mathbf{t})^2\right) + \rho_{1,B}\left(1 - (\mathbf{m}_B \cdot \mathbf{t})^2\right) \\ &= \rho_0 + \rho_{1,A}\cos^2(\alpha_\mathrm{H} + \xi_A) + \rho_{1,B}\cos^2(\alpha_\mathrm{H} + \xi_B) \\ &= \rho_0 + \rho_1(1 - \cos(\xi_A - \xi_B) + 2\cos(\xi_A - \xi_B) \cdot \cos^2(\alpha_\mathrm{H} + (\xi_A + \xi_B)/2)). \qquad (2.14)\end{aligned}$$

This corresponds to a $\cos^2(\alpha_\mathrm{H})$ dependence shifted by an angle $(\xi_A + \xi_B)/2 = (30° - 56°)/2 = -13°$, as indicated by the green dotted line in Fig. 2.3 (d). In the following, we therefore refer to this as a finite phase shift of the SMR angular dependence. The SMR response obtained by summing up contributions of individual magnetic sublattices according to Eq. (2.13) is therefore qualitatively different from the resistivity modulation expected in the macrospin model (see Fig. 2.3 (a)). Note that at this point, the focus lies on the angular dependence of the resistivity and not on the quantitative extraction of the SMR amplitude, since the latter crucially depends on the normalization chosen in different models. However, according to Eq. (2.14) the modulation amplitude and the constant offset of the resistivity also depend on the canting angle.

In addition to the canting angle, the relative contributions $\rho_{1,A,B}$ of the two sublattices also qualitatively impact the shift of the angular dependence (as well as the SMR amplitude). It is important to stress again that in the current theoretical model, the SMR contributions of different sublattices do not depend on the magnitude of the (bulk) sublattice magnetization vector $|\mathbf{M}_X|$, i.e. we assume that the SMR is not affected by the temperature dependence of the sublattice magnetization and is independent of the FMI thickness (see Sect. 2.2). This is also reflected in the microscopic description of the SMR, since only the projection of the normalized magnetization vector $\mathbf{m}_X$ enters Eq. (2.13). However, as discussed in Sect. 2.2 and 4.1, there are indications that the

---

[2] In Fig. 2.3 only angles in the range −90° to 270° are considered. Note that a positive (negative) canting angle shifts the $\cos^2(\alpha_\mathrm{H})$ function to the left (right).

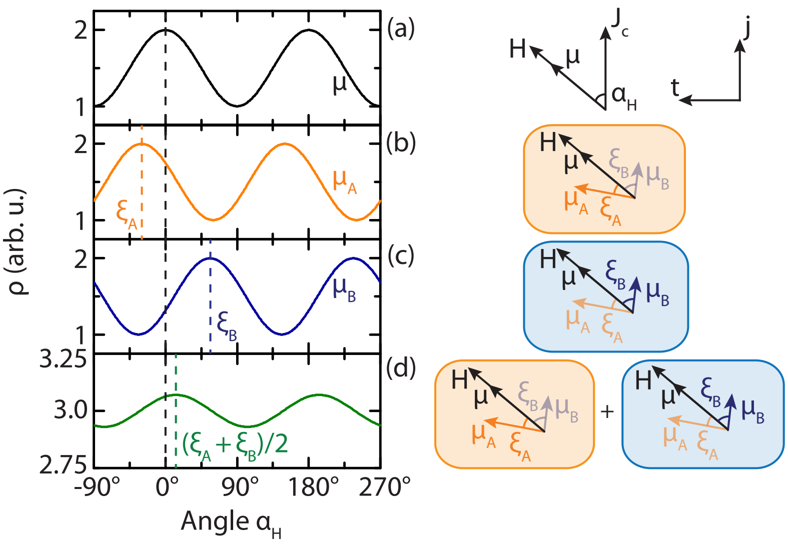

Figure 2.3: Expected SMR response in a two-sublattice FMI/Pt bilayer, where the magnetic moments $\boldsymbol{\mu}_A$ and $\boldsymbol{\mu}_B$ of sublattices A and B are tilted by angles ξ_A and ξ_B with respect to the external magnetic field $\mathbf{H}$. (a) Angular dependence of the Pt resistivity ρ in the macrospin model: the SMR is governed by the orientation of the net magnetic moment $\boldsymbol{\mu}$ which is aligned with the external magnetic field. The resistivity follows a $\cos^2(\alpha_\mathrm{H})$ dependence where α_H is the angle between the applied magnetic field and the current direction $\mathbf{j}$. (b) and (c) Expected angular dependence of ρ assuming that only sublattice A or B contribute to the SMR. The $\cos^2(\alpha_\mathrm{H})$ dependence is shifted by the respective canting angle $\xi_{A,B}$. (d) Total SMR response for equal contributions of both sublattices according to the microscopic model (Eq. (2.14)) with $\rho_{1,A} = \rho_{1,B} = \rho_1$. The angular dependence is shifted by a finite angle $(\xi_A + \xi_B)/2$ compared to the expectations of the macrospin model in panel (a).

magnetic moments at the interface are crucial for the amplitude of the SMR effect. In this context the surface termination, in particular the density of magnetic moments at the interface, may affect the SMR amplitude [49]. Such an effect is covered by our theoretical model, since the corresponding sublattice specific weighing factor can be included in $\rho_{1,A,B}$. This is already relevant for a collinear multi-sublattice ferrimagnet such as yttrium iron garnet (YIG, see Sect. 3.1.1 for details on the magnetic properties): YIG has two antiferromagnetically coupled Fe sublattices (denoted FeA and FeD), which are always antiparallel in experimentally available magnetic fields [50]. The angular dependence of the FeA and FeD sublattice contributions is therefore identical. However, the corresponding $\rho_{1,\mathrm{FeA}}$ and $\rho_{1,\mathrm{FeD}}$ may not be equal due to their different magnetic moment density (2:3, see Sect. 3.1.1). Using YIG/Pt bilayers with different crystal orientations and interface cuts allows to vary the magnetic moment density at the interface [51] and hereby enables a study of the impact of the latter on the SMR amplitude. Furthermore, the sublattice magnetization and more importantly the moment density at the interface can be systematically changed by doping the material with non-magnetic ions [50, 52] (see Sect. 11.2). As long as the exact distribution of the dopants on the magnetic sublattices is known [53], magnetoresistance measurements in this type of sample could allow for a more quantitative understanding of the SMR amplitude and the individual sublattice contributions $\rho_{1,X}$. Further information on the element specific contributions from magnetic moments residing on different sublattices may be gained from the quantitative analysis of the SMR in different material systems.

Coming back to the starting point of our discussion, we conclude that according to Eq. (2.14) a continuous phase shift of the SMR angular dependence is expected when the magnetic sublattice moments are canted with respect to the external magnetic field. The shift of the overall SMR signal depends on the canting angle and on the relative contributions or SMR efficiencies of the magnetic sublattices. From an experimental point of view, the canting angles can be measured directly by XMCD (see Sect. 4.2). However, this method requires beam time at a synchrotron facility and is inconvenient for a systematic study in many different material systems. A quantitative study of the element specific contributions to the SMR is also not straightforward and requires a thorough investigation in samples of comparable quality made of different magnetic materials. In other terms, quantitatively disentangling a SMR phase shift caused by a difference in canting angles from a phase shift originating from different SMR efficiencies $\rho_{1,A,B}$ of the magnetic sublattices is challenging in experiments and further investigations are necessary in the future.

2.3.2 Magnetic sublattice configurations in the canting phase (two dimensional limit)

So far we have tacitly assumed that the orientation of each sublattice is unique, i.e., there are no "sublattice domains". In this spirit, Fig. 2.3 displays a specific sublattice magnetization configuration with $\boldsymbol{\mu}_A$ and $\boldsymbol{\mu}_B$ tilted to the left and right, respectively. However, the orientation of the magnetic moments is determined by the minima of the free energy of the system, including contributions from external magnetic fields, exchange fields and anisotropies [54]. For (canted) sublattice magnetizations lying in the **j-t** plane, there are in general two energetically equivalent configurations mirrored with respect to the external magnetic field (see also Ref. [55]). This is exemplarily sketched in Fig. 2.4 (b) and (c) for sublattice A (orange and purple boxes, respectively). Unless one of the configurations is preferred (e.g. due to crystalline anisotropy), these two magnetic sublattice moment configurations are energetically equivalent. In the following we label the two orientations l (r) with moments $\boldsymbol{\mu}_{A,l}$ ($\boldsymbol{\mu}_{A,r}$) tilted by an angle ξ_A to the left ($-\xi_A$ to the right) with respect to the external magnetic field. The actual distribution of l and r configurations in the ferrimagnet will be discussed in more detail in Sect. 2.3.4. For now we only assume that two different orientations for magnetic moments residing on one specific sublattice are randomly distributed throughout the sample (see sketch in Fig. 2.5).

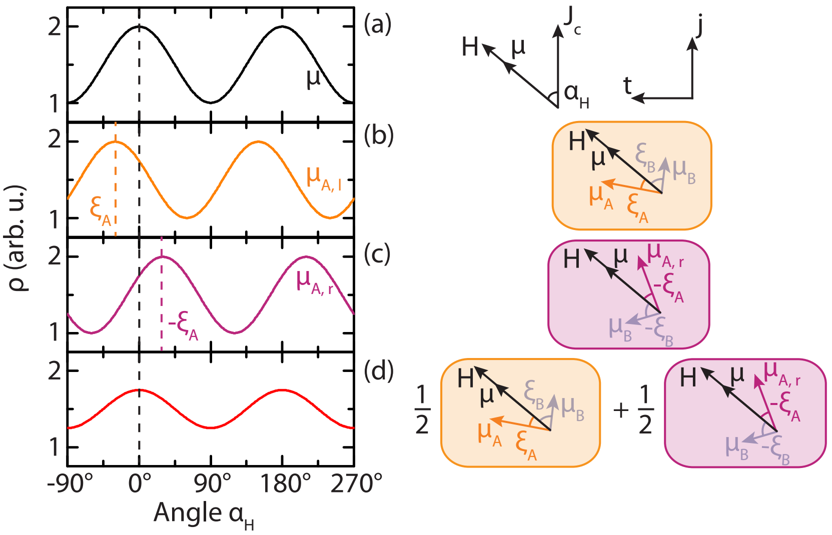

Figure 2.4: Expected angular dependence of the resistivity ρ assuming that only the magnetic moments in sublattice A contribute to the SMR. (a) SMR response based on the macrospin model where the net magnetic moment orientation $\boldsymbol{\mu}$ dominates the SMR. ρ follows a $\cos^2(\alpha_\mathrm{H})$ dependence with α_H the angle between the applied magnetic field $\mathbf{H}$ and the current direction $\mathbf{j}$. (b) and (c) SMR response for sublattice magnetic moments $\boldsymbol{\mu}_{A,l}$ and $\boldsymbol{\mu}_{A,r}$ tilted with respect to $\mathbf{H}$ by the angle ξ_A and $-\xi_A$, respectively. The $\rho(\alpha_\mathrm{H})$ angular dependence is shifted in opposite directions for the two configurations. (d) Total resistivity modulation assuming that both configurations r and l contribute equally, i.e. equal numbers of magnetic moments on sublattice A are tilted by $\pm\xi_A$. The extrema of the resulting angular dependence are at the same position as for the macrospin model, but the modulation amplitude is smaller.

In order to understand the influence of the distribution of the magnetic configurations on the SMR response, we focus on the magnetic moments residing on sublattice A (the same line of argument applies to sublattice B)[3]. In analogy to the two-sublattice model discussed in Sect. 2.3.1, two different SMR contributions shifted by ξ_A and $-\xi_A$ are expected from the two configurations as plotted in Fig. 2.4 (b) and (c). Assuming that both orientations are equally likely, the resistivity is given by a superposition of SMR responses according to Eq. (2.13) and reads

$$\begin{aligned}
\rho(\alpha_\mathrm{H}) &= \rho_0 + \rho_{1,A,l}\cos^2(\alpha_\mathrm{H}+\xi_A) + \rho_{1,A,r}\cos^2(\alpha_\mathrm{H}-\xi_A) && (2.15)\\
&= \rho_0 + \frac{1}{2}\rho_{1,A}\cos^2(\alpha_\mathrm{H}+\xi_A) + \frac{1}{2}\rho_{1,A}\cos^2(\alpha_\mathrm{H}-\xi_A) && (2.16)\\
&= \rho_0 + \frac{1}{2}\rho_{1,A}(1-\cos(2\xi_A) + 2\cos(2\xi_A)\cdot\cos^2(\alpha_\mathrm{H})) && (2.17)\\
&= \rho_0 + \rho_{1,A}(\sin^2(\xi_A) + \cos(2\xi_A)\cdot\cos^2(\alpha_\mathrm{H})) && (2.18)
\end{aligned}$$

---

[3] The presence of sublattice B in Fig. 2.4 is necessary to ensure the canting of the antiferromagnetically coupled sublattice moments.

where $\rho_{1,A,l} = \rho_{1,A,r} = \frac{1}{2}\rho_{1,A}$. Note that in Eq. (2.18), the weighing factors $\rho_{1,X}$ are proportional to the number of magnetic moments oriented along $\pm\xi_A$ and are normalized such that $\rho_{1,A,l} + \rho_{1,A,r} = \rho_{1,A}$. This allows for a quantitative comparison of the SMR response for different canting angles and magnetic sublattice moment configurations. The total resistivity response, i.e. the sum of the contributions stemming from both configurations, is plotted in Fig. 2.4 (d). Clearly, there is no more shift of the angular dependence and the extrema of the resistivity are at the same position as for the macrospin model depicted in Fig. 2.4 (a). This behavior is to be expected from Eq. (2.18), where a simple $\cos^2(\alpha_\mathrm{H})$ is obtained regardless of the tilting angle ξ_A. However, we find that the modulation amplitude of the resistivity

$$\Delta\rho = \rho(\alpha_\mathrm{H} = 0°) - \rho(\alpha_\mathrm{H} = 90°) \tag{2.19}$$

in Fig. 2.4 (d) is smaller compared to a scenario where $\xi_A = 0$ (equivalent to a collinear ferrimagnet in the macrospin model, see Fig. 2.4 (a)) or when all moments in sublattice A are aligned and tilted by ξ_A (Fig. 2.4 (b)). Indeed, according to Eq. (2.18), the amplitude of the resistivity modulation is

$$\Delta\rho = \rho_{1,A}\cos(2\xi_A) \tag{2.20}$$

and thus depends on the canting angle. Note that for a collinear system ($\xi_A = 0°$, $180°$) $\Delta\rho = \rho_{1,A}$, i.e. the resistivity modulation amplitude is given by the sublattice specific SMR efficiency.

To clarify the impact of the magnetic configurations on the phase shift and the modulation amplitude, the l and r configuration specific resistivity response for different canting angles $\xi_A = 10°$, $40°$ and $55°$ is exemplarily plotted in Fig. 2.5 (a) and (b). Similar to Fig. 2.4 (d), the corresponding total SMR response with equal contributions from both configurations according to Eq. (2.18) is displayed in Fig. 2.5 (c) for the different values of ξ_A. While no continuous phase shift is observed, the amplitude changes for different canting angles and the SMR response is even inverted for $\xi_A = 55°$ (dotted red line in Fig. 2.5 (c)). Figure 2.5 (d) depicts the normalized amplitude of the resistivity modulation $\Delta\rho/\rho_{1,A} = \cos(2\xi_A)$ as a function of the canting angle ξ_A given by Eq. (2.20). The three angles used in panels (a)-(c) are marked by the orange continuous, dashed and dotted lines in Fig. 2.5 (d). $\Delta\rho$ decreases with increasing canting angle until reaching zero for $\xi_A = 45°$. When further increasing the canting angle, $\Delta\rho$ changes sign, following the $\cos(2\xi_A)$ dependence obtained from Eq. (2.20). The phase shift of the SMR angular dependence, i.e. the position of the $\cos^2(\alpha_\mathrm{H})$ extrema, is plotted in Fig. 2.5 (e) and is zero independent of the canting angle. Note that the sign change of the SMR amplitude can also be interpreted as an abrupt phase change by 90° at $\xi_A = 45°$, while keeping the modulation amplitude positive. In this context, the maximum negative modulation

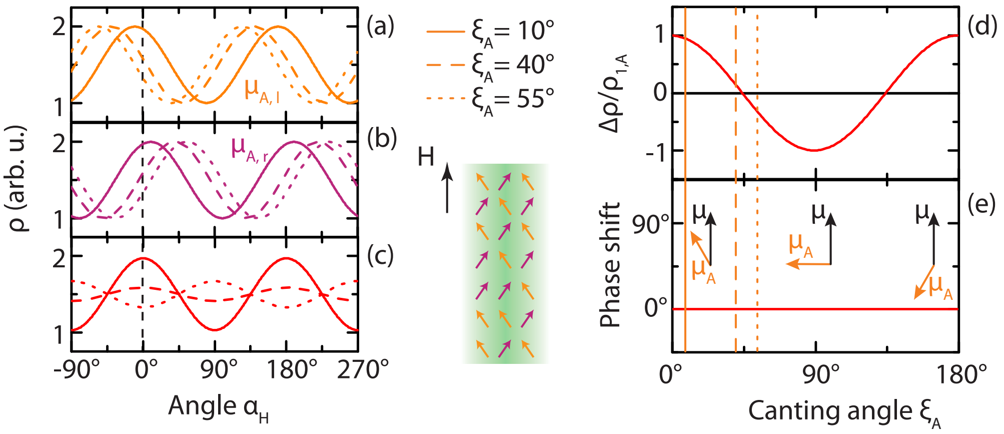

Figure 2.5: (a) and (b) Expected SMR response stemming from magnetic moments $\boldsymbol{\mu}_{A,l}$ and $\boldsymbol{\mu}_{A,r}$ oriented along $\pm\xi_A$ for different canting angles $\xi_A = 10^\circ$, 40° and 55°. (c) Total SMR response assuming an equal number of moments in l and r configuration for different canting angles. (d) Amplitude of the normalized resistivity modulation $\Delta\rho/\rho_{1,A}$ as a function of the canting angle ξ_A according to Eq. (2.20). The amplitude decreases with increasing canting angle and goes through zero at $\xi_A = 45^\circ$, leading to a sign change of $\Delta\rho$. (e) Phase shift of the resistivity angular dependence as a function of ξ_A. As expected from Eq. (2.18), no phase shift is observed.

amplitude obtained for $\xi_A = 90^\circ$ in Fig. 2.5 (d) can also be understood intuitively: for a collinear system where all sublattice moments are aligned with the external magnetic field ($\xi_A = 0^\circ$), $m_{A,t}(\alpha_\mathrm{H} = 0^\circ) = 0$ and $m_{A,t}(\alpha_\mathrm{H} = 90^\circ) = 1$. When the sublattice magnetic moments are perpendicular to the external magnetic field ($\xi_A = 90^\circ$), the magnetic field orientations corresponding to the maximum and minimum of $m_{A,t}$ are inverted (or shifted by 90°). Consequently, the SMR angular dependence is shifted by 90°, or in other words the modulation amplitude $\Delta\rho$ calculated according to Eq. (2.20) changes sign compared to the collinear configuration.

For a ferrimagnet where both sublattices A and B contribute to the SMR (see Sect. 2.3.1), the same line of argument can be applied to sublattice B. As long as the moments residing on sublattice B are also equally distributed between l and r configurations, the individual sublattice responses and consequently the total resistivity yield no phase shift.

We will see later on in Sect. 4.2 that the behavior predicted in this model based on multiple energetically equivalent magnetic moment configurations is indeed observed experimentally in the magnetic canting phase of the compensated garnet (In,Y) doped GdIG (InYGdIG). In particular, an inversion of the SMR amplitude but no continuous phase shift is observed when crossing the canting phase, i.e. changing the sublattice canting angles[4].

---

[4] The corresponding data was published in Ref. [30]. A similar behavior is observed in pure GdIG and dysprosium iron garnet (DyIG) [55].

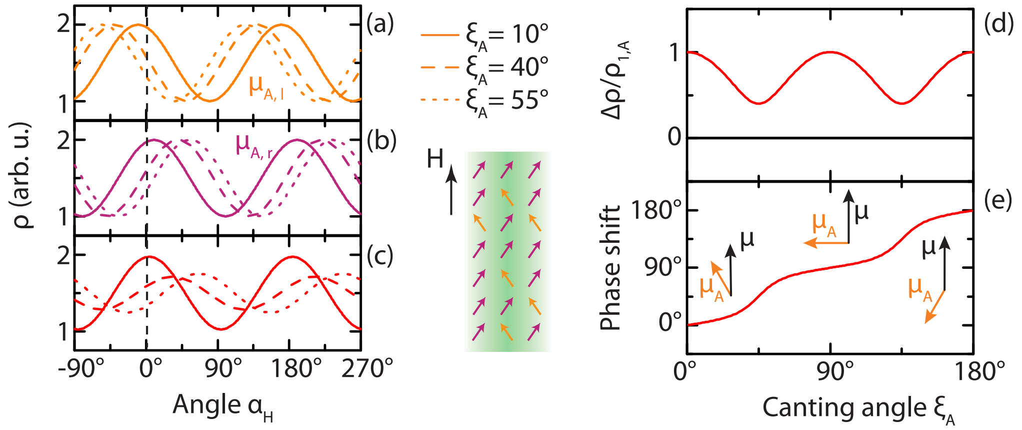

Figure 2.6: (a) and (b) Expected SMR response stemming from configurations l and r for different canting angles $\xi_A = 10°$, $40°$ and $55°$. (c) Corresponding total SMR response assuming 30% and 70% of the magnetic moments in l and r type configurations, respectively. (d) Amplitude $\Delta\rho = \rho_{\text{max}} - \rho_{\text{min}}$ of the resistivity modulation as a function of the canting angle ξ_A according to Eq. (2.21). The amplitude oscillates when changing the canting angle. (e) Phase shift, i.e. position of the resistivity maximum, as a function of ξ_A. The phase shift increases continuously with increasing canting angle.

2.3.3 Origin of a continuous SMR phase shift

We now turn to a scenario where the number of magnetic moments oriented along $\pm\xi_A$ are no longer equal, such that one orientation dominates, as sketched in Fig. 2.6. For this discussion we choose a distribution ratio of 30 : 70 for l and r configurations. The expected angular dependence for a configuration where all moments point along ξ_A (l) and $-\xi_A$ (r) is depicted in Fig. 2.6 (a) and (b), respectively, for $\xi_A = 10°$, $40°$ and $55°$. Based on Eq. (2.13), the total resistivity for an unequal magnetic configuration distribution becomes (see Appendix B)

$$\begin{aligned}
\rho(\alpha_{\text{H}}) &= \rho_0 + \rho_{1,A,l}\,\cos^2(\alpha_{\text{H}} + \xi_A) + \rho_{1,A,r}\,\cos^2(\alpha_{\text{H}} - \xi_A) \\
&= \rho_0 + \frac{\rho_{1,A,l} + \rho_{1,A,r}}{2} + \frac{\rho_{1,A,l} + \rho_{1,A,r}}{2}\cos(2\xi_A)\left(2\cos^2(\alpha_{\text{H}}) - 1\right) \\
&- \frac{\rho_{1,A,l} - \rho_{1,A,r}}{2}\sin(2\xi_A)\left(2\cos^2(\alpha_{\text{H}} - 45°) - 1\right). \qquad (2.21)
\end{aligned}$$

For the exemplary 30:70 ratio with $\rho_{1,A,l} = 3/10 \cdot \rho_{1,A}$ and $\rho_{1,A,r} = 7/10 \cdot \rho_{1,A}$ such that $\rho_{1,A,l} + \rho_{1,A,r} = \rho_{1,A}$, the result is plotted in Fig. 2.6 (c) for the different canting angles. Similar to our previous results, the total SMR response also follows a $\cos^2(\alpha_{\text{H}})$ type angular dependence. However, in contrast to the equally distributed moment configuration in Fig. 2.5, the position of the total resistivity extrema is no longer independent of the canting angle. This phase shift, i.e. the position of the resistivity maximum extracted from Fig. 2.6 (c), is plotted in Fig. 2.6 (e) as a function of the canting angle ξ_A. The phase shift continuously increases from 0° to 180° when ξ_A increases. This behavior is reflected in Eq. (2.21), as the total resistivity is the sum of a $\cos^2(\alpha_\mathrm{H})$ and $\cos^2(\alpha_\mathrm{H} - 45°)$ function. The obtained phase shift depends on the respective prefactors which are linked to the canting angle via $\cos(2\xi_A)$ and $\sin(2\xi_A)$. Furthermore, the modulation amplitude $\Delta\rho = \rho_\mathrm{max} - \rho_\mathrm{min}$ also oscillates as a function of the canting angle, as shown in Fig. 2.6 (d). In particular, the resistivity reaches a maximum when the sublattice moments are collinear ($\xi_A = 0°$ or 180°) or exactly perpendicular ($\xi_A = 90°$) to the applied magnetic field.

The microscopic model presented here can therefore also give rise to a continuous phase shift in the SMR response, assuming an unequal distribution of the l and r oriented magnetic moments within one sublattice. This kind of phase shift was indeed qualitatively observed in SMR experiments conducted in erbium iron garnet (ErIG)/Pt bilayers [56, 57], although the experimental results are not fully understood to date. This raises the question what the origin of such an asymmetric configuration is. A preferred direction for the sublattice magnetic moments, such that the r and l configurations are no longer energetically equivalent, can be obtained by introducing hard and easy magnetic axes, e.g. a crystalline magnetic anisotropy which was neglected up to now. A similar effect can be induced by strain and magnetoelastic effects [58], for instance due to a lattice mismatch of the ferrimagnetic thin film and the substrate.

Note that when taking into account anisotropic effects, the resulting magnetic configuration becomes even more complex, since the orientation of the magnetic moments is determined by minimizing the total free energy. The latter includes the Zeeman energy provided by the external field H, the anisotropy energy and the exchange energy between different sublattices. In addition to an unequal distribution of r and l configurations with opposite canting angles $\pm\xi_A$, anisotropies can therefore also lead to configurations with different canting angles within one sublattice. This is depicted in Fig. 2.7 in a simplified sketch: panel (a) represents the magnetic moment configuration in an isotropic magnet for $\alpha_\mathrm{H} = 40°$, where all sublattice A moments are canted by $\pm\xi_A$ with respect to the applied field, corresponding to the two orientations of minimum energy. By introducing for example a uniaxial anisotropy, i.e. an easy axis along the blue line in Fig. 2.7 (b), the purple moments tilt closer to the easy axis in order to minimize the free energy. In this specific configuration, two different canting angles for moments residing on the same sublattice are obtained. We can then apply the multi-sublattice picture discussed in Sect. 2.3.1 (see Fig. 2.3) with canting angles $\xi_{A,l} \neq \xi_{A,r}$, also leading to a phase shift of the SMR angular dependence. We would like to emphasize here, that due to the anisotropic nature of the energy landscape, the canting angles can also vary during an in-plane rotation of the applied magnetic field. Figure 2.7 (c) depicts the scenario where the applied field is exactly perpendicular to the easy axis, such that the magnetic system is again symmetric with respect to the external field and we find $|\xi_{A,l}(\alpha_\mathrm{H} = 90°)| = |\xi_{A,r}(\alpha_\mathrm{H} = 90°)|$, i.e.

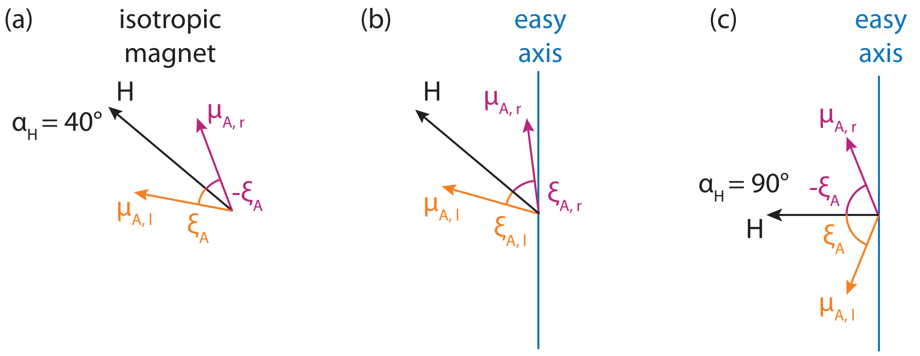

Figure 2.7: Configuration of the magnetic moments residing on sublattice A. (a) For an isotropic system, there are two energetically equivalent orientations with respect to the external field $\mathbf{H}$, i.e. $\pm\xi_A$, as sketched in Fig. 2.4. (b) When introducing a uniaxial anisotropy with an easy axis along the blue line, there can be two energetically equivalent configurations exhibiting different canting angles $\xi_{A,l} \neq \xi_{A,r}$ with respect to the external magnetic field. (c) The canting angle may furthermore depend on the orientation of the magnetic field with respect to the easy axis. For $\alpha_\mathrm{H} = 90°$, the system is symmetric with respect to the applied field such that the absolute value of the canting angles in both l and r configurations is the same.

the absolute value of the canting angles within sublattice A are the same. In a system with strong anisotropies, the angular dependence can therefore deviate from a simple $\cos^2(\alpha_\mathrm{H})$ dependence (with or without phase shift) as we will see in Sect. 9.2. In general, the magnetic configuration depends on the relative strengths and orientations of the contributions to the effective magnetic field which acts on the sublattice moments.

Based on our theoretical model, we conclude that a phase shift in the SMR angular dependence can originate from different canting angles of moments within one sublattice, or to an unequal distribution of moments tilted to the left and right with respect to the magnetic field. In both scenarios, the phase shift of the SMR response reflects a symmetry breaking in the magnetic system, or in more general terms, an anisotropic energy landscape.

2.3.4 Magnetic sublattice configurations in the canting phase (three dimensions)

So far, the discussion of sublattice magnetic moment configurations was limited to the sample plane, with two energetically equivalent magnetic moment orientations, which we labeled l and r configurations (see Fig. 2.4). In experiments however, this description is not sufficient since the magnetic moments can also exhibit out of plane components such that 3D modeling is required. Accordingly, in an isotropic three dimensional system there are no longer only two energetically equivalent in-plane moment configurations with canting angles $\pm\xi_A$. Rather, the magnetic moments are distributed on a cone with opening angle ξ_A around the magnetic field axis as sketched in Fig. 2.8 (a). In an infinite 3D bulk

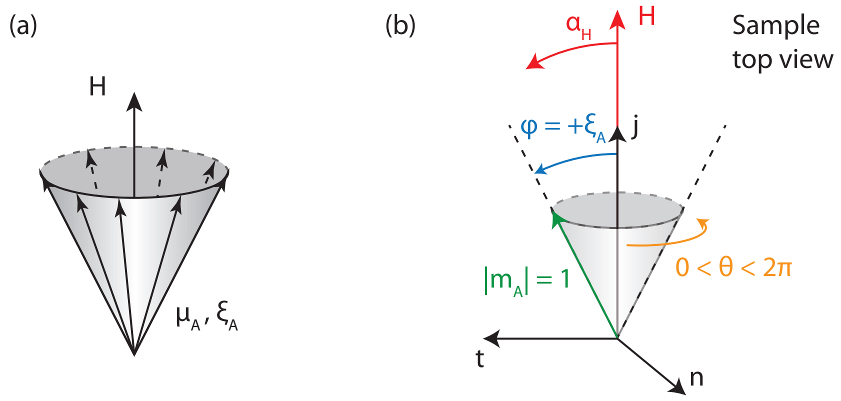

Figure 2.8: (a) Sketch of a cone representing all energetically equivalent orientations of the sublattice moment $\boldsymbol{\mu}_A$ in the canting phase. The opening angle of the cone corresponds to the canting angle ξ_A with respect to the external magnetic field. (b) Representation of the unit magnetic moment vector $\mathbf{m}_A = \boldsymbol{\mu}_A/|\boldsymbol{\mu}_A|$ in spherical coordinates with $r = 1$, $\varphi = \xi_A$ the canting angle and $0 < \theta < 2\pi$ the position on the cone. The magnetic field is rotated in the sample plane **j-t** by an angle α_{H}.

system without anisotropy the energy landscape is radially symmetric with respect to the applied magnetic field, such that no preferred orientation on this cone is imposed onto the sublattice moments (see also Appendix B). The concept of a finite number of possible orientations as depicted in Fig. 2.5 and 2.6, where regions with different magnetic configurations are clearly delimited, is then no longer applicable. A continuous distribution on the cone is more realistic, since the magnetic sublattice moments can assume any of the energetically equivalent orientations with canting angle ξ_A[5].

In experiments, i.e. at finite temperature, the orientation of the sublattice moments is also affected by thermal fluctuations, which lead to additional fluctuations of the canting angle around the equilibrium position. However, in the following we focus on a simplified model where the thermal fluctuations of the canting angle are neglected and we consider a constant (average) ξ_A (for a magnetically isotropic system).

In order to take into account the continuous distribution of the magnetic moments on the cone, we apply Eq. (2.12) and calculate the average contribution from all orientations on the cone to the resistivity response. In spherical coordinates the orientation of the magnetic moment unit vector is $\mathbf{m}_A = \boldsymbol{\mu}_A/|\boldsymbol{\mu}_A| = (r, \varphi, \theta)$, where $r = 1$ is the radial component, $\varphi = \xi_A$ is the canting angle or cone opening angle and $0 < \theta < 2\pi$ describes the position on the cone. This is sketched in Fig. 2.8 (b) for a magnetic field $\mathbf{H}$ applied in the sample plane along $\mathbf{j}$. In cartesian coordinates $\mathbf{m}_A$ reads

---

[5] Note that the ferromagnetic exchange coupling between magnetic moments residing on the same sublattice tends to align these moments. This may also affect the spatial distribution of the moment orientations, as neighboring magnetic moments prefer a collinear configuration (see Appendix B).

$$\begin{pmatrix} m_{A,j} \\ m_{A,t} \\ m_{A,n} \end{pmatrix} = \begin{pmatrix} \cos(\xi_A) \\ \sin(\xi_A)\sin(\theta) \\ \sin(\xi_A)\cos(\theta) \end{pmatrix} \tag{2.22}$$

Due to the geometry of the SMR effect [10], the out of plane magnetization component does not contribute to the longitudinal resistivity modulation for an in-plane magnetic field rotation as measured in Sect. 4.2. It is therefore sufficient to discuss the projection $m_{A,t}$ of the magnetic moments onto the **t** direction. In the coordinate system chosen in Fig. 2.8 (b) $m_{A,t}(\theta = 0) = 0$ and the out of plane component $m_{A,n}(\theta = 0)$ reaches a maximum.

We now discuss the dependence of the projection $m_{A,t}$ on the in-plane magnetic field orientation for a rotation in the **j**-**t** plane. This is achieved by applying the rotation matrix $R_{\mathbf{n}}$ about the **n** direction to the magnetic moment orientation $\mathbf{m}_A$

$$R_{\mathbf{n}}\mathbf{m}_A = \begin{pmatrix} \cos(\alpha_{\mathrm{H}}) & -\sin(\alpha_{\mathrm{H}}) & 0 \\ \sin(\alpha_{\mathrm{H}}) & \cos(\alpha_{\mathrm{H}}) & 0 \\ 0 & 0 & 1 \end{pmatrix} \begin{pmatrix} \cos(\xi_A) \\ \sin(\xi_A)\sin(\theta) \\ \sin(\xi_A)\cos(\theta) \end{pmatrix} \tag{2.23}$$

Here, α_{H} is the angle between the magnetic field **H** and the **j** direction, as sketched in Fig. 2.8 (b). We obtain

$$m_{A,t}(\alpha_{\mathrm{H}}, \theta) = \sin(\alpha_{\mathrm{H}})\cos(\xi_A) + \cos(\alpha_{\mathrm{H}})\sin(\xi_A)\sin(\theta). \tag{2.24}$$

Assuming equally distributed moment orientations on the cone, the average $\langle m_{A,t}^2 \rangle$ is given by the integral over θ from 0 to 2π normalized to 2π, such that Eq. (2.12) yields[6]:

$$\begin{aligned} \rho(\alpha_{\mathrm{H}}) &= \rho_0 + \rho_{1,A}\left(1 - \langle (m_{A,t}(\alpha_{\mathrm{H}}, \theta))^2 \rangle\right) \\ &= \rho_0 + \rho_{1,A}\left(1 - \int_0^{2\pi} \mathrm{d}\theta \frac{1}{2\pi}\left(\sin(\alpha_{\mathrm{H}})\cos(\xi_A) + \cos(\alpha_{\mathrm{H}})\sin(\xi_A)\sin(\theta)\right)^2\right) \\ &= \rho_0 + \rho_{1,A}\left(1 + \frac{1}{8}\left(-3 - \cos(2\xi_A) + \cos(2\alpha_{\mathrm{H}})(1 + 3\cos(2\xi_A))\right)\right). \end{aligned} \tag{2.25}$$

In analogy to the 2D limit, we obtain a $\cos(2\alpha_{\mathrm{H}})$ dependence (which can easily be rewritten as a $\cos^2(\alpha_{\mathrm{H}})$ dependence using Eq. (B.1)) where the phase of the overall angular dependence is constant and independent of the canting angle. This can be understood intuitively since the individual phase shifts of the resistivity contributions stemming from moments mirrored with respect to the applied field cancel out. The amplitude of the resistivity modulation

$$\Delta\rho = \rho(\alpha_{\mathrm{H}} = 0°) - \rho(\alpha_{\mathrm{H}} = 90°) = \frac{1}{4}\rho_{1,A}(1 + 3\cos(2\xi_A)) \tag{2.26}$$

---

[6] Calculated using Wolfram Mathematica.

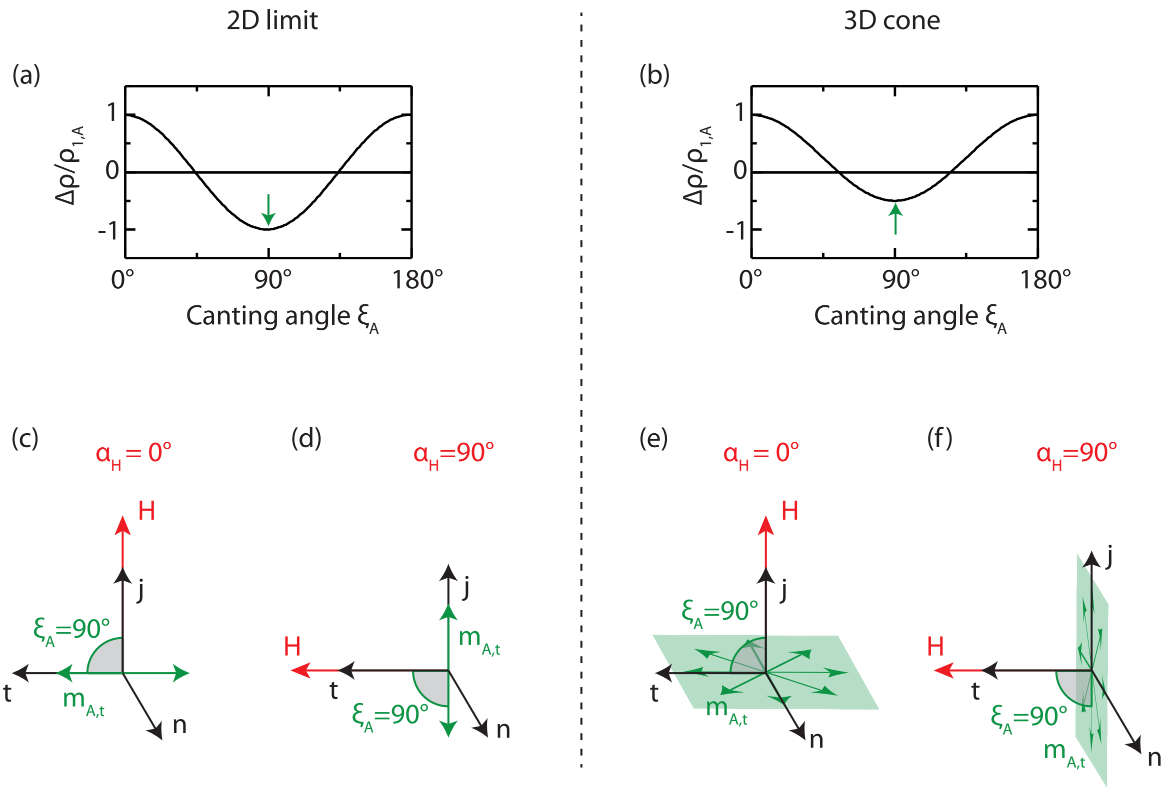

Figure 2.9: (a) Amplitude of the resistivity modulation $\Delta\rho/\rho_{1,A}$ in the 2D limit according to Eq. (2.20) as a function of the canting angle ξ_A. Here, $|\Delta\rho|$ is identical for $\xi_A = 0^\circ$ (collinear phase) and $\xi_A = 90^\circ$ (perpendicular configuration). (b) Amplitude of the resistivity modulation for the 3D cone model calculated according to Eq. (2.26). $|\Delta\rho|$ for $\xi_A = 90^\circ$ is smaller in the 3D scenario compared to the 2D limit. (c) and (d) Sketch of the magnetic moment orientations residing on sublattice A for a canting angle of $\xi_A = 90^\circ$ and in-plane magnetic field orientations $\alpha_\mathrm{H} = 0^\circ$ and 90°, respectively. In the 2D limit the moments represented by green arrows are confined to the **j**-**t** plane. (e) and (f) Sketch of the energetically equivalent orientations in 3D for moments on sublattice A with a canting angle $\xi_A = 90^\circ$. In an isotropic system the moments can assume any orientation within the green plane perpendicular to the applied field and exhibit a finite out of plane component.

however depends on the canting angle and is plotted in Fig. 2.9 (b). Interestingly, the dependence of the modulation amplitude on the canting angle obtained in Eq. (2.26) is different from the one calculated in the 2D model (Eq. (2.20)) which is displayed in Fig. 2.9 (a) for comparison. While the overall dependence on ξ_A looks very similar, exhibiting a sign change in both scenarios, in the 3D model $\Delta\rho$ changes sign only for $\xi_A \approx 54^\circ > 45^\circ$ and furthermore $|\Delta\rho(\xi_A = 0^\circ)| > |\Delta\rho(\xi_A = 90^\circ)|$.

In order to understand this behavior, we sketch the magnetic moment configurations of sublattice A for an in-plane magnetic field in the extreme case of $\xi_A = 90^\circ$ (Fig. 2.9). In the two dimensional limit, there are only two possible orientations (green arrows in Fig. 2.9 (c) and (d)), such that for $\alpha_\mathrm{H} = 0^\circ$ the moments orient along the $\pm\mathbf{t}$ direction and $m^2_{A,t}(\alpha_\mathrm{H} = 0°) = 1$, while for $\alpha_\mathrm{H} = 90°$ all moments point along the $\pm\mathbf{j}$ direction and $m^2_{A,t}(\alpha_\mathrm{H} = 90°) = 0$. Therefore, the modulation amplitude for a canting angle $\xi_A = 90°$ is $\Delta\rho = -\rho_{1,A}$ (see Fig. 2.9 (a)).

In three dimensions however, for a canting angle of $\xi_A = 90°$ the moments on the cone lie in the plane perpendicular to the magnetic field direction as indicated by the arrows in the green plane in Fig. 2.9 (e) and (f). In particular, for $\alpha_\mathrm{H} = 0°$, all moments reside in the **t**-**n** plane (Fig. 2.9 (e)). While the moments oriented exactly along **t** still give rise to a maximum $m^2_{A,t} = 1$, all moments with an out of plane component along **n** yield $m^2_{A,t} < 1$. On average, $\langle m^2_{A,t}(\alpha_\mathrm{H} = 0°)\rangle < 1$ for the 3D cone is therefore smaller than in the 2D limit, where $\langle m^2_{A,t}(\alpha_\mathrm{H} = 0°)\rangle = 1$. For $\alpha_\mathrm{H} = 90°$, all moments reside in the **j**-**n** plane, such that $m^2_{A,t}$ is always zero (Fig. 2.9 (f)). The amplitude of the resistivity modulation for the 3D scenario obtained from Eq. (2.26) then yields $\Delta\rho = -1/2\rho_{1,A}$ (see Fig. 2.9 (b)). Note that in the collinear phase, i.e. for $\xi_A = 0$, all magnetic moments point along the magnetic field in both 2D and 3D. Thus, for $\xi_A = 0$ the amplitude of the resistivity modulation $\Delta\rho = \rho_{1,A}$ is equal for both scenarios (see Fig. 2.9 (a) and (b)). In this context, we would like to emphasize once more that we are interested in the relative change of the modulation amplitude as a function of the canting angle. All sublattice specific SMR parameters (element and magnetic moment density dependent factors) can be included in $\rho_{1,A}$.

From this simple model where the magnetic sublattice moments lie on a three dimensional cone, we conclude that no phase shift in the SMR response is expected as long as each orientation has equal probability. In this regard, the 2D and 3D models therefore yield similar results. Comparing $\Delta\rho$ in the collinear phase ($\xi_A = 0°$) and for $\xi_A = 90°$ can furthermore indicate whether the magnetic moments are confined to the sample plane (2D) or have additional out of plane components suggesting a conical moment distribution[7]. Good candidates for an experimental verification of this prediction are conical/helical magnets. First SMR measurements in the conical spiral phase of $\mathrm{Cu_2OSeO_3}$ (CSO) [59] have indeed recently been put forward. In CSO the axis of the magnetic spiral orients along the external magnetic field, such that for **H** applied in the sample plane the SMR probes the different magnetic moment orientations on a cone. In Ref. [59], no phase shift is observed in the SMR, indicating that the magnetic moment orientations are equally distributed on the conical spiral. Furthermore the sign of the SMR amplitude changes from negative to positive when the magnetic field is increased, i.e. when the cone angle is decreased from close to 90° until reaching a collinear configuration. These results are consistent with the theoretical model presented here. We can therefore also apply this generalized microscopic SMR model to conical magnets in order to gain insight into the magnetic moment orientations in 3 dimensions[8].

---

[7] A more general discussion of the difference between these two scenarios in terms of their free energy landscape will be presented later on (see also Appendix B).

[8] The SMR amplitude for large cone angles (close to 90°) predicted by the theoretical model in CSO in Ref. [59] is smaller than the amplitude observed in experiments. Since their model is based on

On a more general note, whether a system requires a description in 2D or 3D depends on the free energy landscape. The latter can be deformed by an anisotropy leading to hard and easy magnetic axes or planes. Instead of the conical distribution sketched in Fig. 2.8 (a), i.e. a radially symmetric energy minimum with respect to the applied field, an easy plane (e.g. the **j**-**t** plane) gives rise to local minima on the cone, corresponding to the energetically most favorable orientations. A 2D description may therefore become relevant for thin magnetic films where the demagnetization field leads to a preferred in-plane orientation of the moments. In order to give an intuitive picture of this effect, the influence of a uniaxial anisotropy on the magnetic moment configurations is qualitatively discussed in Appendix B. As discussed in Sect. 2.3.2, as long as there is no additional anisotropy, no SMR phase shift is expected for an in-plane magnetic field rotation in the 2D limit.

However, similar to the asymmetry described in the 2D limit in Sect. 2.3.3, additional, more complex anisotropies can lead to an unequal distribution of the magnetic moment orientations on the three dimensional cone. Depending on the magnetic field orientation with respect to an anisotropy axis, the cone may also be deformed, giving rise to different canting angles within one sublattice, similar to the scenario depicted in Fig. 2.7. If the deformation of the cone corresponds to a symmetry breaking with respect to the magnetic field, this can give rise to a phase shift of the SMR response in analogy to the 2D limit. We would like to emphasize that a detailed description of the magnetic moment configuration in a real three dimensional system can be very complex, in particular since the SMR is mostly sensitive to the orientation of magnetic moments at the interface, where additional effects such as surface roughness and defects come into play.

In summary, we have discussed the expected spin Hall magnetoresistance response of a model ferrimagnet with two canted magnetic sublattices in a microscopic model, assuming that all magnetic moments contribute individually to the SMR. In general, the resistivity response of each sublattice magnetic moment depends on the orientation of the magnetic field $\mathbf{H}$ with respect to the current direction $\mathbf{j}$ and follows a $A\cos^2(\alpha_\mathrm{H}+\phi)$ dependence. The amplitude A and phase ϕ of these $\cos^2$ functions are determined by both the sublattice specific SMR efficiency (usually parametrized as $\rho_{1,X}$) and the sublattice canting angles. The total resistivity of the FMI/Pt bilayer is given by the sum of all sublattice contributions and therefore also follows a $\cos^2$ type dependence. In particular, the model proposed here includes the possibility of multiple energetically equivalent magnetic moment orientations within one sublattice, which we discussed in the 2D limit as well as in 3 dimensions. The orientation of the individual magnetic moments and consequently the amplitude and phase shift of the SMR angular dependence is affected by

---

a 3D distribution of the moments on the cone, the larger experimental amplitude may indicate a confinement (possibly due to surface effects) of the moments to the sample plane as discussed in this section. However, as CSO exhibits a multi-domain state in the helical phase ($\xi = 90°$) the verification of this hypothesis requires further study.

anisotropy contributions or in more general terms by the symmetry of the magnetic system. By comparison with experimental results the model proposed here can give insights into the magnetic moment configurations in real systems, as we will see in Sect. 4.2, and is therefore of key importance for the future study of the SMR effect in systems with complex magnetic structures.

Chapter 3

Sample properties and experimental details

3.1 Material systems

In Chap. 4 we will present experimental results from SMR measurements conducted in two different FMI/NM bilayers. As discussed in Sect. 2.1, we choose Pt as the NM, since Pt exhibits strong spin orbit coupling and allows for an efficient electron charge to spin current conversion (and vice versa) via the SHE (ISHE). For the FMI layers we use yttrium iron garnet (YIG) and gadolinium iron garnet (GdIG). The crystalline and magnetic properties of these two material systems will be introduced in detail in the following.

3.1.1 Collinear ferrimagnet yttrium iron garnet

As previously mentioned in Sect. 2.2, most SMR experiments to date have been performed on bilayers containing the ferrimagnetic insulator yttrium iron garnet ($Y_3Fe_5O_{12}$, YIG), which has a bandgap of 2.8 eV [60, 61]. YIG has a body-centered-cubic (bcc) crystal structure. The conventional unit cell has a lattice constant $a = 1.24\,\mathrm{nm}$ [52, 62] and contains 8 times the formula unit (see Ref. [63]). The middle-layer of the YIG unit cell is depicted in Fig. 3.1 (a), where the O^{2-} ions are represented in dark blue. The dodecahedrally coordinated Y^{3+} (light blue in Fig. 3.1 (a)) has a noble gas electron configuration and therefore carries no magnetic moment. The magnetic properties of YIG originate from two octahedrally coordinated Fe^{3+} moments (FeA, green in Fig. 3.1 (a)) and three tetrahedrally coordinated Fe^{3+} moments (FeD, orange) per formula unit, each ion carrying spin $S = 5/2$. The FeA and FeD moments within one sublattice are ferromagnetically coupled by exchange energies $J_{\mathrm{AA}} = 0.92 \times 10^{-21}\mathrm{J}$ and $J_{\mathrm{DD}} = 3.24 \times 10^{-21}\mathrm{J}$, respectively [64]. Furthermore, the two Fe sublattices are strongly antiferromagnetically coupled by $J_{\mathrm{AD}} = -9.6 \times 10^{-21}\mathrm{J}$ [64]. YIG therefore is a collinear two-sublattice ferrimagnet and the total magnetization $\mathbf{M}$ is given by the net Fe magnetization $\mathbf{M}_{\mathrm{Fe,net}}$. The latter can be calculated at $T = 0\,\mathrm{K}$ as

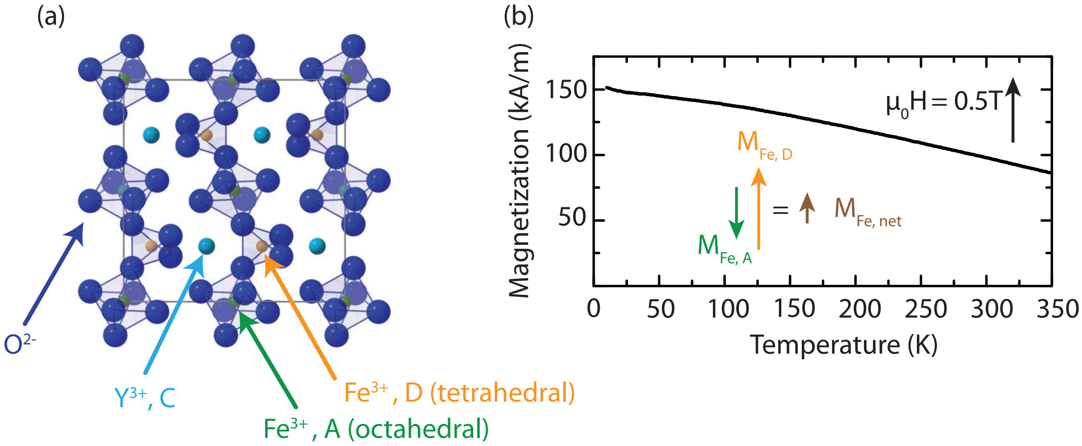

Figure 3.1: (a) Middle layer of the unit cell of the ferrimagnetic insulator yttrium iron garnet (YIG) with two magnetic sublattices FeA and FeD (courtesy of S. Geprägs, WMI). (b) Typical SQUID magnetometry measurement of a YIG thin film as a function of temperature for a fixed external magnetic field $\mu_0 H = 0.5\,\mathrm{T}$. Since the two Fe sublattices are antiparallel in the whole temperature range, YIG can be described as a single sublattice ferromagnet with a net Fe magnetization $\mathbf{M}_{\mathrm{Fe,net}}$.

$$M^0_{\mathrm{Fe,net}} = M^0_{\mathrm{FeD}} - M^0_{\mathrm{FeA}} = \frac{N_{\mathrm{FeD}} - N_{\mathrm{FeA}}}{V} g_{\mathrm{Fe}} S \mu_{\mathrm{B}} = 194.5\,\mathrm{kA/m} \tag{3.1}$$

where N_X is the number of magnetic ions per unit cell on sublattice X, $V = a^3$ is the volume of the unit cell, μ_{B} is the Bohr magneton and we use $g_{\mathrm{Fe}} = 2.01$ [65] as the g factor of YIG. This magnetization value is indeed observed experimentally at low temperatures for bulk YIG crystals [65, 66]. Figure 3.1 (b) displays a typical temperature dependent SQUID magnetometry measurement of a YIG thin film grown via pulsed laser deposition (PLD)[1] (see Sect. 3.2), similar to the one studied in Sect. 4.1. The net magnetization of the thin film measured at low temperatures is lower than the bulk literature value and the one expected from calculations. This deviation can be attributed to oxygen vacancies in the YIG thin film. We furthermore observe a monotonic decrease of the YIG magnetization with increasing temperature. This is consistent with theoretical expectations as the YIG magnetization follows a Brillouin function (see Ref. [68, 69] for details) and decreases monotonically with temperature until reaching the ferrimagnetic ordering temperature (Curie temperature) $T_{\mathrm{C}} = 559\,\mathrm{K}$ [70].

YIG exhibits a crystalline cubic anisotropy [71], determining easy and hard axes for the magnetization orientation. The anisotropy field extracted via ferromagnetic resonance measurements (FMR) in a YIG sphere is of the order of a few mT [65]. An additional shape anisotropy field (determined by the net magnetization magnitude) needs to be

---

[1] The sample fabrication and the SQUID magnetometry measurement were done by S. Altmannshofer during his master's thesis at WMI [67].

considered in thin films when tilting the magnetization out of the sample plane. In our experiments, we typically rotate a magnetic field $\mu_0 H \geq 0.5\,\mathrm{T}$ in the sample plane such that the net magnetization, and in particular the Fe sublattice moments, are always aligned (anti-)parallel to the external field. Note that for magnetic fields larger than $\mu_0 H_{c1} \approx 250\,\mathrm{T}$, the FeA and FeD magnetic moments start to cant with respect to the applied magnetic field [15, 50, 72, 73]. However, these magnetic field magnitudes are not available in typical experimental setups, such that we consider YIG to be a collinear ferrimagnet.

YIG is one of the most frequently used magnetic insulators in the field of spintronics. This is mostly due to the comparatively small Gilbert damping coefficient reaching values of $\alpha = 4 \times 10^{-5}$ for bulk YIG [65, 74, 75]. In thin films, larger values of the order of $\alpha \approx 10^{-4}$ are found, since surface defects become more important and affect the damping properties [74, 76, 77]. The small Gilbert damping allows for long distance transport of spin wave excitations within the insulator, which is desirable for information transport in future spintronics applications. Indeed, propagation lengths of the order of a few mm have been observed in YIG for coherently excited spin waves (using microwave excitations) [78]. For comparison, larger Gilbert damping constants have been reported for other ferrimagnetic insulators, such as gadolinium iron garnet (GdIG) ($\alpha \approx 10^{-3}$ [79]), and for metallic ferromagnets ($\alpha > 10^{-3}$ [80]).

3.1.2 Compensated ferrimagnet gadolinium iron garnet

[2]In addition to the collinear ferrimagnet YIG, we study the SMR in gadolinium iron garnet ($Gd_3Fe_5O_{12}$, GdIG). GdIG is also insulating and has the same crystalline structure as YIG, but the non-magnetic Y^{3+} on the C sublattice is replaced by Gd^{3+}, which carries a magnetic moment. More specifically, the electron configuration of Gd^{3+} is $[\mathrm{Xe}]4f^7$, i.e. the $4f$ shell is half full, such that the Gd^{3+} ions carry spin 7/2 but no orbital angular momentum. Similar to the two Fe sublattices in YIG, the FeA and FeD magnetic sublattices in GdIG are strongly antiferromagnetically coupled [81] and can therefore be considered as antiparallel for typical magnetic fields $0\,\mathrm{T} \leq \mu_0 H \leq 29\,\mathrm{T}$ and temperatures $2\,\mathrm{K} \leq T \leq 300\,\mathrm{K}$ used in our experiments (see Sect. 3.3). The Gd sublattice moments are ferromagnetically coupled to the FeA moments and antiferromagnetically coupled to the FeD moments. However, the intra-sublattice exchange coupling of the Gd moments is weak and typically neglected ($J_{\mathrm{CC}} = 0$) [82]. The Gd sublattice exhibits a paramagnetic behavior (also referred to as "exchange-enhanced paramagnetism" in literature [81]), leading to a strong increase of the magnetic moment $\boldsymbol{\mu}_{\mathrm{GdC}}$ at low temperatures. The temperature dependence

---

[2] This section contains calculations of the magnetic phase diagram of GdIG conducted by J. Barker, which were published in Ref. [30] together with the experimental data presented in Chap. 4. Parts of the text and figures in this section were adapted from Ref. [30].

of the sublattice magnetic moments in GdIG was calculated in Ref. [83] by J. Barker[3] using a classical atomistic Heisenberg model (see Ref. [83] for details on the model). The system size used by J. Barker is 16 × 16 × 16 unit cells (131072 spins) with periodic boundary conditions. The sublattice ($\boldsymbol{\mu}_{\mathrm{FeA}}$, $\boldsymbol{\mu}_{\mathrm{FeD}}$, $\boldsymbol{\mu}_{\mathrm{GdC}}$) and net magnetic moment ($\boldsymbol{\mu} = \boldsymbol{\mu}_{\mathrm{FeA}} + \boldsymbol{\mu}_{\mathrm{FeD}} + \boldsymbol{\mu}_{\mathrm{GdC}}$) calculated as a function of temperature for zero magnetic field are displayed in Fig. 3.2 (a) (Figure adapted from the supplement of Ref. [83]). The sign of the magnetic moments corresponds to the relative orientation (parallel or antiparallel) of the sublattices. Due to the temperature dependence and the relative orientation of the sublattice magnetic moments, the net (remanent) magnetic moment (purple in Fig. 3.2 (a)) at zero external magnetic field changes sign at the magnetic compensation temperature $T_{\mathrm{comp}}^{\mathrm{sim}} = 320\,\mathrm{K}$. Note that in pure bulk GdIG compensation temperatures between $T_{\mathrm{comp}} = 286\,\mathrm{K}$ and $295\,\mathrm{K}$ were reported from experiments [15, 84, 85].

Since the two Fe sublattices can be considered as antiparallel in experimentally available magnetic fields, the three-sublattice ferrimagnet GdIG is typically described as a two sublattice system with a net Fe magnetic moment $\boldsymbol{\mu}_{\mathrm{Fe,net}} = \boldsymbol{\mu}_{\mathrm{FeD}} + \boldsymbol{\mu}_{\mathrm{FeA}}$ and a Gd magnetic moment $\boldsymbol{\mu}_{\mathrm{GdC}}$. When a finite external magnetic field is applied, the net magnetization always points along the external field (neglecting anisotropies). In this case, the measured μ does not change sign at T_{comp} and is always positive. The orientations of the sublattice and net magnetic moments with respect to the external magnetic field are sketched as arrows in Fig. 3.2 (b): above T_{comp} the net Fe magnetic moment (brown arrow) dominates the net magnetic moment and points along the external field, while for $T < T_{\mathrm{comp}}$ the Gd magnetization (blue) starts to dominate. Since $\boldsymbol{\mu} = \boldsymbol{\mu}_{\mathrm{Fe,net}} + \boldsymbol{\mu}_{\mathrm{GdC}}$ (purple) always points along $\mathbf{H}$, all sublattice magnetizations switch direction at $T = T_{\mathrm{comp}}$.

For temperatures far away from the compensation point, GdIG is in a collinear phase, i.e. all sublattice moments are either parallel or antiparallel to the external magnetic field. However, close to T_{comp} a magnetic canting phase can be induced with fields available in our experimental setup, where the net Fe and the Gd moments are no longer collinear [30, 72, 73]. Such a configuration is exemplarily sketched in Fig. 3.2 (b), with the net magnetic moment $\boldsymbol{\mu}$ (purple arrow) still oriented along $\mathbf{H}$. The magnetic structure of GdIG was also modeled by J. Barker based on the same atomistic simulations as described above [30, 83]. A Metropolis Monte Carlo algorithm with a combination of different moves to avoid trapping in metastable minima [86], was used to calculate the equilibrium magnetic configuration as a function of applied field and temperature, disregarding the small crystalline anisotropy [30]. Figure 3.2 (c) and (d) show the magnetic phase diagram of GdIG, i.e. the (average) canting angles ξ_{FeA} and ξ_{GdC} of the FeA and GdC sublattice moments with respect to the applied magnetic field direction (Figure adapted from Ref. [30]). The red and blue colors correspond to a parallel ($\xi = 0°$) and antiparallel ($\xi = 180°$) alignment with respect to the external field. As discussed above, $\xi_{\mathrm{FeD}} = \xi_{\mathrm{FeA}} + 180°$ and the orientation of the FeD moments is therefore not displayed here.

---

[3] Institute of Materials Research, Tohoku University, Sendai, Japan.

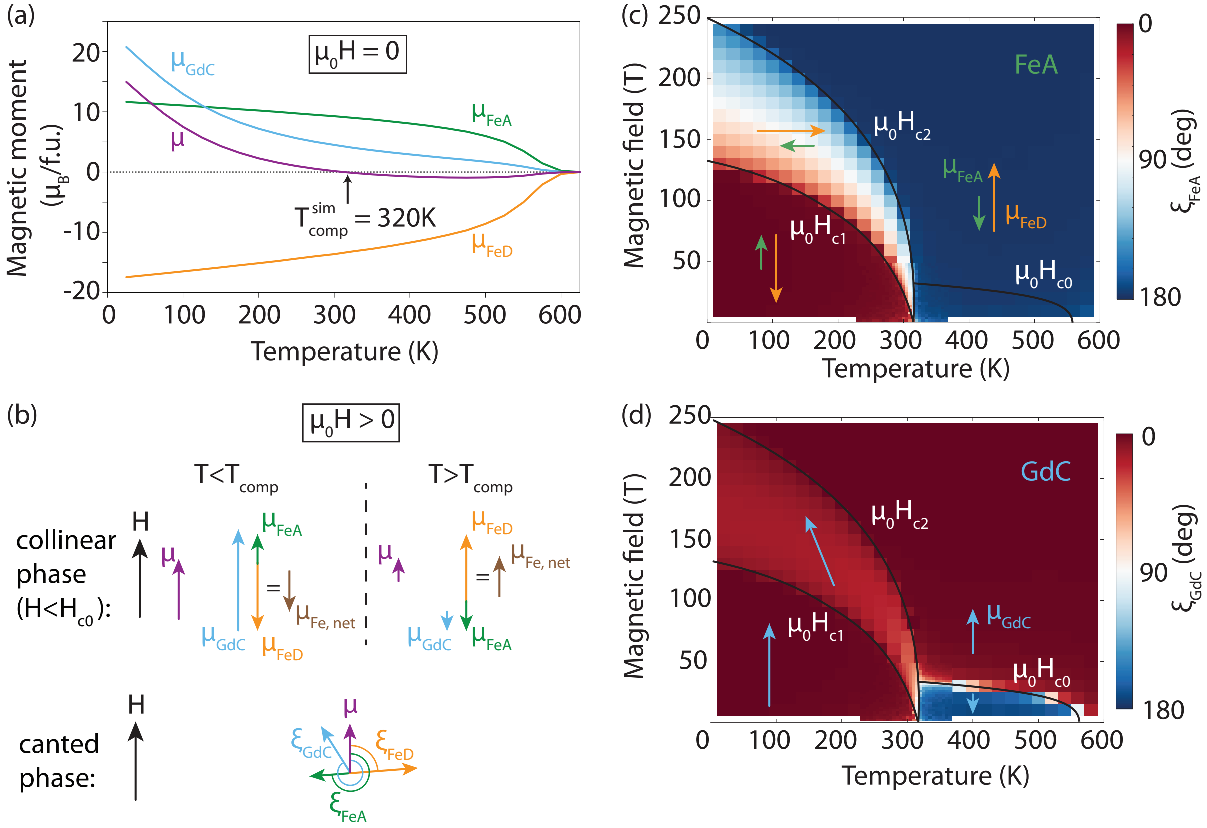

Figure 3.2: (a) Sublattice and net magnetic moment of GdIG calculated in an atomistic Heisenberg model by J. Barker as a function of temperature at zero external magnetic field. The calculated magnetic compensation temperature $T_{\mathrm{comp}}^{\mathrm{sim}} = 320\,\mathrm{K}$ is marked by the black arrow, where the net magnetic moment $\boldsymbol{\mu}$ (purple line) changes sign. Panel (a) was adapted from the Supplement of Ref. [83]. (b) Sketch of the magnetic sublattice orientations in the collinear magnetic phase for $T < T_{\mathrm{comp}}$ (left) and $T > T_{\mathrm{comp}}$ (right). For a finite magnetic field, the net magnetic moment $\boldsymbol{\mu}$ (purple arrow) is always aligned with $\mathbf{H}$, such that the orientation of the sublattice moments is inverted when crossing the compensation temperature. An exemplary sublattice moment configuration within the magnetic canting phase close to T_{comp} is sketched below. (c) and (d) Magnetic phase diagram of GdIG calculated via atomistic simulations by J. Barker. The color code represents the average canting angle ξ_X with respect to the external magnetic field direction for magnetic moments residing on the FeA sublattice (panel (c)) and the GdC sublattice (panel (d)), respectively. The red (blue) color corresponds to a parallel (antiparallel) alignment with respect to the external magnetic field direction. The black solid lines represent the critical magnetic fields which delimit the different magnetic phases (see main text for details). Panels (c) and (d) are adapted from Ref. [30].

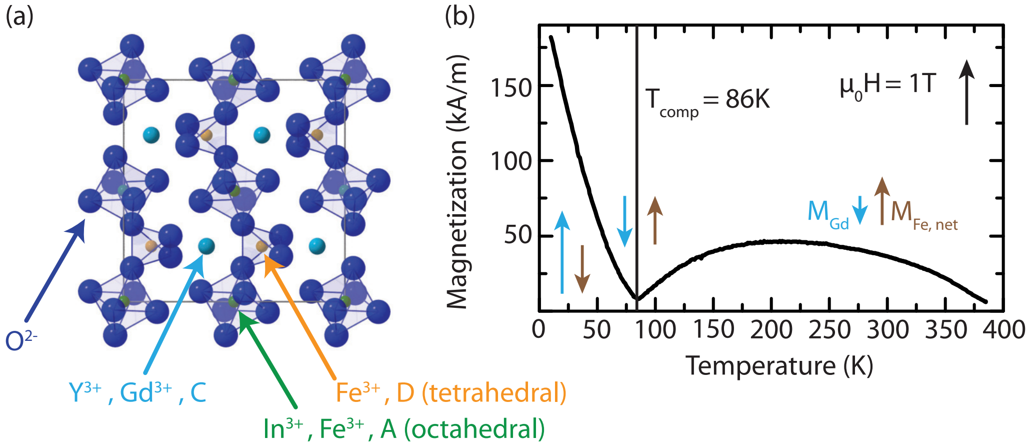

Figure 3.3: (a) Middle layer of the unit cell of In, Y doped gadolinium iron garnet (InYGdIG) (courtesy of S. Geprägs, WMI). (b) SQUID magnetometry measurement of an InYGdIG thin film as a function of temperature for an external magnetic field $\mu_0 H = 1\,\mathrm{T}$. The non-magnetic dopants dilute the magnetic sublattices and reduce the compensation temperature to $T_{\mathrm{comp}} = 86\,\mathrm{K}$.

For better visibility, the orientation of the sublattice moments is exemplarily sketched as arrows for different magnetic fields and temperatures within the phase diagram. In agreement with literature, Fig. 3.2 (c) and (d) reveal a canting of the Fe and Gd magnetic moments already for small magnetic fields of the order of a few tesla (or less) in the vicinity of the magnetic compensation point $T_{\mathrm{comp}}^{\mathrm{sim}}$. The canting phase is delimited by the critical fields $\mu_0 H_{c1}$ and $\mu_0 H_{c2}$, as indicated by the black lines in Fig. 3.2 (c) and (d). In particular, when crossing the canting phase, either by increasing the magnetic field or the temperature, the FeA magnetic moments continuously rotate from a parallel to an antiparallel alignment with respect to the magnetic field. The white coloring in the center of the canting phase corresponds to $\xi_{\mathrm{FeA}} = 90°$, i.e. the Fe moments are perpendicular to $\mathbf{H}$. Above $T_{\mathrm{comp}}^{\mathrm{sim}}$, an additional critical field $\mu_0 H_{c0}$ is defined based on the orientation of the Gd magnetic moments: for $H < H_{c0}$ the Gd moments are antiparallel to the external field. With increasing field the weakly coupled Gd moments are depolarized and are eventually repolarized along the external magnetic field for $H > H_{c0}$, as depicted in Fig. 3.2 (d).

As mentioned above, the literature value for T_{comp} in GdIG is close to room temperature, such that no measurements can be performed far above the compensation temperature in our standard cryostats, which enable magnetotransport measurements in the temperature range $2\,\mathrm{K} \leq T \leq 300\,\mathrm{K}$ (see Sect. 3.3). However, T_{comp} and the critical fields can be reduced by alloying non-magnetic ions into GdIG [82, 87–89], which dilute the magnetic sublattices. Thereby, a large part of the magnetic canting phase is accessible in our setup. In Sect. 4.2, we therefore study a GdIG sample doped with indium (In) and yttrium (Y): Figure 3.3 (a) depicts the corresponding unit cell, where the magnetic ions on the C and A sublattices are partly substituted with non-magnetic Y^{3+} and In^{3+}, respectively, corresponding to a chemical composition $(Gd_2Y_1)(Fe_4In_1)O_{12}$ (InYGdIG).

From the SQUID magnetometry measurement in such an InYGdIG thin film[4] (Fig. 3.3 (b)), we can extract $T_{\mathrm{comp}} = 86\,\mathrm{K}$, where the net magnetization nearly vanishes. Note that this measurement was conducted for a finite external magnetic field $\mu_0 H = 1\,\mathrm{T}$, such that the measured net magnetization is always positive. Due to its comparatively low compensation temperature, InYGdIG is a good candidate for measurements sufficiently far above and below T_{comp} in our standard magnet cryostat system.

3.2 Sample fabrication

In the following, we discuss spin Hall magnetoresistance experiments in one YIG/Pt and one InYGdIG/Pt bilayer (see sample list in Appendix A). Both FMI layers were epitaxially grown onto single crystalline, [111]-oriented yttrium aluminum garnet ($Y_3Al_5O_{12}$, YAG) substrates via pulsed laser deposition (PLD). The yttrium iron garnet ($Y_3Fe_5O_{12}$, YIG) film was grown by S. Meyer (WMI) using a substrate temperature of 500 °C, an oxygen atmosphere of $2.5 \cdot 10^{-2}\,\mathrm{mbar}$, and an energy fluence of the KrF excimer laser of $2.0\,\mathrm{J/cm^2}$ at the target surface (see Ref. [67] for details). The 40 nm thick YIG film was covered *in-situ* (i.e. without breaking the vacuum) with $t = 4\,\mathrm{nm}$ of Pt deposited via electron beam evaporation.

The same growth parameters were used for the indium and yttrium doped gadolinium iron garnet ($(Y_1Gd_2)(Fe_4In_1)O_{12}$, InYGdIG) film (grown by F. Della Coletta [90, 91]), which has a thickness of 61.5 nm and was covered with $t = 3.6\,\mathrm{nm}$ of Pt. The InYGdIG sample features a magnetization compensation temperature $T_{\mathrm{comp}} = 86\,\mathrm{K}$ obtained from the SQUID magnetometry measurement plotted in Fig. 3.3 (b).

For the magnetoresistance experiments, the InYGdIG/Pt and YIG/Pt bilayers were patterned into Hall bars with width $w = 80\,\mathrm{\mu m}$ and length $l = 600\,\mathrm{\mu m}$ (for a schematic see Fig. 2.2 (a)) using optical lithography followed by Ar ion beam milling.

3.3 Experimental setup

3.3.1 Superconducting magnet cryostat

After fabrication, the samples are glued onto a chip carrier [92], wire bonded in a 4 point configuration (see Fig. 2.2) and mounted on a dipstick equipped with dc measuring wires, as well as a temperature sensor and heater. The dipstick is placed in the variable temperature insert (VTI) of a superconducting split-coil magnet cryostat ($2\,\mathrm{K} \leq T \leq 300\,\mathrm{K}$) at the Walther-Meissner-Institut (WMI), enabling magnetotransport measurements at magnetic fields up to $\mu_0 H = 7\,\mathrm{T}$. Additional measurements up to $\mu_0 H = 29\,\mathrm{T}$ were conducted using a resistive magnet setup with a variable temperature insert at the high-field magnet

---

[4] The sample fabrication and SQUID magnetometry measurement were done by F. Della Coletta during his master's thesis at WMI [90].

laboratory (LNCMI) in Grenoble. In both setups, a dc charge current of 0.2 mA was applied along the Hall bar using a Keithley 2400 sourcemeter. We carried out angle-dependent magnetoresistance (ADMR) measurements [10] by rotating the sample with respect to the external magnetic field of fixed magnitude $\mu_0 H \leq 29\,\mathrm{T}$ applied in the sample plane. The longitudinal voltage drop V along the direction of charge current was recorded as a function of the angle α_H between the current direction $\mathbf{J}_\mathrm{c}$ and the external magnetic field $\mathbf{H}$ using a Keithley 2182 nanovoltmeter.

3.3.2 Sensitive transport experiments via the current switching method

The charge current applied for the 4 point measurement gives rise to Joule heating in the Pt, leading to additional thermal voltages, e.g. due to the spin Seebeck effect [93–95] (see Sect. 5.4). In order to disentangle the resistive (V_res) and thermal voltage response (V_therm) we use a current switching method (or "delta method"), i.e. we apply a positive and negative dc driving current in an alternating sequence [95]. This enables the separation of contributions which depend on the current direction (resistive or higher order effects which are uneven in J_c)

$$V_\mathrm{res} = \frac{V(+J_c) - V(-J_c)}{2} \tag{3.2}$$

from the ones which are proportional to quadratic (or higher order even) terms in J_c

$$V_\mathrm{therm} = \frac{V(+J_c) + V(-J_c)}{2}. \tag{3.3}$$

In addition to disentangling resistive and thermal contributions, the current switching method also allows to reach higher sensitivity in resistivity measurements. In order to improve the signal to noise ratio in the ADMR measurements described in Sect. 3.3.1, we apply the current switching $N_\mathrm{switch} = 5$ times for each magnetic field orientation (or magnitude) and calculate the average of V_res and V_therm separately. Hereby, thermal drifts can be corrected which arise on the time scale of the order of seconds, e.g. related to thermal fluctuations during the rotation of the dipstick in the He exchange gas of the cryostat. For reference, the relative fluctuations of the 5 values of V_res taken for one magnetic field orientation or magnitude are typically of the order of about 10^{-6} to 10^{-5} (using standard Keithley 2182 settings: repeating filter 10 counts, 1 power line cycle). Overall, the resulting sensitivity of the current switching method is therefore sufficient for our SMR measurements, where resistivity modulation amplitudes of the order of 10^{-4} to 10^{-3} are expected (see Sect. 2.2). Note that the sensitivity can further be increased by changing the filter settings of the nanovoltmeter (see Sect. 6.2) or increasing the number of switching cycles N_switch.

Chapter 4

Spin Hall magnetoresistance experiments

In this chapter, we turn to the experimental investigation of the spin Hall magnetoresistance in two different FMI/Pt bilayers, i.e. with the collinear ferrimagnet YIG (Sect. 4.1) and the compensated ferrimagnet GdIG (Sect. 4.2) as the two FMI, and compare the experimental observations to the microscopic model introduced in Sect. 2.3. This chapter contains results which were published in Phys. Rev. B **94**, 094401 (2016) [30] and reuses part of the text and figures from this publication.

4.1 Spin Hall magnetoresistance in a YIG/Pt bilayer

We first study the spin Hall magnetoresistance in the YIG/Pt bilayer (see Sect. 3.2 for details on the sample fabrication) as a function of the angle α_H between the in-plane magnetic field orientation $\mathbf{H}$ and the current direction $\mathbf{j}$ (see Fig. 2.2 (a)). Figure 4.1 (a)-(c) shows a typical set of ADMR measurements, where the angular dependence of the Pt resistivity

$$\frac{\rho(\alpha_\mathrm{H}) - \rho_0}{\rho_0} \tag{4.1}$$

is plotted as a function of the magnetic field orientation. ρ_0 is the constant offset resistivity for $\alpha_\mathrm{H} = 90°$ (see Fig. 2.2 (d)). The data displayed here is taken at fixed temperatures of $T = 10\,\mathrm{K}, 85\,\mathrm{K}, 300\,\mathrm{K}$ and fixed external magnetic field magnitude of $\mu_0 H = 7\,\mathrm{T}$. The magnetoresistance behavior is fully consistent with the $\cos^2(\alpha_\mathrm{H})$ dependence expected for a collinear ferrimagnet, where the macrospin model according to Eq. (2.9) can be applied [10, 40]. We extract the SMR ratio (see Eq. (2.10) and (2.19))

$$\mathrm{SMR} = \frac{\Delta\rho}{\rho_0} = \frac{\rho(0°) - \rho_0}{\rho_0} \tag{4.2}$$

from a series of ADMR measurements in the temperature range from $10\,\mathrm{K} \leq T \leq 300\,\mathrm{K}$. The data is compiled in Fig. 4.1 (d) for an external magnetic field magnitude $\mu_0 H = 1\,\mathrm{T}$ (green) and $7\,\mathrm{T}$ (black). The SMR ratio decreases towards lower temperatures by about a

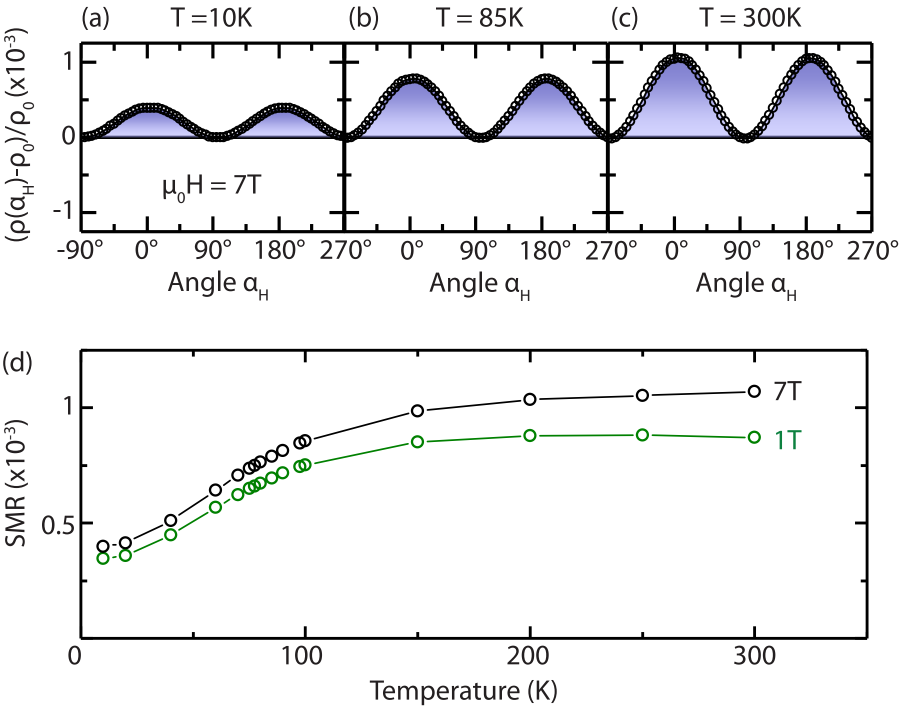

Figure 4.1: (a)-(c) Resistivity measurements in a YIG/Pt bilayer as a function of the angle α_H between the in-plane magnetic field orientation $\mathbf{H}$ and the current direction $\mathbf{j}$. We observe the $\cos^2(\alpha_\mathrm{H})$ dependence expected for a collinear ferrimagnet with a maximum resistivity for $\mathbf{H} \parallel \mathbf{j}$. The measurements were conducted at a fixed magnetic field $\mu_0 H = 7\,\mathrm{T}$ for $T = 10\,\mathrm{K}, 85\,\mathrm{K}, 300\,\mathrm{K}$. (d) SMR ratio $(\rho(0^\circ) - \rho_0)/\rho_0$ extracted from ADMR measurements as a function of temperature for $\mu_0 H = 1\,\mathrm{T}$ and $7\,\mathrm{T}$. Figure adapted from Ref. [30].

factor of 2 and we obtain a qualitatively similar temperature dependence as in previous SMR measurements in YIG/Pt [40]. This behavior was attributed to a decrease of the spin Hall angle towards low temperatures [40], i.e. a property of the Pt film. While the SMR effect increases slightly with magnetic field, the qualitative temperature dependence is the same for $\mu_0 H = 1\,\mathrm{T}$ and $7\,\mathrm{T}$.

We would like to emphasize here that we expect no temperature dependence of the SMR due to a change of the net magnetization amplitude. Although the latter increases towards low temperatures (see Fig. 3.1 (b)), the SMR effect in YIG is currently described in a macrospin model which only depends on the direction of the net magnetization vector $\mathbf{m}$ (see Sect. 2.2). This also implies that once the magnetization of the ferrimagnet is saturated, i.e. in a single domain state oriented along the external magnetic field, no dependence of the SMR amplitude on the magnetic field strength is expected. Since the coercive field of YIG is usually of the order of a few Oe [96], the field dependence between $1\,\mathrm{T}$ and $7\,\mathrm{T}$ observed in Fig. 4.1 (d) is rather surprising. We therefore systematically study the field dependence of the SMR ratio extracted from ADMR measurements up to $7\,\mathrm{T}$ for $10\,\mathrm{K} \leq T \leq 300\,\mathrm{K}$. The result is plotted in Fig. 4.2 (a), the lines are guides to the eye.

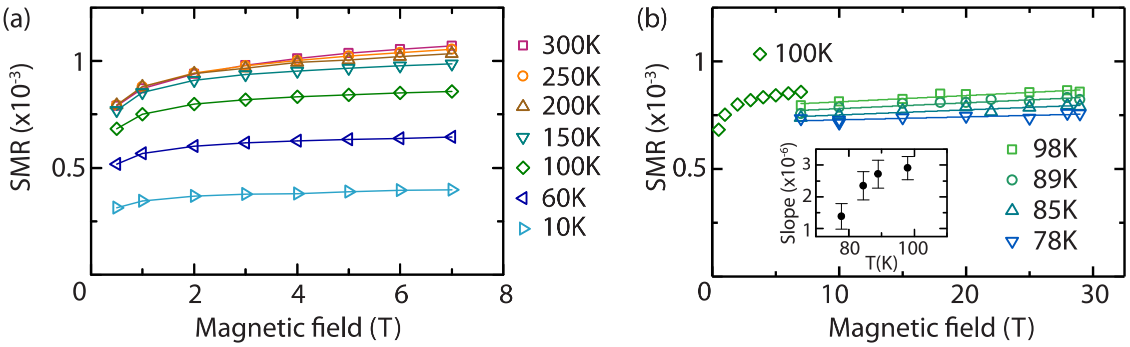

Figure 4.2: (a) SMR ratio extracted from ADMR measurements as a function of the magnetic field magnitude up to 7 T in the temperature range $10\,\mathrm{K} \leq T \leq 300\,\mathrm{K}$ measured at the WMI. (b) SMR ratio for magnetic fields up to 29 T for temperatures between 78 K and 98 K measured in the high magnetic field laboratory in Grenoble (LNCMI). The solid lines represent linear fits to the data. The slope extracted from the linear fit is plotted in the inset as a function of temperature with the standard deviation as error bars. For comparison the SMR amplitude between 0.5 T and 7 T at 100 K from panel (a) is also included. Note that the two data sets were taken in different cryostat systems, such that small deviations in the measured sample temperature are possible.

We find a comparatively strong increase of the SMR magnitude between 0.5 T and 1 T and a weaker increase up to 7 T. In order to confirm this behavior, we measured the SMR amplitude in the high field laboratory in Grenoble (LNCMI) up to 29 T for temperatures $78\,\mathrm{K} \leq T \leq 98\,\mathrm{K}$[1] as plotted in Fig. 4.2 (b). The lines in Fig. 4.2 (b) represent linear fits to the high field data. The slope is extracted as a function of temperature and plotted in the inset where the error bars correspond to the standard deviation from the linear fit. While the slope is of the order of 10^{-6}/T and therefore close to our measurement resolution, the data suggests that the SMR saturates only at fields much higher than the coercive field of YIG. The SMR amplitude taken at the WMI at 100 K for low magnetic fields between 0.5 T and 7 T is also included in Fig. 4.2 (b) for a comparison of the slope of the magnetic field dependence. Note that the low and high field data sets were taken in different magnet cryostat setups (WMI and LNCMI Grenoble, respectively), possibly leading to small deviations of the measured sample temperature[2].

Although we expect no magnetic field dependence of the SMR amplitude once the bulk magnetization is saturated, the observed increase of the SMR with magnetic field may

---

[1] This corresponds to a temperature range which can be easily stabilized in the high field setup.

[2] The temperature sensor in the dipstick used at WMI is in direct thermal contact with the sample (via a Cu plate). On the dipstick used at LNCMI the temperature sensor is placed within the exchange He gas, such that the measured temperature can deviate from the actual sample temperature. A calibration of the sample temperature based on the Pt resistivity was challenging due to a deterioration of the Pt film over time. Since the studied temperature range close to 100 K corresponds to a region where the SMR amplitude has a comparatively strong temperature dependence (see Fig. 4.1), small differences in the sample temperature can lead to visible deviations of the SMR amplitudes.

be related to specific magnetic thin film properties. The thin film sample used for the measurements displayed in Fig. 4.1 and 4.2 was grown onto a YAG substrate. The latter is 500 µm thick and the corresponding volume is therefore several orders of magnitude larger than the volume of the FMI thin film. At high magnetic fields, the SQUID magnetometry measurement is therefore dominated by the diamagnetic contribution of the YAG substrate, giving rise to a negative slope in the magnetic moment vs applied magnetic field curve. It is therefore currently challenging to relate the field dependence of the SMR amplitude to the YIG magnetization in this particular sample. We can however assume that changes in the overall YIG magnetization for fields of several tesla are not sufficient to explain the observed field dependence of the SMR. One can speculate that there is a thin layer at the YIG/Pt interface where the magnetic structure is different due to the interface roughness, such that a higher magnetic field is necessary to saturate the magnetic moments at the interface. There is indeed evidence that the interface properties, e.g. *ex-situ* vs *in-situ* fabrication [48] or Ar ion etching prior to the Pt deposition [97], affect the SMR amplitude as well as its temperature and magnetic field dependence [98]. Furthermore, as discussed in Sect. 2.2 and 9.2, there are indications that the SMR is mostly sensitive to the top FMI layers instead of the integral magnetic volume in the sample. It is therefore possible that the field dependence observed in Fig. 4.2 is related to particular interface properties. However, further experimental investigations are required to test this hypothesis.

Another possible explanation is that the magnetic field affects the SHE or the spin accumulation in the Pt. Recent studies of the SMR effect in YIG/Pt at magnetic fields up to 9 T were put forward, where an increase of the SMR amplitude with increasing magnetic field was observed [99]. The authors attribute this effect to an additional contribution from the so-called Hanle magnetoresistance: the spin accumulation at the Pt interface is suppressed by the applied magnetic field via the Hanle effect [99–101], leading to an additional resistivity modulation which has the same symmetry as the SMR. However, for a better understanding of different contributions to the observed magnetic field dependence of the resistivity in YIG/Pt, a more detailed study is required in the future.

In summary, we have studied the temperature and magnetic field dependence of the SMR effect in a YIG/Pt bilayer. The observed increase of the SMR amplitude by a factor of 2 from low temperature to room temperature is consistent with previous measurements in similar YIG/Pt samples. We furthermore observe a slight increase of the SMR amplitude with magnetic field magnitude, the origin of which is still under investigation. However, for all temperatures and magnetic fields studied here, the overall angular dependence of the resistivity is consistent with the expectations from the macrospin (and microscopic) model for a collinear ferrimagnet, i.e. we observe a $\cos^2(\alpha_\mathrm{H})$ dependence with positive amplitude $\Delta\rho$.

4.2 Spin Hall magnetoresistance in a GdIG/Pt bilayer

The SMR measurements in YIG/Pt presented in Sect. 4.1 are consistent with theoretical predictions based on a macrospin model, where only the orientation of the net magnetic moment $\boldsymbol{\mu}$ in the FMI is relevant, while the magnitude of the bulk magnetization is not important. In a system where all sublattice moments and the net magnetic moment are collinear, using the sublattice moment orientation or the net magnetization orientation to model the SMR effect yields the same SMR angular dependence as discussed in Sect. 2.3.1. This is due to the fact that the SMR is 180° symmetric. However, for a non-collinear magnetic structure it is no longer *a priori* obvious to describe the SMR response in terms of the net magnetic moment orientation. In Sect. 2.3, we therefore discussed the SMR in a microscopic model based on the SMR contributions of individual sublattice moment orientations. We found that for a non-collinear, canted magnetic system the macrospin and microscopic models yield qualitatively different SMR angular dependencies. Since the magnet/metal exchange coupling in the SMR theory is formulated in terms of the spin mixing conductance (see Sect. 2.2), which is determined by the local magnetic moments at the interface [45], we assert that for a non-collinear magnetic structure the SMR requires a microscopic modeling.

In the following we will therefore verify this hypothesis by studying a bilayer consisting of Pt and the compensated ferrimagnetic insulator GdIG. The latter has three magnetic sublattices (FeA, FeD and Gd, see Sect. 3.1.2) which adopt a canted configuration in the vicinity of the compensation temperature T_{comp} when a finite external magnetic field is applied (see magnetic phase diagram in Fig. 3.2). As discussed in Sect. 3.1.2, the canting angle of the individual sublattice moments depends on the temperature and external magnetic field magnitude (see Fig. 3.2 (c) and (d)). GdIG therefore allows for a systematic study of the SMR as a function of the microscopic magnetic structure. The results and part of the figures presented in this section were published in Phys. Rev. B **94**, 094401 (2016) [30] and are adapted here for the format of this thesis.

As mentioned in Sect. 3.1.2, the compensation temperature T_{comp} of GdIG shifts to lower temperatures when the material is doped with In and Y. Consequently, in InYGdIG a large portion of the canted phase becomes accessible using standard magnet cryostats in the temperature range $2\,\text{K} \leq T \leq 300\,\text{K}$ (see Sect. 3.3) and we therefore use InYGdIG instead of pure GdIG for the SMR experiments. We assume the magnetic phase diagram of InYGdIG to be qualitatively similar to the one calculated by J. Barker for pure GdIG (see Fig. 3.2) [30]. In order to verify this experimentally, we investigate the magnetic properties of the InYGdIG sample - in particular the orientation of the individual magnetic sublattices close to T_{comp} - via element specific x-ray magnetic circular dichroism (XMCD) [102–104] measurements performed at the European Synchrotron Radiation Facility (ESRF) at the beam line ID12 [104]. The XMCD experiments are based on element specific x-ray absorption: as shown in Fig. 4.3 (a) (adapted from Ref. [103]) for a transition metal, the x-ray photons excite core electrons from the lower s or p shells into the partially filled d shell. The energy of the incoming photons is tuned to the absorption edge of the investigated element and we measure the x-ray absorption near edge spectra (XANES) (see Fig. 4.3 (c) for the Fe K edge in InYGdIG). Depending on the helicity $\pm\Lambda$ ($\pm\hbar$) of the circularly polarized incoming photons, the excited photoelectrons have different spin. In a magnetic material which exhibits an imbalance of the available spin up and down states at the Fermi edge, this leads to different absorption probabilities for left and right polarized photons. For instance in the scenario depicted in Fig. 4.3 (a), right (left) polarized photons mainly induce transitions into the spin down (up) empty states [103]. At the beam line ID12, the XANES is measured via total fluorescence yield (TFY) [104], i.e. the excited electrons relax back to the equilibrium state and emit photons which can be detected. The XMCD signal is defined as the difference of the XANES measured for the two helicities: $\mathrm{XMCD} = \mathrm{XANES}(+\Lambda, +H) - \mathrm{XANES}(-\Lambda, +H)$. Here, the magnetic field is applied parallel to the $\mathbf{k}$ vector of the incoming x-ray beam. Instead of inverting the photon polarization, one can also invert the magnetic field direction while keeping the polarization fixed, such that $\mathrm{XMCD} = \mathrm{XANES}(+\Lambda, +H) - \mathrm{XANES}(+\Lambda, -H)$. The obtained XMCD signal is proportional to the scalar product between the magnetic moment $\boldsymbol{\mu}_X$ and $\mathbf{k}$, i.e. the projection of the magnetic moment onto $\mathbf{k}$. Therefore, a rotation of the sublattice magnetic moments with respect to the external field from a parallel to an antiparallel configuration, as expected in a compensated ferrimagnet close to T_{comp} (see phase diagram in Fig. 3.2), will manifest itself as a sign change of the XMCD signal. In particular for $\boldsymbol{\mu}_X \perp \mathbf{k}$, the XMCD signal goes to zero.

For the experiments presented in this section, the InYGdIG sample was glued onto a wedge such that the x-ray beam has a grazing incidence angle of 10° with respect to the sample plane, as depicted schematically in Fig. 4.3 (b). In order to conduct temperature and magnetic field dependent XMCD measurements, the wedge was mounted on a cold finger cryostat ($2.1\,\mathrm{K} \leq T \leq 300\,\mathrm{K}$) and inserted into the bore of a superconducting magnet allowing for magnetic fields up to $17\,\mathrm{T}$ (for a more detailed description of the measurement setup see Ref. [104]). In this configuration the incident x-ray beam is therefore parallel to the applied magnetic field. XANES were recorded at the Fe K edge [105] with right and left circularly polarized light, as well as positive and negative in-plane magnetic fields. One XANES taken at $17\,\mathrm{T}$ and $50\,\mathrm{K}$ is exemplarily plotted in Fig. 4.3 (c) as a black line. The pre-edge at $7114\,\mathrm{eV}$ marked by a black arrow arises mainly from the tetrahedrally ordered FeD sublattice [106]. Since the FeA moments are antiparallel to the FeD moments for the magnetic field magnitudes accessible in our experiments as also shown in the atomistic simulations, it is sufficient to analyze the pre-edge. Several XANES were recorded to improve the signal-to-noise ratio and normalized to an edge jump of unity. The XMCD signal was calculated as the direct difference between consecutive normalized XANES recorded either with right and left circularly polarized light or while

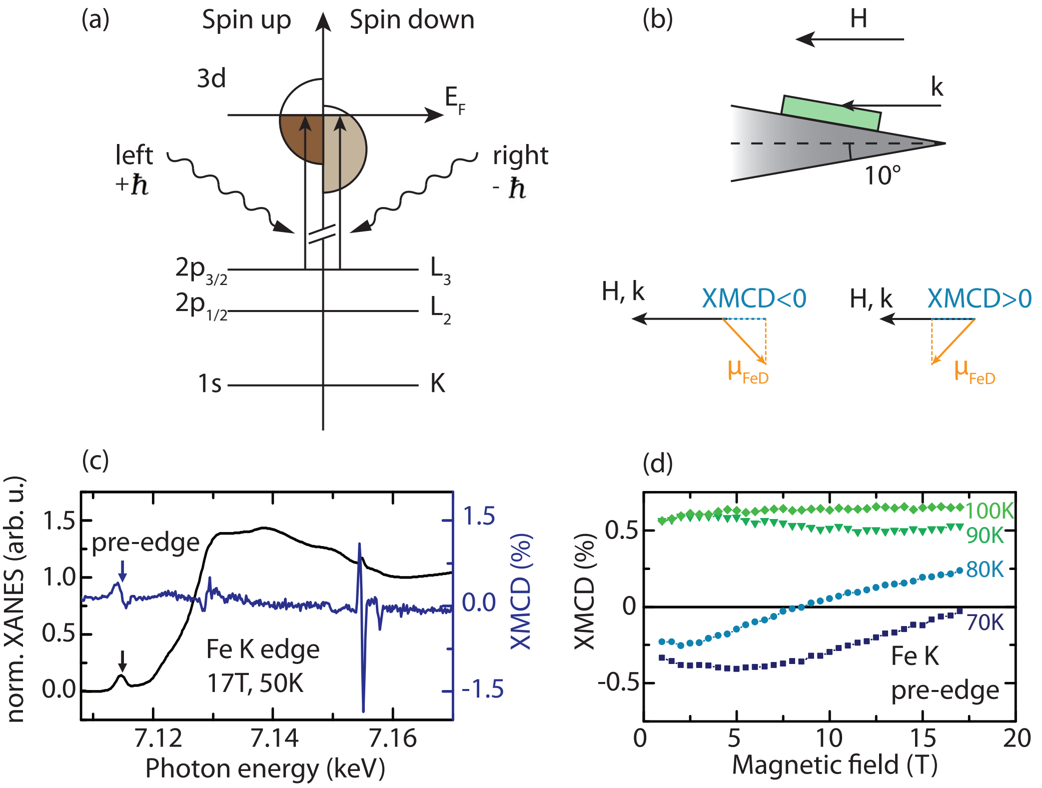

Figure 4.3: (a) Sketch of the electron configuration for a transition metal with an imbalance of spin up and down electrons at the Fermi level E_F. Incoming x-ray photons excite core electrons into the partially filled d shells. Due to the different density of states at the Fermi edge different transition probabilities are expected for right and left circularly polarized photons. Figure adapted from Ref. [103]. (b) Sketch of the XMCD measurement configuration: the sample is mounted on a wedge to ensure a grazing angle of 10° for the incident x-ray beam with respect to the sample plane. The wedge is mounted on a coldfinger cryostat and placed in the coil of a superconducting magnet (not shown here) with magnetic field **H** along the **k**-vector of the incident x-ray beam. (c) Normalized XANES recorded at the Fe K edge in the InYGdIG/Pt sample at 50 K and 17 T. The pre-edge marked by a black arrow arises mainly from the tetrahedrally ordered FeD moments. The blue curve represents the corresponding XMCD signal, which is dominated by the signal at the pre-edge. (d) XMCD amplitude, i.e. the projection of the FeD moments onto the external field axis, measured as a function of field strength at various temperatures around T_comp. Figure adapted from Ref. [30].

applying positive and negative magnetic fields. The resulting XMCD spectrum at the Fe K edge for 17 T and 50 K is also depicted in Fig. 4.3 (c) in blue.

In order to map out the canted phase in InYGdIG, the XMCD signal at the Fe K pre-edge was measured as a function of magnetic field for temperatures between 70 K and 100 K. For a quantitative evaluation of the XMCD signal, the peak to peak amplitude of the pre-edge XMCD signal was calculated as the difference between the extrema at 7115 eV and 7114 eV [107]. As shown in Fig. 4.3 (d), the XMCD amplitude is positive and independent of field strength for $T = 100\,\mathrm{K}$ and $90\,\mathrm{K} > T_\mathrm{comp}$, indicating that the FeD moments are saturated and parallel to the external field. For $T = 80\,\mathrm{K}$, however, the XMCD amplitude changes sign as a function of magnetic field strength, with positive amplitude at high magnetic fields and negative amplitude at low magnetic fields. Finally, for $T = 70\,\mathrm{K}$, the XMCD amplitude is negative for all fields studied. This sign change of the XMCD amplitude as a function of temperature and magnetic field strength provides clear evidence for the reorientation of the FeD sublattice moments close to the compensation temperature, which was determined to $T_\mathrm{comp} = 86\,\mathrm{K}$ using SQUID magnetometry measurements in this sample (see Fig. 3.3). The zero-crossings of the XMCD amplitude correspond to a perpendicular orientation of the FeD sublattice with respect to the external field, i.e. to the white region in the Fe phase diagram in Fig. 3.2 (c). The XMCD measurements in particular confirm that the InYGdIG sample studied here features all the characteristic magnetic properties of a compensated ferrimagnet, i.e. a compensation temperature and a magnetic canting phase similar to the one calculated for pure GdIG. We can therefore qualitatively compare the experimental results to the calculated phase diagram of GdIG. Note also that we take the spin configuration at the surface - which mainly determines the SMR response - to be similar to that of the bulk as obtained from these calculations.

After confirming the magnetic canting phase via a direct measurement method, we now turn to the magnetoresistance measurements in InYGdIG/Pt: Figure 4.4 (a)-(c) show a set of ADMR curves for $T = 10\,\mathrm{K}, 85\,\mathrm{K}$ and $300\,\mathrm{K}$ measured for a fixed in-plane magnetic field magnitude $\mu_0 H = 7\,\mathrm{T}$. The measurements at $T = 10\,\mathrm{K}$ and $T = 300\,\mathrm{K}$ (panels (a) and (c)) show the same positive SMR as for YIG/Pt (see Fig. 4.1). However, at $T = 85\,\mathrm{K} \approx T_\mathrm{comp}$ (panel (b)), the SMR amplitude determined via Eq. (4.2) has negative sign. In other words, the magnetic field orientations for minimum and maximum resistivity are inverted (shifted by 90°). This observation cannot be accounted for by the standard macrospin SMR theory as expressed by Eq. (2.8) [12, 108], where the SMR amplitude is always positive. However, the microscopic model proposed in Sect. 2.3 predicts a sign change of the SMR amplitude when the sublattice magnetic moments are canted by an angle $\xi > 45°$ (in the 2D limit, see Sect. 2.3.2) with respect to the external field.

To substantiate the observation of a SMR sign change, systematic ADMR measurements were conducted at 7 T as a function of temperature from $T = 10\,\mathrm{K}$ to $T = 300\,\mathrm{K}$ and the SMR amplitude extracted according to Eq. (4.2) is compiled in Fig. 4.4 (d)[3]. The overall temperature dependence looks similar to our observations in YIG, where the SMR amplitude decreases by a factor 2 at low temperatures compared to room temperature (see Fig. 4.1 (d)). However, in InYGdIG the SMR ratio suddenly drops and changes sign in a narrow temperature window between 79 K and 91 K, i.e. in a small temperature range around $T_\mathrm{comp}(\mathrm{InYGdIG}) = 86\,\mathrm{K}$, where a canting of the Fe sublattice moments is observed in the XMCD measurements (Fig. 4.3 (d)). The observed sign change of the

---

[3] The temperature dependent SMR measurements at 7 T shown here were conducted by R. Schlitz in the course of his master's thesis at WMI [55].

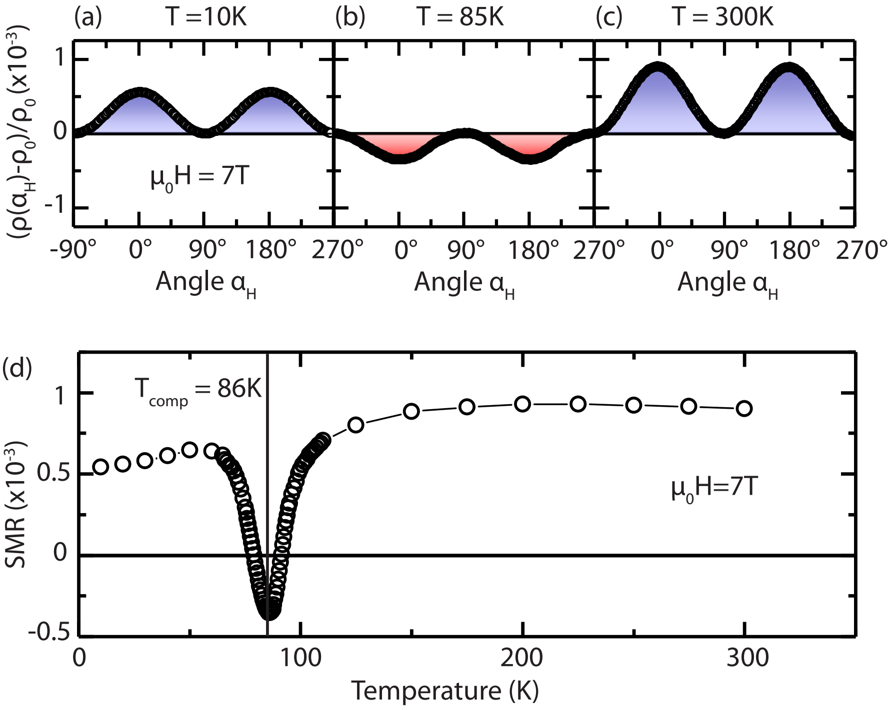

Figure 4.4: Measured evolution of the SMR in GdIG/Pt. (a)-(c) The data were recorded at $T = 10\,\mathrm{K}, 85\,\mathrm{K}$ and $300\,\mathrm{K}$ as a function of the angle α_H between the current direction $\mathbf{J}_\mathrm{c}$ and the orientation of the external, in-plane magnetic field $\mu_0 H = 7\,\mathrm{T}$. The SMR amplitude in InYGdIG/Pt changes sign for $T = 85\,\mathrm{K}$ close to the magnetization compensation temperature $T_\mathrm{comp} = 86\,\mathrm{K}$ (panel (b)), but the extrema stay at the same α_H orientation for all temperatures. (d) SMR amplitude extracted from ADMR measurements as a function of temperature at fixed magnetic field $\mu_0 H = 7\,\mathrm{T}$. The SMR sign change is clearly evident between 79 K and 91 K. Figure adapted from Ref. [30].

SMR in the magnetic canting phase is consistent with the predictions of the microscopic model proposed in Sect. 2.3 and gives first experimental evidence that the SMR is not governed by the orientation of the net magnetization, but by the orientation of individual sublattice magnetic moments.

The XMCD measurements displayed in Fig. 4.3 (d) confirm that the Fe sublattice magnetic moments rotate continuously with respect to the external magnetic field when the temperature is swept across the canting phase. However, for all temperatures in the investigated range, the extrema of the measured resistivity angular dependence occur at 0° and 90°, i.e. no continuous phase shift of the SMR is observed. According to the theoretical model discussed in Sect. 2.3.2, this indicates that equal numbers of magnetic moments within one sublattice are canted by an angle $\pm\xi$ (in the 2D limit, assuming all magnetic moments lie in the sample plane), or that the magnetic moments are equally distributed on a cone with opening angle ξ if the magnetic moments also have out of plane components (three dimensional distribution, see Sect. 2.3.4). In both cases, the overall phase shift of the resistivity ρ vanishes on average. For such a scenario the microscopic model predicts a sign change of the SMR amplitude for canting angles $\xi > 45°$ in the two dimensional limit (see Fig. 2.5 (d)), or $\xi > 54°$ in 3D (see Fig. 2.9 (b)).

Note that the XMCD measurements presented in Fig. 4.3 only probe the projection of the sublattice magnetic moment onto the x-ray $\mathbf{k}$ vector, which (in the used measurement setup) is parallel to the applied magnetic field. In other words, only the magnetic moment component parallel to the applied field can be determined. However, in order to distinguish between different magnetic moment orientations on a cone with opening angle ξ, additional measurements of the magnetic moment components perpendicular to the external field are required. A direct measurement of the different orientations of magnetic moments within one sublattice, e.g. via spatially resolved XMCD experiments probing both the magnetic moment components parallel and perpendicular to the applied magnetic field, should therefore be conducted in the future to further confirm the theoretical model proposed in Sect. 2.3.

In a second set of experiments we study the evolution of the SMR amplitude with magnetic field strength and temperature in order to map out the magnetic canting phase in the InYGdIG/Pt sample. Figure 4.5 (a) shows the corresponding data obtained for $\mu_0 H \leq 7\,\mathrm{T}$ in the superconducting magnet cryostat at WMI, as well as $\mu_0 H \leq 29\,\mathrm{T}$ at the high field magnet laboratory in Grenoble, in a false color plot. In the collinear state at high temperatures $T \approx 150\,\mathrm{K}$, the SMR measurements up to 29 T displayed in Fig. 4.5 show no indication of a pronounced field dependence. This is consistent with the SMR description based on spin transfer torque [12] and the high field SMR measurements in YIG/Pt presented in Sect. 4.1. The SMR sign change on the other hand is clearly evident as a red pocket around $T_{\mathrm{comp}}(\mathrm{InYGdIG}) = 86\,\mathrm{K}$. With increasing magnetic field (up to $\mu_0 H \approx 15\,\mathrm{T}$), the temperature range in which the SMR sign change takes place broadens. This is consistent with the magnetic canting phase calculated for GdIG (Fig. 3.2). Since the exchange parameters of InYGdIG are not well known, we first compare the experimental SMR data obtained in InYGdIG/Pt with the SMR calculated for GdIG/Pt. As no continuous phase shift of the resistivity angular dependence is observed in experiments, the modulation amplitude can be calculated according to Eq. (2.19): $\Delta\rho = \rho(\alpha_{\mathrm{H}} = 0°) - \rho(\alpha_{\mathrm{H}} = 90°)$. For simplicity, we start by assuming that only the Fe sublattice moments contribute to the SMR in InYGdIG and that equal numbers of magnetic moments are tilted by $\pm\xi$ in the sample plane (2D limit, see Sect. 2.3.2). Since the FeA and FeD moments are always antiparallel, we use the FeA canting angles calculated in Fig. 3.2 (c). The resistivity modulation amplitude can be rewritten based on Eq. (2.15) and we obtain[4]

---

[4] This expression is equivalent to Eq. (2.20).

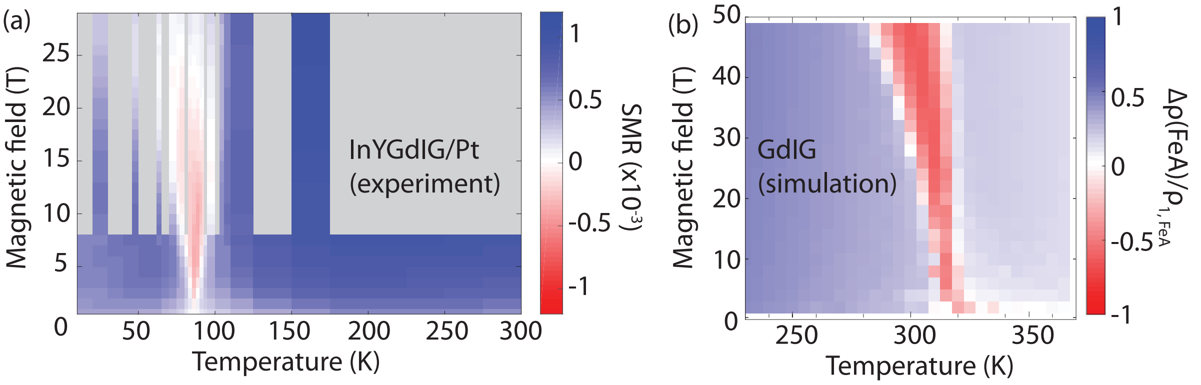

Figure 4.5: (a) SMR amplitude obtained from Eq. (4.2) as a function of temperature and magnetic field measured in the InYGdIG/Pt sample. In the blue regions the SMR is positive, i.e. has the same sign and α_H-dependence as for the collinear ferrimagnet YIG (see Sect. 4.1). The red regions indicate negative SMR (as in Fig. 4.4 (b)). No data has been taken in the regions shaded in gray. (b) Amplitude of the resistivity modulation $\Delta\rho(\mathrm{FeA})$ calculated using Eq. (4.3) for the FeA moments in GdIG. The calculations are based on the canting angles ξ_{FeA} displayed in Fig. 3.2 (c) and $\Delta\rho$ is normalized to the sublattice specific SMR efficiency $\rho_{1,\mathrm{FeA}}$. Figure adapted from Ref. [30]

$$\begin{aligned}
\frac{\Delta\rho}{\rho_{1,\mathrm{FeA}}} &= \left(\frac{1}{2}\cos^2(0^\circ+\xi_{\mathrm{FeA}})+\frac{1}{2}\cos^2(0^\circ-\xi_{\mathrm{FeA}})\right) \\
&- \left(\frac{1}{2}\cos^2(90^\circ+\xi_{\mathrm{FeA}})+\frac{1}{2}\cos^2(90^\circ-\xi_{\mathrm{FeA}})\right) \\
&= \left(\frac{1}{2}\cos^2(\xi_{\mathrm{FeA}})+\frac{1}{2}\cos^2(-\xi_{\mathrm{FeA}})\right)-\left(\frac{1}{2}\sin^2(\xi_{\mathrm{FeA}})+\frac{1}{2}\sin^2(-\xi_{\mathrm{FeA}})\right) \\
&= \cos^2(\xi_{\mathrm{FeA}})-\sin^2(\xi_{\mathrm{FeA}}). \qquad (4.3)
\end{aligned}$$

Note that here $\Delta\rho$ is normalized to the SMR efficiency $\rho_{1,\mathrm{FeA}}$ of the FeA sublattice. Since we are only interested in a qualitative study of the SMR in the canting phase, the exact amplitude of the resistivity modulation is not relevant here. $\Delta\rho/\rho_{1,\mathrm{FeA}}$ was therefore calculated by J. Barker based on Eq. (4.3) using the canting angle ξ_{FeA} calculated for GdIG (Fig. 3.2 (c)). The results for temperatures $225\,\mathrm{K} \leq T \leq 375\,\mathrm{K}$ and magnetic fields up to $\mu_0 H = 50\,\mathrm{T}$ are compiled in Fig. 4.5 (b). The red and blue color again corresponds to a positive and negative $\Delta\rho$, respectively. The calculated amplitude of the resistivity modulation indeed reveals a sign change close to $T_{\mathrm{comp}}^{\mathrm{sim}}$ similar to the experimental observations. Interestingly, a reasonable agreement between model and experiment is obtained already upon taking into account only the Fe moments.

In the canting phase at high magnetic fields $\mu_0 H \approx 20\,\mathrm{T}$ however, the absolute value of the measured SMR amplitude in Fig. 4.5 decreases and yields a small positive value (blue color) for $\mu_0 H \geq 25\,\mathrm{T}$. This is no longer consistent with the calculations based on the FeA sublattice contribution (Fig. 4.5 (b)). While the plot of the $\Delta\rho$ amplitude in Fig. 4.5 (b) is cut off at 50 T and below 225 K, the SMR behavior at much higher magnetic fields and low temperatures can be extrapolated from the complete phase diagram in Fig. 3.2 (c). According to the latter, the red pocket in Fig. 4.5 (b) - where the FeA moments are perpendicular to the applied field and the SMR ratio is negative - should still be observed at high fields and low temperatures in GdIG. The same applies for InYGdIG, although the critical fields for the canting phase are expected to be lower, as discussed in Sect. 3.1.2.

We further illustrate this point based on additional calculations of the SMR effect in a mean field model which were conducted by R. Schlitz during his master's thesis at WMI [55] (see Fig. 4.6). The calculations are based on a simplified two-sublattice system with a net Fe and a Gd magnetic sublattice. Since the exchange constants of this model ferrimagnet are unknown, they were chosen such that the compensation and Curie temperatures in the calculations are close to the ones measured for the InYGdIG sample studied in this section. Details about the calculations and assumptions introduced in this model can be found in Ref. [55]. In a first step, the canting angles ξ_X for the net Fe and the Gd magnetic moments were calculated as a function of temperature and magnetic field (not shown here). Based on these results, the expected temperature and magnetic field dependence of the Fe and Gd sublattice contributions to the total resistivity modulation (normalized to the sublattice specific SMR efficiency) were calculated as $\Delta\rho(X)/\rho_{1,\mathrm{X}} = \cos^2(\xi_X) - \sin^2(\xi_X)$ (in analogy to Eq. (4.3)) and are displayed in Fig. 4.6. The red and blue color represents regions of negative and positive $\Delta\rho$, respectively. Note that the magnetic field axis only goes up to 60 T, which is much lower compared to the magnetic field range used for the calculations of the phase diagram in GdIG (Fig. 3.2). However, the doping of the magnetic sublattices also leads to lower critical fields for the calculated canting in InYGdIG, consistent with expectations, such that the whole canting phase is covered in Fig. 4.6. The resistivity response calculated from the orientation of the Fe sublattice moments is compiled in Fig. 4.6 (a). The results are in good agreement with the atomistic calculations displayed in Fig. 4.5 (b), only with lower critical fields. We therefore expect a negative $\Delta\rho(\mathrm{Fe})$ response within the canting phase also for low temperatures and in a specific magnetic field range.

However, no SMR sign change occurs at low temperatures in the experiments in Fig. 4.5 and the red pocket seems limited to $\mu_0 H \approx 25\,\mathrm{T}$. This may indicate that the model based only on the orientation of the Fe sublattice magnetic moments is not sufficient to describe the low temperature SMR response of (doped) GdIG at high magnetic fields.

We therefore discuss a possible additional contribution of the Gd sublattice moments. The expected $\Delta\rho(\mathrm{GdC})$ is depicted in Fig. 4.6 (b) and we find a qualitatively different form of the sign change region (red pocket) compared to the results for the Fe sublattice. As already indicated in Fig. 3.2 (d), the Gd moments are only canted in a small region around the compensation temperature. For large magnetic fields, the Gd moments are

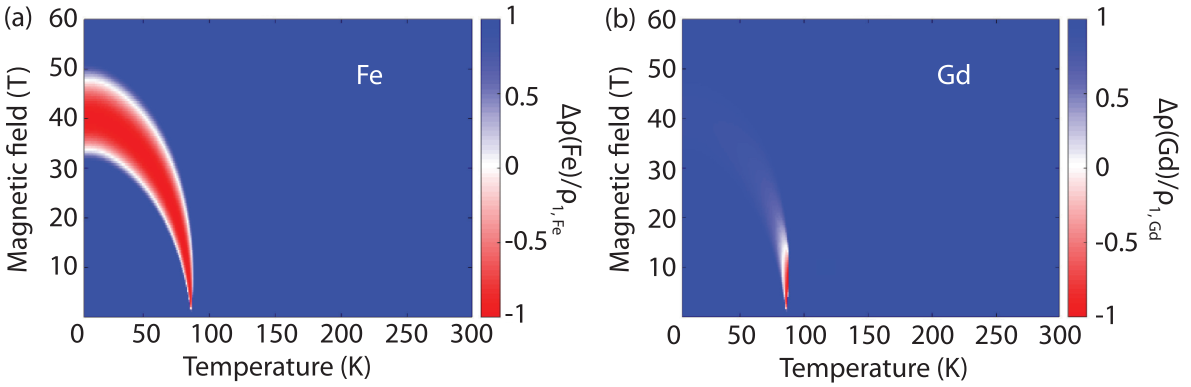

Figure 4.6: Calculation of the expected SMR response in a simplified two sublattice system with a net Fe and a Gd sublattice magnetization. The magnetic properties of this model system are similar to the ones of the InYGdIG sample studied here. The calculations are based on a mean field model and were conducted by R. Schlitz in the course of his master's thesis at WMI [55]. The sublattice specific (normalized) resistivity modulation amplitude $\Delta\rho$ calculated from the orientation of the sublattice magnetizations ξ_X is depicted as a function of magnetic field and temperature for the net Fe sublattice moments (a) and the Gd moments (b). The red and blue color represent negative and positive $\Delta\rho$, respectively.

mostly aligned with the external field, giving rise to a positive SMR ratio. Assuming that both the Gd and Fe sublattice moments contribute to the SMR, the sum of $\Delta\rho$(Fe) and $\Delta\rho$(Gd) obtained from Fig. 4.6, can qualitatively reproduce the experimental observation in Fig. 4.5, i.e. no sign change at high fields and low temperatures. The size of the red pocket where the SMR sign change occurs then depends on the relative contributions of the two sublattices[5]. One could interpret this as indications that both the Fe and Gd moments contribute to the SMR. Once again, we would like to emphasize that the simulations discussed here only give a qualitative idea of the SMR response considering both the Fe and Gd moments. A quantitative analysis of the relative sublattice specific contributions is not straightforward as discussed in more detail in Sect. 2.3.2 and requires further investigations in the future.

It is important to point out that the magnetic properties of (doped) GdIG can also be described based on the Néel vector orientation $\mathbf{N}/N = (\mathbf{M}_{\mathrm{Fe,net}} - \mathbf{M}_{\mathrm{Gd}})/|\mathbf{M}_{\mathrm{Fe,net}} - \mathbf{M}_{\mathrm{Gd}}|$ [55]. Assuming that the SMR is sensitive to the Néel vector orientation, the resistivity should obey $\rho = \rho_0 + \rho_1(1 - (\frac{\mathbf{N}}{N} \cdot \mathbf{t})^2)$. In this description, the magnitudes of the sublattice magnetizations enter the SMR response: due to the strong magnetic field and temperature dependence of the Gd sublattice magnetization, the Néel vector is dominated by the Gd moments at low temperatures and high magnetic fields, whereas at high temperatures and low magnetic fields where the Gd is disordered, $\mathbf{N} \approx \mathbf{M}_{\mathrm{Fe,net}}$. This is very different from

---

[5] Note that the Gd contribution alone already seems to reproduce the SMR response in InYGdIG. However, neglecting the contribution of the Fe sublattice is unrealistic, as SMR measurements in YIG demonstrate that the Fe moments give rise to an SMR effect.

our model based on the individual contributions of the sublattice moments according to Eq. (2.12) where the lengths of the magnetization vectors are not relevant. Furthermore, the question arises whether the Gd moments need to be ferromagnetically ordered to contribute to the SMR. In other words: is a long range magnetic order required for spin transfer torque, or can the SMR effect also be measured in a bilayer consisting of a NM and a paramagnetic insulator? There is up to now no clear evidence of a SMR effect in a paramagnetic system, however, this specific issue requires further investigation [109]. While a SMR effect based on the Néel vector cannot unambiguously be excluded at this point, the SMR theory based on individual sublattice moments appears to be at least qualitatively consistent with the measured SMR response in the collinear and canted phase. We therefore adhere to this model in the following. In particular, domain formation in the canted phase could play an important role for the quantitative SMR amplitudes (see Sect. 2.3), which can be easily integrated in the microscopic model (Eq. (2.12)). Furthermore, this model allows for a more general description of systems where no Néel vector is defined (e.g. chiral magnets).

We would also like to emphasize that the SMR sign changes discussed here are qualitatively different from those observed in spin Seebeck effect (SSE) experiments in GdIG/Pt heterostructures [83]. While the sign change of the SMR is found only in the canting phase, Geprägs et al. report a second sign change of the SSE at low temperatures attributed to the contribution of multiple magnon branches [83] (see Sect. 5.2.2). These observations are consistent with our physical picture that the SMR reflects the orientation of the sublattice magnetic moments and is therefore independent of magnon modes.

To summarize the discussion above, in the collinear magnetic phase of InYGdIG (far away from the compensation temperature), the same SMR signature with a positive modulation amplitude as in YIG/Pt is observed. However, around T_{comp} we find a sign inversion of the SMR amplitude. We therefore attribute this behavior to the non-collinear reorientation of the sublattice moments in the spin canting phase, as corroborated by complementary XMCD measurements. We show that the experimental data can be understood based on the microscopic model proposed in Sect. 2.3, assuming that the magnetic moments residing on different sublattices contribute independently to the SMR. In particular, for sufficiently large canting angles ($\xi > 45°$, assuming all moments lie in the sample plane) a shift of the SMR angular dependence by 90° is observed, corresponding to an inversion of the SMR amplitude. The experimental data therefore clearly rule out that the SMR effect in a non-collinear magnet is governed by the net magnetization orientation. Additional SMR measurements in FMI/Pt bilayers with different PLD-grown rare-earth iron garnet thin film as the FMI layer (pure $Gd_3Fe_5O_{12}$ and $Dy_3Fe_5O_{12}$ [55]) reveal a similar sign change of the SMR amplitude close to the respective magnetic compensation temperature, confirming the reproducibility of our observation. These results therefore demonstrate that simple transport experiments can identify non-collinear magnetic phases in highly resistive magnets contacted by heavy metals. This is also confirmed by recent reports on SMR measurements conducted in Cu_2OSeO_3, where a sign change of the SMR amplitude was observed for a transition from the helical to the conical magnetic phase [59].

4.3 Summary: spin Hall magnetoresistance in FMI/Pt bilayers

In this chapter we discussed the spin Hall magnetoresistance (SMR) in bilayers consisting of a ferrimagnetic insulator (FMI) and the normal metal Pt. In a heterostructure where the FMI is a collinear ferrimagnet, the Pt resistivity simply depends on the orientation of the net magnetization in the FMI. This macrospin model is well established for YIG, where the two antiferromagnetically coupled Fe sublattice magnetizations are always collinear for magnetic fields available in experiments (see Sect. 4.1). In a non-collinear magnet however, the macrospin model is no longer applicable and we assert that the SMR is governed by the orientation of the individual magnetic moments (see Sect. 2.3) [30]. This is experimentally confirmed by SMR measurements in the compensated ferrimagnet In, Y doped GdIG which exhibits a collinear as well as a canted magnetic phase (see Sect. 4.2). While the signature of the SMR response in the collinear phase of InYGdIG is the same as in YIG, a sign change of the SMR amplitude (phase shift by 90°) is observed in the canted magnetic phase. We attribute this sign change to a reorientation of the magnetic sublattice moments away from the applied magnetic field, even reaching a perpendicular alignment at specific temperatures and magnetic fields. These results were published in Phys. Rev. B **94**, 094401 (2016) [30] and represent the first observation of the SMR effect in a canted magnetic phase, demonstrating that in a non-collinear magnet the SMR cannot be described in terms of the net magnetization orientation. This is an important insight since the SMR probes the orientation of the sublattice moments and therefore opens the path for SMR measurements in antiferromagnetic insulators (AFMI), which do not exhibit a net magnetization. Resistivity measurements in a AFMI/Pt bilayer can for example be used to read out information encoded in the magnetic system, similar to the read out of magnetic states via the anisotropic magnetoresistance in conductive antiferromagnets [13].

In addition to a mapping of the magnetic phase diagram in GdIG, i.e. differentiating between collinear and canted configurations, a more detailed analysis of the SMR angular dependence can give further insights into the microscopic magnetic structure. In Sect. 2.3, we proposed a generalized SMR model based on the assumption that each magnetic moment gives rise to an individual SMR contribution. In particular, we find that the amplitude and phase shift of the overall resistivity modulation depends on the canting angle of each moment and on the symmetry of the system. In an isotropic magnet, we expect multiple energetically equivalent magnetic moment orientations within one sublattice, which are all occupied with equal probability. In such a scenario, only the amplitude of the resistivity is affected by the canting angle and changes sign, while the phase of the angular dependence stays constant. This is indeed observed in the canting phase of InYGdIG in Sect. 4.2. On the other hand, the finite phase shift observed in other compensated garnets such as ErIG [56, 57] can also qualitatively be reproduced by our theoretical model, e.g. by including anisotropies leading to different canting angles within one sublattice and/or an unequal distribution of magnetic moment orientations between energetically equivalent states. We can furthermore extend this picture to describe three dimensional magnetic structures, i.e. magnetic moments with out of plane components, conical magnets [59, 109] or even more complex magnetic structures. While a detailed understanding of the impact of the latter on the resistivity response still requires further investigation, the SMR effect might prove a powerful tool not only to map out magnetic phase transitions, but also to gain insights into the microscopic magnetic structure by simple magnetotransport measurements.

Part II

Non-local magnon transport in FMI/Pt bilayers

In Part I of this thesis, we have shown that spin Hall magnetoresistance (SMR) measurements in a ferrimagnetic insulator (FMI)/Pt heterostructure allow for the electrical mapping of magnetic phase transitions and give information on the (sublattice) magnetization orientation. For the description of the SMR only the ability to torque the magnetic moments in the FMI is relevant. The SMR thus depends on the orientation of the sublattice magnetic moments, while magnetic excitations in the form of spin waves/magnons are currently not included (or required) in the theoretical model in good approximation. However, in addition to the read-out of static magnetic states or configurations via magnetoresistive effects, the investigation of magnetic excitations is also of great relevance in the field of spintronics. In particular, different concepts have been put forward for information transfer and processing based on propagating spin waves. Several building blocks for magnon based logic have been implemented using coherently excited spin waves, including a magnon transistor [110], a magnon multiplexer [111] and first concepts on how to direct spin waves around the curvature of a wave guide [112].

Recent experiments have furthermore shown that information can also be transported in the ferrimagnetic insulator yttrium iron garnet (YIG) via non-equilibrium magnons which are excited and detected electrically using two parallel Pt strips deposited on top of the YIG [3, 4]. By applying a dc charge current to the injector Pt strip, an electron spin accumulation is generated at the Pt/YIG interface via the spin Hall effect (SHE, see Sect. 2.1). This spin accumulation is converted into a magnon accumulation in the ferrimagnetic insulator and the excited magnons diffuse through the magnetic material, away from the injector [113, 114]. If the second, electrically isolated Pt (detector) strip is placed within the magnon diffusion length, the magnons are converted back to an electron spin accumulation in the detector Pt strip. This gives rise to a charge current due to the inverse spin Hall effect (ISHE, see Sect. 2.1) in the Pt, which is detected as a non-local voltage in open circuit conditions. The amplitude of the detected non-local voltage is modulated by the magnetization orientation following a $\sin^2(\alpha_\mathrm{H})$ dependence, where α_H is the angle between magnetization and charge current direction, and we therefore label this effect magnon mediated magnetoresistance (MMR) [4].

In addition to the electrical magnon injection, non-equilibrium magnons can also be generated thermally by locally heating the YIG via the Pt injector strip [3, 115–117]. Similar to the MMR, the diffusing magnons can be detected in the second Pt strip and we call this the non-local spin Seebeck effect, in analogy to its well established local counterpart the (longitudinal) spin Seebeck effect [93–95, 118–122].

In this part we therefore study the non-local magnon transport in FMI/Pt heterostructures. In Chap. 5, we start by presenting the current theoretical model for the electrical and thermal magnon injection and transport. We then turn to the experimental study of the MMR effect, i.e. the electrical injection of non-equilibrium magnons, in YIG/Pt in Chap. 6. Our measurements as a function of temperature, magnetic field and injector-detector distance give first insights into the microscopic processes involved in the MMR.

Based on our findings, we present a proof-of-principle device in Chap. 7, which performs logic operations within the magnonic system. These results were published in Appl. Phys. Lett. **109**, 022405 (2016) [123]. In Chap. 8, we address the non-local SSE in YIG/Pt, i.e. the transport of thermally excited magnons in a non-local geometry, as a function of temperature, magnetic field and injector-detector distance. The corresponding results were published in AIP Adv. **7** 085102 (2017). Chapter 9 is dedicated to the MMR effect in gadolinium iron garnet (GdIG)/Pt, i.e. a system which exhibits both collinear and canted magnetic phases (see Sect. 3.1.2 and 4.2), as well as a more complex magnon spectrum including multiple thermally populated magnon modes with opposite precession direction (polarization) at room temperature. The temperature and magnetic field dependent measurements of the non-local MMR signal in GdIG/Pt therefore allow for the investigation of magnon transport in a canted magnetic phase and give further insight into the injection and transport properties in the presence of multiple thermally populated magnon modes. Finally, Chap. 10 gives a short summary of our most important findings on magnon transport in a non-local geometry.

Chapter 5

Magnon transport in a non-local geometry: theoretical overview

In this chapter, we give a theoretical overview on the transport of non-equilibrium magnons in a heterostructure consisting of a ferrimagnetic insulator and two parallel, electrically isolated Pt strips deposited on top of the FMI. The non-equilibrium magnons can be injected electrically or thermally, leading to the magnon-mediated magnetoresistance (MMR) and the non-local spin Seebeck effect (SSE), respectively. Both effects will be shortly introduced in the following. For the electrical magnon injection, a dc charge current is applied to the first Pt strip (injector), inducing a spin accumulation at the Pt/FMI interface via the spin Hall effect (SHE) (see Sect. 2.1). This spin accumulation is converted into a non-equilibrium magnon population in the ferrimagnet, which diffuses through the FMI and is converted back into an electron spin accumulation in the second Pt strip (detector). The ensuing spin current in the detector induces a non-local voltage due to the ISHE. The combined action of the charge current in the injector strip and non-local voltage in the detector strip corresponds to the MMR effect. In general, we therefore distinguish two main physical processes in the MMR effect, namely the injection/detection of non-equilibrium magnons via the Pt strips and the magnon diffusion through the FMI. The electrical injection and detection processes are based on the transfer of magnetic moment across the Pt/FMI interface and will be discussed in Sect. 5.1. In Sect. 5.2, we look into the spin-wave spectra of the two material systems under investigation, i.e. YIG and GdIG (see Sect. 3.1), and discuss the thermal magnon population of different magnon modes. The magnon diffusion process in the FMI is addressed in Sect. 5.3 and finally the thermal magnon injection and ensuing non-local SSE are introduced in Sect. 5.4.

5.1 Magnetic moment transfer at the Pt/FMI interface

In order to understand the electrical magnon injection and detection, we first focus on the transfer of angular momentum from the Pt, where it is carried by electrons, to the FMI where the angular momentum is carried by magnons. A theoretical model for the electron spin to magnon conversion (injection) and vice versa (detection) has been put forward by

Zhang and Zhang [113, 114] based on previous calculations by Takahashi *et al.* [124]. In this model, an *s*-*d* type interaction $-J_{sd}\boldsymbol{\sigma}\cdot\boldsymbol{S}_i$ is assumed at the Pt/FMI interface, with $\boldsymbol{\sigma}$ the electron spin in the Pt and $\boldsymbol{S}_i$ the local spin in the FMI layer [113, 125]. The total angular momentum is conserved. Following Zhang and Zhang, we thus can write down the following boundary condition at the Pt/FMI interface for the electron spin current density $J_s(0^-)$ in the Pt and the magnon current density $J_m(0^+)$ in the FMI

$$J_s(0^-) = J_m(0^+). \tag{5.1}$$

The total angular momentum current across the interface is given by [114]

$$J_t(0) = G_{em}\delta m_s(0^-) - G_{me}\delta m_m(0^+) \tag{5.2}$$

where G_{em} (G_{me}) denotes the interface spin conductance for the conversion of the electron spin (magnon) accumulation $\delta m_s(0^-)$ ($\delta m_m(0^+)$) to the magnon (electron spin) accumulation.

The spin convertances in Eq. (5.2) were calculated by Zhang and Zhang [114] based on the magnon and electron spin distribution functions as well as the corresponding densities of states. Assuming simple parabolic bands for electrons and magnons, they obtain the dominant temperature dependencies of $G_{em} \sim (T/T_c)^{3/2}$ and $G_{me} \sim (T/T_F)$, i.e. at low temperatures the injection and detection become inefficient such that the measured MMR effect (the non-local voltage in the detector Pt strip) vanishes.

Before addressing this temperature dependence in more detail, we first introduce a simplified picture for the transfer of angular momentum across the interface, as sketched in Fig. 5.1. In the following, we consistently use the electron spin magnetic moment $\mathbf{m}_s = -g_s\mu_{\mathrm{B}}\boldsymbol{\sigma}/\hbar$ in the Pt and the magnetic moment $\mathbf{m}_m$ carried by the magnons, which is antiparallel to the net magnetization $\mathbf{M}$ in the FMI. The directions of the spin magnetic moment current $\mathbf{J}_{\mathrm{s}}^{\mathrm{SHE}}$ and charge current $\mathbf{J}_{\mathrm{c}}^{\mathrm{ISHE}}$ induced in the Pt layer by the SHE and ISHE, respectively, (see Sect. 2.1) are then defined as[1] [38]

$$\mathbf{J}_{\mathrm{s}}^{\mathrm{SHE}} = \Theta_{\mathrm{SH}}\frac{\hbar}{2e}\mathbf{J}_{\mathrm{c}} \times \boldsymbol{\sigma} \propto -\Theta_{\mathrm{SH}}\mathbf{J}_{\mathrm{c}} \times \mathbf{m}_{\mathrm{s}} \tag{5.3}$$

$$\mathbf{J}_{\mathrm{c}}^{\mathrm{ISHE}} = \Theta_{\mathrm{SH}}\frac{2e}{\hbar}\mathbf{J}_{\mathrm{s}} \times \boldsymbol{\sigma} \propto -\Theta_{\mathrm{SH}}\mathbf{J}_{\mathrm{s}} \times \mathbf{m}_{\mathrm{s}}. \tag{5.4}$$

According to Eq. (5.3), a charge current $\mathbf{J}_c$ applied to the Pt injector along the $-\mathbf{x}$-direction gives rise to an electron spin magnetic moment accumulation $\delta\mathbf{m}_s$ along $\mathbf{y}$ at the Pt/YIG interface (red arrows in Fig. 5.1) due to the SHE[2]. By flipping one of

---

[1] We only focus on the direction of the induced currents, not on a quantitative analysis of the current amplitude.

[2] The magnetic moment current $\mathbf{J}_s$ in the Pt is not shown here for clarity.

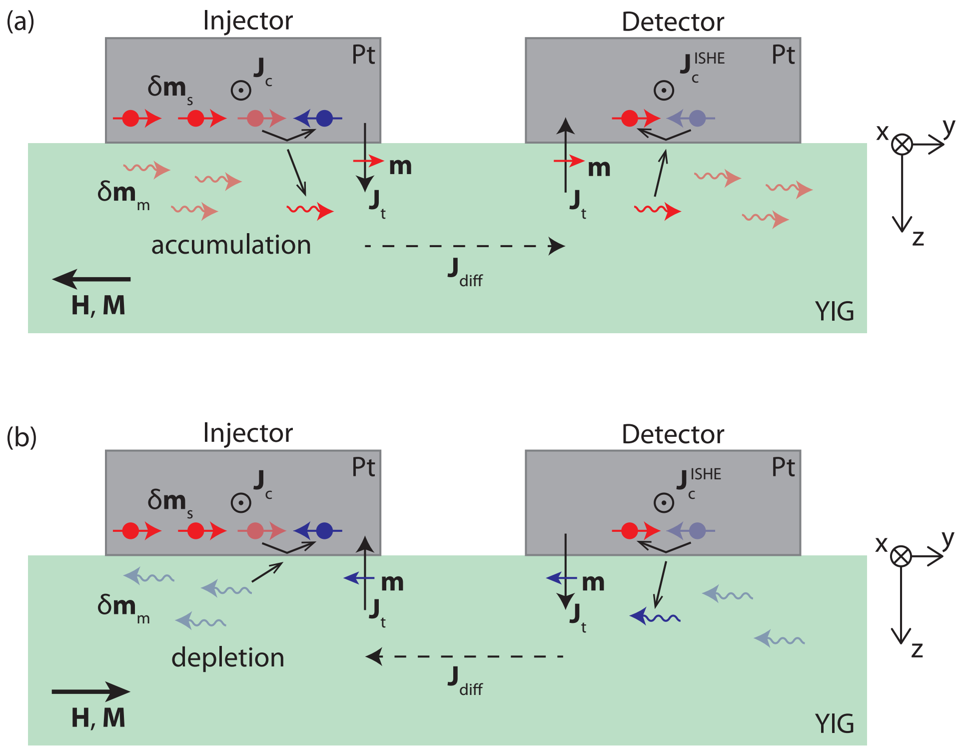

Figure 5.1: Sketch of the electron spin magnetic moment to magnon conversion at a YIG/Pt interface for (a) **M** antiparallel to the electron spin magnetic moment $\mathbf{m}_s$ and (b) **M** parallel to $\mathbf{m}_s$. The semi-transparent magnons (wiggly lines with arrows, for more details see main text) correspond to equilibrium thermal magnons. Depending on the magnetization direction a magnon is either generated or annihilated when an electron flips its spin in the Pt, leading to a magnon accumulation or depletion beneath the injector. Both processes give rise to a magnetic moment current $\mathbf{J}_t$ across the detector interface with opposite flow and polarization direction, leading to the same effective current $\mathbf{J}_\mathrm{c}^\mathrm{ISHE}$. Note that the color of the thermally excited magnons corresponds to the orientation of the carried magnetic moment with respect to the coordinate system and therefore changes upon inversion of **M**.

these electrons from right to left (red to blue), the spare magnetic moment $\Delta\mathbf{m}_s = g_s\mu_\mathrm{B}$ generates a magnetic excitation in the FMI called magnon (red wiggly arrow in Fig. 5.1 (a)). The transfer of spin magnetic moment across the interface can be described as a flow of magnetic moment $\mathbf{J}_t$ in positive **z**-direction from the Pt to the FMI. An accumulation of non-equilibrium magnons $\delta\mathbf{m}_m \parallel \mathbf{y}$ is subsequently generated in the ferrimagnet in addition to the equilibrium thermal magnon population (semi-transparent red wiggly arrows). Here, the wiggly arrows represent the direction of the carried magnetic moment, not the magnon propagation direction. The non-equilibrium magnons diffuse through the FMI[3] (see Sect. 5.3) and are detected in the second Pt strip via the inverse process: the flow of magnetic moment flips electron spins at the Pt/FMI interface, such that the

---

[3] The direction of the diffusion current $\mathbf{J}_\mathrm{diff}$ in the FMI is sketched as a dashed arrow in Fig. 5.1. In general, we expect magnons to diffuse in both + and −**y**-direction away from the injector (see Chap. 7).

electrons which are originally in equilibrium become polarized. The ensuing spin magnetic moment current $\mathbf{J}_s$ in the Pt induces a charge current $\mathbf{J}_c^{\mathrm{ISHE}}$ due to the ISHE according to Eq. (5.4). Note that $\mathbf{J}_c$ and $\mathbf{J}_c^{\mathrm{ISHE}}$ in injector and detector both flow along the same direction.

We now discuss the dependence of the MMR on the magnetization orientation. Neglecting magnetic anisotropy, we assume that the net magnetization points along the external magnetic field. In Fig. 5.1 (a), $\mathbf{M}$ is oriented along the $-\mathbf{y}$-direction and therefore antiparallel to the electron spin magnetic moment $\mathbf{m}_s$ at the Pt/FMI interface. As discussed above, the excess moment from the electron spin flip therefore reduces the total magnetization in the FMI, corresponding to the generation of a magnon (red wiggly arrow in Fig. 5.1 (a)). In the scenario depicted in Fig. 5.1 (b), however, the external magnetic field is inverted and the net magnetization points along the $+\mathbf{y}$-direction. The corresponding thermally excited magnons (blue, semi-transparent, wiggly arrows in Fig. 5.1 (b)) still reduce the net magnetization and the magnetic moment they carry now points along the -$\mathbf{y}$-direction[4]. The excess magnetic moment from the electron spin flip in the Pt is now parallel to $\mathbf{M}$ and increases the total magnetization of the FMI, corresponding to the annihilation or absorption of one already thermally excited magnon. Note that in both cases the (net) flow of magnetic moment across the injector interface is identical, since both the current and polarization direction are inverted (a current of “left” polarized (blue) moments flowing along $-\mathbf{z}$ is effectively the same as a current of “right” polarized (red) moments flowing along $+\mathbf{z}$). In Fig. 5.1 (b), the magnon population underneath the injector is thus depleted, such that the magnon diffusion current $\mathbf{J}_{\mathrm{diff}}$ changes sign and magnons flow from the detector towards the injector. The ensuing magnetic moment current across the detector interface has once more opposite current and polarization direction compared to Fig. 5.1 (a). The detected ISHE current in the second Pt strip is therefore the same for both scenarios depicted in Fig. 5.1. At finite temperatures, assuming that the magnon excitation and absorption is equally efficient, we expect a 180° symmetric MMR effect.

In experiments, the non-local MMR voltage is extracted using the current switching method (see Sect. 3.3.2 and 6.2), and a modulation of the MMR effect amplitude, following a $\sin^2(\alpha_{\mathrm{H}})$ dependence on the in-plane magnetic field orientation α_{H} with respect to the current direction $\mathbf{J}_c$, is found (with the same angle definition as in Fig. 2.2) [3, 4]. As discussed later on in Sect. 6.3.1, the non-local voltage goes to zero for $\mathbf{M} \parallel \mathbf{J}_c$ ($\alpha_{\mathrm{H}} = 0°$). We note that in the context of SMR theory, the configuration $\mathbf{M} \parallel \mathbf{J}_c$, i.e. $\mathbf{M} \perp \boldsymbol{\sigma}$, corresponds to a maximum spin transfer torque, such that the interface spin current is

---

However, in the scenario depicted here, only the diffusion current which can be detected in the second Pt strip is represented.

[4] Note that the red and blue color in Fig. 5.1 represents the direction of magnetic moment with respect to the fixed coordinate system, not the magnon polarization with respect to the magnetization direction $\mathbf{M}$ as discussed later on in Sect. 5.2.

absorbed by the FMI macrospin (see Sect. 2.2). The fact that no magnons are detected non-locally for $\alpha_{\mathrm{H}} = 0°$, suggests that either the interfacial scattering process described in Fig. 5.1 is suppressed or that the transverse magnetic excitations for $\mathbf{M} \perp \boldsymbol{\sigma}$ have comparatively short lifetime [126]. In the following we therefore define the maximum non-local signal measured for $\alpha_{\mathrm{H}} = 90°$ as the MMR amplitude.

5.2 Relevance of the thermal magnon population

As discussed in the previous section, the MMR amplitude is expected to vanish at low temperatures [114]. This is indeed confirmed by experiments, as shown in Sect. 6.3.2 [4]. Furthermore, a suppression of the MMR effect in YIG/Pt with increasing external magnetic field is observed in experiments (see Sect. 6.3.3) [127]. These findings suggest that the thermal magnon population (which is suppressed by low temperatures and high magnetic fields) is of importance for a qualitative understanding of the temperature and magnetic field dependence of the MMR amplitude. In the following, we discuss the transfer of magnetic moment across the Pt/YIG interface and focus on the injection efficiency. In the theoretical description proposed by Zhang and Zhang [114, 124], the relevant parameters are the non-equilibrium electron distribution function, i.e. the electron spin magnetic moment accumulation at the interface arising from the spin Hall effect, and the equilibrium magnon distribution function in the FMI, i.e. the thermal magnon population [114, 124]. Discussing the magnon spectrum of the FMI is therefore of great relevance for the MMR.

5.2.1 YIG magnon spectrum

We start with the spin-wave spectrum of YIG calculated from atomistic spin dynamics by Barker and Bauer [64] which is displayed in Fig. 5.2 for different temperatures $1\,\mathrm{K} \leq T \leq 300\,\mathrm{K}$ (Figure taken from Ref. [64]). The red and blue color corresponds to a counterclockwise and clockwise precession of the magnon mode with respect to the external magnetic field, which we label "+" and "−" polarization in the following. While the spectrum consists of multiple magnon branches due to the complex unit cell of YIG, for temperatures up to about 300 K mainly the FMR-like fundamental mode is thermally populated as indicated by the black dashed line in Fig. 5.2, which corresponds to the thermal energy $k_{\mathrm{B}}T$ [64]. In YIG we therefore only consider the lowest energy magnon branch for the discussion of the magnon injection in the MMR effect. Note that the fundamental mode has positive polarization and counterclockwise precession direction as expected for the FMR mode in YIG.

Figure 5.2 then gives a qualitative explanation for the MMR power law dependence, as calculated in Ref. [114]: only magnons with energy $\hbar\omega \leq k_B T$ are thermally populated, leading to a vanishing equilibrium magnon population at low temperatures. According to

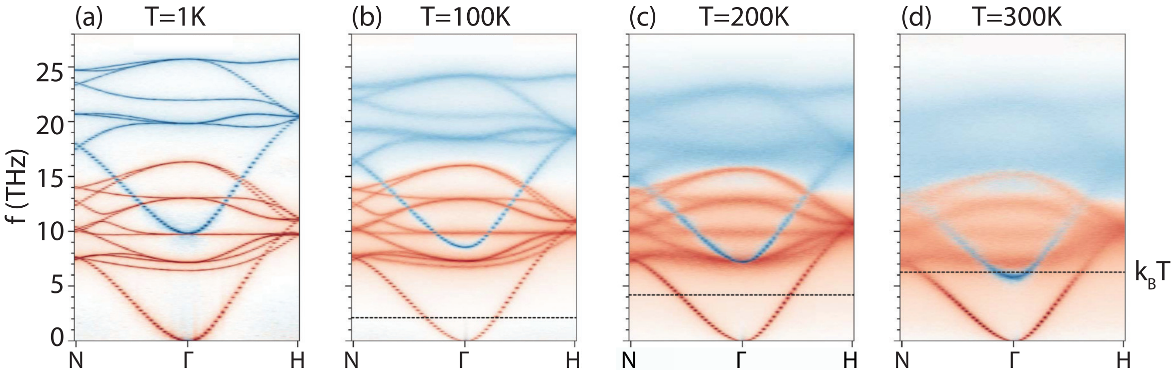

Figure 5.2: Spin-wave spectrum of YIG calculated for different temperatures. The black dashed line represents the thermal energy $k_\mathrm{B}T$ and the red and blue color corresponds to positive and negative magnon polarization/precession direction, respectively. Figure taken from Ref. [64].

Refs. [114, 124] the injection efficiency is proportional to the thermal magnon population and therefore becomes inefficient at low temperatures, such that the MMR vanishes.

A similar line of argument can be applied to the magnetic field dependence of the MMR. In the presence of an external magnetic field the fundamental mode shifts to higher frequencies due to the opening of the Zeeman gap. This is intuitive as the magnons of the FMR-like branch reduce the net magnetization in the ferrimagnet. When a large magnetic field is applied, the magnon excitation is energetically more costly, such that low energy/frequency magnons are suppressed, leading to a reduction of the overall thermal magnon population. In particular, when the Zeeman gap is larger than the thermal energy $k_\mathrm{B}T$, magnons are frozen out. This effect has already been observed in the context of spin Seebeck effect and magnon heat conductivity measurements in YIG/Pt [119, 120, 128].

Indeed the experimental MMR measurements in YIG/Pt summarized in Chap. 6 reveal a vanishing MMR at low temperatures and a suppression of the signal with increasing magnetic field, indicating that the thermal magnon population already allows for a qualitative understanding of the MMR behavior in YIG/Pt bilayers.

5.2.2 GdIG magnon spectrum

[5]We now turn to the three-sublattice ferrimagnet GdIG (introduced in Sect. 3.1.2), which exhibits several magnon branches in the low THz regime, such that multiple magnon modes are thermally populated even below room temperature. Figure 5.3 displays the GdIG magnon spectrum also obtained from atomistic simulations conducted by J. Barker [129]. At low temperatures, the spectrum looks very similar to YIG since only the fundamental mode with positive polarization (red) is populated. This suggests that at low temperatures

---

[5] This section contains calculations of the GdIG magnon spectrum conducted by J. Barker which are being prepared for publication together with our experimental data shown in Sect. 9.1 [129]. Parts of the text and figures from Ref. [129] are adapted here for the format of this thesis.

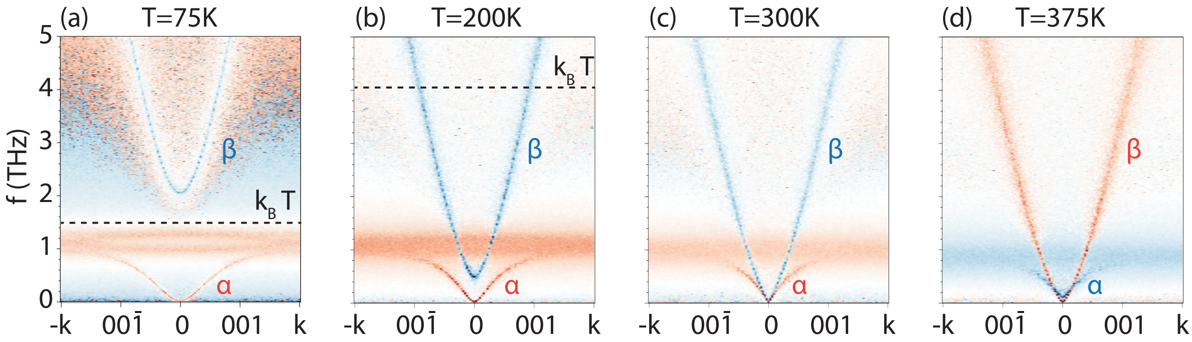

Figure 5.3: Spin-wave spectrum of GdIG calculated by J. Barker for different temperatures. The compensation temperature obtained in the simulation is $T_{\mathrm{comp}}^{\mathrm{sim}} \approx 320\,\mathrm{K}$. The red and blue color corresponds to positive and negative magnon polarization, respectively. We label the dispersive mode α and the high energy parabolic mode β. Figure adapted from Ref. [129].

when only the FMR-like mode is relevant, GdIG behaves similar to YIG. Only at higher temperatures $T \gtrsim 100\,\mathrm{K}$ a second gapped mode with negative polarization (blue mode in Fig. 5.3 (a)) shifts down below $k_{\mathrm{B}}T$. For simplicity we label the magnon modes according to their type of dispersion relation: the low energy dispersive mode α and the high energy parabolic mode β (red and blue modes in Fig. 5.3 (a), respectively). The frequency gap of the β-mode depends on the exchange energy between the Fe and Gd moments [83]. With increasing temperature, the Gd loses order, leading to a decrease of the exchange gap and a red-shift of the gapped mode. For high temperatures around $T = 300\,\mathrm{K}$ (Fig. 5.3 (c)), both the α- and β-mode lie at similar frequencies. At the magnetic compensation temperature ($T_{\mathrm{comp}}^{\mathrm{sim}} \approx 320\,\mathrm{K}$), the two modes eventually exchange roles and polarization due to the reorientation of the Fe and Gd sublattice magnetizations (see Sect. 3.1.2), such that the α mode now has "$-$" (blue) and the β mode "+" polarization (red). In the following we assume that these two modes dominate the magnon transport in GdIG. The additional flat bands around $f = 1\,\mathrm{THz}$ are neglected since they are expected to be nearly dispersionless and have large line width (and thus short magnon lifetime). This assumption, together with the dominance of the α- and β-mode, has already proven reasonable for the description of the spin Seebeck effect in GdIG/Pt bilayers [83], where the contributions from different magnon modes have been studied extensively. In particular, it was found that upon thermal excitation the two dominating modes yield different signs in the detected SSE signal, depending on their polarization. We can understand this behavior intuitively, as magnons with opposite polarization carry opposite magnetic moment. The excitation of FMR-like magnons with positive polarization (red modes) reduces the net magnetization. On the other hand, the magnon modes at higher frequencies originate from the precession of magnetic sublattice moments in an effective field, which includes the external field and the exchange fields provided by the other sublattices (similar to the excitations in an antiferromagnet) [130–132]. Magnons with negative polarization (blue modes) correspond

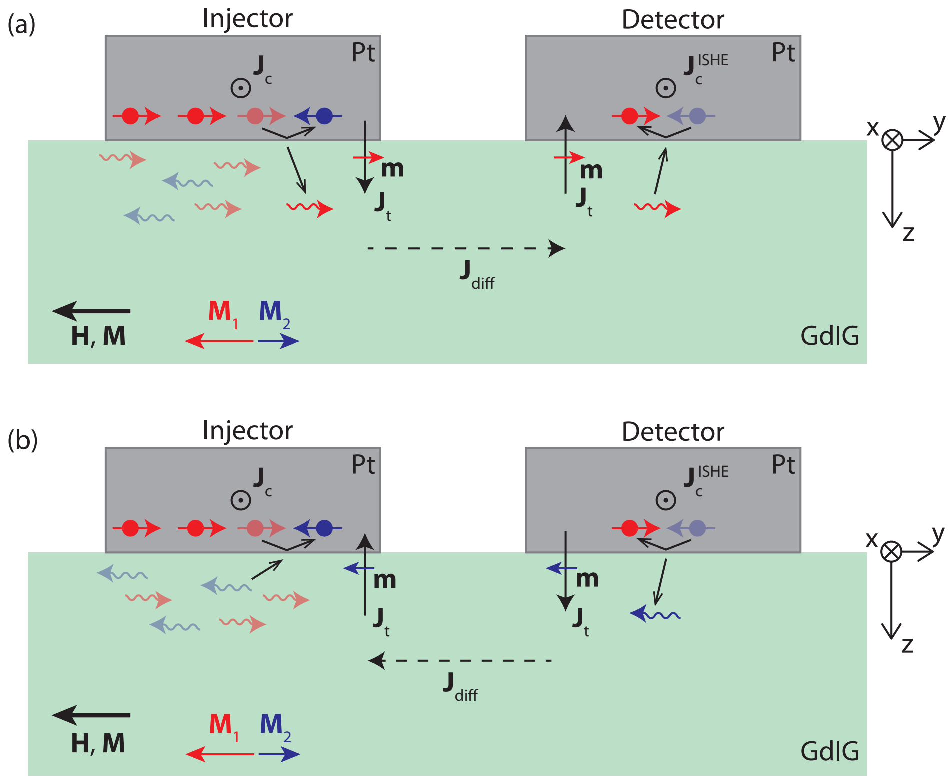

Figure 5.4: Sketch of the electron spin magnetic moment to magnon conversion at a GdIG/Pt interface. The α- and β magnon modes are both thermally populated (semi-transparent red and blue wiggly arrows). Due to the SHE in the Pt injector, there is an accumulation of right polarized (red) electrons at the interface. When an electron flips its spin, either (a) a "+" polarized (red) magnon is generated or (b) a "−" polarized (blue) magnon is absorbed (b). In both scenarios, the net flow of magnetic moment across the injector (detector) interface is the same, such that the ensuing ISHE current $\mathbf{J}_c^{\mathrm{ISHE}}$ in the detector is identical.

to the precession of sublattice moments aligned antiparallel to the external field and their excitation therefore increases the net magnetization. When the magnetic moment is transferred across the GdIG/Pt interface, the sign of the ensuing ISHE current depends on the polarization of the dominating magnon mode. Comparing the SSE sign in YIG/Pt and GdIG/Pt confirms that at low temperatures only the positively polarized fundamental α mode contributes. With increasing temperature, when the β-mode in GdIG red-shifts sufficiently to gain a relevant thermal population, the SSE signal changes sign, indicating that the high energy mode dominates the SSE. A second sign change is then observed at T_{comp}, where the magnon modes switch polarization [83, 133].

As discussed in Sect. 5.1, the MMR also originates from the transfer of angular momentum across the FMI/Pt interface. It is therefore crucial to investigate the impact of differently polarized magnon modes on the MMR effect. However, the different physical origins of SSE and MMR need to be taken into account: in the SSE, magnons from both modes are thermally excited in the FMI, leading to an excess of magnons for both polarizations. The sign of the ensuing ISHE current is then determined by the dominating magnon polarization. In the MMR effect however, the injection is not thermal but originates from scattering processes at the injector Pt/FMI interface. In this case the injected magnetic moment is determined by the SHE induced spin accumulation at the Pt/FMI interface. In Fig. 5.4, the scattering processes in YIG (single magnon mode, see Fig. 5.1) are extended to GdIG (two dominating magnon modes). The red and blue magnons in Fig. 5.4 correspond to "+" and "−" polarized magnons, i.e. excitations which reduce or increase the net magnetization, respectively. We describe the three sublattice ferrimagnet in terms of a net Fe and a Gd magnetization, or in a more general way as two magnetizations $\mathbf{M}_1$ and $\mathbf{M}_2$ (see Sect. 3.1.2) and focus on the collinear magnetic phase, where all sublattice moments are aligned (anti)-parallel to the applied magnetic field. Based on Fig. 5.4, we discuss the configuration where the charge current is applied along $+\mathbf{x}$ and the net magnetization $\mathbf{M}$ points along the $-\mathbf{y}$-direction. In analogy to the scenario described in Fig. 5.1 (a), an electron polarized along $\mathbf{y}$ flips its spin and generates one "+" polarized (red) magnon, reducing the net magnetization. However, the same electron moment flip can occur when a "−" polarized (blue) magnon is absorbed, also leading to a reduction of the total magnetization (Fig. 5.4 (b)). For a given spin polarization, "+" polarized (red) magnons accumulate underneath the injector and diffuse towards the detector, while "−" polarized (blue) magnons are depleted at the injector, leading to a diffusion of "−" polarized magnons towards the latter. For both processes, the effective magnetic moment current across the GdIG/Pt interface is therefore the same. In this picture, the electrically injected magnetic moment can be carried by either of the two magnon modes with opposite polarization, but always induces the same sign of the MMR signal at the detector. In contrast to the SSE, we therefore expect no sign change of the MMR signal as a function of temperature in GdIG/Pt.

While both magnon modes contribute with the same sign to the detected MMR signal, the injection/absorption efficiency for the α and β modes can be different. In order to quantitatively determine the contributions of the two modes, one needs to calculate the probability of the different scattering processes shown in Fig. 5.4. This probability depends on the availability of initial and final states for the injection and detection, i.e. on the electron and magnon distribution functions and densities of states, which should be subject to future theoretical work. However, the magnon modes shift in frequency as a function of temperature and magnetic field, changing the thermal magnon population. Since this is expected to affect the detected MMR signal [114, 124], first insights into the contributions from different magnon modes may be gained by studying the temperature and magnetic field dependence of the MMR in GdIG/Pt and comparing it to the calculations of the magnon spectra. The corresponding experimental results will be discussed in Chap. 9.

The injection (absorption) efficiency of the different magnons discussed up to now is independent of the distance between injector and detector. In the next section, we turn to the second important aspect in the description of the MMR, i.e. the transport properties of the magnons in the FMI.

5.3 Diffusion process

The magnon transport was studied in a 1D model, i.e. a trilayer consisting of Pt/FMI/Pt, by Zhang and Zhang in the frame of a general Boltzmann equation [113, 114]

$$v_z \frac{\partial N_m}{\partial z} + v_z \frac{\partial N_m}{\partial T} \frac{dT}{dz} + v_z \frac{\partial N_m}{\partial \boldsymbol{H}} \frac{d\boldsymbol{H}}{dz} = - \left(\frac{\partial N_m}{\partial t} \right)_{\text{scatt.}} \tag{5.5}$$

where $N_m(z, T(z), \boldsymbol{H}(z))$ is the magnon distribution and $v_z = \frac{1}{\hbar} \frac{\partial \epsilon_k}{\partial k_z}$ is the z component of the magnon velocity. The first term describes the magnon diffusion due to a spatial gradient in the magnon accumulation. The second and third term represent transport driven by a spatial temperature or magnetic field gradient. The right hand side of Eq. (5.5) is the scattering term obtained from relaxation time approximation

$$\left(\frac{\partial N_m}{\partial t} \right)_{\text{scatt.}} = \frac{N_m - \bar{N}_m}{\tau_m} + \frac{N_m - N_m^0}{\tau_{\text{th}}} \tag{5.6}$$

where $\bar{N}_m(z) = \int d\mathbf{k} N_m(z,\mathbf{k}) / \int d\mathbf{k}$ is the momentum averaged magnon distribution and $N_m^0(z,\mathbf{k}) = \left[e^{\epsilon_k / k_{\text{B}} T(z)} - 1 \right]^{-1}$ is the local equilibrium magnon distribution. Note that the theoretical model put forward by Zhang and Zhang is based on a single magnon band with parabolic dispersion relation $\epsilon_k = D\mathbf{k}^2 + \Delta_g$, where D is the spin wave stiffness and Δ_g the spin wave gap. The relaxation processes are separated into magnon conserving and non-conserving relaxation processes (first and second term in Eq. (5.6), respectively). This can be understood intuitively as the first term relaxes to the momentum averaged distribution, e.g. the magnon momentum can change from $\mathbf{k}$ to $\mathbf{k}'$ due to a scattering event keeping the number of magnons constant, while the second term relaxes back to the equilibrium thermal distribution, i.e. a state of lower excitation number.

For the simplest case of uniform temperature and magnetic field, the authors obtain the diffusion equation for non-equilibrium magnons [113]

$$\frac{d^2}{dz^2} \delta m_m(z) = \frac{\delta m_m(z)}{\lambda_m^2} \tag{5.7}$$

with the magnon accumulation $\delta m_m(z) = \frac{1}{(2\pi)^3} \int d\mathbf{k} \left[N_m(\mathbf{k}, z) - N_m^0(\mathbf{k}) \right]$ and the magnon diffusion length $\lambda_m \propto \sqrt{\tau_{th} \tau_m}$. The solution of Eq. (5.7) is of the form $\delta m_m(z) =$

$a\,\exp(-z/\lambda_m) + b\,\exp(z/\lambda_m)$. Assuming the detector is a perfect spin sink, i.e. $\delta m_m(0) = m_0$ and $\delta m_m(d) = 0$ [3], this leads to a magnon current density $j_m = -D(\partial m_m/\partial z)$

$$j_m(d) = -2D\frac{m_0}{\lambda_m}\frac{\exp(d/\lambda_m)}{1-\exp(2d/\lambda_m)}. \tag{5.8}$$

If the detector absorbs practically no spin and the magnon accumulation relaxes only far away from the detector, we expect [55]

$$j_m(d) = D\frac{m_0}{\lambda_m}\exp(-d/\lambda_m). \tag{5.9}$$

In both cases the diffusion process leads to a decay of the MMR signal as a function of the distance between injector and detector. This is confirmed by experimental observations as discussed in Sect. 6.3.4.

Note that the diffusion model described here is valid for a 1D diffusion process, i.e. in a trilayer consisting of Pt/FMI/Pt [113, 114]. While this configuration has also been studied experimentally [134, 135], the measurements presented in this thesis are conducted in a 2D configuration (two Pt strips on top of the FMI), such that the theoretical model might need to be adapted. However, the 1D transport model reproduces the data sufficiently well and can be applied in good approximation [3].

As mentioned above, this theoretical model only includes a single magnon branch with parabolic dispersion relation. A more detailed description of the magnon diffusion in GdIG requires taking into account multiple magnon branches with different dispersion relations (see Fig. 5.3). In particular, the magnon group velocity is determined by the dispersion relation and varies for different magnon branches and **k** vectors. It is therefore likely that in GdIG the two dominating magnon modes of opposite polarization have very different transport properties and contribute differently to the detected non-local signal, depending on the injector-detector distance. Furthermore, while magnon-magnon scattering is included in some of the current theoretical descriptions [126], interactions between magnon modes have not been considered yet. The latter are particularly relevant for the scenarios depicted in Fig. 5.3 (c) and (d) where the two magnon branches in GdIG with opposite polarization cross. Changes in the damping of the magnon modes, especially close to the compensation temperature [79, 84, 132, 136], may also become relevant for a detailed description of magnon transport properties in GdIG, as discussed in Sect. 9.1.

5.4 Thermal excitation of non-equilibrium magnons

We have up to now only discussed magnon injection via transfer of magnetic moment from the electron to the magnon system (see Sect. 5.1). However, non-equilibrium magnons can also be generated thermally by locally heating one Pt strip. This is also the origin of

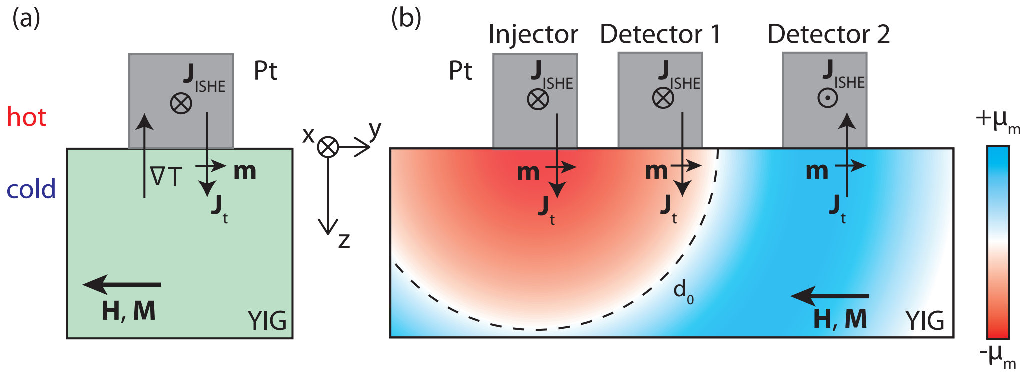

Figure 5.5: (a) Schematic representation of the local (longitudinal) SSE in YIG/Pt. A temperature gradient ∇T applied across the YIG/Pt interface generates a current $\mathbf{J}_t$ of magnetic moment $\mathbf{m}$ along the temperature gradient into the YIG. The ensuing ISHE current $\mathbf{J}_{\mathrm{ISHE}}$ can be measured in the Pt. (b) Schematic representation of the magnon accumulation profile in YIG where the blue and red color corresponds to a magnon accumulation and depletion (compared to thermal equilibrium), respectively. The sign change of the magnon accumulation occurs at d_0 (black dashed line) and leads to an inversion of the interfacial magnetic moment current $\mathbf{J}_t$ for $d > d_0$. Consequently, the measured ISHE voltage is opposite in detector 1 and 2. The white region on the right edge of the YIG film corresponds to thermal equilibrium, where the thermally excited magnon accumulation is relaxed.

the well established spin Seebeck effect [93–95, 118, 137], where a temperature gradient ∇T applied across the YIG/Pt interface induces a current of magnetic moment which flows along ∇T from the Pt into the YIG (see Fig. 5.5 (a)). The electron spin magnetic moment current in the Pt is converted into a charge current via the ISHE (Eq. (5.4)), which can be detected as a voltage in open circuit conditions. While the SSE has been studied as a function of YIG thickness in order to investigate the relevant length scales [121, 122], the (longitudinal) SSE is usually described in a 1D geometry, where only the dimensions in the $\mathbf{z}$ direction are relevant [137]. The non-local MMR measurements, however, show that non-equilibrium magnons also diffuse laterally (see Chap. 6). It is therefore of great interest to study the lateral transport of the thermally excited magnons in the same non-local geometry as for the MMR. First experimental confirmation of a non-local voltage of thermal origin has been given by Cornelissen *et al.* [3], and we call this effect non-local spin Seebeck effect in analogy to its local counterpart. In particular, both local and non-local SSE follow a $\sin(\alpha_{\mathrm{H}})$ dependence on the angle α_{H} between the external in-plane magnetic field and the direction $\mathbf{x}$ in which the voltage drop is measured (see Fig. 5.5).

In our typical two strip nanostructure (see Fig. 6.1), the local heating required for the excitation of non-equilibrium magnons is a byproduct of the MMR measurement: by driving a charge current through the Pt injector strip, energy is dissipated via Joule heating, leading to a temperature gradient across the Pt/YIG interface. This method is already successfully used for local SSE measurements [95]. In order to distinguish the thermal contribution from the electrical magnon injection (MMR) contribution (see Sect. 5.1), we use the current switching method described in Sect. 3.3.2 and extract the signal which originates from Joule heating and is therefore independent of the current direction. Alternatively, the same effect can also be achieved with laser heating as demonstrated for the local SSE [94] and recently for the non-local SSE [115]. However, the current heating method presents the advantage of measuring MMR and non-local SSE simultaneously in the same structure and is therefore applied in this thesis.

The non-local SSE has been investigated as a function of distance d between the injector (heater) strip and the detector in a YIG/Pt bilayer by Cornelissen *et al.* [3, 138] in order to extract the magnon diffusion length. While part of these results suggests that the diffusion length of thermally and electrically injected magnons are very similar (of the order of 10 µm), it is not straightforward to extract a length scale from all measurements, as a sign change arises in the non-local thermal signal at a characteristic distance d_0 [3]: for short distances $d < d_0$, local and non-local SSE have the same sign, whereas for larger distances $d > d_0$ the sign of the non-local signal is inverted. Additional measurements as a function of the YIG thickness t_{YIG} [117, 139] show that d_0 increases linearly with t_{YIG}.

The authors of Ref. [139] propose a theoretical model for the non-local SSE based on the profile of the non-equilibrium magnon accumulation in YIG, which can qualitatively reproduce the experimental observations. We retrace this line of argument in the following. First, we shortly discuss the possible origins of a magnon current (of thermal origin) flowing from the injector to the detector strip. Magnon currents carry magnetic moment ($\mathbf{j}_m$) as well as heat ($\mathbf{j}_{Q,m}$) [126, 139] according to the following equation

$$\begin{pmatrix} \frac{2e}{\hbar}\mathbf{j}_m \\ \mathbf{j}_{Q,m} \end{pmatrix} = - \begin{pmatrix} \sigma_m & \frac{L}{T} \\ \frac{\hbar L}{2e} & \kappa_m \end{pmatrix} \begin{pmatrix} \nabla\mu_m \\ \nabla T_m \end{pmatrix} . \tag{5.10}$$

The source of these magnon currents is either a gradient in the magnon accumulation $\nabla\mu_m$ or temperature ∇T_m. Here, σ_m is the magnon spin conductivity, L is the bulk spin Seebeck coefficient and κ_m is the magnon heat conductivity. The magnon current induced in the local SSE is connected to the temperature gradient via the spin Seebeck coefficient L and more precisely originates from a difference ΔT_{me} between the magnon temperature T_m in the YIG and the electron temperature T_e in the Pt [137]. In the metal, the electron and phonon temperatures are approximately the same and the phonon temperature T_p is continuous at the YIG/Pt interface. The magnons however cannot cross the interface, giving rise to a finite temperature difference ΔT_{mp} between phonon and magnon temperature (as well as a finite ΔT_{me}) as depicted in Fig. 5.6 (Figure taken from [126]). Microscopically the magnon and phonon systems thermalize by exchanging energy via scattering processes. These scattering processes conserve the magnon number, i.e. magnetic moment, and do not change the magnon accumulation μ_m in first approximation. It was shown that the magnon and phonon temperatures equilibrate on a length scale of a few

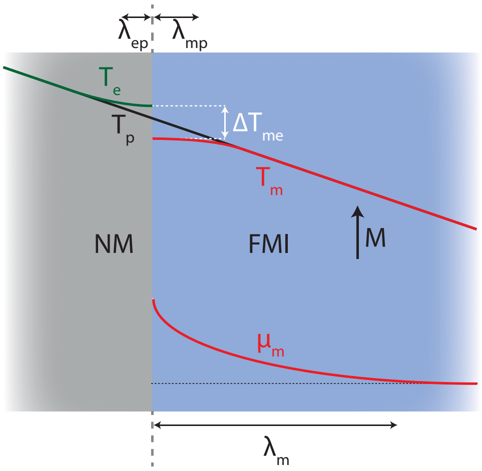

Figure 5.6: Temperature and magnon accumulation profile at a normal metal (NM)/ferrimagnetic insulator (FMI) interface, illustrating the theoretical model proposed by Cornelissen *et al.* [126]. The magnon-phonon thermalization length λ_{mp} is much shorter than the relaxation length of the magnon accumulation λ_m. Figure taken from Ref. [126].

nm in lateral direction [137] and can therefore not drive a lateral magnon current over several µm as observed in the non-local SSE experiments. The magnon accumulation μ_m however, is related to the number of non-equilibrium magnons and is therefore sensitive to scattering processes which do not conserve magnons. The scattering times for the latter are longer ($\sim 1\,\text{ns}$) than for magnon conserving processes ($\sim 1\,\text{ps}$) [126], leading to different decay lengths λ_m and λ_{mp} for μ_m and ΔT_{mp}, respectively. Since the magnon accumulation changes on the length scale of the diffusion process, it is reasonable to assume that the gradient of the magnon accumulation is the dominating origin of the non-local SSE: according to the model presented in Ref. [139], magnons which are thermally excited in the ferrimagnet due to Joule heating in the injector strip diffuse vertically towards the GGG/YIG interface as well as laterally to the sample edges. This leads to a depletion of magnons ($\mu_m < 0$, red in Fig. 5.5 (b)) compared to the thermal equilibrium population beneath the injector. On the other hand, diffusing magnons accumulate further away from the injector, giving rise to $\mu_m > 0$ (blue in Fig. 5.5 (b)). The dashed black line corresponds to d_0, i.e. the transition from magnon depletion to accumulation. The interfacial spin current $\mathbf{J}_t$ at the detector flows along the $+\mathbf{z}$-direction for a magnon depletion, i.e. $\mu_m < 0$, beneath the detector strip and in opposite direction (along $-\mathbf{z}$) when there is a magnon accumulation $\mu_m > 0$. This leads to opposite ISHE current in detector 1 ($d < d_0$) and 2 ($d > d_0$) for the scenario depicted in Fig. 5.5 (b). Note that for distances larger than the magnon relaxation length, the magnon accumulation decreases (white region on the right edge of the sketch in Fig. 5.5 (b)), since the magnon population relaxes towards thermal equilibrium.

Based on the assumption that the magnon accumulation profile has radial symmetry with respect to the heated strip[6] as shown in Fig. 5.5 (b), this model also qualitatively explains the increase of d_0 with increasing YIG thickness t_{YIG} observed by Shan *et al.* [139]. The non-equilibrium magnons accumulate at the YIG/GGG interface since they cannot cross into the GGG substrate. When decreasing the YIG thickness, the sign change of the magnon accumulation shifts closer to the Pt/YIG interface and the observed d_0 decreases.

In order to gain further insight into the microscopic origin of the non-local SSE in YIG/Pt, experimental results on the temperature and magnetic field dependence of the latter will be discussed in Chap. 8.

---

[6] The d_0 extracted from experiments is measured in lateral $\mathbf{x}$ direction. However the boundary conditions used for the calculations in Ref. [139] are only valid for a 1D model in $\mathbf{z}$ direction. It is likely that for thin films the transition from $\mu_m < 0$ to $\mu_m > 0$ is no longer isotropic, i.e. d_0 along $\mathbf{x}$ is larger than along $\mathbf{z}$. A 2D modeling might therefore be necessary to fully understand the position of the sign change.

Chapter 6

Magnon mediated magnetoresistance in YIG/Pt

In this chapter, we study the transport of electrically injected magnons through the ferrimagnetic insulator YIG, using two parallel Pt strips as injector and detector. These experiments are referred to as magnon mediated magnetoresistance (MMR) measurements, as introduced in Chap. 5. We start with a description of the sample preparation (Sect. 6.1) and experimental setup (Sect. 6.2). These techniques are also relevant for the next chapters. The experimental MMR results in YIG/Pt as a function of temperature, magnetic field and injector-detector distance are discussed in Sect. 6.3.

6.1 Sample preparation

In the following, we study the MMR effect in YIG/Pt heterostructures fabricated starting from commercially available YIG films[1]. The latter are grown onto a (111) oriented $Gd_3Ga_5O_{12}$ substrate via liquid phase epitaxy (LPE) and are typically a few µm thick. In contrast to the PLD grown thin films fabricated at the Walther-Meissner-Institute (see Sect. 3.2), an *in-situ* Pt deposition is not possible on the LPE films, since these are shipped via mail from the company/lab where the LPE growth took place. The samples therefore need to be carefully cleaned and prepared before the deposition of a Pt layer in order to guarantee a good quality interface [48]. The films are first cleaned in acetone and isopropanol in an ultrasonic bath, followed by chemical Piranha etching (3 volumes H_2SO_4 mixed with 1 volume H_2O_2) for 2-5 min. Immediately afterwards, the sample is rinsed in DI water and inserted into the load-lock of the UHV cluster at the Walther-Meissner-Institute. After annealing in 75 µbar O_2 atmosphere at 500 °C for 40 min, a Pt film of a few nm thickness is deposited via electron beam evaporation. A list of all the samples used throughout this thesis is compiled in Appendix A.

For the non-local measurements, we use nanostructures consisting of two parallel Pt strips of width $w = 500\,\mathrm{nm}$, edge-to-edge separation $20\,\mathrm{nm} \leq d \leq 10\,\mu\mathrm{m}$ and strip length

---

[1] The YIG LPE films used in this section were provided by Matesy (Magnetic Technology and Sytems).

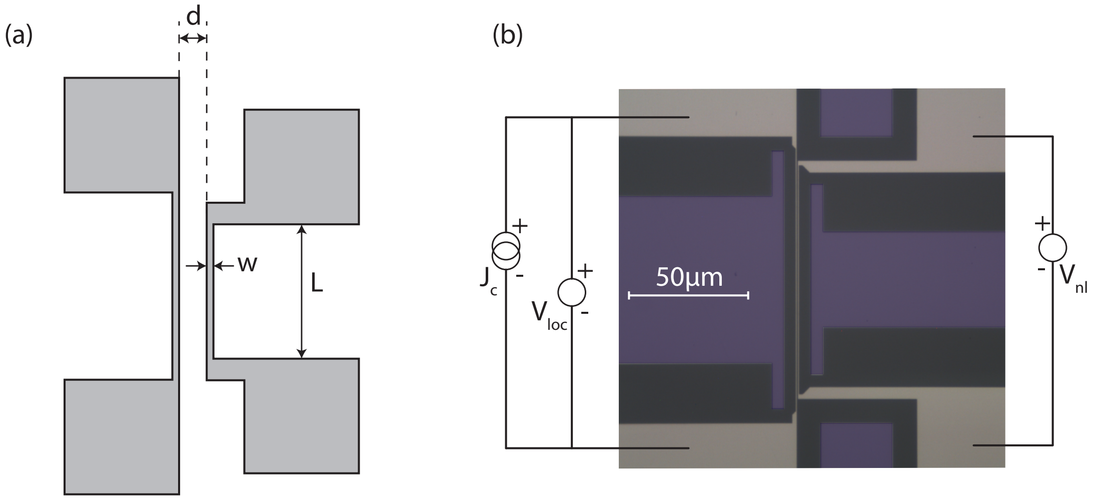

Figure 6.1: (a) Sketch of the two parallel Pt strips with width w, edge-to-edge separation d and length L used for the non-local measurements. (b) Optical micrograph of a non-local YIG/Pt nanostructure with $w = 500\,\text{nm}$, $d = 400\,\text{nm}$ and $L = 100\,\mu\text{m}$. The black and grey color corresponds to YIG and Pt, respectively. The blue shaded areas are proximity pads made of Pt as well. The electric wiring is depicted in black with the corresponding voltage and current polarities.

$L = 100\,\mu\text{m}$ as depicted schematically in Fig. 6.1 (a). An optical micrograph of one of the nanostructures taken on a YIG/Pt sample is displayed in Fig. 6.1 (b). The black and grey color corresponds to YIG and Pt, respectively. The areas shaded in blue are proximity pads (Pt) helpful for the electron beam lithography fabrication process but are not relevant for the functionality of the device. Note that electron beam lithography is used for the fabrication of the non-local structures in order to reach the necessary resolution down to a few 10 nm.

After a cleaning step using acetone and isopropanol, the FMI/Pt bilayer is preheated at 200 °C to remove excess water and allow for a better spreading of the resist. The sample is then covered with CSAR 62 resist (Allresist AR-P 6200) via spin coating at 2000 rpm for 60 s and baked at 150 °C for 60 s [55]. Subsequently, gold nanoparticles are applied to the edges of the sample as a reference for focusing the electron beam. The sample is then loaded into the NanoBeam nB5 electron beam lithography system and the pattern is written with a dose of $0.8\,\text{C}\,\text{m}^{-2}$. After the lithography process the resist is developed in Allresist AR 600-549 for 60 s and rinsed twice in isopropanol. The sample is subsequently etched for 60 to 120 s via argon ion beam milling to define the final Pt structure.

6.2 Experimental setup

After fabrication, the sample is glued onto a chip carrier and bonded with Al-wires. The left “injector” Pt strip is typically used for local measurements, where a charge current J_c

Option	Setting
Digits	7.5
Number of power line cycles (NPLC)	2
Filter type	repeating
Filter count	30

Table 6.1: Keithley 2182 nanovoltmeter filter settings used for non-local measurements.

is applied using a Keithley 2400 sourcemeter and the corresponding local voltage V_{loc} is measured in a 4-point geometry using a Keithley 2182 nanovoltmeter. Simultaneously the non-local voltage drop V_{nl} at the right "detector" Pt strip is measured in open circuit conditions using an additional Keithley 2182 nanovoltmeter. The wiring scheme is depicted in Fig. 6.1 (b). In order to disentangle resistive from thermal voltage contributions the current switching method described in Sect. 3.3.2 is applied. For a typical non-local measurement in this setup we use the Keithley 2182 settings listed in Tab. 6.1.

For temperature and magnetic field dependent measurements the sample is placed on a dipstick which is inserted into a superconducting magnet cryostat reaching magnetic fields $\mu_0 H \leq 7\,\mathrm{T}$ and temperatures $2\,\mathrm{K} \leq T \leq 300\,\mathrm{K}$ as described in Sect. 3.3. Additional measurements were conducted in a superconducting solenoid magnet cryostat allowing for magnetic fields $\mu_0 H \leq 15\,\mathrm{T}$ in the same temperature range. For the latter, a new rotator dipstick was designed in the course of this thesis enabling angle dependent magnetoresistance measurements in this particular setup. The dipstick was mostly assembled by C. De Rose during his bachelor's thesis at WMI, which I supervised. Details on the design and wiring of the dipstick can be found in Ref. [140].

Combining the settings in Tab. 6.1 with the current switching method (average over 5 switching cycles), a resolution of $5\,\mathrm{nV}$ can be reached for the non-local resistive signal, as long as the dipstick temperature is stable.

6.3 Experimental results in YIG/Pt

In this section we discuss the experimental results on magnon mediated magnetoresistance in YIG/Pt nanostructures. The sample used in the following was fabricated from a $2\,\mu\mathrm{m}$ thick YIG LPE film covered *ex-situ* with 10 nm of Pt (see Sect. 6.1). The experimental data presented in this section were obtained together with T. Wimmer, who I supervised during his master's thesis at WMI [141]. The measurements were conducted in the temperature range $5\,\mathrm{K} \leq T \leq 300\,\mathrm{K}$ with an external magnetic field $1\,\mathrm{T} \leq \mu_0 H \leq 15\,\mathrm{T}$. The charge current applied to the Pt injector strip is $100\,\mu\mathrm{A}$ throughout all measurements in this section and we apply Eq. (3.2) to extract the MMR contribution[2], i.e. the non-local

---

[2] The contributions of thermal origin are also extracted from this set of data according to Eq. (3.3) and will be discussed in Chap. 8.

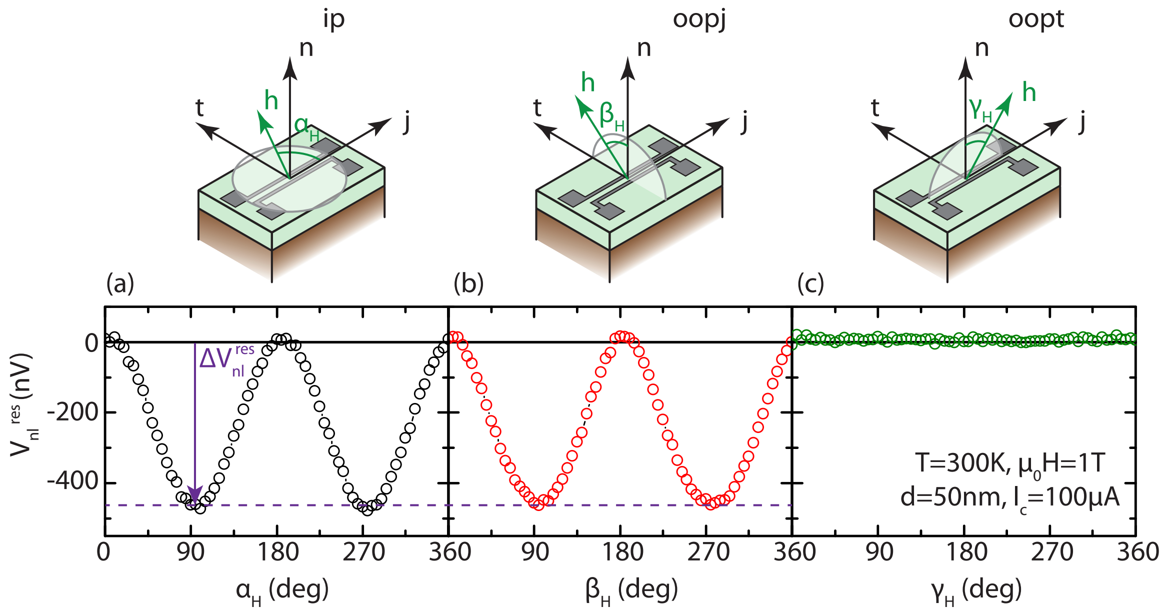

Figure 6.2: Non-local resistive voltage $V_{\mathrm{nl}}^{\mathrm{res}}$ in a YIG/Pt bilayer measured at $T = 300\,\mathrm{K}$ for (a) the in-plane, (b) out of plane rotation with respect to $\mathbf{j}$ and (c) out of plane rotation with respect to $\mathbf{t}$ for a fixed magnetic field amplitude $\mu_0 H = 1\,\mathrm{T}$. The two Pt strips are separated by an edge-to-edge distance $d = 50\,\mathrm{nm}$. The non-local voltage goes to zero when the magnetization direction $\mathbf{M}$ is perpendicular to the electron spin polarization $\boldsymbol{\sigma} \parallel \mathbf{t}$ ($\alpha_{\mathrm{H}} = 0°, 180°$), otherwise a finite negative voltage is observed.

voltage originating from electrical magnon injection. In the following, we discuss the experimental results and most important findings concerning the non-local resistive signal in YIG/Pt as a function of temperature, magnetic field and injector-detector distance.

6.3.1 Angular dependence

We start with the study of the angular dependence of the MMR effect by rotating the sample in a fixed external magnetic field magnitude $\mu_0 H = 1\,\mathrm{T}$ at $T = 300\,\mathrm{K}$. The measured non-local resistive voltage $V_{\mathrm{nl}}^{\mathrm{res}}$ is depicted in Fig. 6.2 for all three rotation planes, i.e. in-plane (ip), out of plane with respect to the current axis $\mathbf{j}$ (oopj) and out of plane with respect to the transverse direction $\mathbf{t}$ (oopt). As discussed in Sect. 5.1 [3, 4], a finite MMR signal is expected when the magnetic field is applied perpendicular to the charge current direction $\mathbf{J}_c \parallel \mathbf{j}$ in the Pt, such that $\boldsymbol{\sigma} \parallel \mathbf{M}$, while no non-local signal is detected for $\boldsymbol{\sigma} \perp \mathbf{M}$. Here, $\boldsymbol{\sigma} \parallel \mathbf{t}$ is the electron spin polarization induced by the SHE at the Pt/YIG interface (see Sect. 2.1). This behavior is confirmed by the experimental data in Fig. 6.2: in the ip rotation the signal vanishes for $\alpha_{\mathrm{H}} = 0°$, while a finite negative voltage is observed for $\alpha_{\mathrm{H}} = 90°$. The same applies for the oopj rotation. In oopt however, the MMR is always zero, since the magnetic field/magnetization is always perpendicular to the electron spin polarization at the Pt/YIG interface.

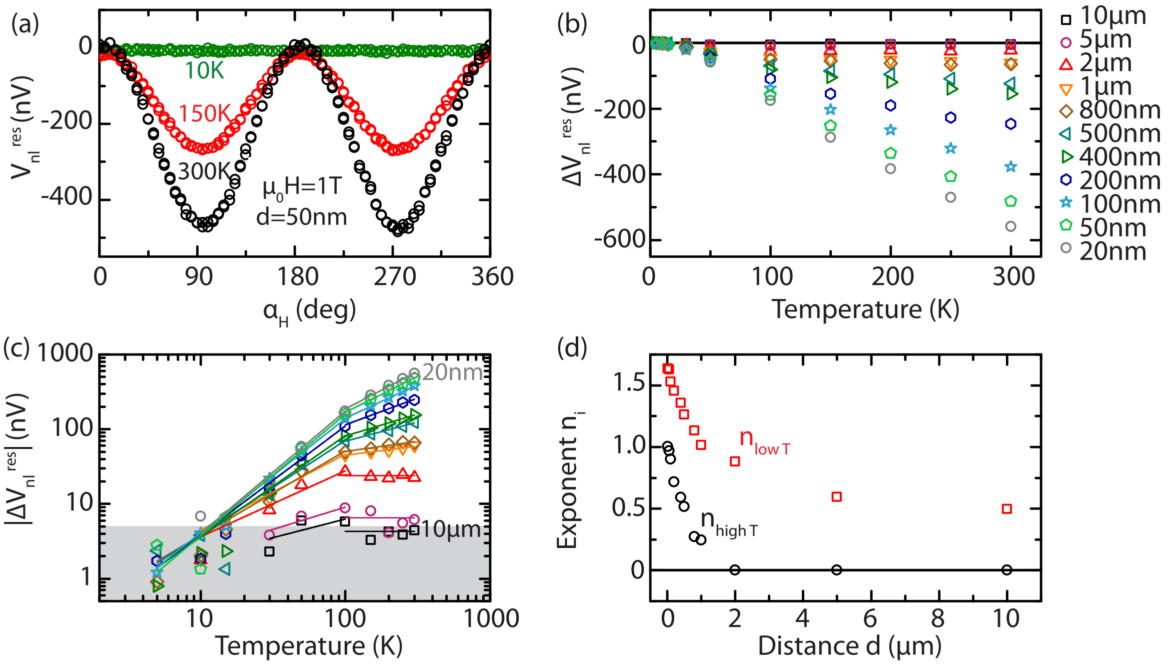

Figure 6.3: (a) Non-local resistive voltage $V_{\mathrm{nl}}^{\mathrm{res}}$ in a YIG/Pt bilayer measured for $T = 10\,\mathrm{K}, 150\,\mathrm{K}$ and $300\,\mathrm{K}$ as a function of the in-plane magnetic field orientation α_{H} for $\mu_0 H = 1\,\mathrm{T}$. (b) $\Delta V_{\mathrm{nl}}^{\mathrm{res}}$ extracted from the ADMR measurements as a function of temperature for all available strip separations $20\,\mathrm{nm} \leq d \leq 10\,\mu\mathrm{m}$. (c) Double-logarithmic plot of $|\Delta V_{\mathrm{nl}}^{\mathrm{res}}|$. The solid lines represent power law fits and the gray shaded area corresponds to the 5 nV noise floor of the measurement setup. (d) Exponent of the power law fit in panel (c) for the high and low temperature regime (black and red, respectively) as a function of the strip separation d.

In the following, we focus on the ip magnetic field rotation. $V_{\mathrm{nl}}^{\mathrm{res}}$ follows a $\sin^2(\alpha_{\mathrm{H}})$ dependence and we can extract the MMR amplitude $\Delta V_{\mathrm{nl}}^{\mathrm{res}} = V_{\mathrm{nl}}^{\mathrm{res}}(90°) - V_{\mathrm{nl}}^{\mathrm{res}}(0°)$ as indicated by the purple arrow in Fig. 6.2 (a). Note that $\Delta V_{\mathrm{nl}}^{\mathrm{res}}$ is negative for the measurement configuration depicted in Fig. 6.1 (b), which is consistent with previous observations using the same wiring scheme [4].

6.3.2 Temperature dependence

We now turn to the temperature dependence of the extracted MMR amplitude. Figure 6.3 (a) displays the non-local resistive signal $V_{\mathrm{nl}}^{\mathrm{res}}$ as a function of the ip magnetic field orientation α_{H} for $T = 10\,\mathrm{K}, 150\,\mathrm{K}$ and $300\,\mathrm{K}$ with $\mu_0 H = 1\,\mathrm{T}$. As predicted by theory [114] (see Sect. 5.1), the MMR vanishes for low temperatures around 10 K [4]. In order to quantitatively analyze the temperature dependence, we extract the MMR amplitude $\Delta V_{\mathrm{nl}}^{\mathrm{res}}$ from $\sin^2(\alpha_{\mathrm{H}})$ fits to the angle dependent magnetoresistance (ADMR) measurements in various devices with Pt strip separations $20\,\mathrm{nm} \leq d \leq 10\,\mu\mathrm{m}$. The result is plotted in Fig. 6.3 (b) in a linear scale and $|\Delta V_{\mathrm{nl}}^{\mathrm{res}}|$ is shown in Fig. 6.3 (c) in a double-logarithmic scale. The gray shaded region up to 5 nV in Fig. 6.3 (c) represents the noise floor of our measurement setup. The double-logarithmic plot reveals a power law dependence in T for all studied devices. However, the slope varies for different strip separations and we clearly observe different slopes for the high and low temperature regime. The data is therefore fitted with functions of the form $A \cdot T^{n_{\mathrm{lowT}}}$ for $5\,\mathrm{K} \leq T \leq 100\,\mathrm{K}$ and $B \cdot T^{n_{\mathrm{highT}}}$ for $100\,\mathrm{K} \leq T \leq 300\,\mathrm{K}$ for all strip separations (solid lines in Fig. 6.3 (c)). The exponents n_{lowT} (red) and n_{highT} (black) obtained from the power law fits are displayed in Fig. 6.3 (d) as a function of the strip separation d. Both n_{lowT} and n_{highT} are highest for short distances, but strongly decrease with d and start to saturate around $2\,\mu\mathrm{m}$. n_{highT} even goes to zero for large distances, corresponding to a temperature independent MMR.

For the description of the MMR temperature dependence, contributions from injection/detection efficiency as well as transport need to be taken into account. Since the former can be considered independent of distance, the behavior observed for different d suggests that the transport properties indeed play an important role in the temperature dependence of the MMR effect. The distance dependence of the MMR amplitude will be discussed in more detail in Sect. 6.3.4.

Here, we start with the temperature dependence of the injection and detection efficiency, which was calculated in Ref. [114] (see Sect. 5.1) as $G_{\mathrm{em}} \propto (T/T_c)^{3/2}$ and $G_{\mathrm{me}} \propto (T/T_F)$, respectively. The authors calculate that for d much smaller than the magnon diffusion length, the detector efficiency can be neglected, such that the MMR follows $T^{3/2}$. As we will show in Sect. 6.3.4, the magnon diffusion length λ_m in this sample is of the order of a few 100 nm. While the limit of $d \ll \lambda_m$ is therefore not applicable to all studied devices, λ_m is an order of magnitude larger than the shortest distances investigated here. The temperature dependence of the non-local signal observed in the short distance regime at low temperatures is therefore in good agreement with theoretical predictions of $n = 1.5$. For larger d and higher temperatures however, the slope of the temperature dependence is much weaker.

This behavior underlines that in the short distance regime, the temperature dependence is dominated by the injection efficiency, while in the long distance regime the diffusive properties dominate the amplitude of the MMR effect. In order to disentangle the contributions from transport and injection, a more detailed investigation of the MMR distance dependence is necessary. However, before addressing the latter in Sect. 6.3.4, we first turn to the magnetic field dependence of the MMR.

6.3.3 Magnetic field dependence

We have seen in Sect. 5.2 that the thermal magnon population and magnon injection can be suppressed by a magnetic field due to the opening of the Zeeman gap. We therefore measure the non-local resistive voltage as a function of the in-plane magnetic field orientation for $\mu_0 H = 1\,\mathrm{T}$, $4\,\mathrm{T}$ and $7\,\mathrm{T}$. Figure 6.4 (a) displays the ADMR measurements taken at 300 K for a device with $d = 100\,\mathrm{nm}$ and $w = 500\,\mathrm{nm}$. Indeed, the MMR amplitude decreases

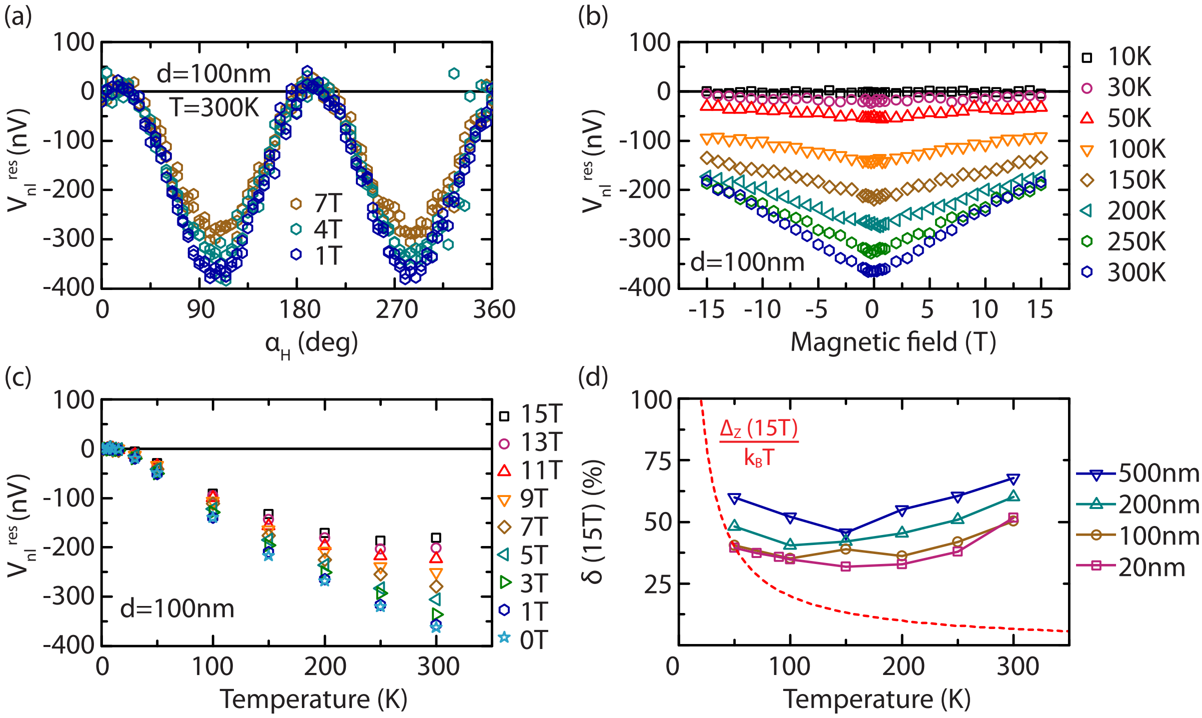

Figure 6.4: (a) $V_{\mathrm{nl}}^{\mathrm{res}}$ measured in a YIG/Pt bilayer at 300 K for $d = 100\,\mathrm{nm}$ as a function of the in-plane magnetic field orientation α_{H} for $\mu_0 H = 1\,\mathrm{T}, 4\,\mathrm{T}, 7\,\mathrm{T}$. (b) $V_{\mathrm{nl}}^{\mathrm{res}}$ as a function of magnetic field amplitude for $10\,\mathrm{K} \leq T \leq 300\,\mathrm{K}$. The magnetic field was applied perpendicular to the Pt strip and swept from -15 T to 15 T. (c) Non-local resistive voltage measured in the $d = 100\,\mathrm{nm}$ device as a function of temperature for different magnetic fields. (d) Relative field suppression $\delta(15\,\mathrm{T})$ of $V_{\mathrm{nl}}^{\mathrm{res}}$ calculated from the data in panel (c) according to Eq. (6.1) for different strip separations. The red dashed line represents the ratio of the Zeeman energy $\Delta_{\mathrm{Z}}(15\,\mathrm{T})$ and the thermal energy $k_{\mathrm{B}}T$ and gives an approximation for the expected field suppression arising from the Zeeman gap in the magnon dispersion relation.

with increasing magnetic field, as expected from a shift of the magnon spectrum and subsequent suppression of the magnon injection. To further analyze the influence of the magnon spectrum on the non-local voltage we measure the MMR signal in the $d = 100\,\mathrm{nm}$ structure while sweeping the magnetic field from $\mu_0 H = -15\,\mathrm{T}$ to $15\,\mathrm{T}$. Here, the magnetic field is applied in the plane and perpendicular to the Pt strip ($\alpha_{\mathrm{H}} = 90°$). The resulting $V_{\mathrm{nl}}^{\mathrm{res}}$ is shown in Fig. 6.4 (b) for different temperatures in the range $10\,\mathrm{K} \leq T \leq 300\,\mathrm{K}$. A suppression with increasing field is observed for all studied temperatures. For better visualization, the same data is plotted as a function of temperature for different magnetic fields in Fig. 6.4 (c). Since the signal amplitude at low temperatures is generally smaller, we calculate the relative suppression $\delta(\mu_0 H)$ of the MMR effect in %

$$\delta(\mu_0 H) = \frac{V_{\mathrm{nl}}^{\mathrm{res}}(0\,\mathrm{T}) - V_{\mathrm{nl}}^{\mathrm{res}}(\mu_0 H)}{V_{\mathrm{nl}}^{\mathrm{res}}(0\,\mathrm{T})} \tag{6.1}$$

The resulting relative suppression for $\mu_0 H = 15\,\mathrm{T}$ is depicted in Fig. 6.4 (d) as a function of temperature for different strip separations ranging from 20 nm to 500 nm. According to Eq. (6.1), $\delta = 100\%$ corresponds to the total suppression of the signal. Note that the relative suppression cannot be calculated reliably for $T < 50\,\mathrm{K}$, where the MMR vanishes.

While the overall temperature dependence for all devices displayed in Fig. 6.4 (d) is very similar, displaying a strong field suppression at 50 K as well as room temperature, the amplitude of the suppression varies for different distances. This again suggests that not only the injection efficiency is field dependent, but also the transport properties come into play, consistent with previously published results [127]. Here, we focus on a qualitative discussion of the observed field dependence in the context of the injection/detection efficiency and the magnon spectrum in YIG. In particular we discuss the field dependence of the MMR measured in the device with the smallest gap $d = 20\,\mathrm{nm}$, which we consider as the local limit, i.e. in this structure the MMR amplitude is dominated by the magnon injection efficiency, while the magnon diffusion properties are expected to play a minor role.

The low temperature field suppression can be understood intuitively from the magnon spectrum. The Zeeman gap induced in the dispersion relation due the external field is $\Delta_\mathrm{Z}(15\,\mathrm{T}) = g\mu_\mathrm{B} 15\,\mathrm{T} = 1.7\,\mathrm{meV}$, where $g \approx 2$ is the g-value for YIG [142] and μ_B the Bohr magneton. At 50 K, magnons are thermally populated up to $k_\mathrm{B} 50\,\mathrm{K} = 4\,\mathrm{meV}$. The experimental observation $\delta(15\,\mathrm{T}, 50\,\mathrm{K}) \approx 39\%$ for the 20 nm structure therefore agrees well with the ratio $\Delta_\mathrm{Z}(15\,\mathrm{T})/k_\mathrm{B} 50\,\mathrm{K} = 40\%$ calculated in a simple approximation[3]. However, with increasing temperature the relative suppression $\Delta_\mathrm{Z}(15\,\mathrm{T})/k_\mathrm{B} T$ expected from the Zeeman gap at 15 T decreases (red dashed line in Fig. 6.4 (d)) and deviates from the experimental observation.

A similar behavior was observed in the local spin Seebeck effect [119] (see also Sect. 8.2): a strong field suppression of the SSE is consistently found at low temperature, which is once more attributed to the opening of the Zeeman gap. The SSE suppression with magnetic field at room temperature is larger than the expected value obtained from the shift of the magnon mode and the authors of Ref. [119] therefore argue that low energy magnons (which are suppressed by magnetic field for all temperatures) provide a dominant contribution to the SSE. A similar line of argument could be applied to the MMR effect. However, the MMR suppression $\delta(15\,\mathrm{T}, 300\,\mathrm{K}) \approx 50\%$ in Fig. 6.4 (d) is much higher than for local SSE measurements conducted in the same sample, where a suppression of $\delta_\mathrm{SSE}(15\,\mathrm{T}, 300\,\mathrm{K}) \approx 10\%$ (discussed in Sect. 8.2, see Fig. 8.3 (d)) was obtained. These results suggest that the model used for the local SSE in YIG/Pt is not sufficient to reproduce the relative field suppression of the MMR effect at room temperature. Our observations may be related to the different physical origins of the MMR and local SSE, i.e. to the type of magnons (in terms of energy and k-vector) that contribute to each effect.

---

[3] The energy dependence of the density of states and distribution function, i.e. the number of magnons at a given energy, is not taken into account here.

However, for a quantitative model of the MMR temperature and magnetic field dependence in the small distance limit, a better understanding of the frequency distribution of the electrically injected magnons is necessary.

We furthermore point out, that according to the calculated YIG magnon spectrum displayed in Fig. 5.2 [64], a second high energy magnon mode becomes thermally populated around 300 K. As discussed in Sect. 5.2.2, the additional exchange mode may also contribute to transport if the mode is thermally populated. However, the influence of this second mode on the MMR effect in YIG is not well known up to now and requires further investigation in the future, in particular at temperatures above 300 K and large magnetic fields, where the high energy mode is more strongly occupied.

6.3.4 Distance dependence

In the temperature as well as in the magnetic field dependence of the MMR we have found strong evidence that the magnon injection/detection and the magnon diffusion processes both affect the detected non-local signal. We therefore now address the distance dependence of the MMR effect. We start with ADMR measurements of the non-local resistive signal as a function of the ip magnetic field orientation α_H displayed in Fig. 6.5 (a) for $d = 50\,\mathrm{nm}$, $500\,\mathrm{nm}$ and $1\,\mathrm{\mu m}$ at $T = 300\,\mathrm{K}$ and $\mu_0 H = 1\,\mathrm{T}$. As expected from a diffusive magnon transport, the non-local signal decreases for increasing injector-detector distance d. To get further insight into the length scales relevant for the MMR, $|\Delta V_\mathrm{nl}^\mathrm{res}|$ is extracted from ADMR measurements for all available strip separations. The results are shown in Fig. 6.5 (b) for different temperatures, where the gray shaded area corresponds to the noise floor of 5 nV in our setup. The solid lines represent fits to the data using a simple exponential decay function [139]

$$|\Delta V_\mathrm{nl}^\mathrm{res}| = V_\mathrm{nl,0}^\mathrm{res} \exp\left(-\frac{d}{\lambda_\mathrm{m}}\right) \tag{6.2}$$

where λ_m is the magnon diffusion length. Since the non-local signal is expected to vanish for infinitely large d, the offset of the fit function is set to zero. This function allows to disentangle the contributions from injection efficiency and magnon diffusion by extracting $V_\mathrm{nl,0}^\mathrm{res}$ in the local limit of $d = 0$ and λ_m separately. We find that the fit function reproduces the experimental data in Fig. 6.5 (b) well in the short distance limit, but deviates for larger distances. Note that Cornelissen *et al.* use Eq. (5.8) to analyze their data [3]. However, this function does not fit our data well either. This may be attributed to the fact that we study a different distance regime than the authors of Ref. [3], where a diffusion length of about 10 µm is obtained by fitting Eq. (5.8) to data up to 30 µm[4]. In contrast, the signal in Fig. 6.5 (b) drops beneath the noise floor around $d = 5$ to 10 µm. In the

---

[4] It is also important to point out that Eq. (5.8) is obtained for specific boundary conditions, i.e. assuming that the detector is a perfect spin sink. As we will discuss in Chap. 7, an additional detector strip

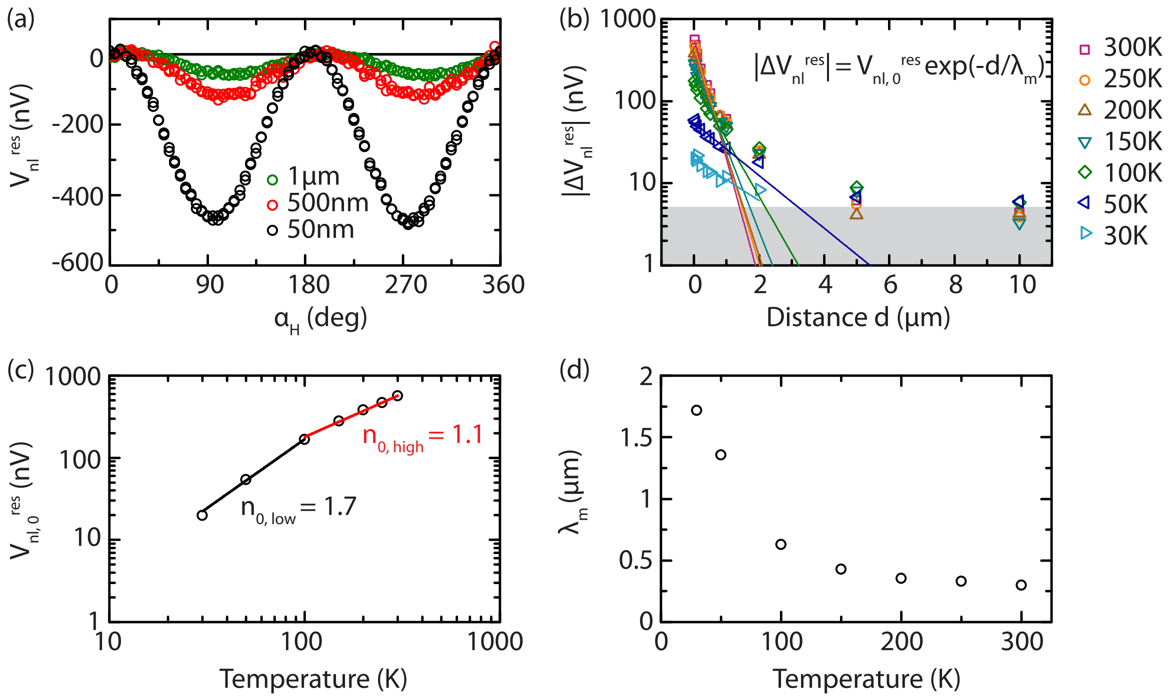

Figure 6.5: (a) $V_{\mathrm{nl}}^{\mathrm{res}}$ as a function of the ip magnetic field orientation α_{H} for $d = 50\,\mathrm{nm}$, $500\,\mathrm{nm}$ and $1\,\mu\mathrm{m}$ at $T = 300\,\mathrm{K}$ and $\mu_0 H = 1\,\mathrm{T}$. (b) $V_{\mathrm{nl}}^{\mathrm{res}}$ extracted from the ADMR measurements as a function of the strip separation d for different temperatures. The solid lines are fits to the data using Eq. (6.2). (c) $V_{\mathrm{nl,0}}^{\mathrm{res}}$ - the non-local voltage in the local limit ($d = 0$) - obtained from the fits in panel (b) as a function of temperature. The solid lines represent power law fits of the form $A \cdot T^{\mathrm{n}}$. (d) Magnon diffusion length λ_m extracted from the exponential decay in panel (b) as a function of temperature.

short distance limit $d \ll \lambda_m$ Eq. (5.8) can be approximated by a $1/d$ dependence which reproduces the experimental data in Ref. [3] well, but yields no satisfying fit for the data displayed in Fig. 6.5.

For now, we therefore focus on the short distance regime up to $5\,\mu\mathrm{m}$ using Eq. (6.2) to fit the data as shown in Fig. 6.5 (b). The fit parameters $V_{\mathrm{nl,0}}^{\mathrm{res}}$ and λ_{m} are plotted in Fig. 6.5 (c) and (d), respectively. In analogy to the analysis of the data in Fig. 6.3 (c), $V_{\mathrm{nl,0}}^{\mathrm{res}}$ is fitted with two power law functions $A \cdot T^{n_{0,\mathrm{low}}}$ and $B \cdot T^{n_{0,\mathrm{high}}}$ for $30\,\mathrm{K} \leq T \leq 100\,\mathrm{K}$ and $100\,\mathrm{K} \leq T \leq 300\,\mathrm{K}$, respectively. We find $n_{0,\mathrm{low}} = 1.7$ and $n_{0,\mathrm{high}} = 1.1$, which is consistent with the values obtained in Fig. 6.3 (c) for the shortest distance $d = 20\,\mathrm{nm}$. The temperature dependence of the injection efficiency in the local limit, especially at high temperatures, therefore slightly deviates from the theoretical prediction by Zhang and Zhang [114] who calculated $n = 1.5$. However, the temperature dependence of the magnon spectrum, in particular the dispersion relation was not taken into account in

---

within the diffusion path of the magnons does not visibly affect the non-local signal [141], suggesting that a Pt strip is in general not a perfect spin sink and making the use of Eq. (5.8) questionable.

those calculations. The authors assume a quadratic dispersion relation, which is a good approximation for small $\mathbf{k}$ vectors, but is no longer true for larger $\mathbf{k}$. The calculations of the YIG spectrum [64] displayed in Fig. 5.2 show that the magnon dispersion changes from quadratic to linear and becomes flat towards the edge of the Brillouin zone. This change in the slope of the dispersion relation occurs around energies corresponding to 100 K [143], i.e. the temperature where the power law dependence in Fig. 6.5 (c) changes slope. We therefore qualitatively discuss the influence of the dispersion relation on the density of states of the magnon system and the total number of magnon excitations.

For a general quadratic dispersion relation

$$\omega(\mathbf{k}) = \frac{J_A S a^2}{\hbar^2}\mathbf{k}^2 \tag{6.3}$$

where J_A is the exchange constant, S the spin-wave stiffness and a the lattice constant, the density of states can be calculated as [54]

$$D(\omega) = \frac{V}{4\pi^2}\left(\frac{\hbar^2}{J_A S a^2}\right)^{3/2}\sqrt{\omega}. \tag{6.4}$$

The total number of magnon excitations is

$$\begin{aligned}\sum_{\mathbf{k}} n_{\mathbf{k}} &= \frac{V}{4\pi^2}\left(\frac{\hbar}{J_A S a^2}\right)^{3/2}\int_0^\infty d\omega \frac{\sqrt{\omega}}{e^{\hbar\omega/k_\mathrm{B}T}-1} \\ &= \frac{V}{4\pi^2}\left(\frac{k_\mathrm{B}T}{J_A S a^2}\right)^{3/2}\int_0^\infty dx \frac{\sqrt{x}}{e^x-1} \approx 2.31\frac{V}{4\pi^2}\left(\frac{k_\mathrm{B}T}{J_A S a^2}\right)^{3/2}. \qquad (6.5)\end{aligned}$$

In the case of a linear dispersion

$$\omega(\mathbf{k}) = \frac{J_A S a^2}{\hbar^2}\mathbf{k} \tag{6.6}$$

the density of states becomes

$$D(\omega) = \frac{V}{4\pi^2}\left(\frac{\hbar^2}{J_A S a^2}\right)^{3}\omega^2 \tag{6.7}$$

and the total number of magnon excitations

$$\begin{aligned}\sum_{\mathbf{k}} n_{\mathbf{k}} &= \frac{V}{4\pi^2}\left(\frac{\hbar}{J_A S a^2}\right)^{3}\int_0^\infty d\omega \frac{\omega^2}{e^{\hbar\omega/k_\mathrm{B}T}-1} \\ &= \frac{V}{4\pi^2}\left(\frac{k_\mathrm{B}T}{J_A S a^2}\right)^{3}\int_0^\infty dx \frac{x^2}{e^x-1} \approx 2.4\frac{V}{4\pi^2}\left(\frac{k_\mathrm{B}T}{J_A S a^2}\right)^{3} \qquad (6.8)\end{aligned}$$

increases more strongly with a T^3 dependence instead of the $T^{3/2}$ expected in the quadratic case. This means that the number of available magnon states for the injection increases when the dispersion becomes flatter, which should lead to a stronger increase of the MMR with temperature starting around $T = 100\,\mathrm{K}$. This is however not consistent with the experimental observations, where the slope of the T^n dependence decreases in the temperature regime where the dispersion becomes linear.

The change in slope of the temperature dependence in Fig. 6.5 (c) can therefore not be rationalized easily, even including a deviation from the quadratic dispersion relation in the theory by Zhang and Zhang [114]. This model however applies to the 1D geometry of a Pt/YIG/Pt trilayer instead of the bilayer with two Pt strips that was used in our experiments. Furthermore, it is unclear how (and if) the detection efficiency affects the MMR, since up to here only the injection was discussed. The authors of Ref. [114] obtain a different temperature dependence of the injection ($n = 3/2$) and detection ($n = 1$) efficiency. Since in our experiments only the combination of injection and detection is measured, the two contributions cannot be disentangled in a straightforward way and further investigations are required.

We now turn to the temperature dependence of the transport properties, i.e. the magnon diffusion length λ_m plotted in Fig. 6.5 (d). λ_m extracted from fits to the short distance limit decreases with increasing temperature and reaches about 300 nm at room temperature. This is very different from observations by Cornelissen *et al.* who extracted a constant magnon diffusion length of the order of a few µm over the whole temperature range from 25 K to 300 K [138]. As discussed above, these deviations can be attributed to different distance regimes and the applied fit function.

In order to understand the temperature dependence of the magnon diffusion length, it is important to keep in mind that magnons with different **k** vectors contribute to the transport. In particular, the group velocity $v_{\mathbf{k}} = \frac{1}{\hbar}\frac{\partial \epsilon}{\partial \mathbf{k}}$ as well as the scattering times $\tau_{\mathbf{k}}$ strongly depend on the **k** vector. The diffusion length extracted from the exponential decay fits in Fig. 6.5 (d) is therefore an average over the contributions from all non-equilibrium magnons

$$\lambda_m = \frac{1}{N_{\mathrm{mag}}} \int_0^\infty d\mathbf{k} \lambda_{\mathbf{k}} Z(\mathbf{k}) f_{\mathrm{BE}}(\mathbf{k}, T) \tag{6.9}$$

where $N_{\mathrm{mag}} = \int_0^\infty d\mathbf{k} Z(\mathbf{k}) f_{\mathrm{BE}}(\mathbf{k}, T)$ is the total number of magnons, $Z(\mathbf{k})$ the density of states in **k** space, $\lambda_{\mathbf{k}} = v_{\mathbf{k}}\tau_{\mathbf{k}}$ the diffusion length for a specific **k** vector and $f_{\mathrm{BE}}(\mathbf{k}, T)$ the Bose-Einstein-distribution function.

The magnon group velocity can be obtained from the dispersion of the YIG fundamental mode in Fig. 5.2: $v_{\mathbf{k}}$ is always positive but decreases for large **k** when the mode flattens. High **k** magnons are therefore expected to contribute less to the MMR, in particular at large distances. Furthermore, the scattering times $\tau \propto \frac{1}{\mathbf{k}^\alpha}$, where α depends on the type of relaxation process, decrease for large **k** vectors [143, 144]. This effect, in combination with the **k** dependence of the group velocity suggests that the magnon transport is

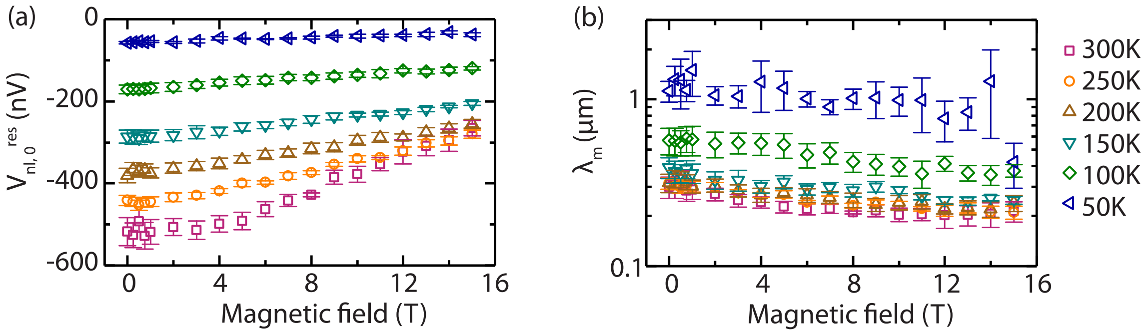

Figure 6.6: Non-local voltage in the local limit $V_{\mathrm{nl},0}^{\mathrm{res}}$ (a) and magnon diffusion length λ_m (b) obtained from fits to the $V_{\mathrm{nl}}^{\mathrm{res}}$ data measured as a function of injector-detector distance using Eq. (6.2). The values are extracted as a function of external magnetic field for temperatures between 50 K and 300 K.

dominated by the low **k** magnons which have the largest diffusion length. With this we can qualitatively rationalize the temperature dependence of the overall diffusion length λ_m: at high temperatures more magnons with high energies and high **k** but small $\lambda_{\mathbf{k}}$ are thermally populated. This reduces the average diffusion length λ_m calculated from Eq. (6.9) with increasing temperature.

We now turn to the magnetic field dependence of the magnon diffusion length. As mentioned in Sect. 6.3.3, the thermal magnon population (and therefore the non-equilibrium magnons which contribute to the MMR) is affected by a magnetic field, since low frequency magnons are suppressed. At the same time, magnons with large **k** right around $k_{\mathrm{B}}T$ are suppressed when the dispersion relation is shifted to higher energies. Following a similar line of argument as for the temperature dependence of λ_m discussed above, we therefore expect a change of the diffusion length since the frequencies and **k**-vectors of the contributing magnons are modified by the applied magnetic field [141]. However, at high temperatures corresponding to energies $k_{\mathrm{B}}T$ much larger than the Zeeman energy, the magnon population is large and this effect should be rather small. On the other hand, theoretical calculations predict that the magnon-phonon scattering of subthermal (low **k**) magnons, which contribute considerably to the long range magnon transport, increases with magnetic field [145]. This leads to a shorter diffusion length for these magnons and should affect the overall diffusion length observed in experiments.

In analogy to the analysis of the temperature dependence of the diffusion length, we therefore extract λ_m and the non-local voltage in the local limit $V_{\mathrm{nl},0}^{\mathrm{res}}$ as a function of magnetic field for different temperatures. To this end, we fit the MMR amplitude $V_{\mathrm{nl}}^{\mathrm{res}}$ obtained from the magnetic field sweeps (exemplarily shown in Fig. 6.4 (b) for $d = 100\,\mathrm{nm}$) as a function of the injector-detector distance using the exponential fit given by Eq. (6.2). The extracted values for $V_{\mathrm{nl},0}^{\mathrm{res}}$ and λ_m are plotted in Fig. 6.6 (a) and (b), respectively, where the error bars represent the standard deviation. The amplitude of the non-local voltage $V_{\mathrm{nl},0}^{\mathrm{res}}$ displayed in Fig. 6.6 (a) is suppressed by magnetic field, consistent with the results discussed in Sect. 6.3.3.

For the diffusion length λ_m displayed in Fig. 6.6 (b), a slight decrease with increasing magnetic field is observed for all temperatures. This is qualitatively consistent with previous measurements conducted in YIG/Pt by Cornelissen *et al.* at room temperature, who observe a decrease of the magnon diffusion length λ_m from approximately 9.6 µm for $\mu_0 H = 10\,\mathrm{mT}$ to 4.2 µm for 3.5 T [127]. However, the values we extracted for λ_m are prone to large errors and scatter, in particular at temperatures below 100 K (mostly related to the difficulty to fit the experimental data as discussed above). Based on the current data, it is therefore not possible to quantitatively analyze the origin of the small change in diffusion length with magnetic field.

In summary, we have studied the magnon mediated magnetoresistance effect (MMR) originating from the diffusion of electrically injected non-equilibrium magnons through the ferrimagnetic insulator YIG. The MMR was investigated systematically as a function of temperature, magnetic field and injector-detector separation. We distinguish between distance independent contributions to the MMR, i.e. magnon injection and detection efficiency, and the diffusive properties in the YIG film. In experiments, we observe a suppression of the injection efficiency at low temperatures and high magnetic fields, indicating that the magnon injection depends strongly on the thermal magnon population. This is consistent with the theoretical MMR model proposed by Zhang and Zhang [114].

From the temperature and magnetic field dependence of the MMR amplitude we also conclude that non-equilibrium magnons with different energies and **k**-vectors contribute to transport. In particular, the magnon diffusion length extracted from experiments corresponds to the average diffusion length obtained for all non-equilibrium magnons. Consequently, a decrease of the diffusion length is observed at high temperatures, where more magnons with large **k** and comparatively small diffusion length contribute, reducing the average diffusion length. In a similar way, the diffusion length can be affected by the change in thermal magnon population when a magnetic field is applied. Additionally, the magnetic field is expected to influence the lifetime of specific magnons [145]. In order to understand the diffusive properties as a function of temperature and magnetic field, changes in the type of non-equilibrium magnons as well as their specific transport properties need to be considered.

Chapter 7

Magnon based logic

Based on the results discussed in Sect. 6.3, we extend the two strip YIG/Pt structure displayed in Fig. 6.1 to a four strip device, enabling the implementation of a magnon majority gate performing several logic operations in one and the same device. The study of this proof-of-principle device has been published in Appl. Phys. Lett. **109**, 022405 (2016) [123] and the corresponding text and figures are reused and adapted in the following. The measurements presented in this chapter were conducted together with T. Wimmer during his master's thesis at WMI [141], which I supervised. Further characterization measurements have been conducted in a three strip device, confirming that the non-local signal is not affected by the presence of an additional Pt strip placed in-between the injector and detector strips. Details on these measurements can be found in Ref. [141].

In recent years, different propositions for the implementation of magnonic logic elements and their integration into the present electronic circuits have been made [110, 146–149], using e.g. the phase or the amplitude of magnon modes to encode a logical bit. One important step towards magnonic logic is the implementation of a majority gate [148], with three inputs and one output. The output of the majority gate assumes the same logical state ("0" or "1") as the majority of the input signals. Additionally, one of the input channels can be used as a control channel to switch between "OR" and "AND" operations (see Tab. 7.1), allowing for multiple types of logic operations in a single structure. Recently, a design for an all magnonic majority gate based on single magnon mode operations has been proposed theoretically [150, 151] and implemented experimentally [152], using the phase of coherent spin waves (magnons) to encode the logical "1" and "0". However, in order to realize this magnonic majority gate, phase sensitive generation and detection of the spin waves is required. Furthermore, the selected magnon modes and therefore the functionality of the logic gate depend crucially on the waveguide geometry, making down-scaling challenging.

In this chapter, we present a proof-of-principle device implementing a multi-terminal magnonic majority gate based on the incoherent superposition of magnons, requiring neither microwave excitation nor phase sensitive detection of the spin waves. For the implementation, we exploit the magnon mediated magnetoresistance (MMR) previously studied in Chap. 6 in a heterostructure consisting of two parallel Pt strips deposited on

Control C	Injector 1	Injector 3	Detector 2
1	1	1	1
1	0	1	1
1	1	0	1
1	0	0	0
0	1	1	1
0	0	1	0
0	1	0	0
0	0	0	0

I_c	I_1	I_3	V_2
+	+	+	−
+	−	+	−
+	+	−	−
+	−	−	+
−	+	+	−
−	−	+	+
−	+	−	+
−	−	−	+

Table 7.1: Truth table of a majority gate [150]. The bottom half of the table shows the sign of the bias currents for the input channels as well as the sign of the resulting non-local voltage V_2 in a MMR based majority gate. Positive and negative bias currents in the injectors are defined as logical "1" and "0" respectively. Since a positive bias current in the injector yields a negative non-local voltage V_2 (see Ref. [4]), we define $V_2 < 0$ as "1" and $V_2 > 0$ as "0". Table taken from Ref. [123].

top of a YIG film. As discussed in Sect. 5.1, driving a charge current through one of the Pt strips induces an electron spin polarization at the Pt/YIG interface via the SHE. When the polarization of the electron spin magnetic moment accumulation in the Pt is antiparallel (parallel) to the YIG magnetization, magnons are generated (annihilated) in the YIG, creating a magnon accumulation (magnon deficiency) beneath the injector strip via scattering processes at the interface [113, 114] (see Fig. 5.1). This leads to magnon diffusion currents polarized antiparallelly to the magnetization, which flow away from (towards) the injector strip. In more general terms, the magnetic moment accumulation determined by the SHE in the Pt is carried by magnons through the YIG to the detector. By inverting the charge current direction, the magnetic moment direction is also inverted due to the geometry of the SHE (Eq. (5.3)).

Here, we extend the basic two Pt strip structure to a device with three magnon injectors and one detector as shown schematically in Fig. 7.1 (a). The YIG/Pt four-strip device is fabricated as described in Sect. 6.1, using a 2 µm thick LPE-YIG film with 10 nm of Pt deposited on top (see sample list in Appendix A). For the magnon injection and detection, we pattern four Pt strips with a width of $w = 500\,\mathrm{nm}$ and a edge-to-edge separation of

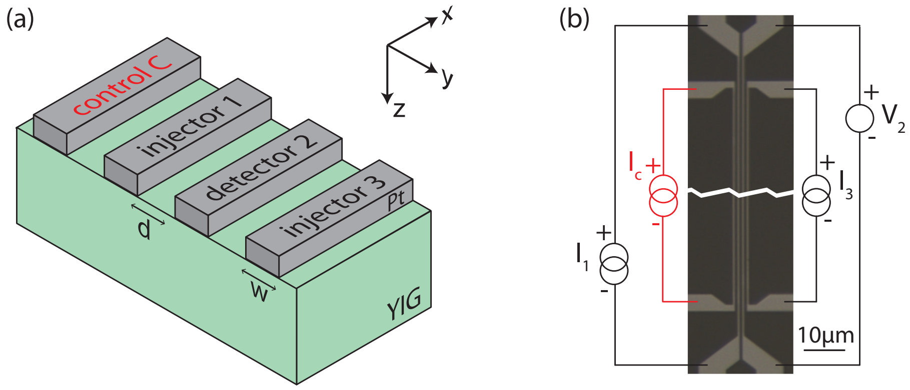

Figure 7.1: (a) Schematic of the YIG/Pt nanostructure consisting of four Pt strips with width w and edge-to-edge separation d. We label the strips as C (control), 1 (injector), 2 (detector) and 3 (injector) from left to right. (b) Optical micrograph of the YIG/Pt device: the bright strips are the Pt strips, the dark parts the YIG. Current sources are attached to the injector strips 1 and 3 as well as to the control strip. The ensuing non-local voltage drop V_2 is recorded at strip 2. Figure adapted from Ref. [123].

$d = 500\,\mathrm{nm}$. An optical micrograph of the final device is shown in Fig. 7.1 (b). The two center strips (strip 1 and 2 in Fig. 7.1 (b)) have a length of $l = 162\,\mu\mathrm{m}$ and the outer strips (strip C on the left and strip 3 on the right) are $148\,\mu\mathrm{m}$ long. The wiring scheme for the measurements is also sketched in Fig. 7.1 (b). All experiments are performed at $T = 275\,\mathrm{K}$ with an external magnetic field $\mu_0 H = 1\,\mathrm{T}$ applied in the thin film plane perpendicular to the strips. Note that the external field is applied in order to saturate the ferrimagnet. Since the coercive field of YIG is usually of the order of a few Oe [96], much smaller magnetic fields could be used for these experiments if necessary.

In the first part of the experiments we demonstrate the incoherent superposition of magnons in the simple three-strip device with strips 1, 2, and 3 (black wiring in Fig. 7.1 (b)): for the generation of the magnon spin accumulation beneath strip 1 and 3 we drive the charge currents I_1 and I_3 through the respective strips. As the number of magnons generated beneath one Pt strip is proportional to the electron spin accumulation at the interface, which in turn scales with the charge current I flowing in the strip times the area A of the YIG/Pt interface [114], the different lengths of injector strips 1 and 3 need to be taken into account for quantitative analysis. In order to detect the spin accumulation beneath strip 2, we therefore measure the open-circuit voltage $V_2(I_1 A_1, I_3 A_3)$. To increase the measurement precision and exclude additional thermal contributions originating from Joule heating, we use the current switching method described in Sect. 3.3.2.

Firstly, we focus on measuring the voltage response $V_2(I_1 A_1, I_3 A_3)$ while applying a current bias only to strip 1 ($I_1 \neq 0, I_3 = 0$) or to strip 3 ($I_1 = 0, I_3 \neq 0$), in order to compare the injection efficiency of both strips. The results are shown in Fig. 7.2 (a). As

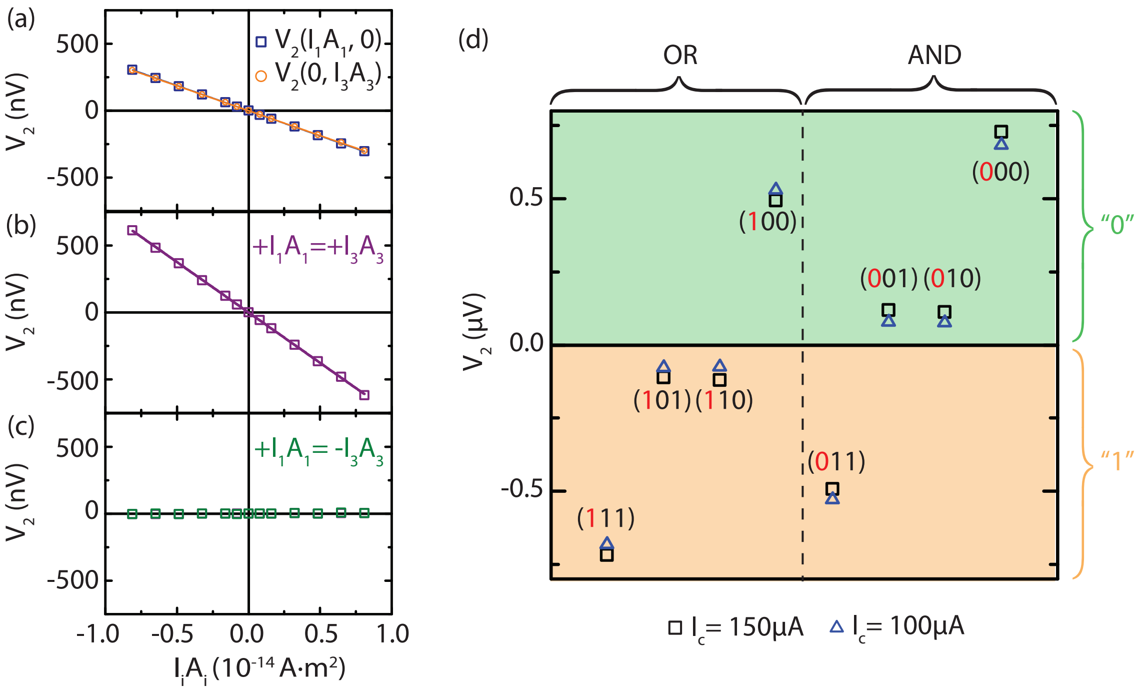

Figure 7.2: (a) The non-local voltage $V_2(I_1A_1,0)$ while current-biasing only along strip 1, and $V_2(0,I_3A_3)$ while driving strip 3 are measured as a function of the applied current and are represented by blue open squares and orange open circles, respectively. The blue and orange lines represent linear fits to the data. Note that we quote $I \cdot A$ as the relevant bias, since the spin Hall current across the entire interface area A contributes to the MMR. (b) $V_2(I_1A_1,I_3A_3)$ measured while current-biasing strips 1 and 3 with the same current magnitude and polarity is represented by the purple open squares. The purple line is a linear fit. (c) The green open squares represent V_2 measured when biasing strips 1 and 3 with currents of opposite polarity. In this configuration, the non-local voltage goes to 0 within experimental error. (d) Test measurement of the four-strip majority gate. The detected non-local voltage V_2 is depicted for different input signals (I_c I_1 I_3), where the logical bit of the control channel is marked in red. The magnitudes of the injector currents I_1 and I_3 are kept constant, and V_2 is measured for control current magnitudes $I_c = 150$ and $100\,\mu$A (black and blue symbols). The experimental data faithfully reproduce all the properties of a majority gate. Figure adapted from Ref. [123].

expected, V_2 scales linearly with I_1 and I_3, respectively, since the non-local voltage is proportional to the number of non-equilibrium magnons accumulating beneath strip 2 [113, 114]. Since at zero bias current no magnons are injected, $V_2(0,0) = 0$. For positive driving currents along the +**x**-direction in Fig. 7.1 (a), the accumulation of electron spin magnetic moment in the Pt is polarized along the −**y**-direction (see Fig. 5.1) and thus the diffusing magnons carry magnetic moment pointing along −**y** towards the detector (strip 2). There, the magnetic moment is transferred to the Pt and a negative voltage V_2 is induced via the inverse spin Hall effect, consistent with previous measurements using the same configuration [4] (see Chap. 6). By inverting the driving charge current in the injector, the net magnetic moment carried by the diffusing magnons is inverted and consequently a positive non-local voltage is recorded. In general, depending on the charge current direction, either a magnon accumulation or depletion is generated beneath the injector. The ensuing magnon diffusion currents flow in opposite directions, such that effectively the opposite magnetic moment is transferred to the detector when the charge current direction is inverted. Taking these properties together, our detection method is therefore sensitive to the number of non-equilibrium magnons reaching the detector as well as to the direction of the carried magnetic moment. Note also that the magnons diffuse isotropically, i.e. to the left as well as to the right in Fig. 7.1 (a). Therefore, it does not matter for the sign of the detected voltage whether the injector strip is on the right or left side of the detector strip. This is to be expected, as the sign of the detected voltage is determined by the orientation of the transferred (net) magnetic moment across the YIG/Pt interface, and not by the actual diffusion direction.

Within the experimental uncertainty of 5 nV of our setup (limited by the nanovoltmeter noise and/or thermal stability of the setup), $V_2(I_1A_1, 0) = V_2(0, I_3A_3)$ for $I_1A_1 = I_3A_3$, showing that the magnon generation efficiency of both strips is identical. To quantify this in more detail, we fit $V_2(I_1A_1, 0) = \alpha_1 \cdot I_1A_1$ and $V_2(0, I_3A_3) = \alpha_3 \cdot I_3A_3$ to the data. We find $\alpha_1 = -3.77 \times 10^7 \mathrm{V\,A^{-1}\,m^{-2}}$ and $\alpha_3 = -3.72 \times 10^7 \mathrm{V\,A^{-1}\,m^{-2}}$, showing that $\alpha_{1,3}$ are identical within less that 2%.

Next, we investigate the non-local voltage $V_2(I_1A_1, I_3A_3)$ while simultaneously biasing strips 1 and 3. For identical current polarity ($I_1A_1 = I_3A_3$) equal numbers of magnons carrying identical magnetic moment are generated beneath both strips. The results are shown in Fig. 7.2 (b) as purple open squares. The purple line represents a linear fit to the data with a slope of $\alpha_{1+3} = -7.53 \times 10^7 \mathrm{V\,A^{-1}\,m^{-2}}$. Assuming an incoherent superposition of the magnons created beneath strip 1 and strip 3 we expect $\alpha_{1+3} = \alpha_1 + \alpha_3$, which is in good agreement with the experimental data. This result is further corroborated by the V_2 values obtained for opposite current directions in strip 1 and strip 3, i.e. $I_1A_1 = -I_3A_3$, shown in Fig. 7.2 (c). A linear fit to the data reveals a slope of $0.05 \times 10^7 \mathrm{V\,A^{-1}\,m^{-2}}$ and therefore $\alpha_{3-1} = \alpha_3 - \alpha_1$. Additional measurements were conducted using different driving current amplitudes and polarities for strips 1 and 3 (not shown here). From these data, we consistently find $V_2(I_1A_1, I_3A_3) = \alpha_1 \cdot I_1A_1 + \alpha_3 \cdot I_3A_3$.

Taken together, we observe incoherent superposition of non-equilibrium magnons, injected independently by the different injector Pt strips.

We now show that a magnon-based majority gate can be implemented in the four-strip nanostructure, with three input and one output channel as shown in Fig. 7.1 (a). A majority gate returns true if more than half the inputs are true, otherwise it returns false, as shown in Tab. 7.1. The third input can be used as a so-called control channel (wire "C" in Fig. 7.1 (a)), which allows for switching between "AND" and "OR" operations. We define positive and negative currents in the injectors as the logical "1" and "0" respectively. Since for positive bias currents a negative non-local voltage is detected, for the output signal $V_2 < 0$ is defined as “1” and $V_2 > 0$ as “0”. The bias currents for input 1 and 3 are chosen such that $|I_1 A_1| = |I_3 A_3| = 0.81 \times 10^{-14}\,\mathrm{A\,m}^2$ and $V_2(I_1 A_1, I_3 A_3)$ is subsequently measured for fixed values of $I_c = \pm 150\,\mu\mathrm{A}$. The resulting voltage is shown as black open squares in Fig. 7.2 (d) for different input combinations $(I_c\ I_1\ I_3)$. For convenience, we do not quote the real charge current values, but rather the corresponding bit values (“0” or “1”), with the control bit marked in red. For example, if all three injectors are biased with a positive current, corresponding to the input (111), a negative voltage is detected at the output, corresponding to a logical “1”. The experimental data successfully reproduces the truth table (Tab. 7.1): by changing the control bit from “1” to “0”, one can switch from an “OR” to an “AND” operation (left and right side of the graph respectively). The majority function is furthermore visible in the sign of the output signal (green and orange area in Fig. 7.2 (d)), as the output mirrors the majority of the input signals.

Since the control channel is further away from the detector, due to the exponential decay of the magnon accumulation with distance (see Sect. 6.3.4) [3, 4], the number of magnons from the control channel reaching the detector is smaller by about a factor 5 compared to the other injectors. However, the actual amplitude of the control signal I_c is not crucial for the functionality of the majority gate and can be further reduced without affecting the majority function as shown in Fig. 7.2 (d) for $I_c = 100\,\mu\mathrm{A}$ (blue triangles). We can therefore choose any amplitude for I_c as long as the induced ISHE voltage is detectable. This allows for a high flexibility in the device operation. In this context, another advantage of this magnon based logic gate is the possibility to reprogram the device by simply interchanging the injector, detector and control channels. To guarantee the functionality of the majority gate, the input bias currents only need to be adapted to the geometry of the device, in particular to the distance between the injector and detector strips.

Note that logic operations are already feasible in a three strip device with two injectors and one detector. In this case the threshold chosen for the detector determines whether the gate performs “AND” or “OR” operations. However, the four strip device allows for the same functions, without requiring a redefinition of the output threshold.

Apart from flexibility, an important aspect for the application of spintronic logic is the clocking frequency. The relevant time scale for a MMR based majority gate is dominated by two processes: the generation of a spin/magnon accumulation beneath the injector and the diffusion of the incoherent magnons. It has been shown experimentally that the spin Hall effect induced spin accumulation persists up to frequencies of at least a few GHz [153], corresponding to spin accumulation build up times well below a nanosecond. Concerning the propagation of the spin waves, the average group velocity of magnons in YIG is of the order of $1\,\mu\mathrm{m\,ns}^{-1}$ [110]. In the device shown in Fig. 7.1, the magnons therefore have a lower limit of about 2 ns for their travel time from the control to the detector strip, resulting in a maximum switching frequency $f = 1/T$ of about 500 MHz. This can be further improved by changing the design of the four-strip device. For example reducing both the width of the Pt strips and their edge-to-edge separation to 50 nm already leads to a factor 10 increase of the switching frequency, to several GHz. This value is comparable to clocking frequencies in current devices and to those expected in other spintronic based logic gates [154]. Down-scaling not only leads to faster switching, but also decreases the device footprint, and increases the energy efficiency of the logic gate: for smaller distances between strips, the output signal increases exponentially [3], such that the required bias currents are lower. Since the logical bit is encoded in the magnetic moment carried by the magnons and not in the frequency, phase or amplitude of the spin waves, down-scaling does not perturb the functionality of the logic gate. Note that in the short distance limit, assuming ballistic magnon transport and neglecting interface losses, the non-local voltage is limited by the bias voltage times Θ_{SH}^2, where Θ_{SH} is the spin Hall angle in the normal metal (see Sect. 2.1). This corresponds to the conversion efficiency from charge to spin and back to a charge current in the Pt layer. Using a material with a larger spin Hall angle than Pt (e.g. $\mathrm{Bi_2Se_3}$ [155]) will therefore significantly increase the detected non-local voltage, making this device more suitable for applications.

In summary, we have measured the non-local voltage (the magnon mediated magnetoresistance) in a YIG/Pt device with multiple magnon injectors and observe incoherent superposition of the non-equilibrium magnon populations. The measurements show that the detected non-local voltage is sensitive to the number of magnons reaching the detector and to the direction of the magnetic moment transferred across the detector interface. Based on the incoherent superposition of spin waves, we implemented a fully functional four-strip majority gate. The logical bit in this device is encoded in the magnetic moment carried by the magnons that are injected using a dc charge current. The output can be read out as a dc non-local voltage, enabling a simple integration into an electronic circuit. Clocking frequencies of the order of several GHz and straightforward down-scaling make the device promising for applications.

Chapter 8

Non-local spin Seebeck effect in YIG/Pt

In Chap. 6 and 7 we focused on the transport of electrically injected magnons through the ferrimagnetic insulator YIG. Using the same measurement geometry as in Chap. 6, we now investigate the transport of thermally excited magnons in a non-local YIG/Pt structure, i.e. the non-local spin Seebeck effect (SSE). First, we study the non-local SSE as a function of temperature and injector-detector distance, in order to gain a better understanding of the relevant length scales and physical origin of the non-local SSE. The experimental results and discussion have been published in AIP Adv. **7**, 085102 (2017) [116] and the corresponding text and figures are extensively reused in Sect. 8.1. We then turn to our measurements of the non-local SSE response as a function of the applied magnetic field magnitude in Sect. 8.2, giving first insights into the type of magnons that contribute dominantly to the non-local SSE.

8.1 Distance and temperature dependence

We investigate the non-local spin Seebeck effect in two LPE-YIG films with thickness $t_{\mathrm{YIG}} = 2\,\mu\mathrm{m}$ and $5\,\mu\mathrm{m}$ grown onto (111) oriented $\mathrm{Gd_3Ga_5O_{12}}$ (GGG). Both YIG samples are covered with $10\,\mathrm{nm}$ of Pt. A series of nanostructures consisting of 2 parallel Pt strips with length $l = 100\,\mu\mathrm{m}$, width $w = 500\,\mathrm{nm}$ and an edge-to-edge separation of $20\,\mathrm{nm} \leq d \leq 10\,\mu\mathrm{m}$ is patterned into the Pt using electron beam lithography followed by Ar ion etching (see Sect. 6.1 for details on the sample fabrication). Note that the $2\,\mu\mathrm{m}$ thick YIG film discussed in this chapter is the same sample as the one used in Sect. 6.3 (see sample list in Appendix A). The MMR and non-local SSE results from this sample are obtained from the same set of data: the resistive (Sect. 6.3) and thermal contributions (this chapter) are disentangled using the current switching method described in Sect. 3.3.2. The experimental data was obtained together with T. Wimmer, who I supervised during his master's thesis at WMI [141].

The samples are mounted in the variable temperature insert of a superconducting magnet cryostat ($5\,\mathrm{K} \leq T \leq 300\,\mathrm{K}$) and an external magnetic field $\mu_0 H = 1\,\mathrm{T}$ is rotated in the thin film plane. We measure the local longitudinal spin Seebeck effect in one single strip (injector strip in Fig. 8.1 (a)), using the current heating method described in Ref. [95]: a charge current of 100 µA is applied to the Pt strip along the $\mathbf{x}$ direction using a Keithley 2400 sourcemeter, inducing Joule heating in the normal metal. The ensuing temperature gradient across the Pt/YIG interface gives rise to the spin Seebeck effect and generates a magnetic moment current $\mathbf{J}_t$ flowing across the interface, with polarization $\mathbf{m}$ aligned antiparallel to the magnetization $\mathbf{M}$ in YIG, as shown in Fig. 8.1 (a) (see also Sect. 5.4). In the Pt, the corresponding spin current is accompanied by a charge current $\mathbf{J}_{\mathrm{ISHE}}$ flowing along the $\mathbf{x}$-direction in the Pt. The voltage drop V_{loc}, which includes the local SSE and the resistive response of the injector strip is recorded using a Keithley 2182 nanovoltmeter. Since the spin Seebeck effect is of thermal origin, the SSE voltage is proportional to the Joule heating power in the Pt and therefore independent of the heating current direction. Using the current switching scheme of Ref. [95] (see Sect. 3.3.2), we extract $V_{\mathrm{loc}}^{\mathrm{therm}} = (V_{\mathrm{loc}}(+J_c) + V_{\mathrm{loc}}(-J_c))/2$ (which corresponds to quadratic and other even terms in J_c), and thereby eliminate additional resistive effects such as the spin Hall magnetoresistance (as well as other terms that are uneven in J_c).

Figure 8.1 (b) shows $V_{\mathrm{loc}}^{\mathrm{therm}}$ measured as a function of the magnetic field orientation α_{H} with respect to the $\mathbf{x}$-axis at $T = 50\,\mathrm{K}$ for a two-strip device on the YIG/Pt bilayer with $t_{\mathrm{YIG}} = 2\,\mu\mathrm{m}$. We observe the characteristic SSE dependence $V_{\mathrm{loc}}^{\mathrm{therm}} \propto \sin(\alpha_{\mathrm{H}})$ yielding a positive amplitude $A_{\mathrm{SSE,loc}} = V_{\mathrm{loc}}^{\mathrm{therm}}(90°) - V_{\mathrm{loc}}^{\mathrm{therm}}(270°)$ of the local SSE, as expected in YIG/Pt heterostructures for this measurement configuration [156].

Using an additional nanovoltmeter, we simultaneously measure the voltage drop V_{nl} arising along the unbiased and electrically isolated second Pt strip. In analogy to the local thermal signal, the non-local thermal voltage is extracted as $V_{\mathrm{nl}}^{\mathrm{therm}} = (V_{\mathrm{nl}}(+J_c) + V_{\mathrm{nl}}(-J_c))/2$ in order to distinguish it from resistive non-local effects such as the magnon mediated magnetoresistance (see Chap. 6) [4]. $V_{\mathrm{nl}}^{\mathrm{therm}}$ as a function of the external magnetic field orientation at 50 K is depicted in Fig. 8.1 (c) and (d) for strip separations of $d = 200\,\mathrm{nm}$ and $2\,\mu\mathrm{m}$ on the YIG/Pt bilayer with $t_{\mathrm{YIG}} = 2\,\mu\mathrm{m}$. In both devices, we observe a $\sin(\alpha_{\mathrm{H}})$ dependence, with an amplitude $A_{\mathrm{SSE,nl}}$ about one order of magnitude smaller than for the local SSE. While the signal amplitude $A_{\mathrm{SSE,nl}}$ is positive for the $d = 200\,\mathrm{nm}$ device, a negative $A_{\mathrm{SSE,nl}}$ is observed in the device with a larger injector-detector separation of $d = 2\,\mu\mathrm{m}$. In order to confirm this sign change, we extract the amplitude of the non-local SSE measured at 50 K in different two-strip devices on the 2 µm thick YIG sample, with strip separations ranging from 20 nm to 10 µm. The resulting data is shown in Fig. 8.1 (e) as green symbols. Indeed, a sign change is observed at a strip separation $d_0 \approx 560\,\mathrm{nm}$. Repeating these measurements as a function of temperature in the range between 10 K and 300 K yields the data compiled in Fig. 8.1 (e). For all temperatures, a sign change in $A_{\mathrm{SSE,nl}}$ is observed as a function of the strip separation. Invariably, for small gaps the local and non-local SSE are both positive, but for large gaps the non-local SSE becomes negative. The experimental data in Fig. 8.1 (e) show that the

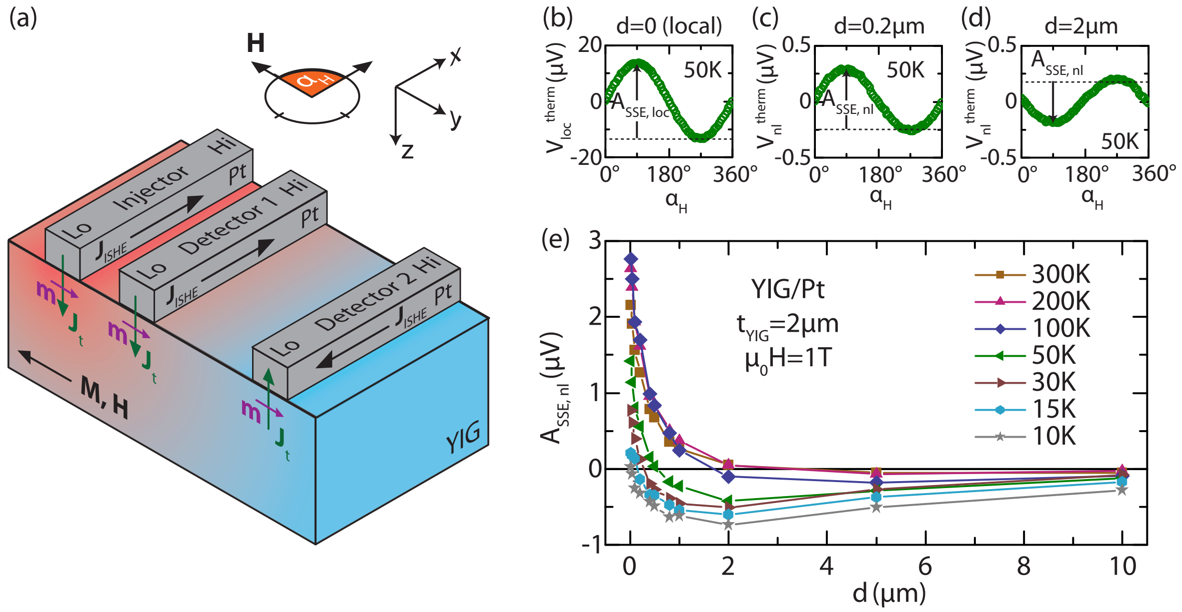

Figure 8.1: (a) Sketch of the YIG/Pt heterostructure: a dc charge current $\mathbf{J}_c$ (not shown here) is applied to the injector strip (left) and the spin Seebeck signal $V_{\mathrm{loc}}^{\mathrm{therm}}$ is detected locally via the ISHE. The corresponding non-local thermal signal $V_{\mathrm{nl}}^{\mathrm{therm}}$ is measured along the detector strips for different strip separations. The color coding gives a qualitative profile of the magnon accumulation μ_m in the YIG film, where red corresponds to $\mu_m < 0$ (magnon depletion) and blue to a positive μ_m (magnon accumulation). In the short distance regime (detector 1), $\mu_m < 0$ at the injector and detector, such that the same sign is expected for local and non-local SSE. With increasing distance from the injector (detector 2), μ_m and consequently the spin current across the interface as well as the detected ISHE voltage change sign. (b) Local spin Seebeck voltage in a $t_{\mathrm{YIG}} = 2\,\mu\mathrm{m}$ thick YIG film detected at the injector strip at 50 K as a function of the in-plane magnetic field orientation α_{H} with respect to the $\mathbf{x}$ axis. (c), (d) Non-local thermal voltage measured at $T = 50\,\mathrm{K}$ at the detector strip for a device with a strip separation of $d = 200\,\mathrm{nm}$ and $2\,\mu\mathrm{m}$, respectively. (e) Non-local SSE amplitude $A_{\mathrm{SSE,nl}}$ extracted from in-plane field rotations at temperatures between 10 K and 300 K as a function of the injector-detector separation d. Figure adapted from Ref. [116].

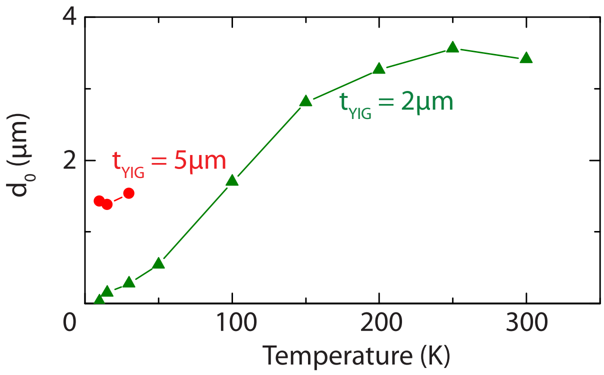

Figure 8.2: Temperature dependence of the critical strip separation d_0 at which the non-local SSE changes sign for the two LPE-YIG films with $t_{\mathrm{YIG}} = 5\,\mu\mathrm{m}$ (red dots) and $2\,\mu\mathrm{m}$ (green triangles). Figure adapted from Ref. [116].

critical strip separation d_0, which is defined by $A_{\mathrm{SSE,nl}} = 0$, shifts to larger values as the temperature increases. The values d_0 extracted from Fig. 8.1 for different temperatures are shown in Fig. 8.2 as green symbols for the 2 µm thick YIG film. With increasing temperature, d_0 increases monotonically and seems to saturate around $T = 200\,\mathrm{K}$.

The same experiments as a function of temperature and strip separation were performed on the 5 µm thick YIG sample and the resulting d_0 is included in Fig. 8.2 as red dots. The overall value of d_0 obtained for the $t_{\mathrm{YIG}} = 5\,\mu\mathrm{m}$ sample is larger than for the 2 µm thick YIG film but could only be extracted at low temperatures since the largest investigated strip separation was $d = 5\,\mu\mathrm{m}$ and the corresponding $V_{\mathrm{nl}}^{\mathrm{therm}}$ signal is close to zero.

The characteristic sign change in the non-local SSE in YIG/Pt heterostructures above a particular separation d_0 has been previously observed by Shan et al. [139] at room temperature and was attributed to the spatial profile of the non-equilibrium magnon accumulation μ_m in the YIG film, as discussed in Sect. 5.4. The magnon accumulation profile expected according to this picture is schematically depicted in Fig. 8.1 (a), where the red and blue color represents the magnon depletion ($\mu_m < 0$) and accumulation ($\mu_m > 0$), respectively. As shown in Fig. 8.1 (a), the sign of μ_m determines the direction of the interfacial spin current $\mathbf{J}_t$ at the detector, i.e. towards (away from) the YIG for negative (positive) μ_m at detector 1 (detector 2), and consequently governs the sign of the measured non-local ISHE voltage. Non-local SSE measurements as a function of the strip separation therefore allow us to map out the non-equilibrium magnon distribution (of thermal origin) in the YIG film. In particular, the characteristic length d_0 for the sign change of μ_m can be determined.

In order to rationalize the measured temperature dependence of d_0, the parameters governing the angular momentum transfer across the YIG/Pt interface as well as the magnon diffusion process need to be analyzed. It has been shown by Shan *et al.* that the transparency of the YIG/Pt interface, described by the effective spin-mixing conductance g_s, influences the magnon accumulation and hence the sign-reversal distance d_0 [139]. For a fully opaque interface (obtained using an Al_2O_3 interlayer), that suppresses angular momentum backflow from the injector into the YIG and therefore preserves a strong magnon depletion, an increase of the sign-reversal distance d_0 was observed [139]. Previous measurements of the MMR effect in a YIG/Pt heterostructure as a function of temperature have shown that the MMR signal decreases with decreasing temperature [4] (see Sect. 6.3.2), consistent with $g_s \propto T^{3/2}$ as predicted by theory [114, 126]. However, this temperature dependence corresponds to a decreasing transparency of the YIG/Pt interface with decreasing temperature, leading to an increase of d_0 at low temperatures according to the model presented in Ref. [139]. Since this is not consistent with our experimental observations depicted in Fig. 8.2, the interface properties alone (parametrized by an effective spin mixing conductance) are not sufficient to describe the temperature dependence of the non-local SSE.

In addition to the interfacial transparency, the magnon diffusion length λ_m and the magnon spin conductivity σ_m determine the spatial distribution of the non-equilibrium magnons in YIG [126]. We extracted the magnon diffusion length from temperature dependent MMR measurements conducted in the sample with $t_{\mathrm{YIG}} = 2\,\mu\mathrm{m}$ and found an increase of λ_m with decreasing temperature by about a factor of 3 between 300 K and 50 K (see Sect. 6.3.4). This is different from the temperature independent diffusion length reported by Cornelissen et al. [138], who extracted $\lambda_m(T) = \text{const.}$ together with a magnon spin conductivity σ_m vanishing at low temperatures. While the detailed evolution of λ_m and σ_m with T thus must be studied more systematically in future work, it is clear that these quantities depend on temperature. This implies that they can qualitatively impact the magnon diffusion process and consequently the non-local SSE. Indeed, the strong dependence of d_0 on the relative amplitudes of g_s, λ_m and σ_m at a fixed temperature has been demonstrated by Shan *et al.* using a one-dimensional analytical model for the spin Seebeck effect [139].

In addition to the temperature dependence, we also find an increase of d_0 with increasing YIG thickness as shown in Fig. 8.2, similar to what has previously been observed by Shan *et al.* [139]. This behavior can also be explained based on the magnon accumulation profile: in contrast to phonons, the magnons cannot cross the YIG/GGG interface and accumulate there. For thinner films, the sign change of μ_m is pushed towards the YIG/Pt interface, resulting in a smaller d_0. However, in the 2 µm thick YIG film the high temperature value of $d_0 = 3.4\,\mu\mathrm{m}$ is larger than t_{YIG}. Note that this is also consistent with measurements by Shan *et al.*, who found a dependence $d_0 \approx 1.6 t_{\mathrm{YIG}}$ [139]. These observations indicate that either (i) the profile of the magnon accumulation is not radially symmetric with respect to the injector, i.e. $d_{0,y}$ is larger than $d_{0,z}$, or (ii) for $d_0 \gg t_{\mathrm{YIG}}$ there is no magnon accumulation at the YIG/GGG interface for $y = 0$ (right below the injector), i.e. the magnons reaching the GGG interface diffuse to both sides. A more systematic study of d_0 as a function of the temperature and YIG thickness is therefore necessary. In particular large distances need to be investigated in order to measure a sign change at high temperatures in the thicker YIG films. The profile of the magnon accumulation can furthermore be investigated in Pt/YIG/Pt trilayers, where the top Pt layer is structured into strips, such that $d_{0,y}$ and $d_{0,z}$ can be extracted separately by systematically varying the strip separation and the YIG thickness.

8.2 Magnetic field dependence

We now turn to the magnetic field dependence of the non-local SSE effect in the YIG/Pt sample with $t_{\mathrm{YIG}} = 2\,\mu\mathrm{m}$. Figure 8.3 (a) depicts the non-local thermal voltage $V_{\mathrm{nl}}^{\mathrm{therm}}$ obtained from magnetic field sweeps from -15 T to 15 T with $\mu_0 H$ applied perpendicular to the Pt strips, i.e. along the **y**-direction in Fig. 8.1 (a). The results for a strip separation $d = 200\,\mathrm{nm}$ are shown for all measured temperatures in the range $10\,\mathrm{K} \leq T \leq 300\,\mathrm{K}$. The non-local SSE amplitude $A_{\mathrm{SSE,nl}} = V_{\mathrm{nl}}^{\mathrm{therm}}(\mu_0 H) - V_{\mathrm{nl}}^{\mathrm{therm}}(-\mu_0 H)$ extracted from the field sweeps is displayed in Fig. 8.3 (b). The sign change of $A_{\mathrm{SSE,nl}}$ between 15 K and 30 K is also observed in the field sweeps, consistent with the results obtained from rotations at fixed magnetic field in Fig. 8.1 (e). For positive as well as negative amplitude the non-local SSE is suppressed by the external magnetic field. The same data is plotted in Fig. 8.3 (c) as a function of temperature for different magnetic fields. We find a maximum of the signal around $T = 100\,\mathrm{K}$, which is consistent with other observations in non-local SSE measurements [117]. A similar behavior was observed in the local SSE and was attributed to the temperature dependence of the phonon heat conductivity [157, 158]. Additionally, the temperature dependence of the magnon diffusion length is expected to influence the local SSE amplitude [122]: for decreasing temperatures, λ_m increases such that more magnons can reach the detector. At very low temperatures this is counteracted by the freeze out of magnons such that the signal decreases again. However, applying the model proposed for the local SSE to non-local measurements is not straightforward, in particular since a sign change is observed in the latter around 30 K.

We find that the sign change of the non-local SSE amplitude in Fig. 8.3 (c) seems to be mostly independent of the magnetic field strength. As this sign change is related to the position where the magnon accumulation μ_m changes sign, we conclude that the latter is also not significantly affected by the applied magnetic field, although the overall number of magnons in the system is expected to change with magnetic field, due to the suppression of low energy magnons in the Zeeman gap. This behavior is consistent with the current non-local SSE model where the magnon accumulation profile is determined by the boundary conditions (Pt/YIG and YIG/GGG interface) which are independent of magnetic field, and by the magnon spin conductivity and diffusion length [139]. From MMR measurements in the same sample we found that the magnon diffusion length has only a weak field dependence (see Sect. 6.3.4). These observations are consistent with the

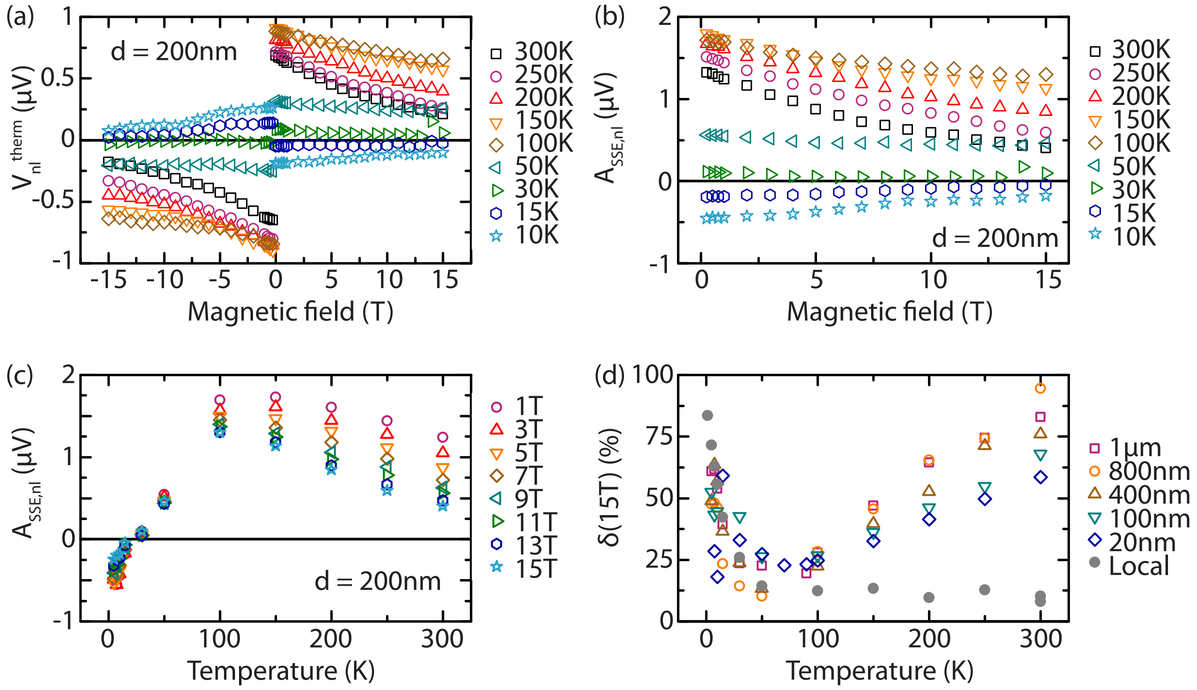

Figure 8.3: (a) Non-local thermal voltage obtained from field sweeps in a YIG/Pt non-local structure with strip separation $d = 200\,\mathrm{nm}$ for different temperatures. (b) Non-local SSE amplitude $A_{\mathrm{SSE,nl}}$ extracted from the magnetic field sweeps in panel (a). (c) $A_{\mathrm{SSE,nl}}$ as a function of temperature for different magnetic fields up to 15 T. (d) Relative suppression $\delta(\mu_0 H)$ of the non-local SSE for $\mu_0 H = 15\,\mathrm{T}$ as a function of temperature for different strip separations $20\,\mathrm{nm} \leq d \leq 1\,\mu\mathrm{m}$ (open symbols). The full gray symbols represent the field suppression of the local SSE amplitude in the same sample.

fact that the position of the non-local SSE sign change is mostly independent of magnetic field.

We now analyze the magnetic field suppression of the non-local SSE amplitude, which is very pronounced at high temperatures in Fig. 8.3 (c). Since the overall signal amplitude decreases towards low temperatures, we calculate the relative suppression $\delta(\mu_0 H)$ in % according to

$$\delta(\mu_0 H) = \frac{V_{\mathrm{nl}}^{\mathrm{therm}}(0.25\,\mathrm{T}) - V_{\mathrm{nl}}^{\mathrm{therm}}(\mu_0 H)}{V_{\mathrm{nl}}^{\mathrm{therm}}(0.25\,\mathrm{T})}. \tag{8.1}$$

The resulting suppression for the maximum field $\delta(15\,\mathrm{T})$ is displayed in Fig. 8.3 (d) as open symbols for different Pt strip separations ranging from $20\,\mathrm{nm} \leq d \leq 1\,\mu\mathrm{m}$. The gray full symbols correspond to the field suppression of local SSE measurements on the same sample[1]. The temperature dependence of the local SSE field suppression has been reported previously [119] and was already discussed in the context of the MMR measurements in Sect. 6.3.3: at low temperatures $\delta(\mu_0 H)$ is largest since the thermal magnon population

---

[1] The raw data is not shown here, but can be found in Ref. [141].

can be easily suppressed by an external field due to the opening of the Zeeman gap. At high temperatures, the suppression is much lower but still finite, indicating that low energy magnons contribute strongly to the SSE [119].

The magnetic field suppression of the non-local SSE amplitude also increases strongly at low temperatures for all strip separations and we attribute this once more to the opening of the Zeeman gap leading to an efficient suppression of the thermal magnon population. Around 50 K to 100 K, $\delta(\mu_0 H)$ reaches a minimum since the overall magnon population increases and the relative suppression decreases. At high temperatures however, $\delta(15\,\mathrm{T})$ reaches around 85% for $d = 1\,\mu\mathrm{m}$, which is very different from the behavior of the local SSE amplitude (gray full symbols in Fig. 8.3 (d)). We observed a similar increase of the suppression at high temperatures for the MMR effect as shown in Fig. 6.4 (d). While it seems likely that the high temperature field suppression in the MMR and non-local SSE are related to similar effects, the origin of this behavior in the MMR is not yet fully understood, as discussed in Sect. 6.3.3.

For the non-local SSE, an additional effect related to the YIG magnon spectrum needs to be considered: as shown in the calculated YIG magnon spectrum in Fig. 5.2, around 300 K an additional high energy exchange magnon mode with negative polarization (blue colored mode) starts to become thermally populated in addition to the positively polarized fundamental mode. In order to discuss the influence of this high energy mode on the non-local SSE, a sketch of the two relevant magnon modes for different temperatures at zero and finite magnetic field is depicted in Fig. 8.4 (not to scale). The red and blue color represents the polarization, i.e. counter-clockwise and clockwise precession with respect to the external magnetic field. We only consider the dominant fundamental mode (“+” polarized, red) and the lowest energy exchange mode (“−” polarized, blue), since all other modes become very broad at high temperatures and can no longer be interpreted in terms of coherent spin waves [64] (see Fig. 5.2). Intuitively, the “−” polarized (blue) mode can be attributed to one Fe sublattice magnetization oriented antiparallel to the external field and precessing in an effective field dominated by the exchange field of the second Fe sublattice. By increasing the external magnetic field, the effective field is therefore reduced and the precession frequency decreases. Therefore the “−” polarized (blue) mode is expected to shift to lower frequencies when an external magnetic field is applied. As long as the exchange mode is far above $k_\mathrm{B}T$, the thermal population is not affected by such a shift (see Fig. 8.4 (a)-(d)). However, around 300 K, when the exchange mode is thermally populated, its occupancy increases with increasing magnetic field, as depicted in Fig. 8.4 (e) and (f).

It was shown recently that magnon modes with opposite polarization give rise to opposite signs of the local SSE in GdIG/Pt [83, 159] (see Sect. 5.2.2). Following this line of argument, an increase of the “−” polarized magnon population around room temperature should lead to a suppression of the non-local SSE with magnetic field, consistent with experimental observations (Fig. 8.3 (d)). The strong suppression of the non-local SSE

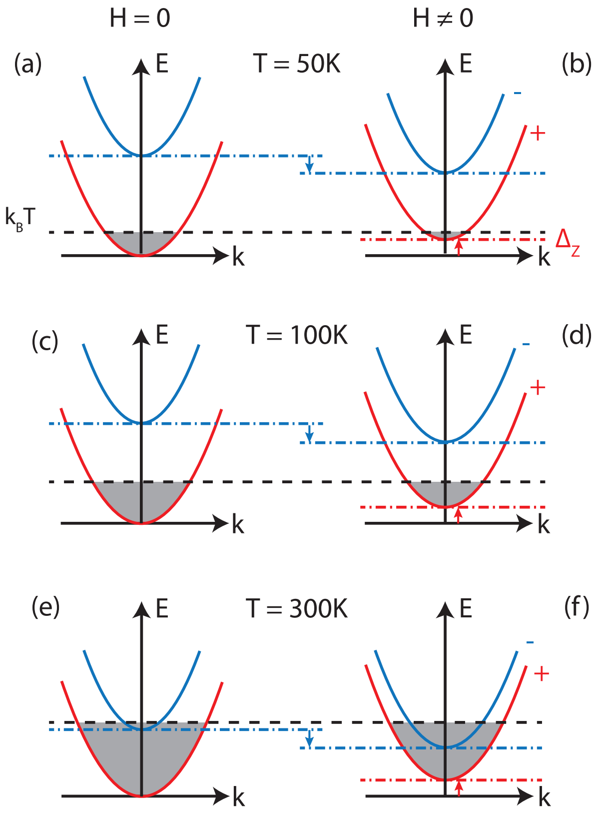

Figure 8.4: Sketch of the two dominating modes in the YIG magnon spectrum as calculated in Ref. [64] (see Fig. 5.2). The red and blue color corresponds to the polarization/precession direction of the two modes, i.e. counter-clockwise for the FMR-like fundamental mode ("+" polarized, red) and clockwise for the first (lowest energy) exchange mode ("−" polarized, blue). The panels on the left and right hand side correspond to zero and finite magnetic field, respectively. The spectra are sketched for three temperatures representative of different temperature regimes. (a)-(b) In the low temperature regime only low energy magnons of the fundamental ("+" polarized) mode are thermally populated and can be significantly suppressed by an external magnetic field. (c)-(d) In the intermediate temperature range, the thermal population of the fundamental mode ("+" polarized, red) becomes larger with increasing temperature, such that the relative suppression with magnetic field is smaller. (e)-(f) Close to room temperature, the exchange mode ("−" polarized, blue) is thermally populated and shifts down when an external field is applied. Assuming the exchange mode gives rise to an opposite sign in the non-local voltage of thermal origin, this leads to a stronger field suppression of the non-local SSE amplitude.

close to room temperature may therefore be partially attributed to the contribution of a second high energy magnon mode carrying opposite magnetic moment.

The increase of the field suppression $\delta(\mu_0 H)$ with increasing strip separation observed in Fig. 8.3 (d) could also indicate that the "−" and "+" polarized magnons have different diffusion lengths. In order to verify this hypothesis and determine the contribution of the high energy magnon modes, further measurements at high temperatures and large magnetic fields are required: once the population of the exchange mode ("−" polarized, blue) mode in Fig. 5.2 (d) becomes large enough to compensate the magnons of the fundamental mode ("+" polarized, red), a sign change of the nl-SSE is expected, similar to the temperature dependent SSE sign change observed in GdIG/Pt [83].

We also note that the suppression observed for $d = 20\,\mathrm{nm}$ at 300 K in Fig. 8.3 (d) is much larger than for the local SSE. This is unintuitive since $d = 20\,\mathrm{nm}$ is very close to the local limit. It has been shown that magnons generated over the whole thickness of the YIG film contribute to the local SSE [121]. Since the strip separation is several orders of magnitude smaller than $t_{\mathrm{YIG}} = 2\,\mu\mathrm{m}$, it is reasonable to assume that the magnons generated in the bulk cover the same distance to reach the local and non-local Pt strip and therefore contribute equally in both local and non-local SSE. We furthermore assume that the detection efficiency of the local and non-local strip is independent of the external field, since the only difference is that one strip is heated by current and the other one is not. In order to explain the discrepancy in the field dependence an additional effect which vanishes on the length scale of about 20 nm in lateral direction is therefore required. In this context, it was calculated that the lateral temperature difference of the magnon and phonon subsystems in YIG - which is at the origin of the local SSE - goes to zero within a few nm [137]. As discussed in Sect. 5.4, a magnon current can originate from both the magnon-phonon temperature difference and a gradient in the magnon accumulation. Assuming that the former is less affected/suppressed by the applied magnetic field than the latter, this could explain the weak field suppression in the local signal compared to the strong effect on the non-local SSE in the $d = 20\,\mathrm{nm}$ structure. However, more experimental proof is required to confirm this hypothesis. It is also possible that in addition to the quadratic Joule heating term, the non-local thermal signal extracted using the current switching method (see Eq. (3.3)) contains other higher order terms which are even in current. A more systematic study of the non-local SSE, e.g. measuring IV-curves, may give further insight into the origin of the non-local thermal effect and its field dependence. Furthermore, a different heating method can be used, for example a Au strip instead of Pt, in order to exclude any contributions from spin currents and the SHE in the Pt injector.

In summary, we have measured the non-local spin Seebeck effect (SSE) in YIG/Pt nanostructures as a function of the Pt strip separation, temperature and magnetic field. The amplitude of the non-local SSE changes sign at a characteristic distance d_0 which depends strongly on the temperature and YIG thickness. The experimental results can be qualitatively explained based on the non-equilibrium magnon accumulation profile in the YIG film, as proposed in Ref. [139]. The non-local SSE therefore originates from a gradient of the magnon accumulation and in contrast to the local SSE is not dominated by the temperature difference of the magnon and phonon subsystems right at the injector interface. We have furthermore studied the field dependence of the non-local SSE and observe a strong suppression with increasing field at low temperatures where low energy magnons are efficiently suppressed by the Zeeman gap. The strong signal suppression at high temperatures observed only in the non-local signal needs to be studied in more detail, but may partially be attributed to a contribution from an additional high energy exchange magnon mode. The latter becomes more strongly populated with increasing temperature and magnetic field and is expected to give rise to an opposite sign in ISHE voltage for the non-local SSE.

Chapter 9

Magnon mediated magnetoresistance in GdIG/Pt

In this chapter, we study the transport of electrically injected magnons through the compensated ferrimagnet gadolinium iron garnet ($Gd_3Fe_5O_{12}$, GdIG). The magnetic properties of GdIG were introduced in detail in Sect. 3.1.2: due to the temperature dependence and relative orientations of the sublattice magnetizations, the remanent magnetization of GdIG goes to zero at a characteristic magnetization compensation temperature T_{comp} [15]. As shown in the magnetic phase diagram depicted in Fig. 3.2, for temperatures far above and below T_{comp}, GdIG is in a collinear phase, i.e. the sublattice magnetizations are all aligned (anti)parallel to the applied magnetic field. However, in the vicinity of T_{comp}, a magnetic canting phase can be reached already for magnetic field magnitudes available in experiments, such that the magnetic moments residing on the different sublattices are no longer collinear to the applied field [15, 30, 72, 73]. In Sect. 4.2, we demonstrated that in a GdIG/Pt bilayer the magnetization texture at the interface can be probed electrically via the spin Hall magnetoresistance effect [10–12, 27] (SMR), since the latter is determined by the orientation of the individual sublattice magnetic moments relative to the polarization of the spin accumulation at the Pt/GdIG interface [30, 59]. However, magnon transport or spin diffusion through a non-collinear magnetic structure has not been investigated to date and will be discussed in this chapter based on MMR measurements in GdIG. In addition to the complex magnetic phase diagram, GdIG also exhibits a rich spin wave spectrum featuring several magnon modes in the low THz regime, which are thermally populated at room temperature (see Sect. 5.2). This can be attributed to the additional magnetic Gd sublattice. GdIG therefore also allows to study the influence of multiple magnon modes and their transport properties on the MMR effect. In Sect. 9.1, we first focus on the MMR response in the collinear phase in GdIG. The experimental results and theoretical discussion are being prepared for publication [129] and the corresponding text and figures are reused in the following and adapted to the format of this thesis. We then turn to the MMR response close to the compensation temperature of GdIG, i.e. in the canting phase, and discuss the influence of the (sublattice) moment orientations on the MMR angular dependence (see Sect. 9.2).

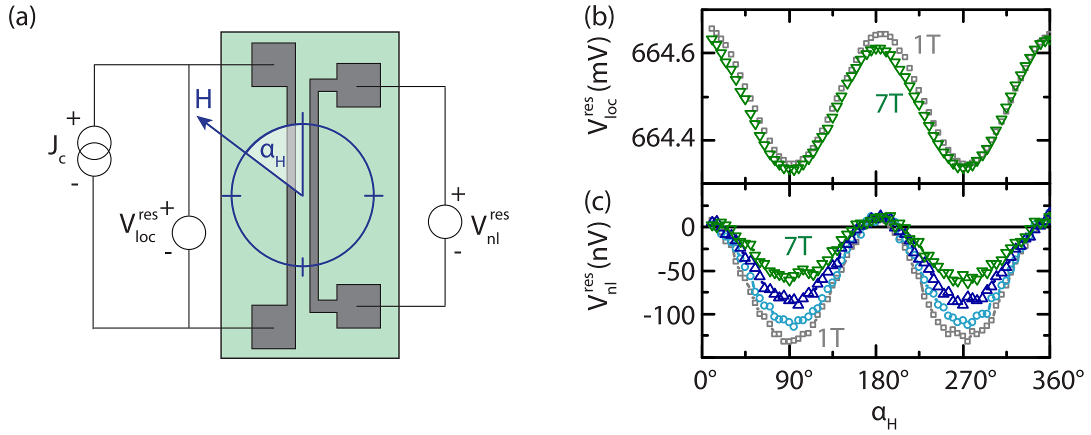

Figure 9.1: (a) Schematic representation of a GdIG (green)/Pt (gray) nanostructure with two parallel Pt strips. The wiring for the measurements is sketched in black. (b) Local voltage $V_{\mathrm{loc}}^{\mathrm{res}}$ as a function of the angle α_{H} between the charge current $\mathbf{J}_c$ and the external magnetic field $\mathbf{H}$ at 290 K for $\mu_0 H = 1\,\mathrm{T}$ and 7 T. (c) Non-local voltage $V_{\mathrm{nl}}^{\mathrm{res}}$ as a function of α_{H} at 290 K for $1\,\mathrm{T} \leq \mu_0 H \leq 7\,\mathrm{T}$. Figure adapted from Ref. [129].

9.1 Collinear magnetic phase of GdIG

For the magnon mediated magnetoresistance measurements, i.e. electrical injection and non-local detection of magnons, we study a 2.6 µm thick GdIG film grown on top of a (111)-oriented $Gd_3Ga_5O_{12}$ substrate via liquid phase epitaxy (LPE)[1] with an *ex-situ* 10 nm thick Pt layer deposited at WMI (see Sect. 6.1 for details on the fabrication). Two Pt strips with edge-to-edge separation $d = 200\,\mathrm{nm}$ and strip width $w = 500\,\mathrm{nm}$ (see Fig. 9.1 (a), not to scale) are defined by electron beam lithography followed by Ar ion etching. The electric wiring scheme used for the following measurements is depicted in Fig. 9.1 (a): a charge current of 100 µA is applied to the injector strip (left) and the corresponding local voltage V_{loc} and non-local signal V_{nl} are measured simultaneously at the two strips (see Sect. 6.2). To eliminate thermal signals due to Joule heating in the local strip (e.g. spin Seebeck effect [95]) and to increase the signal-to-noise ratio, we use the current switching method described in Sect. 3.3.2 and extract $V_{\mathrm{loc}}^{\mathrm{res}}$ and $V_{\mathrm{nl}}^{\mathrm{res}}$. The SMR and MMR amplitudes are obtained from angle dependent magnetoresistance (ADMR) measurements. Most of the measurements on the LPE-grown GdIG sample presented in this section were conducted by T. Wimmer during his master's thesis at WMI [141], which I supervised.

The local response $V_{\mathrm{loc}}^{\mathrm{res}}$ measured at 290 K as a function of the angle α_{H} between $\mathbf{J}_c$ and $\mathbf{H}$ is shown in Fig. 9.1 (b) for $\mu_0 H = 1\,\mathrm{T}$ (gray) and 7 T (green). From these ADMR measurements, the SMR amplitude $\Delta V_{\mathrm{loc}}^{\mathrm{res}} / V_{\mathrm{loc,min}}^{\mathrm{res}} = \left(V_{\mathrm{loc}}^{\mathrm{res}}(0°) - V_{\mathrm{loc}}^{\mathrm{res}}(90°)\right) / V_{\mathrm{loc}}^{\mathrm{res}}(90°)$ is extracted (see Eq. (4.2)) and plotted as a function of temperature for magnetic field strengths $\mu_0 H = 1\,\mathrm{T}, 3\,\mathrm{T}, 5\,\mathrm{T}$ and 7 T in Fig. 9.2 (a). Towards low temperatures, the

---

[1] The GdIG LPE-film was provided by Z. Qiu and E. Saitoh, Tohoku University (see Appendix Tab. A.1).

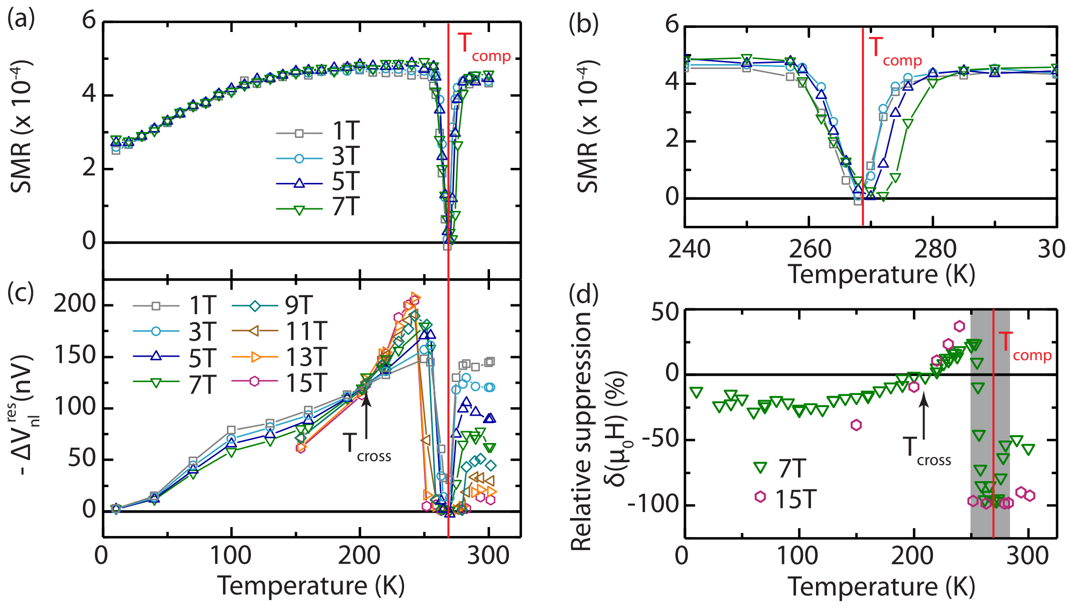

Figure 9.2: (a) Temperature dependent SMR ratio $\left(V_{\mathrm{loc}}^{\mathrm{res}}(0^{\circ}) - V_{\mathrm{loc}}^{\mathrm{res}}(90^{\circ})\right)/V_{\mathrm{loc}}^{\mathrm{res}}(90^{\circ})$ extracted from the local voltage amplitude for magnetic fields of $1\,\mathrm{T} \leq \mu_0 H \leq 7\,\mathrm{T}$. (b) Close-up of the SMR amplitude around the compensation temperature $T_{\mathrm{comp}} = 268\,\mathrm{K}$ (red vertical line). The region where the SMR amplitude goes to zero broadens when the magnetic field is increased, indicating that the magnetic canting phase is at the origin of the vanishing SMR. (c) Temperature dependence of the MMR amplitude $-\Delta V_{\mathrm{nl}}^{\mathrm{res}} = V_{\mathrm{nl}}^{\mathrm{res}}(0^{\circ}) - V_{\mathrm{nl}}^{\mathrm{res}}(90^{\circ})$ obtained from ADMR measurements for magnetic fields up to 15 T. (d) Relative magnetic field dependence $\delta(7\,\mathrm{T})$ (green) and $\delta(15\,\mathrm{T})$ (purple) of the MMR effect defined by Eq. (9.1). A negative (positive) value corresponds to a suppression (enhancement) with increasing field. The gray shaded region indicates the temperature range around T_{comp} where the MMR becomes very small, impeding a reliable quantification of $\delta(\mu_0 H)$. Figure adapted from Ref. [129].

SMR amplitude decreases by a factor 2 compared to room temperature, consistent with measurements in YIG/Pt [40] and (In, Y) doped GdIG/Pt bilayers [30] (see Chap. 4). In a narrow temperature range around the compensation temperature ($T_{\mathrm{comp}} = 268\,\mathrm{K}$ determined via SQUID magnetometry), the SMR decreases to zero. We observed a similar behavior in (In, Y) doped GdIG (see Sect. 4.2) [30] and attributed this to the formation of the canting phase in GdIG close to the compensation temperature, where the sublattice magnetizations are no longer collinear. According to our discussion of the SMR in Sect. 2.3, a sign change of the (sublattice specific) SMR arises when the (sublattice) canting angle with respect to the external field is larger than 54° (see Fig. 2.9). The lack of a sign change in the present data may therefore originate from a constant canting angle of approximately 54° in the narrow region around T_{comp}. However, it seems coincidental that the SMR amplitude goes exactly to zero at the compensation temperature, independent of the magnetic field strength up to 7 T. We therefore rather attribute the vanishing SMR amplitude to the formation of magnetic domains, i.e. regions in the sample with different sublattice orientations and canting angles due to inhomogeneities in the ferrimagnet, such that the overall magnetoresistive modulation vanishes on average. The qualitatively different SMR responses observed in Fig. 9.2 and Fig. 4.5 may thus be related to the sample fabrication method and/or the ensuing interface properties, i.e. LPE growth with *ex-situ* Pt evaporation versus PLD growth followed by *in-situ* Pt evaporation. In order to clarify this point, the influence of different growth methods will be discussed in more detail in Sect. 9.2. It is nevertheless reasonable to attribute the vanishing SMR around T_{comp} to the magnetic canting phase, as the region where the SMR goes to zero broadens with increasing magnetic field. This is clearly visible in the close-up of the compensation region displayed in Fig. 9.2 (b). The observed broadening is in good agreement with previous results discussed in Sect. 4.2 [30] and is expected for the magnetic canting phase in GdIG [72]. As stated in Sect. 4.1 and 4.2, in the collinear phase the SMR hardly depends on the applied magnetic field (see Fig. 9.2 (a)), since mainly the orientation of the sublattice moments is relevant.

We now turn to the angular dependence of the non-local response $V_{\mathrm{nl}}^{\mathrm{res}}$ at 290 K shown in Fig. 9.1 (c) for different magnetic field strengths. The non-local voltage signature has the same dependence on the external magnetic field orientation as in previous MMR measurements in YIG/Pt nanostructures for the same wiring scheme (see Sect. 6.3.1) [4], i.e. $V_{\mathrm{nl}}^{\mathrm{res}}(90°) < 0$ and $V_{\mathrm{nl}}^{\mathrm{res}}(0°) = 0$. For convenience, we plot a positive MMR amplitude $-\Delta V_{\mathrm{nl}}^{\mathrm{res}} = V_{\mathrm{nl}}^{\mathrm{res}}(0°) - V_{\mathrm{nl}}^{\mathrm{res}}(90°) > 0$ as a function of temperature in Fig. 9.2 (c), first for fields up to 7 T. In contrast to the local SMR, where no substantial field dependence is observed in the collinear phase, the non-local MMR signal displays a more complex magnetic field and temperature dependence. To confirm this behavior, additional non-local data was taken in magnetic fields up to 15 T for temperatures between 150 K and 300 K, as shown in Fig. 9.2 (c), which will be discussed later on. We first focus on the MMR temperature dependence and analyze the data taken at 1 T (gray open squares in Fig. 9.2 (c)). At low temperatures, $\Delta V_{\mathrm{nl}}^{\mathrm{res}}$ vanishes, similar to our observations in YIG/Pt (see Sect. 6.3.2) [4, 134, 138] where a temperature power law dependence of $\Delta V_{\mathrm{nl}}^{\mathrm{res}}$ was observed. This temperature dependence in YIG is in agreement with theoretical expectations based on the magnon density of states and distribution function [113, 114, 126], i.e. general properties of the magnonic system. At low temperatures, we therefore expect GdIG to behave very similar to YIG.

With increasing temperature, the non-local signal measured at 1 T increases up to 150 nV just below the compensation temperature. The MMR then vanishes at T_{comp} and recovers a finite value above T_{comp}, similar to what is observed in the local SMR (see Fig. 9.2 (a)). We attribute the vanishing MMR signal at T_{comp} to the change of the magnetic structure of GdIG into the canted phase. A vanishing non-local signal in the canted phase suggests two possible scenarios, either (i) the magnon injection/detection becomes inefficient due to the non-collinear alignment of the magnetic sublattice moments and/or (ii) the damping close to the compensation point is enhanced, leading to shorter magnon lifetimes as suggested by the previously observed increase of the ferromagnetic resonance line width at the magnetization compensation temperature in GdIG [79, 84, 136]. Additional magnon scattering effects may arise due to magnetic domain formation in the canting phase as discussed above, which further suppresses magnon transport. For now we focus on the discussion of the MMR effect in the collinear phase and will discuss MMR measurements in the canted phase of GdIG in more detail in Sect. 9.2.

We now turn to the magnetic field dependence of the MMR effect in the collinear magnetic phase. The relative field dependence $\delta(\mu_0 H)$ is defined as

$$\delta(\mu_0 H) = \frac{\Delta V_{\mathrm{nl}}^{\mathrm{res}}(\mu_0 H) - \Delta V_{\mathrm{nl}}^{\mathrm{res}}(1\,\mathrm{T})}{\Delta V_{\mathrm{nl}}^{\mathrm{res}}(1\,\mathrm{T})} \tag{9.1}$$

and plotted as a function of temperature in Fig. 9.2 (d) for $\mu_0 H = 7\,\mathrm{T}$ (green triangles). Note that here, a negative value corresponds to a suppression of the signal, while a positive value represents an increase of the MMR with increasing magnetic field. We distinguish three temperature regimes: (i) for $0 < T < T_{\mathrm{cross}} \approx 210\,\mathrm{K}$, the MMR is suppressed with applied magnetic field $\mu_0 H = 7\,\mathrm{T}$ by about 25%, (ii) in the range $T_{\mathrm{cross}} < T < T_{\mathrm{comp}}$ an enhancement with field is observed, while (iii) for $T_{\mathrm{comp}} < T$ the MMR is suppressed by up to 50 %. The MMR suppression in the canted phase (gray shaded area in Fig. 9.2 (d)) appears to be very large, but since the MMR amplitude is close to zero, the relative field effect is prone to large errors. Additional measurements of $\delta(\mu_0 H)$ up to $\mu_0 H = 15\,\mathrm{T}$ between $T = 150\,\mathrm{K}$ and $300\,\mathrm{K}$ (purple hexagons in Fig. 9.2 (d)) qualitatively confirm the low field data, displaying a more pronounced suppression and enhancement of the MMR. In particular, the non-local signal can be almost completely suppressed above T_{comp} by a magnetic field of 15 T.

In YIG/Pt, a magnetic field induced reduction of the MMR was observed for the entire investigated temperature range from 50 K to 300 K, reaching up to $\delta(7\,\mathrm{T}) \approx -25\%$ as discussed in Sect. 6.3.3 (see Fig. 6.4). This behavior was partially attributed to the field dependence of the thermal magnon population. Additionally, a small suppression of the magnon diffusion length with increasing magnetic field was found in YIG/Pt [127].

While the low temperature field suppression of the MMR in GdIG/Pt is similar to that of YIG/Pt, the field suppression above T_{comp} is much stronger. Furthermore, the enhancement of the MMR with magnetic field in the temperature range 200 K to 250 K as shown in Fig. 9.2 (c) and (d) is not observed in YIG/Pt.

As previously discussed in Chap. 5, contributions from both magnon injection (i.e. thermal magnon population) as well as transport properties need to be taken into account for a description of the MMR. For the injection efficiency, we first focus on the magnetic field and temperature dependence of the thermal magnon population in GdIG. To this end, we discuss the characteristic changes in the GdIG spin wave spectrum as a function of temperature and magnetic field calculated by J. Barker using atomic spin dynamics

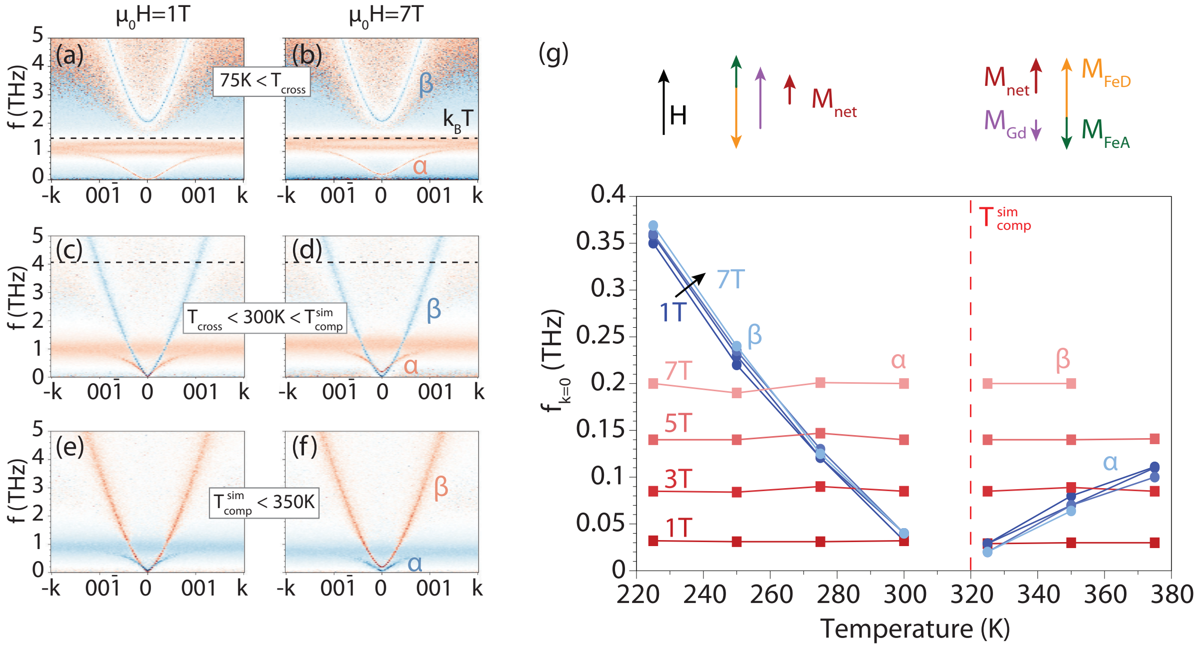

Figure 9.3: Magnon spectrum of GdIG obtained from atomistic simulations, calculated (a)-(b) at $T = 75\,\mathrm{K}$, (c)-(d) just below $T_{\mathrm{comp}}^{\mathrm{sim}} = 320\,\mathrm{K}$ and (e)-(f) above the compensation point. The red and blue color indicates counterclockwise and clockwise precession directions relative to the external magnetic field direction, i.e. positive and negative polarization, respectively. The spectra are calculated for $\mu_0 H = 1\,\mathrm{T}$ and $7\,\mathrm{T}$ revealing the effect of the Zeeman shift of the "+" polarized mode (red). The black dashed line corresponds to the thermal energy $k_\mathrm{B}T$. (g) Temperature and magnetic field dependence of the frequency of the $k = 0$ magnons for the α and β modes. The red and blue colored symbols mark the positive and negative polarization of the magnon branches. The orientation of the sublattice and net magnetization with respect to the external field is depicted by arrows for temperatures above and below the compensation point $T_{\mathrm{comp}}^{\mathrm{sim}}$. The calculations were conducted by J. Barker and the figures are adapted from Ref. [129].

simulations [129] (see Sect. 5.2). The calculations are based on a classical Heisenberg model where the Landau-Lifshitz-Gilbert equation is used to solve the spin dynamics and a Langevin thermostat introduces temperature. The spin wave spectrum is calculated from the space-time Fourier transform of the spin fluctuations. Details of the model including the parameters used for GdIG can be found in Refs. [30, 83, 129]. Figure 9.3 (a)-(f) displays the spin wave spectra calculated by J. Barker at $T = 75\,\mathrm{K}, 300\,\mathrm{K}$ and $350\,\mathrm{K}$ for magnetic fields $\mu_0 H = 1\,\mathrm{T}$ and $7\,\mathrm{T}$ (left and right panels, respectively). The polarization ("+"/"−") of the spin wave modes, which describes the precession direction with respect to an applied magnetic field [64], i.e. counterclockwise/clockwise, is encoded by a red/blue coloring in the figures (see Sect. 5.2.2). We use the same terminology as in Sect. 5.2.2 and label the modes according to their dispersion, i.e. α - the lowest frequency dispersive mode at 75 K and β - the parabolic exchange mode with opposite polarization

(Fig. 9.3 (a)). The modes move in frequency space with temperature and magnetic field and change polarization across the compensation point at $T_{\mathrm{comp}}^{\mathrm{sim}} = 320\,\mathrm{K}$, but we retain the same α, β designations throughout. The flat, broadened bands around 1 THz do not contribute significantly to transport because of their small group velocity and large damping (linewidth). As detailed in Sect. 5.2, it was recently shown that the temperature dependence of the spin Seebeck effect in GdIG/Pt bilayers [83] can easily be rationalized based on the calculated spin wave spectra: the SSE in GdIG reveals two sign changes as a function of temperature, which can be understood considering that the transport of thermal magnons in GdIG is dominated by the α and β magnon modes which carry opposite magnetic moment [83].

For the MMR however, the orientation of the transferred magnetic moment is given by the spin accumulation arising from the SHE in the Pt (see Sect. 5.2.2). In the scenario sketched in Fig. 5.4, the electrical injection of a given magnetic moment can either excite a "+" polarized magnon (red) or absorb a "−" polarized (blue) magnon beneath the injector Pt strip. The direction of the corresponding diffusion currents between injector and detector is therefore also opposite, such that the effective magnetic moment detected in the second Pt strip is the same, whether it is carried by "+" or "−" polarized magnons. This is consistent with the fact that in contrast to the SSE [83], no temperature dependent sign change is observed in the MMR amplitude in Fig. 9.2 (c).

Since theory predicts that the MMR amplitude is proportional to the number of thermally populated magnons [114], an increase (decrease) in the overall magnon population of both modes should lead to an increase (decrease) of the MMR amplitude. We therefore study the influence of temperature and applied magnetic field on the magnon population. The frequency values at $k = 0$ for the α and β modes from Fig. 9.3 (a)-(f) are compiled in Fig. 9.3 (g) for temperatures between 220 K and 380 K. The orientation of the sublattice magnetizations with respect to the external field $\mathbf{H}$ above and below the compensation point is indicated by arrows. Similar to the FMR-like mode in YIG, the "+" polarized fundamental mode (red in Fig. 9.3) shifts up in frequency proportional to the applied field as the Zeeman gap opens, but has a very weak temperature dependence (red squares in Fig. 9.3 (g)). The "−" polarized exchange mode (blue) has a much stronger temperature dependence (blue dots in Fig. 9.3 (g)) caused by the increasing disorder of the Gd sublattice towards high temperatures which alters the effective exchange fields, as discussed in Sect. 5.2.2 [83]. We would like to emphasize once more that the labels α and β denote the type of dispersion relation and do not refer to the polarization of the magnon modes. In particular, the α and β modes change polarization at the compensation temperature. The frequency shift obtained from the calculations in Fig. 9.3 (g) is not related to the type of dispersion (α or β), but to the polarization "+" (red) or "−" (blue).

At low temperatures (Fig. 9.3 (a) and (b)), the β-mode ("−" polarized, blue) is not populated and does not contribute to spin transport. The applied magnetic field freezes out the α-magnons ("+" polarized, red), thereby reducing the MMR signal (see Fig. 9.2 (c) and (d)), similar to what is observed in YIG. With increasing temperature, the exchange gap of the β-mode decreases (see Fig. 9.3 (c) and (g)) due to the thermally induced disorder in the Gd system [83]. Naively, at fixed magnetic field amplitude, this should lead to an increase of the non-local signal with increasing temperature as the thermal population of the exchange mode increases. However, the increase of the MMR amplitude with temperature in Fig. 9.2 (c) looks very similar to the one observed in YIG/Pt (see Fig. 6.3) and can therefore not be attributed unambiguously to the contribution of the additional exchange magnon mode.

We now discuss the magnetic field dependence of the exchange mode for a fixed temperature. As shown in Fig. 9.3 (g), below T_{comp}, the $k = 0$ frequency of the "$-$" polarized (blue) β-mode slightly increases when a magnetic field is applied. This is due to the fact that the magnetic field increases the Gd order and thereby increases the β-mode frequencies again. However, according to simulations, the shift is very small compared to the Zeeman shift of the "+" polarized (red) fundamental mode. Furthermore, both modes shift to higher frequencies, leading to a reduction of the overall thermal magnon population. Based on these calculations, the enhancement of the MMR amplitude with magnetic field right below T_{comp} can therefore not be modeled by considering only the thermal magnon population of the α- and β-modes.

In order to understand the complex field dependence of the MMR in GdIG, we therefore turn to the second important factor for the MMR effect, i.e. magnon transport properties. While the calculated magnon spectra in Fig. 9.3 can give a qualitative idea of for instance the group velocity of different magnons, a detailed description including damping or scattering effects requires further experimental studies and theoretical calculations. We can however discuss the experimental observations in an intuitive model: as mentioned above, the Gd moments are only weakly exchange coupled and the Gd sublattice is therefore strongly disordered at high temperatures (above $\approx 70 - 100\,\mathrm{K}$) [81]. This disorder may lead to enhanced scattering for all magnon modes that contribute to transport. However, for $T < T_{\mathrm{comp}}$, this trend is partially reverted by an external magnetic field since the latter increases the order within the Gd sublattice. It is therefore possible that a magnetic field improves the transport properties by polarizing the Gd moments and reducing scattering, giving rise to an enhancement of the detected non-local MMR signal. On the other hand, above the compensation temperature the Gd is aligned antiparallel to the external field. Upon increasing the latter, the Gd is therefore further depolarized, leading to a deterioration of the transport properties and a strong suppression of the MMR amplitude.

While this simple model can reproduce the asymmetric magnetic field dependence of the MMR around T_{comp}, i.e. an enhancement (suppression) with increasing magnetic field for $T < T_{\mathrm{comp}}$ ($T > T_{\mathrm{comp}}$), a more thorough investigation of the transport properties is required to confirm this hypothesis. Looking at the magnetic phase diagram of GdIG (Fig. 3.2 (d)), above T_{comp} when a large enough magnetic field ($H > H_c \approx 30\,\mathrm{T} - 40\,\mathrm{T}$, depending on temperature) is applied, the Gd is eventually repolarized along the applied field. According to the model proposed above, we therefore expect an improvement of the transport properties (i.e. increase of the MMR amplitude) above this critical field, where the Gd moments become increasingly ordered. However, the required magnetic field magnitudes will also lead to changes in the thermal magnon spectrum and thermal population, which have to be taken into account.

Another approach to critically test our model picture is to determine the damping properties of GdIG based on ferromagnetic resonance (FMR) spectroscopy: for temperatures close to T_{comp}, the fundamental mode as well as the lowest energy exchange mode with opposite polarization are at very similar frequencies and can be studied at typical FMR frequencies in the low GHz regime [79]. FMR measurements in GdIG should therefore enable a study of the damping properties of the two magnon modes. While these measurements allow to investigate mainly the $k = 0$ mode, the results should give first important insights, that may be extrapolated to larger k-vectors. Furthermore, it is interesting to study the influence of a crossing (or anti-crossing) of the two magnon modes as a function of the applied magnetic field (see Fig. 9.3 (g)). In the simulations provided by J. Barker (displayed in Fig. 9.3) no anti-crossing is observed. However, dipolar interactions were not included in these calculations. Taking dipolar interactions into account may lead to an anti-crossing of magnon modes in a ferrimagnet such as GdIG, as recently predicted in Ref. [160]. An interaction between magnons from different modes can considerably alter the transport properties as well as the observed MMR response.

In summary, we measured the non-local magnon mediated magnetoresistance effect (MMR) in the collinear as well as in the canted phase of the compensated ferrimagnet GdIG [129]. The data taken close to the compensation temperature suggest that the MMR is suppressed in the canted phase, possibly due to inefficient magnon injection or magnetic domain formation, which will be discussed in more detail in Sect. 9.2. In the collinear magnetic phase, the MMR signal is suppressed by magnetic field at low temperatures and above T_{comp}, but is enhanced just below the compensation point. The enhancement of the MMR amplitude with magnetic field is surprising and was not observed in YIG/Pt or other materials up to now. In order to determine possible influences of the thermal magnon population of different magnon modes, we compared our experimental data to calculations of the magnon spectra in GdIG. However, the temperature and magnetic field dependence of the MMR amplitude cannot straightforwardly be attributed to changes in the thermal magnon population. We therefore proposed a phenomenological model based on transport properties and damping related to the magnetic order of the Gd sublattice, which can qualitatively reproduce the experimental observations close to the compensation temperature. However, this model requires further verification and numerous factors (mode occupancy, magnon group velocity, damping, interactions between magnon modes etc.) need to be taken into account for a detailed understanding of the transport behavior in GdIG, making this an interesting topic for future investigations.

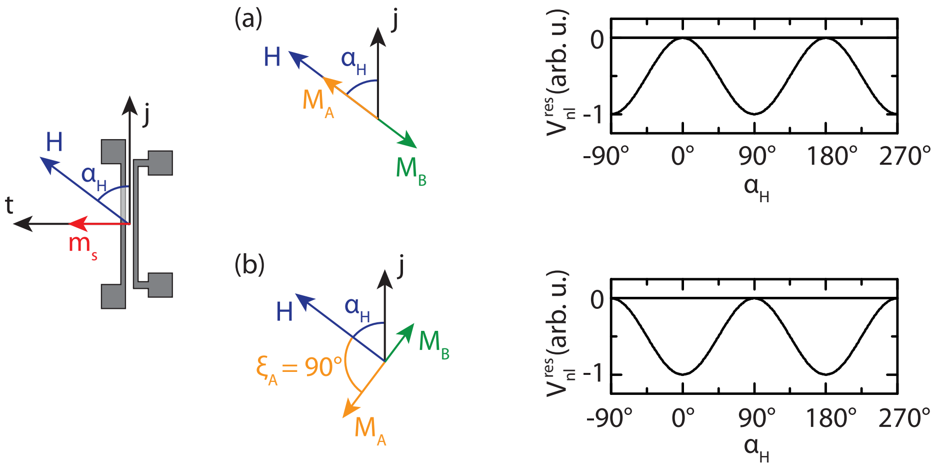

Figure 9.4: Expected dependence of the non-local resistive voltage $V_{\mathrm{nl}}^{\mathrm{res}}$ on the angle α_{H} between the applied magnetic field $\mathbf{H}$ and the current direction $\mathbf{j}$. (a) For a collinear two-sublattice ferrimagnet the magnon injection and detection are most efficient when the sublattice magnetizations $\mathbf{M}_X$ are perpendicular to the applied charge current, i.e. $\alpha_{\mathrm{H}} = 90°$. This configuration corresponds to $\mathbf{M}_X$ collinear to the spin accumulation $\mathbf{m}_s \perp \mathbf{j}$ originating from the spin Hall effect. (b) In the magnetic canting phase the sublattice magnetizations are no longer aligned with the external magnetic field. For canting angles $|\xi_A| = |\xi_B| = 90°$, a maximum MMR amplitude is therefore expected for $\alpha_{\mathrm{H}} = 0°$.

9.2 Magnetic canting phase of GdIG

In the previous section we focused on the MMR effect in the collinear phase of GdIG. However, GdIG also exhibits a magnetic canting phase around the compensation temperature T_{comp}, where the sublattice magnetizations are no longer collinear to the external magnetic field. In Sect. 4.2, we have shown that the local SMR effect is sensitive to the orientation of individual magnetic moments residing on different sublattices, such that a canting of the sublattice magnetizations leads to a phase shift of up to 90° of the SMR angular dependence. While the non-local MMR is based on magnon transport and is therefore strongly affected by the spin wave spectrum and transport properties, the magnon injection (and detection) efficiency also depends on the orientation of the magnetization in the ferrimagnet with respect to the direction of charge current $\mathbf{j}$ in the adjacent Pt (see Sect. 5.1). More specifically, the charge current along $\mathbf{j}$ induces an electron spin accumulation with magnetic moment $\mathbf{m}_s \parallel \mathbf{t}$ (red arrow in Fig. 9.4) due to the spin Hall effect (see Sect. 2.1). We can then describe the magnon injection as a scattering process at the Pt/FMI interface, i.e. one of the accumulated electron spins flips in the Pt and generates or absorbs a magnon in the collinear ferrimagnet, i.e. decreases or increases the net magnetization (see Sect. 5.1 for details). Experimental observations [3, 4] suggest that the transfer of magnetic moment is most efficient when the FMI magnetization is (anti)-parallel to the electron magnetic moment $\mathbf{m}_s$.

In order to discuss the MMR in a canted magnetic structure, we consider a model ferrimagnet with two antiferromagnetically coupled sublattices A and B. In the collinear phase, both magnetizations $\mathbf{M}_A$ and $\mathbf{M}_B$ are aligned (anti)-parallel to the external magnetic field and the MMR amplitude therefore reaches a maximum absolute value for $\mathbf{H} \perp \mathbf{j}$ ($\alpha_\mathrm{H} = 90°$), i.e. $\mathbf{M}_{A,B} \parallel \mathbf{m}_s$. On the other hand, no non-local signal is detected for $\alpha_\mathrm{H} = 0°$, i.e. when $\mathbf{H} \parallel \mathbf{j}$. The corresponding $\sin^2(\alpha_\mathrm{H})$ angular dependence is depicted in Fig. 9.4 (a)[2]. In the canted phase however, the sublattice magnetic moments are no longer collinear to the applied magnetic field. We consider a perpendicular alignment of both sublattice magnetizations $\mathbf{M}_A$ and $\mathbf{M}_B$ with respect to the external magnetic field as sketched in Fig. 9.4 (b), i.e. a canting angle of $\xi_{A,B} = \pm 90°$. Assuming that the spin wave spectrum and overall magnon excitation efficiency for a canting angle of 90° is qualitatively similar to the collinear phase, the MMR amplitude is also finite for the perpendicular moment configuration. However, we now expect a 90° shift of the MMR angular dependence (similar to what is observed in the local SMR signal in Sect. 4.2), as represented in Fig. 9.4 (b): for $\alpha_\mathrm{H} = 90°$, the sublattice magnetizations $\mathbf{M}_X$ are oriented along $\mathbf{j}$, such that the MMR amplitude vanishes, while a finite absolute signal is expected for $\alpha_\mathrm{H} = 0°$. It is important to point out that magnetic excitations in a real canting phase, where the sublattice magnetizations are tilted by different angles and are no longer collinear, are much more complex. The scenario sketched here corresponds to an extreme case, based on which we can motivate the importance of studying the influence of the sublattice magnetization orientation on the non-local response. For a better understanding of the MMR effect in a non-collinear magnetic configuration, atomistic calculations of the GdIG magnon spectra in the canted phase (similar to those displayed in Fig. 9.3 for the collinear phase) are of great interest. However, such calculations are challenging and currently not available.

First insights into the MMR response in a magnetic canted phase, in particular the angular dependence, can however be gained from experiments. The sample studied in Sect. 9.1 is unfortunately not suited for such an investigation, since both the SMR and MMR amplitude vanish around T_comp and therefore the angular dependence could not be analyzed. While the presence of a SMR sign change (and/or phase shift) has been observed consistently in different PLD-grown compensated garnet/Pt heterostructures [30, 55], the origin of the vanishing SMR amplitude at the compensation point in the LPE-grown GdIG film investigated in Sect. 9.1 is not well understood to this point. The lack of a sign change may be attributed to the formation of magnetic domains in the ferrimagnet, e.g. regions exhibiting different canting angles, such that the SMR modulation vanishes on average. Possible causes for such a domain formation are inhomogeneities in the ferrimagnet either due to the LPE growth process or to the surface treatment used for the preparation of a high quality *ex-situ* interface (see Sect. 6.1) [48]. A systematic

---

[2] The negative sign of the non-local voltage shown here is consistent with experimental observations in the measurement configuration used throughout this thesis.

study of the SMR in samples obtained via different fabrication methods is therefore of interest to understand the observed behavior in the canting phase.

Since our PLD-grown samples typically have a thickness of 100 nm at the most, the nanofabrication described in Sect. 6.1 needs to be adapted to thinner FMI films, in order to conduct MMR experiments in PLD-grown thin films. In particular, the etching time must be optimized such that the Pt layer can be structured, without etching too far into the FMI thin film and thereby suppressing the magnon transport channel. As first attempts in fabricating a functional non-local device based on a PLD-grown FMI/Pt heterostructure were unsuccessful, further optimization of the nanostructuring method is necessary in the future.

We can however study a GdIG sample grown via a third method, namely a single crystalline bulk sample with a thickness of several 100 µm grown via traveling solvent floating zone (TSFZ) [161] (see Ref. [48] for details on the growth method). The crystal is covered with an 8 nm thick *ex-situ* Pt layer deposited via electron beam evaporation[3] (see Sect. 6.1). The compensation temperature is determined via SQUID magnetometry and we find $T_{\mathrm{comp}} = 289\,\mathrm{K}$, which is consistent with the literature value [15]. We measure the local and non-local voltage signal in a nanostructure identical to the one studied in Sect. 9.1, i.e. two parallel Pt strips with edge-to-edge separation $d = 200\,\mathrm{nm}$ and strip width $w = 500\,\mathrm{nm}$, for temperatures $10\,\mathrm{K} \leq T \leq 300\,\mathrm{K}$ and magnetic fields $1\,\mathrm{T} \leq \mu_0 H \leq 7\,\mathrm{T}$. We first compare the SMR and MMR response of the bulk GdIG sample in the collinear magnetic phase, i.e. far away from the compensation temperature, to our previous results. Figure 9.5 displays the corresponding ADMR measurements for $V_{\mathrm{loc}}^{\mathrm{res}}$ and $V_{\mathrm{nl}}^{\mathrm{res}}$ at different temperatures $T = 70\,\mathrm{K} < T_{\mathrm{cross}}$, $T_{\mathrm{cross}} < T = 270\,\mathrm{K} < T_{\mathrm{comp}}$ and $T_{\mathrm{comp}} < T = 298\,\mathrm{K}$. The local SMR response $V_{\mathrm{loc}}^{\mathrm{res}}$ (panels (a), (c) and (e) in Fig. 9.5) follows the expected $\cos^2(\alpha_{\mathrm{H}})$ dependence[4], similar to the results obtained in Fig. 9.1 (b). The SMR ratio calculated according to Eq. (4.2) is plotted in Fig. 9.6 (a) as a function of temperature for all studied magnetic fields. The overall SMR temperature dependence looks very similar to the one observed in the PLD and LPE-grown GdIG samples (see Fig. 4.1 and 9.2, respectively), with a decrease of the SMR ratio towards low temperatures. We also note that only few data points are available in the vicinity of $T_{\mathrm{comp}} = 289\,\mathrm{K}$ (marked by a red vertical line in Fig. 9.6 (a) and (b)), where the magnetic canting phase is expected (see phase diagram Fig. 3.2). The lack of data points is due to the fact that in this temperature range the SMR data can no longer be fitted with a $\cos^2(\alpha_{\mathrm{H}})$ function as we will discuss later on in this section (see Fig. 9.7).

For now, we first turn to the non-local MMR measurements in the collinear phase of GdIG. The ADMR measurements conducted on the non-local strip for the different temperature ranges are displayed in Fig. 9.5 (b), (d) and (f): $V_{\mathrm{nl}}^{\mathrm{res}}$ follows the same angular

---

[3] Sample grown by Nynke Vlietstra and Andreas Erb, WMI.

[4] The small deviations from a perfect $\cos^2(\alpha_{\mathrm{H}})$ behavior (linear drift and jumps at certain angles) are attributed to temperature instabilities while rotating the sample in the VTI of the cryostat.

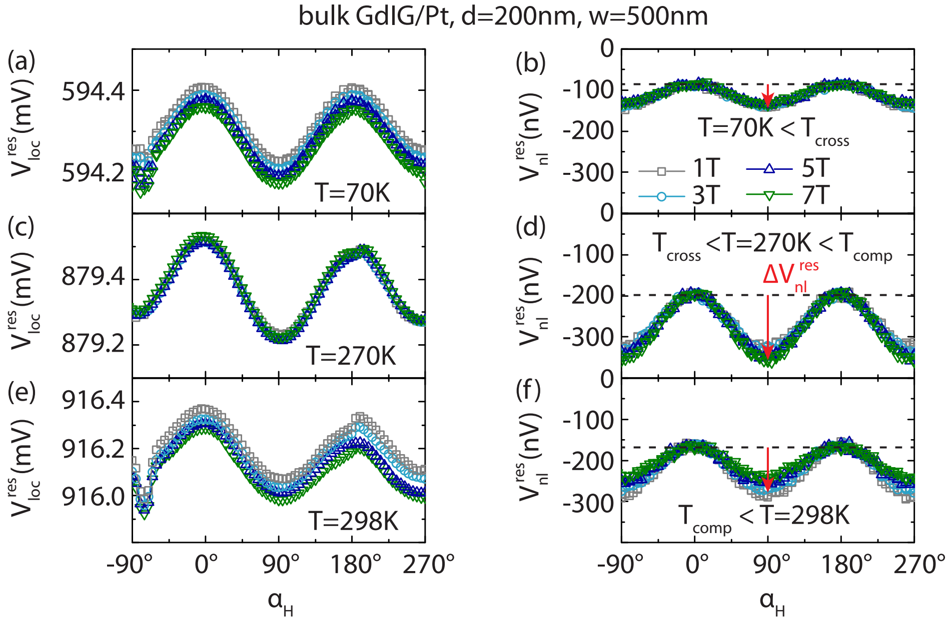

Figure 9.5: ADMR measurements of the local and non-local voltage conducted in a bulk GdIG/Pt sample with two Pt strips with an edge-to-edge separation $d = 200\,\mathrm{nm}$ and strip width $w = 500\,\mathrm{nm}$. The measurements were conducted for magnetic fields $1\,\mathrm{T} \leq \mu_0 H \leq 7\,\mathrm{T}$ at different temperatures $T = 70\,\mathrm{K} < T_{\mathrm{cross}}$ (a)-(b), $T_{\mathrm{cross}} < 270\,\mathrm{K} < T_{\mathrm{comp}}$ (c)-(d) and $T_{\mathrm{comp}} < 298\,\mathrm{K}$ (e)-(f). The black dashed lines in panels (b), (d) and (f) mark the finite negative offset of the non-local signal and the red arrows represent the extracted MMR amplitude $\Delta V_{\mathrm{nl}}^{\mathrm{res}}$.

dependence as in previous non-local measurements, i.e. a maximum absolute value is obtained when the magnetization (in the collinear phase) is perpendicular to the Pt strip for $\alpha_{\mathrm{H}} = 90°$. However, $V_{\mathrm{nl}}^{\mathrm{res}}(\alpha_{\mathrm{H}} = 0°)$ does not vanish as expected from previous experiments (see Sect. 6.3.1 and 9.1 [4]), but exhibits a finite negative offset marked by the dashed black horizontal line in Fig. 9.5. We attribute this offset to a small leakage current between the two Pt strips, stemming from a residual conductivity either in the FMI or at the sample surface. The amplitude of the non-local MMR signal $\Delta V_{\mathrm{nl}}^{\mathrm{res}}$ is therefore extracted as the modulation amplitude $V_{\mathrm{nl}}^{\mathrm{res}}(90°) - V_{\mathrm{nl}}^{\mathrm{res}}(0°)$ represented by the red arrows in Fig. 9.5. In analogy to Sect. 9.1, we plot $-\Delta V_{\mathrm{nl}}^{\mathrm{res}}$ as a function of temperature in Fig. 9.6 (c) for different magnetic fields $1\,\mathrm{T} \leq \mu_0 H \leq 7\,\mathrm{T}$. The temperature and magnetic field dependence of the MMR amplitude confirms the observations presented in Sect. 9.1, revealing a field suppression at low temperatures, an enhancement with field between T_{cross} and T_{comp}, and a stronger suppression above the compensation temperature. In order to clarify this point we extract the relative field dependence $\delta(7\,\mathrm{T})$ according to Eq. (9.1) as a function of temperature and plot the result in Fig. 9.6 (e). The gray shaded area around the compensation temperature (red vertical line) corresponds to the magnetic canting phase, where the MMR amplitude and field dependence cannot be calculated in a reliable

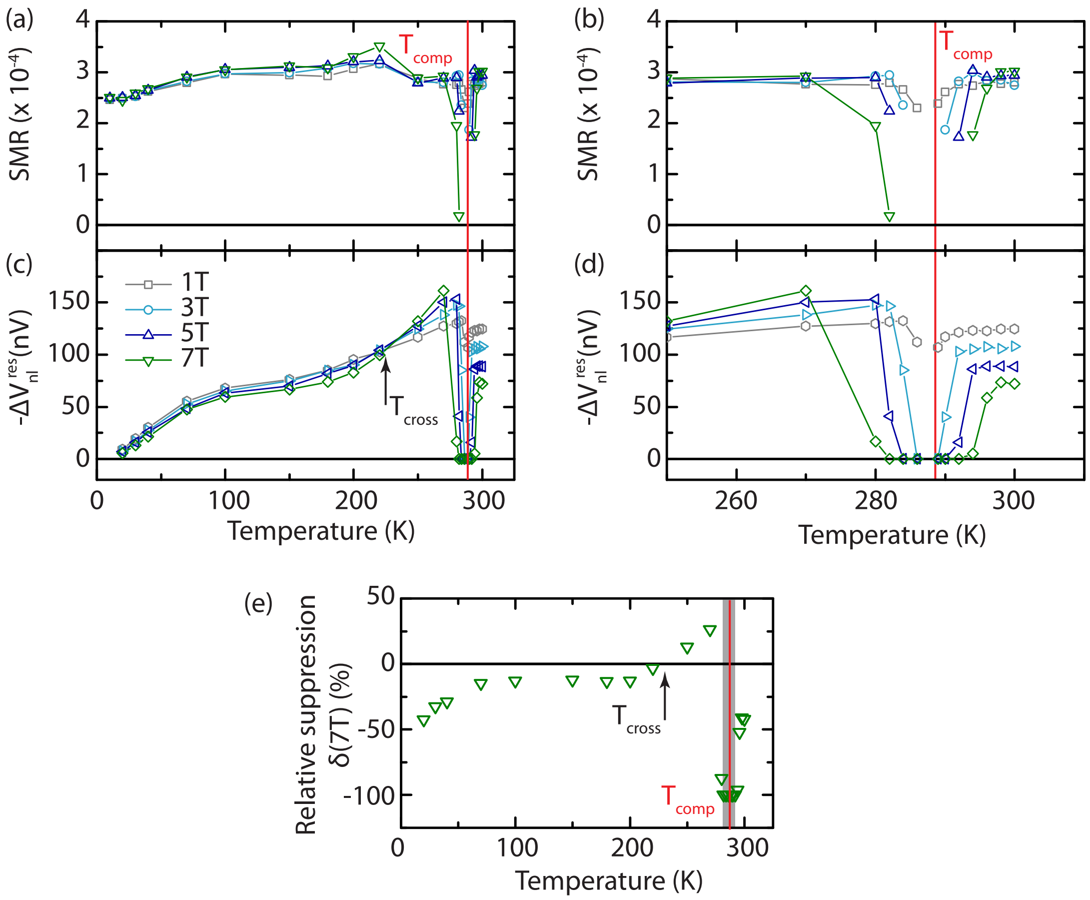

Figure 9.6: (a) SMR amplitude extracted from $\cos^2(\alpha_\mathrm{H})$ fits to the ADMR measurements in Fig. 9.5 as a function of temperature for magnetic fields $1\,\mathrm{T} \leq \mu_0 H \leq 7\,\mathrm{T}$. The compensation temperature is marked by the red vertical line. (b) Close-up of the SMR amplitude in the compensation region. The missing points correspond to temperatures, where no clear $\cos^2(\alpha_\mathrm{H})$ dependence could be fitted (see Fig. 9.7). (c) Negative non-local voltage amplitude $-\Delta V_\mathrm{nl}^\mathrm{res}$ extracted from ADMR measurements as a function of temperature for different magnetic fields. The temperature T_cross, where the field dependence changes from suppression to enhancement is marked by a black arrow. (d) Close-up of the non-local signal amplitude around T_comp: the temperature range in which the MMR effect goes to zero broadens with increasing magnetic field, consistent with the shape of the expected canting phase. (e) Relative field dependence $\delta(7\,\mathrm{T})$ of the MMR amplitude $\Delta V_\mathrm{nl}^\mathrm{res}$ calculated according to Eq. (9.1). $\delta < 0$ (> 0) corresponds to a suppression (enhancement) of the signal with magnetic field. The gray shaded area around T_comp marks the canting region, where the suppression cannot be calculated in a reliable way, as the non-local signal amplitude goes to zero.

way, as we will discuss in more detail in the following. This independent confirmation of the characteristic temperature and magnetic field dependence of the MMR amplitude in the collinear phase of a bulk GdIG sample further supports the results presented in Sect. 9.1.

We now turn to the SMR and MMR measurements in the temperature range close to T_{comp}, where we expect a magnetic canting phase as shown in the calculated GdIG phase diagram displayed in Fig. 3.2. The ADMR measurements of $V_{\mathrm{loc}}^{\mathrm{res}}$ and $V_{\mathrm{nl}}^{\mathrm{res}}$ recorded at $T = 284\,\mathrm{K}$ and $288\,\mathrm{K}$ for different magnetic fields are depicted in Fig. 9.7. At these temperatures, which are close to the magnetic compensation temperature $T_{\mathrm{comp}} = 289\,\mathrm{K}$, the local as well as non-local voltage no longer follow a perfect $\cos^2(\alpha_{\mathrm{H}})$ dependence. Figure 9.7 (a) displays the local signal $V_{\mathrm{loc}}^{\mathrm{res}}$ at $T = 284\,\mathrm{K}$. For better visibility, the curves recorded at different magnetic fields are offset by a constant value in vertical direction. At $\mu_0 H = 1\,\mathrm{T}$ and $3\,\mathrm{T}$ (gray and light blue symbols in Fig. 9.7 (a)), $V_{\mathrm{loc}}^{\mathrm{res}}$ still follows a 180° symmetric angular dependence even though deviations from a simple $\cos^2(\alpha_{\mathrm{H}})$ function are observed, e.g. abrupt jumps in the angular dependence at $\mu_0 H = 3\,\mathrm{T}$. A possible origin for such a behavior is an increase of the anisotropy field close to the compensation point [162]: this can be understood intuitively since around T_{comp} the net magnetization M decreases and the crystalline anisotropy field of the general form $H_{\mathrm{ani}} \propto K/M$, where K is the anisotropy constant, may become comparable to the external magnetic field. The simultaneously recorded non-local signal plotted in Fig. 9.7 (b), follows a qualitatively similar behavior, mostly reproducing the features observed in the local response. These results already suggest that similar to the SMR, the MMR is indeed sensitive to the magnetic structure and anisotropy in the FMI.

At higher magnetic fields of $\mu_0 H = 5\,\mathrm{T}$ and $7\,\mathrm{T}$ however, the local magnetoresistive response is no longer SMR-like and the angular dependence reveals several jumps, which cannot be related straightforwardly to a crystalline anisotropy[5]. This behavior indicates that the magnetic system does not follow the magnetic field in a coherent way, as one would expect for a single domain state. In this context, we use the term “domain” to describe regions with similar magnetic configuration and canting angle with respect to the external field. A multi-domain state on the other hand exhibits regions with different canting angles of the sublattice magnetic moments. This can for example be caused by inhomogeneities (varying T_{comp} throughout the crystal) or impurities in the ferrimagnet [164]. Furthermore, the phase diagram and subsequently the magnetic moment configuration and canting angles at fixed field and temperature may depend on the orientation of the magnetic field with respect to the crystallographic axes. This was already observed experimentally in dysprosium iron garnet [165]. In particular, when rotating the magnetic field in the sample plane, some domains can grow at the expense of others, such that the domain

---

[5] In the simplest model, we expect a contribution from cubic crystalline anisotropy in GdIG (and other iron garnets) [71], leading to a 60° symmetry of the in-plane angular dependence for the (111) oriented crystal studied here [163]. The angular dependence observed in Fig. 9.7 however is much more complex.

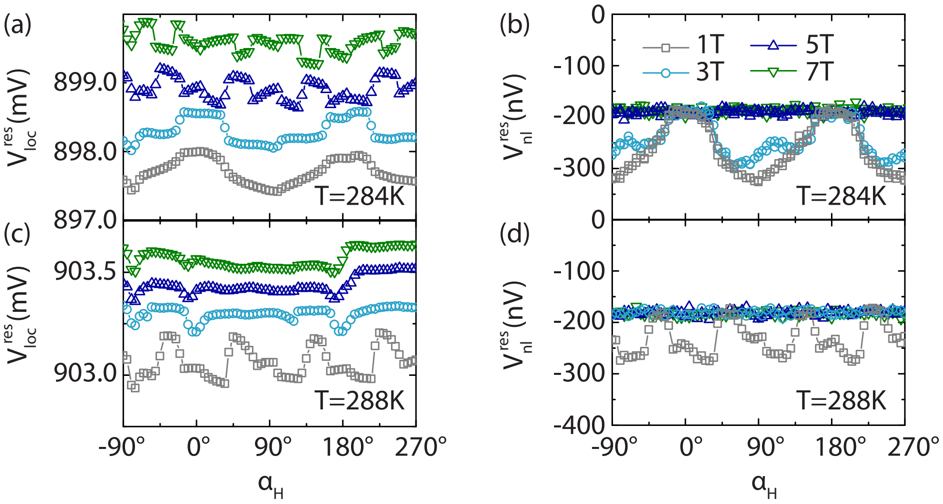

Figure 9.7: Local ADMR measurement at $T = 284\,\mathrm{K}$ (a) and $288\,\mathrm{K}$ (c) for different magnetic fields. $V_{\mathrm{loc}}^{\mathrm{res}}$ no longer follows the typical SMR $\cos^2(\alpha_{\mathrm{H}})$ dependence, but reveals anisotropic behavior and abrupt jumps when rotating the magnetic field in the sample plane. For better visibility, the curves are offset by a constant value in vertical direction. (b) and (d) Non-local voltage $V_{\mathrm{nl}}^{\mathrm{res}}$ measured in the detector strip: at low magnetic fields the non-local voltage reproduces the same features as the local signal. With increasing field, when no clear angular dependence is discernible in the SMR response, the non-local MMR is constant. This behavior is most likely related to domain formation or anisotropies in the FMI. The remaining negative offset of $V_{\mathrm{nl}}^{\mathrm{res}}$ may be attributed to an electrical cross-talk between the injector and detector strip.

distribution is no longer constant during one ADMR measurement, leading to abrupt jumps and hysteretic behavior.

Interestingly, for $\mu_0 H = 5\,\mathrm{T}$ and $7\,\mathrm{T}$, the MMR does not reproduce the features observed in the local signal, but stays constant within the noise level. Note that the curves shown in Fig. 9.7 (b) correspond to the raw data and are not shifted in vertical direction. The constant non-local signal observed at high fields therefore coincides with the value $V_{\mathrm{nl}}^{\mathrm{res}}$ measured at $\alpha_{\mathrm{H}} = 0°$, where a vanishing MMR is expected for a collinear magnetic system. This strongly suggests that the MMR indeed vanishes at $5\,\mathrm{T}$ and $7\,\mathrm{T}$ and is simply offset by a finite value stemming from a cross-talk from the injector strip, similar to the one observed in Fig. 9.5. A vanishing non-local modulation amplitude implies that either the magnon injection becomes inefficient when the magnetic system is in a canted or multi-domain state or that the magnon transport is suppressed by the domain formation, for example due to additional scattering processes at the domain walls.

The second set of ADMR measurements at $T = 288\,\mathrm{K} \approx T_{\mathrm{comp}}$ displayed in Fig. 9.7 (c) and (d) confirms these observations: for the lowest magnetic field of $1\,\mathrm{T}$ the SMR and MMR response reveal similar angular dependencies featuring four peaks in the voltage modulation. For fields above $3\,\mathrm{T}$, virtually no angular dependence is visible in the SMR response and the MMR amplitude goes to zero (with a finite offset again attributed to cross-talk).

Since the SMR response at high magnetic fields in Fig. 9.7 cannot be fitted with a $\cos^2(\alpha_\mathrm{H})$ function, no SMR amplitude can be extracted close to the compensation point. This is reflected in the lack of data points in the close-up of the SMR temperature dependence around T_comp in Fig. 9.6 (b). For the MMR however, we extract $\Delta V_\mathrm{nl}^\mathrm{res} = 0$ when the non-local voltage is constant as a function of the magnetic field orientation (see close-up of the MMR temperature dependence in Fig. 9.6 (d)). The temperature range where the MMR amplitude goes to zero broadens with increasing magnetic field, confirming that the vanishing MMR effect is related to the canting phase. The results presented here are therefore consistent with our previous hypothesis that the vanishing MMR signal in the LPE GdIG/Pt sample in the vicinity of T_comp (Sect. 9.1) can be attributed to inhomogeneities or magnetic domains in the FMI within the magnetic canting phase, which also affect the local SMR response.

Up to now we assumed that the MMR non-local voltage always vanishes at a certain magnetic field orientation. In a collinear magnet this is reasonable since in YIG/Pt no MMR is detected when the magnetization is parallel to the current direction (Sect. 6.3.1). However, it is conceivable that in a canted ferrimagnet, magnons can be injected for all magnetic field orientations if the configuration $\mathbf{M}_X \parallel \mathbf{j}$, i.e. all sublattice moments are oriented along $\mathbf{j}$, no longer occurs. In this case, a finite non-local voltage is expected for all angles α_H. The modulation of the non-local amplitude then reflects the different injection efficiencies which depend on the magnetic field orientation. The observed negative MMR offset in the canting phase may therefore be related to both magnon injection and an electric cross-talk from the injector. While the former should only occur in the canting phase, i.e. in a specific temperature range, the latter also exhibits a non-monotonous temperature dependence (see dashed line in Fig. 9.5). Since both depend on temperature in a non-trivial way, the two contributions cannot be disentangled easily. Determining an offset caused by angle independent magnon injection requires MMR measurements in a sample where no offset is observed in the collinear phase above and below T_comp. Such measurements are subject to future investigations.

Similar to the LPE-grown GdIG film studied in Sect. 9.1, the single crystalline bulk sample does not reveal a phase shift or sign change of the SMR in the canting phase. Since the latter was only observed in PLD-grown GdIG thin films with an *in-situ* Pt layer on top (see Sect. 4.2, and Ref. [55]), we fabricate another GdIG/Pt sample: we use an additional GdIG bulk sample cut from the same crystal as in the measurements discussed above and deposit a 65 nm thick GdIG film on top via PLD. Subsequently, a 5 nm Pt film is deposited *in-situ* on top of the PLD GdIG film (see Sect. 3 for details). The sample

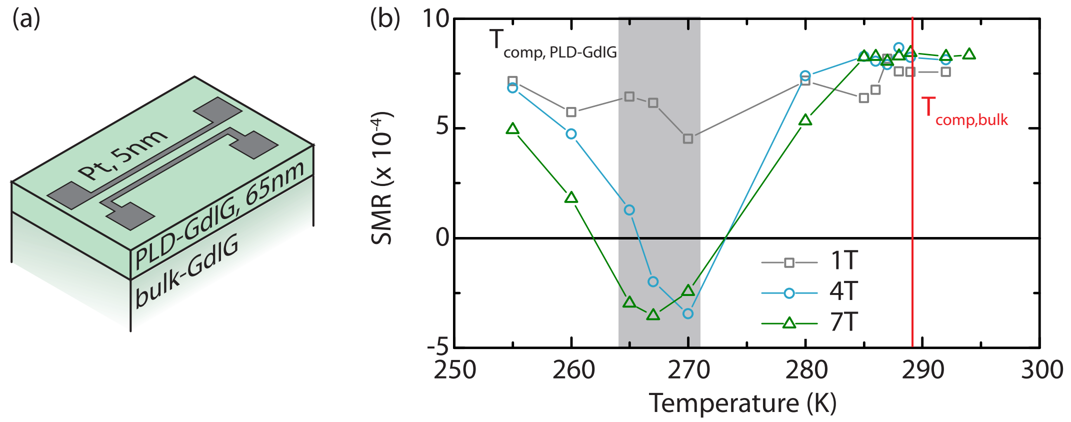

Figure 9.8: (a) Heterostructure consisting of a GdIG thin film grown via PLD onto a single crystalline bulk GdIG substrate and covered *in-situ* with 5 nm of Pt. The Pt layer is structured into two parallel strips as described in Sect. 6.1. (b) SMR amplitude extracted from ADMR measurements in the depicted sample as a function of temperature close to the compensation region. For magnetic fields above 4 T, a sign change of the SMR amplitude is clearly visible around $T = 267\,\mathrm{K}$, which we relate to a canted configuration in the PLD grown thin film. The compensation point $T_{\mathrm{comp,bulk-GdIG}} = 289\,\mathrm{K}$ of the bulk GdIG does not match the SMR sign change, confirming the notion that the SMR is sensitive to the GdIG layer directly at the interface, as asserted in Sect. 2.2 and 4.1.

is then nanopatterned as described in Sect. 6.1 and a sketch of the finished structure is depicted in Fig. 9.8 (a)[6].

Figure 9.8 (b) displays the measured SMR amplitude extracted from ADMR measurements as a function of temperature for different magnetic fields $\mu_0 H = 1\,\mathrm{T}$, $4\,\mathrm{T}$ and $7\,\mathrm{T}$. In analogy to the PLD-grown InYGdIG thin film covered with an *in-situ* Pt layer studied in Sect. 4.2, we observe a sign change of the SMR around a temperature $T = 267\,\mathrm{K}$. Note that no sign change is observed for $\mu_0 H = 1\,\mathrm{T}$, indicating that the transition into the canting phase in this particular sample occurs between 1 T and 4 T. Interestingly, the SMR sign change does not coincide with the compensation temperature $T_{\mathrm{comp,bulk}} = 289\,\mathrm{K}$ of the bulk GdIG obtained from SQUID magnetometry (red vertical line in Fig. 9.8 (b)). We therefore relate the SMR sign change temperature to the compensation point and canting region of the thin film $T_{\mathrm{comp,PLD-GdIG}} \approx 267\,\mathrm{K}$ (gray shaded region in Fig. 9.8 (b)), which can deviate from the bulk value [90] in PLD films. This observation confirms our previous assertion that the SMR is not sensitive to the magnetic structure of the bulk material, but probes the top layer of the FMI, directly at the Pt/FMI interface (see Sect. 2.2 and 4.1).

While the local SMR measurements in this heterostructure yield reasonable results, non-local MMR measurements were not possible: we found $V_{\mathrm{nl}}^{\mathrm{res}}$ of the order of several

---

[6] Sample grown by Nynke Vlietstra and Andreas Erb, WMI.

10 µV (much larger than typical MMR modulation amplitudes of a few 100 nV) suggesting a SMR type signal due to a finite conductivity between the Pt strips. This behavior may be attributed to a residual conductivity, similar to the one observed in Fig. 9.5, or to a metallic short between the Pt strips, where the etching process was not successful.

While we were not able to measure the MMR effect in a sample which exhibits a SMR sign change or phase shift, the variety of local and non-local responses in the canting phase of GdIG samples obtained via different fabrication methods gives important additional insights into the physics behind the two effects. In the case of the SMR response, we find that a clear sign change is only observed in GdIG thin films grown via PLD where the Pt is deposited *in-situ*. In contrast, in the LPE GdIG film and in the bulk sample the SMR goes to zero in the canting phase instead of changing sign, or no longer follows a $\cos^2(\alpha_\mathrm{H})$ angular dependence. Clearly, systematic experiments comparing many samples fabricated via different routes (PLD, LPE, bulk crystal growth, and combinations thereof) are required to unambiguously resolve the SMR and MMR behavior in the vicinity of T_comp. Such a systematic set of experiments was beyond the scope of this thesis and is therefore left for future experiments. In particular, we attributed the lack of sign change in the SMR to the formation of a multi-domain state in the canting phase, such that the SMR response from different domains vanishes on average. Whether this domain formation and the observed anisotropy is connected to the crystalline quality, i.e. the growth process, or to the interface properties (*in-situ* vs *ex-situ*) can for instance be verified in future experiments by measuring the SMR effect in a GdIG thin film grown via PLD and covered with an *ex-situ* Pt layer.

The currently available results obtained from the measurements in a bulk-GdIG/Pt sample, however, already show that the SMR and MMR both reflect the magnetic structure (anisotropy, domain formation) of the FMI in a very similar way, confirming that in addition to the thermal magnon spectrum and transport properties, the orientation of the (sublattice) magnetizations in the FMI is also of key importance for the description of the MMR effect. The complexity of our findings presented in this section demonstrates that some aspects of magnon transport in ferrimagnetic insulators are not yet fully understood and the simultaneous study of SMR and MMR in non-collinear magnets is still of great interest for future investigations.

Chapter 10

Summary: non-local magnon transport in FMI/Pt bilayers

In the second main part of this thesis, we studied the diffusive transport of non-equilibrium magnons through a ferrimagnetic insulator (FMI) using two parallel, electrically isolated Pt strips deposited on top of the FMI for magnon injection and detection. The non-equilibrium magnons can be injected electrically (magnon mediated magnetoresistance, MMR) by driving a dc charge current through the injector strip or thermally (non-local spin Seebeck effect, SSE) via Joule heating in the injector. In both cases, the magnons are detected electrically as a non-local voltage in the second Pt strip. In the following, we give a short summary of the key findings on the transport of non-equilibrium magnons in two different ferrimagnetic insulators, namely YIG and GdIG.

For the description of the MMR, we distinguish between contributions from the magnon injection/detection efficiency and the magnon transport properties. In Chap. 6, we therefore studied the MMR in a YIG/Pt heterostructure as a function of temperature, external magnetic field and injector-detector distance. In the current theoretical model the injection efficiency crucially depends on the thermal magnon population. This is indeed reflected in our experimental observations revealing - for all studied distances - a decrease of the MMR amplitude with decreasing temperature and increasing magnetic field, i.e. when thermal magnons are suppressed. From the distance dependent MMR measurements we furthermore extracted a magnon diffusion length which decreases from $\lambda_m \approx 1.7\,\mu\mathrm{m}$ at 30 K to about 300 nm at room temperature. While a quantitative description of the MMR distance dependence is rather complex and requires further investigation, λ_m can be described as the average over the diffusion lengths of all contributing magnons, which again takes into account the thermal magnon population. This picture allows for a qualitative modeling of the observed temperature dependence of λ_m.

Based on our study of the MMR effect in YIG/Pt, we presented a proof-of-principle device with four Pt strips (three inputs and one output) allowing for the implementation of a magnon based majority gate in Chap. 7. The results were published in Appl. Phys. Lett. **109**, 022405 (2016) [123]. In this device the logical bit is encoded in the polarization of the magnon current reaching the detector/output and the logic operation is based on the incoherent superposition of magnons. In particular, this allows for clocking frequencies of the order of GHz and straightforward down-scaling without perturbing the functionality of the logic operation. This presents an advantage compared to recently proposed concepts for logic gates based on coherently excited magnons [152], where the logical bit is encoded in the phase or frequency of the spin waves, since for such a device, phase sensitive detection is required and down-scaling could strongly affect the performance of the device.

In addition to the electrical injection of non-equilibrium magnons, we studied the thermal magnon excitation, giving rise to a non-local spin Seebeck voltage in the detector strip (see Chap. 8). In contrast to the local SSE which, in a simple picture, is driven by a temperature difference between the phonon and magnon subsystems in the YIG film, the non-local SSE is dominated by the profile of the thermally generated magnon accumulation in the FMI. In other words, the length scale (in lateral direction) on which the non-local SSE can be detected is determined by scattering processes which do not conserve the magnon number and can therefore reach several µm in our samples. The local SSE on the other hand vanishes on the length scale where magnons and phonons thermalize (magnon conserving processes), which was calculated to be a few nm in the lateral direction [137].

In our experiments, we observe a sign change of the non-local SSE voltage at a characteristic injector-detector distance d_0, confirming recent experimental results by Shan *et al.* [139]. This sign change can also be attributed to the profile of the magnon accumulation in the YIG film. We furthermore find a strong temperature dependence of d_0 which suggests a complex dependence of the magnon accumulation on the YIG/Pt interface transparency and the magnon transport properties. The experimental non-local SSE results in YIG/Pt were published in AIP Adv. **7**, 085102 [116].

In Chap. 9, we studied the MMR effect in the collinear and canted magnetic phase of the compensated ferrimagnetic insulator GdIG. In the collinear phase, atomistic calculations reveal that two dominating magnon branches with opposite polarization are already thermally populated around $T = 100\,\mathrm{K}$, making GdIG an ideal candidate to study the influence of multiple magnon modes on the MMR effect. While the opposite polarization of these magnon modes gives rise to two temperature dependent sign changes in the local SSE in GdIG/Pt [83], no such sign change is observed in our MMR experiments. This suggests that in the MMR effect, the contributing magnon modes all carry the same effective magnetic moment, which is determined by the spin Hall electron spin accumulation in the Pt. However, we observed a qualitatively different magnetic field dependence of the MMR amplitude compared to previous observations in YIG/Pt. In particular, right below the magnetic compensation temperature T_{comp} in GdIG, we found a surprising enhancement of the MMR signal with increasing magnetic field. By comparing the experimental results to simulations of the GdIG magnon spectra, we conclude that this observation cannot straightforwardly be attributed to the temperature and magnetic field dependence of the thermal magnon population. As a possible explanation for this behavior we propose an additional damping introduced by the weakly ordered Gd moments in GdIG. Below T_{comp}, the Gd order can be increased by applying a magnetic field, thereby reducing the damping for the non-equilibrium magnons and leading to an increase of the detected MMR amplitude. While this hypothesis requires further investigation and verification, this could open the way towards an efficient manipulation of magnon transport via external magnetic fields. These results are being prepared for publication [129].

As discussed in Chap. 3.1.2, besides the collinear phase in GdIG, a canted magnetic phase can be induced close to the magnetic compensation temperature T_{comp} by magnetic fields accessible in experiments. While the MMR strongly depends on the magnon spectrum and the corresponding transport properties, the orientation of the magnetization is also relevant for the magnon injection efficiency. Since we have shown in Part I of this thesis that the local SMR is sensitive to the orientation of the sublattice magnetic moments, we also studied the influence of a non-collinear magnetic structure on the magnon transport, which has not been investigated up to now. First measurements as a function of the magnetic field orientation indeed suggest that, similar to the SMR, the MMR is also sensitive to anisotropy and domain formation in the ferrimagnet. In particular, the magnon injection and/or transport can apparently be suppressed by magnetic domain formation in the canting phase. Future MMR measurements in a sample exhibiting a canted single domain state giving rise a finite MMR amplitude may prove interesting, thereby providing access to the magnon excitation spectrum in a non-collinear magnetic phase.

Chapter 11

Summary and Outlook

In this thesis, we investigated spin transport in heterostructures consisting of a ferrimagnetic insulator (FMI) and the normal metal Pt. Driving a dc charge current $\mathbf{J}_c$ through a Pt strip gives rise to a transverse spin current $\mathbf{J}_s$ via the spin Hall effect (SHE) and leads to an electron spin accumulation with polarization $\boldsymbol{\sigma} \perp \mathbf{J}_c$ at the Pt/FMI interface. We showed that this spin accumulation can be used to electrically probe the (static) magnetic structure of the underlying FMI via the spin Hall magnetoresistance (SMR) or to generate magnons, i.e. collective spin excitations in the magnetically ordered system. These magnons diffuse through the FMI and can be detected in a second Pt strip, allowing for information transfer within the FMI. Here, we give a short summary of the key findings of this thesis, followed by propositions for future experiments in Sect. 11.2.

11.1 Summary

The first part of this thesis is dedicated to the SMR effect, which appears in FMI/metal heterostructures. We use Pt as the metal layer in all samples studied here, because it has large SHE and the fabrication of FMI/Pt bilayers has been optimized at the Walther-Meissner-Institute in the past years, yielding reproducible results. The SMR effect is well established in collinear ferrimagnets, such as yttrium iron garnet (YIG), where all sublattice magnetizations and the net magnetization $\mathbf{M}$ of the FMI are collinear to the applied magnetic field, allowing for a macrospin-based modeling. The SMR then manifests itself as a modulation of the Pt resistivity depending on the orientation of $\mathbf{M}$ with respect to the electron spin accumulation $\boldsymbol{\sigma}$ at the Pt/YIG interface. More specifically, the Pt resistivity follows a $\cos^2(\alpha_\mathrm{H})$ dependence on the angle α_H between the charge current direction $\mathbf{J}_c$ and the magnetization direction $\mathbf{M} \parallel \mathbf{H}$ in the FMI.

The focus of the SMR experiments presented in this thesis is on the investigation of non-collinear magnetic structures in magnetically ordered insulators. In particular, we expand the current SMR model (macrospin approximation) to a microscopic picture including the orientation of individual magnetic moments in the FMI. We demonstrate that in the more general, non-collinear case, the SMR can no longer be described based on the net magnetization orientation. Rather, the orientation and sublattice specific SMR efficiency of individual magnetic moments must be taken into account. As a prototype system, we discuss a two-sublattice ferrimagnet, where the magnetic moments exhibit a finite canting angle with respect to the applied field, and include the possibility of multiple energetically equivalent orientations for magnetic moments residing on one sublattice. In the special case of a collinear system such as yttrium iron garnet (YIG), the proposed model yields identical results to the current (macrospin) theoretical description and to the experimental results. However, in a canted magnetic phase, based on the microscopic model we predict a phase shift of the SMR angular dependence as well as a change of the resistivity modulation amplitude, compared to what is observed in a collinear configuration. The phase shift can reach up to 90° (also parametrized as a sign change of the SMR amplitude), depending on the canting angle and the microscopic magnetic structure.

In order to verify our model, we investigate the SMR in the collinear and canted magnetic phase of the compensated ferrimagnet gadolinium iron garnet (GdIG). We observe a sign change of the SMR amplitude in the canting phase, which can qualitatively be reproduced by the microscopic SMR model discussed above. These measurements confirm our theoretical predictions and represent a first step towards an electrical mapping of magnetic phase transitions and characterization of complex magnetic structures in insulators. The experimental results were published in Ref. [30]. Recent SMR measurements in the conical magnetic phase of Cu_2OSeO_3 (CSO) [59] and the finite SMR amplitude observed in the antiferromagnetic insulator NiO [166, 167] can also be qualitatively understood based on our model, demonstrating that the microscopic description proposed in this thesis is versatile and can be applied to a variety of magnetically ordered systems.

In Part II of this thesis, we study the diffusive transport of non-equilibrium magnons through the ferrimagnetic insulators YIG and GdIG. The magnon mediated magnetoresistance (MMR), which is based on electrical magnon injection, is first investigated in YIG in Chap. 6, using two parallel, electrically isolated Pt strips deposited on top of the FMI as magnon injector and detector. We distinguish two main contributions to the MMR, namely the magnon injection (and detection) efficiency and the transport properties. Microscopically, the injection process corresponds to the conversion of the spin Hall electron spin accumulation in the Pt to a magnon accumulation in the FMI and can be understood as follows: an electron spin flip at the injector Pt interface generates or absorbs a magnon in the adjacent FMI, leading to a non-equilibrium magnon population, which diffuses away from the injector. In order to gain further insight into the microscopic origin of the MMR, we measure the latter as a function of temperature, magnetic field and injector-detector distance. The observed dependence of the MMR amplitude on temperature and magnetic field magnitude is consistent with current theoretical models, which predict that the injection efficiency strongly depends on the thermal magnon population. We further assert that the experimentally extracted magnon diffusion length corresponds to an average diffusion length of all non-equilibrium magnons. Varying the temperature and applied magnetic field magnitude changes the frequency and k-vector of the contributing magnons as well as their specific transport properties, leading to a complex dependence of the overall diffusive behavior on temperature and applied magnetic field.

In Chap. 7, we propose a concept for information transfer and processing within a ferrimagnetic insulator based on our results on the MMR effect in YIG/Pt and implement a magnon majority gate using a YIG film with three Pt injectors and one detector on top. The logical bit is encoded in the magnetic excitations, i.e. in the polarization of the magnon current and the logic operation is performed via incoherent superposition of magnons in the ferrimagnet. Straightforward down-scaling and switching frequencies of the order of GHz make this device particularly promising for future spintronic applications. These results were published in Ref. [123].

In addition to the electrical injection of magnons, non-equilibrium magnons can also be generated thermally by locally heating the FMI, e.g. via Joule heating in the injector strip. The thermally excited non-equilibrium magnons also diffuse through the FMI and are detected electrically in the second Pt strip as a non-local voltage. This effect called non-local spin Seebeck effect (SSE) is studied in Chap. 8 in a non-local YIG/Pt structure and the results were published in Ref. [116]. We find that the non-local SSE voltage changes sign at a characteristic injector-detector distance d_0, giving an independent confirmation of recent experimental observations by Shan *et al.* [139]. This behavior can be qualitatively modeled based on the profile of the magnon accumulation, suggesting different physical origins of the non-local SSE and its local counter-part: it was already shown that the latter originates from a local difference between the magnon and phonon temperatures, which equilibrate within a few nm in lateral direction. The non-local SSE on the other hand is driven by diffusing non-equilibrium magnons and can therefore still be detected even for injector-detector separations of a few µm. We furthermore observe a strong temperature dependence of the sign change distance d_0 and attribute this to a complex interplay of the interface transparency and magnon transport parameters.

We then turn to a different, more complex material system, and present the first MMR measurements in GdIG/Pt in Chap. 9. GdIG is of particular interest for magnon transport studies since it exhibits two dominating magnon modes with opposite polarization (precession direction) which are thermally populated in the investigated temperature range. We assert that for a given electron spin flip process at the Pt/GdIG interface, magnons of one polarization can be excited while magnons of the opposite polarization can be absorbed. Assuming that both magnon modes contribute to transport, our experimental results indeed suggest that both modes carry the same effective magnetic moment direction and give rise to the same sign in the non-local voltage measured at the detector. We furthermore find a temperature and magnetic field dependence of the MMR amplitude in GdIG/Pt, that is qualitatively different from the one observed in YIG/Pt and attribute this to the magnetic field dependence of the magnon transport properties, which may be related to the additional Gd magnetic sublattice in GdIG. Further MMR measurements in the canted magnetic phase of GdIG reveal that - similar to the SMR effect - the MMR is also sensitive to the magnetic structure, in particular to anisotropies and magnetic domain formation.

11.2 Outlook

The spin Hall magnetoresistance measurements in the canted phase of a compensated ferrimagnet discussed in this thesis open the way towards an all electrical characterization of magnetic structures in different insulating magnetic materials. The SMR should prove particularly relevant for the characterization of antiferromagnetic insulators, which are gaining much interest for future applications, due to their lack of magnetic stray fields and robustness against external magnetic fields. As we have seen, the SMR is not determined by the net magnetization, but allows for a sublattice specific characterization of the magnetic structure based on a simple magnetotransport experiment. The SMR can thus be used to read out information encoded in the sublattice moment configuration of an antiferromagnetic insulator. Indeed, first SMR experiments in NiO/Pt bilayers have been put forward very recently [166, 167], underlining the importance of this topic. On a more general note, the SMR can also be exploited to map magnetic phases in complex systems, such as Cu_2OSeO_3 (CSO) [59], which exhibit collinear, helical/conical and even skyrmionic phases. Detecting these phases usually requires sophisticated methods such as x-ray circular dichroism (XMCD) or spin polarized neutron scattering. SMR measurements on the other hand could allow for a quick, purely electric characterization of materials with rich magnetic phase diagrams, since a distinct change in the angular dependence is expected at the magnetic phase transitions. A particular advantage of the SMR effect as an electrical measurement technique is that it can be straightforwardly scaled to nanometer-size structures, enabling to study canting or other non-collinear magnetic structures in very small samples or with a spatial resolution determined by the size of the Pt contact.

In order to quantitatively analyze the SMR response in more complex magnetic structures, which also exhibit strong anisotropies and/or domain formation, a better understanding of the microscopic origin of the SMR is important. In Sect. 2.3, we proposed a microscopic model including the individual contributions of magnetic moments residing on different sublattices. Based on this model, we predict that the SMR is also sensitive to asymmetries and anisotropies in the magnetic system, which either deform the angular dependence and/or lead to a canting angle dependent phase shift of the SMR response. In order to verify this hypothesis, SMR measurements can for example be conducted in samples with well known anisotropies. Uniaxial strain in a specific material can furthermore be induced (and switched off) in a controlled way, e.g. by placing the sample on top of a piezo-active material, enabling a comparison of the SMR response for the strained and relaxed state in one and the same sample. In our theoretical model we also discussed the possibility of domain formation in the canted phase, e.g. regions where magnetic moments on the same sublattice can be tilted either to the left or right with respect to the applied field. The presence of such domains is expected to affect the phase shift of the SMR angular dependence. In order to confirm this model, a direct reference measurement of the individual sublattice moment orientations, e.g. via spatially resolved XMCD measurements, is of great interest.

Up to now, we focused on the influence of the magnetic moment configuration on the SMR response. However, the sublattice or element-specific SMR amplitude or efficiency is not well understood to date. While the relevance of the Pt properties, such as spin diffusion length, spin Hall angle, etc. have been investigated extensively, the dependence of the SMR on the magnet properties have not been studied quantitatively. We found strong indications that the SMR mainly probes the topmost layer in the FMI. The exact length scale relevant for the SMR should be determined in future experiments via a systematic study of the SMR as a function of the FMI thickness. As the SMR is based on spin transfer torque, we furthermore predict that the transfer efficiency is proportional to the density of magnetic moments at the interface. Note that this corresponds to the number of spin transport channels per unit area and is also included in the spin mixing conductance [45]. Experimentally, the interface magnetic moment density can be varied by changing the crystalline termination of the sample [49, 51], or by systematically diluting the magnetic sublattices with non-magnetic ions. A promising candidate for such an experiment is YIG, which has two antiferromagnetically coupled Fe sublattices. Diluting the FeA sublattice (which contains the smaller number of magnetic ions) should decrease the magnetic moment density at the interface while simultaneously leading to an increase of the net magnetization. Based on the assumption that the SMR efficiency is indeed proportional to the magnetic moment density and unaffected by the net magnetization, we expect a decrease of the SMR amplitude. This experiment would further emphasize that the amplitude of the net magnetization does not play a dominant role for the SMR amplitude. While efforts to optimize the SMR amplitude are currently mainly based on the normal metal properties (spin Hall angle), one can also think about tailoring the magnetic moment density in order to increase the SMR efficiency. The SMR amplitude may also be element specific: while the experimental observations in GdIG can already be modeled qualitatively by taking into account only the Fe magnetic moments, a possible contribution of the Gd sublattice moments should be further investigated, in particular at high magnetic fields and low temperatures, where the Gd sublattice can be treated as exchange-enhanced paramagnetic moments [81].

We now turn to magnon transport experiments in a non-local configuration. In Chap. 9.1, we assumed that two magnon modes with opposite polarization can carry the same electrically injected magnetic moment, both giving rise to the same MMR sign at the detector. However, from the current experimental data, it is not possible to distinguish whether indeed both modes contribute and which one dominates the magnon transport. On

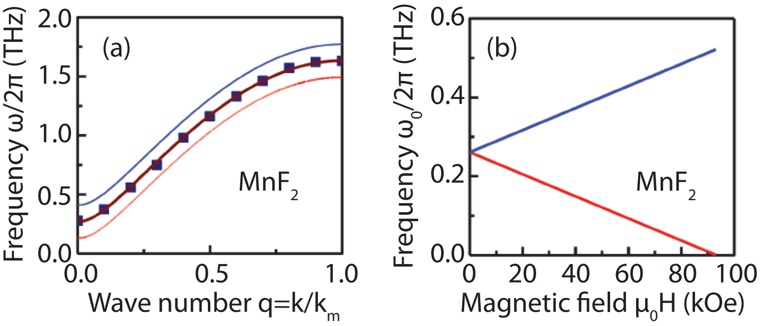

Figure 11.1: (a) Magnon frequencies in MnF$_2$ at low temperatures: the solid squares represent data obtained from inelastic neutron scattering and the solid curve is the dispersion relation of the two (degenerate) magnon modes calculated in Ref. [168] for zero magnetic field. For a finite field the degeneracy of the two magnon modes with opposite polarization is lifted as indicated by the red and blue thin curves representing the calculated dispersion relations at $\mu_0 H = 50\,\mathrm{kOe}$. (b) Frequency of the $k = 0$ magnon mode as a function of the applied magnetic field $\mu_0 H$. The two modes with opposite polarization split up with increasing external field. Figure taken from Ref. [168].

the other hand, contributions from magnon modes with opposite polarizations can be disentangled in spin Seebeck effect measurements, as recently demonstrated in GdIG/Pt [83], since they give rise to SSE voltages with opposite sign. Comparing the local SSE and non-local MMR signal in the same material system could therefore give first insights into the contributions of different magnon modes. In GdIG however, close to the compensation temperature, the two oppositely polarized magnon modes overlap and cross, such that interactions or coupling cannot be excluded. These can affect the overall transport properties, making a quantitative comparison with SSE measurements challenging. Alternatively, we propose to conduct MMR experiments in an antiferromagnetic insulator. Recently, experimental results of SSE measurements in Cr$_2$O$_3$ [169] and MnF$_2$ [170] have been put forward, accompanied by theoretical work based on the temperature and magnetic field dependence of the magnon spectra in MnF$_2$ and FeF$_2$ [168], which reproduces the experimental observations of Ref. [170]. In general, antiferromagnets exhibit two degenerate magnon modes with opposite polarization, which split up when an external magnetic field is applied. This is depicted in Fig. 11.1 (a) (Figure taken from Ref. [168]), where the full symbols represent experimental data taken at zero field. The blue and red curves are the calculated dispersion relations of the "+" and "−" polarized modes, respectively, for a finite magnetic field of 50 kOe: the magnon modes which are degenerate at zero field shift symmetrically towards higher/lower frequencies depending on their polarization. Figure 11.1 (b) displays the calculated field dependence of the $k = 0$ magnon mode frequency: the gap between the two modes increases with increasing magnetic field. At temperatures and magnetic fields, where the oppositely polarized antiferromagnetic modes are equally thermally populated, we expect a vanishing SSE signal [133, 168].

For the MMR however, this kind of compensation should not be observed, since both modes carry the same effective magnetic moment, such that we expect a finite MMR signal, even under conditions for which the SSE vanishes. Comparing the temperature and magnetic field dependence of both SSE and MMR effect in an antiferromagnetic insulator to the calculated thermal magnon spectrum should therefore allow for a more quantitative understanding of the electrical magnon injection process and subsequent diffusion. Furthermore, MMR measurements as a function of injector-detector distance and local SSE measurements as a function of the thickness of the antiferromagnet should also be conducted, in order to compare the relevant length scales of different magnon modes for the local SSE and MMR effect.

Besides the fundamental research point of view, magnon transport in antiferromagnets is also of great interest for applications, as discussed above. In this context, Bender *et al.* recently predicted a divergence of the spin conductance when sweeping the magnetic field across the spin-flop transition of the antiferromagnet [171]. This should be reflected in an enhancement of the non-local MMR voltage, which may prove relevant for applications. In addition to MMR measurements in the collinear phase of antiferromagnetic insulators, experiments close to the spin-flop phase should therefore be conducted to verify the theoretical prediction.

In addition to transport properties of electrically injected magnons, we also investigated the thermal injection of non-equilibrium magnons, i.e. the non-local SSE. As discussed in Chap. 8, the non-local SSE voltage measured at the detector in a YIG/Pt bilayer changes sign at a characteristic injector-detector separation d_0, which depends on the magnon accumulation profile [116, 139]. In this model, the influence of phonons is typically neglected. While the magnetic field dependence of the non-local SSE observed in Sect. 8.2 supports a magnon transport model, additional phonon contributions cannot be excluded a priori, since heat can also be carried by phonons through the YIG film or the substrate. We therefore suggest to conduct reference measurements in a YIG/Pt sample, where the YIG film in-between the Pt strips is etched away, down to the substrate, as sketched in Fig. 11.2. In such a sample, magnon transport between the strips is suppressed, while a phonon current J_{ph} can still transport heat through the substrate (dashed arrow in Fig. 11.2). The heating charge current (not shown in the figure) is driven through the left Pt strip, such that the temperature $T_{\mathrm{Pt,I}}$ of the Pt injector is larger than the YIG temperature $T_{\mathrm{YIG,I}}$ underneath, giving rise to a local SSE current $\mathbf{J}_{\mathrm{SSE}}^{\mathrm{ISHE}}$ in the Pt (see Sect. 5.4). Since the GGG substrate is closer to the heat source than the detector Pt strip which is not heated, we assume $T_{\mathrm{GGG}} > T_{\mathrm{YIG,D}} > T_{\mathrm{Pt,D}}$ on the right hand side. The corresponding temperature gradient at the detector YIG/Pt interface also gives rise to a local SSE signal. We would like to emphasize that in this scenario the temperature gradients at injector and detector are opposite, leading to opposite SSE voltages. It is therefore possible that the experimentally observed non-local SSE signal in YIG/Pt is a superposition of a local spin Seebeck effect at the detector (mediated by phonon heat

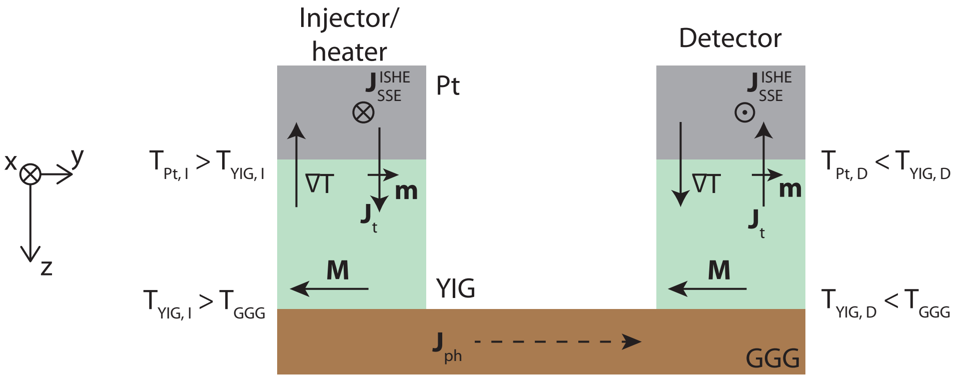

Figure 11.2: Sketch of a GGG/YIG/Pt heterostructure, where part of the Pt and YIG layers is etched away, down to the GGG substrate, leaving two separate YIG/Pt stacks. The left (injector) Pt strip is used as a heater, such that the Pt injector temperature $T_{\mathrm{Pt,I}}$ is larger than the YIG temperature $T_{\mathrm{YIG,I}}$. The induced temperature gradient ∇T at the YIG/Pt injector interface points along $-\mathbf{z}$ and gives rise to a ISHE current $\mathbf{J}_{\mathrm{SSE}}^{\mathrm{ISHE}}$ along $\mathbf{x}$ due to the local SSE. Magnons cannot flow into the GGG substrate, such that a magnon current between injector and detector is suppressed. However, heat can be carried through the GGG by a phonon current J_{ph}, such that at the detector the YIG temperature $T_{\mathrm{YIG,D}}$ is larger than the Pt temperature $T_{\mathrm{Pt,D}}$. The temperature gradients across the YIG/Pt interface and the ensuing local SSE voltages are therefore opposite in injector and detector.

transport across the substrate or the YIG film) and the non-local SSE originating from the magnon accumulation profile. Conducting SSE measurements in the structure depicted in Fig. 11.2 should allow for an estimation of the phonon contribution to the non-local SSE signal in typical YIG/Pt samples.

In experiments we furthermore observed a strong temperature dependence of the characteristic sign change distance d_0 [116]. In this context, the question arises which parameters play a relevant role for the magnon accumulation profile. Since the Pt resistance R and therefore the Joule heating power $P_h = RJ_c^2$ for a fixed current J_c in the injector strip increases with temperature, it is important to study the dependence of d_0 on P_h. In particular, the number of thermally excited magnons should increase with the heating power. However, the boundary conditions (position of the Pt/YIG and YIG/GGG interface) which determine the qualitative profile of the magnon accumulation remain unchanged. In order to check whether d_0 is affected by the heating power, i.e. the number of non-equilibrium magnons, the non-local SSE should therefore be measured as a function of the charge current J_c in the injector strip. On a similar note, reference measurements using a different heating method, e.g. laser heating, or using a metal with a

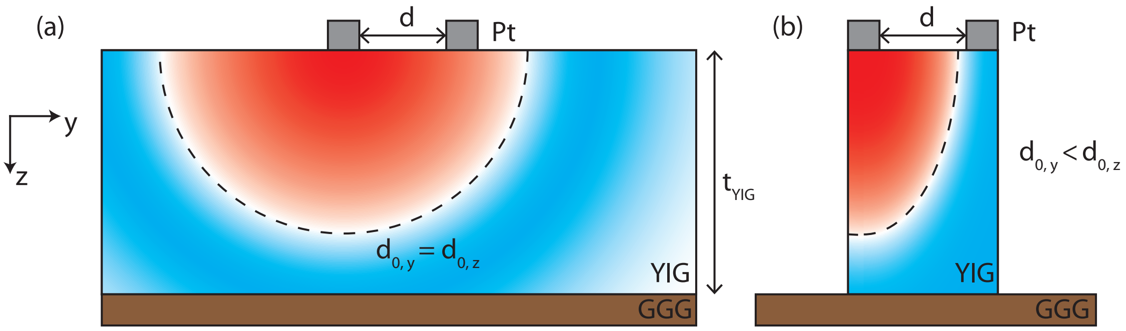

Figure 11.3: (a) Sketch of a Pt/YIG bilayer structure with a YIG thickness t_{YIG}: the Pt layer is structured into two parallel strips separated by a distance d. The left strip is used as a heater for thermal magnon injection and the corresponding non-local SSE voltage is detected in the right strip. The red and blue color in the YIG film represent a magnon depletion and accumulation, respectively, according to the model proposed in Ref. [139]. The black dashed line represents the characteristic distance d_0 where the transition from magnon depletion to accumulation takes place. This also determines the characteristic strip separation where the detected non-local SSE voltage changes sign. The white coloring close to the edge of the YIG film represents the thermal equilibrium, i.e. in this region the non-equilibrium magnons have relaxed. (b) Sketch of a YIG/Pt structure, where the YIG film was etched away outside of the injector and detector strips. The diffusing magnons are expected to accumulate at the right border of the YIG film since the magnons cannot cross this interface. In this case, we expect an opposite sign of the non-local SSE voltage compared to the unetched film in panel (a) where $d < d_{0,y}$.

small spin Hall effect (e.g. Al or Au [39]) as a heating strip, can be conducted to exclude any additional effects related to the spin accumulation at the Pt interface.

Once the relevant factors determining the profile of the magnon accumulation are understood, it is possible to manipulate the latter in a more controlled way. This can also be achieved by defining physical boundaries for the diffusing magnons. In the non-local YIG/Pt sample studied in this thesis, the lateral size of the sample (several mm) is very large compared to the strip separation or the film thickness of the order of micrometer, such that the magnons likely decay before reaching the edge of the sample. This is exemplarily sketched in Fig. 11.3 (a), where the red and blue color in the YIG film represent the magnon depletion and accumulation, respectively. The white coloring at the edge of the YIG film corresponds to the relaxed thermal equilibrium state, where there are no more non-equilibrium magnons. The characteristic length scale associated with this white region is given by scattering processes which do not conserve magnons. The non-local SSE signal is therefore expected to disappear for a detector placed on top of the white region. In the scenario depicted in Fig. 11.3 (a), the local and non-local SSE have the same sign, since $d < d_{0,y}$. By etching away the YIG film outside of the non-local structure as shown in Fig. 11.3 (b), one can change the boundary conditions in lateral directions. The diffusing magnons will accumulate at the end of the YIG film, i.e. just below the detector. In such a structure where the lateral dimensions are smaller than the YIG thickness, the magnon accumulation profile is no longer radially symmetric, such that $d_{0,y} < d_{0,z}$. We therefore expect a sign change of the non-local SSE even for $d < d_{0,z}$. This is an important experiment since it allows for a better understanding of how the magnon accumulation is affected by physical boundary conditions. Etching structures into the YIG film is a first step towards tailoring the magnon diffusion path (also for electrically injected magnons) and may be of interest for future spintronics applications.

Appendix A

List of samples

Sample name	Layer (thickness nm)	FMI growth	FMI Provider	Chapter
YY42	YAG/YIG(40)/Pt(4)	PLD	WMI	4.1
FPGIY001	YAG/InYGdIG(61.5)/Pt(3.6)	PLD	WMI	4.2
YIGM2-G3	GGG/YIG(2000)/Pt(10)	LPE	Matesy GmbH	6 and 8
YIGM2-G1	GGG/YIG(2000)/Pt(10)	LPE	Matesy GmbH	7
GIGQ1	GGG/GdIG($\approx$ 2600)/Pt(10)	LPE	Tohoku University	9.1
bGdIG1	GdIG/Pt(8)	TSFZ	WMI	9.2
bGdIG2	GdIG/GdIG(65)/Pt(5)	TSFZ/PLD	WMI	9.2

Table A.1: List of samples used for SMR (top) and non-local measurements (bottom). (FMI= ferrimagnetic insulator, PLD = pulsed laser deposition, LPE = liquid phase epitaxy, TSFZ = traveling solvent floating zone.)

Appendix B

SMR in the canted magnetic phase

Trigonometric identities

$$\begin{aligned}
\cos^2(x) &= \frac{1}{2} + \frac{1}{2}\cos(2x) && \text{(B.1)}\\
\sin^2(x) &= \frac{1}{2} - \frac{1}{2}\cos(2x) && \text{(B.2)}\\
\cos(x) + \cos(y) &= 2\cos(\frac{x+y}{2}) \cdot \cos(\frac{x-y}{2}) && \text{(B.3)}\\
\cos(x) - \cos(y) &= -2\sin(\frac{x+y}{2}) \cdot \sin(\frac{x-y}{2}) && \text{(B.4)}
\end{aligned}$$

Derivation of the resistivity angular dependence in the canting phase

The general resistivity expression considering SMR contributions from two sublattices A and B is given by

$$\rho = \rho_0 + \rho_{1,A}\cos^2(\alpha_{\mathrm{H}} + \xi_A) + \rho_{1,B}\cos^2(\alpha_{\mathrm{H}} + \xi_B) \tag{B.5}$$

Using the identities B.1, B.3 and B.4, we obtain

$$\begin{aligned}
\rho &= \rho_0 + \frac{1}{2}\rho_{1,A}(1 + \cos(2\alpha_{\mathrm{H}} + 2\xi_A)) + \frac{1}{2}\rho_{1,B}(1 + \cos(2\alpha_{\mathrm{H}} + 2\xi_B)) && \text{(B.6)}\\
&= \rho_0 + \frac{\rho_{1,A} + \rho_{1,B}}{2} + \frac{\rho_{1,A} + \rho_{1,B}}{4}\left(\cos(2\alpha_{\mathrm{H}} + 2\xi_A) + \cos(2\alpha_{\mathrm{H}} + 2\xi_B)\right) &&\\
&+ \frac{\rho_{1,A} - \rho_{1,B}}{4}\left(\cos(2\alpha_{\mathrm{H}} + 2\xi_A) - \cos(2\alpha_{\mathrm{H}} + 2\xi_B)\right) && \text{(B.7)}\\
&= \rho_0 + \frac{\rho_{1,A} + \rho_{1,B}}{2} + \frac{\rho_{1,A} + \rho_{1,B}}{2}\cos(2\alpha_{\mathrm{H}} + \xi_A + \xi_B) \cdot \cos(\xi_A - \xi_B) &&\\
&+ \frac{\rho_{1,A} - \rho_{1,B}}{2}\left(-\sin(2\alpha_{\mathrm{H}} + \xi_A + \xi_B) \cdot \sin(\xi_A - \xi_B)\right) && \text{(B.8)}
\end{aligned}$$

Assuming equal SMR efficiencies $\rho_{1,A} = \rho_{1,B} = \rho_1$ for both sublattices we obtain

$$\begin{aligned} \rho &= \rho_0 + \rho_1 + \rho_1 \cos(\xi_A - \xi_B) \cdot \cos(2\alpha_\mathrm{H} + \xi_A + \xi_B) && \text{(B.9)} \\ &= \rho_0 + \rho_1 (1 - \cos(\xi_A - \xi_B) + 2\cos(\xi_A - \xi_B) \cdot \cos^2(\alpha_\mathrm{H} + (\xi_A + \xi_B)/2)) && \text{(B.10)} \end{aligned}$$

which corresponds to Eq. (2.14).

We now derive Eq. (2.21), i.e. the resistivity angular dependence for sublattice A with magnetic moments tilted to the left (ξ_A) and right ($-\xi_A$) with respect to the applied magnetic field (see Sect. 2.3.3). Starting from Eq. (B.8), we obtain

$$\begin{aligned} \rho &= \rho_0 + \frac{\rho_{1,A,l} + \rho_{1,A,r}}{2} + \frac{\rho_{1,A,l} + \rho_{1,A,r}}{2} \cos(2\alpha_\mathrm{H}) \cos(2\xi_A) \\ &- \frac{\rho_{1,A,l} - \rho_{1,A,r}}{2} \sin(2\alpha_\mathrm{H}) \sin(2\xi_A) && \text{(B.11)} \\ &= \rho_0 + \frac{\rho_{1,A,l} + \rho_{1,A,r}}{2} + \frac{\rho_{1,A,l} + \rho_{1,A,r}}{2} \cos(2\alpha_\mathrm{H}) \cos(2\xi_A) \\ &- \frac{\rho_{1,A,l} - \rho_{1,A,r}}{2} \cos(2\alpha_\mathrm{H} - 90^\circ) \sin(2\xi_A) && \text{(B.12)} \\ &= \rho_0 + \frac{\rho_{1,A,l} + \rho_{1,A,r}}{2} + \frac{\rho_{1,A,l} + \rho_{1,A,r}}{2} \cos(2\xi_A) \left(2\cos^2(\alpha_\mathrm{H}) - 1\right) \\ &- \frac{\rho_{1,A,l} - \rho_{1,A,r}}{2} \sin(2\xi_A) \left(2\cos^2(\alpha_\mathrm{H} - 45^\circ) - 1\right) && \text{(B.13)} \end{aligned}$$

which corresponds to Eq. (2.21).

Energy landscape for a canted magnetic moment

We consider the canted two-sublattice ferrimagnet described in Sect. 2.3 and focus on the magnetic moments $\boldsymbol{\mu}_{A,k}$ residing on sublattice A. Assuming an isotropic system these magnetic moments are tilted by a canting angle ξ_A with respect to the applied magnetic field. As discussed in Sect. 2.3.4 the sublattice moments can assume any orientation on a cone with opening angle ξ_A (see Fig. B.1 (a)). This corresponds to a free energy landscape which is radially symmetric with respect to the applied magnetic field, as sketched in Fig. B.1 (c), where the color code represents the energy scale ranging from the global energy minimum (purple) to the maximum (red). Here, the magnetic field is applied along the **z**-direction and the magnetic moments have finite m_x and m_y components. In particular, the global energy minimum corresponds to a circle in the **x**-**y** plane with radius $m_x = m_y = \sin(\xi_A)$.

We now introduce a uniaxial anisotropy in the form of an easy **y**-**z** plane. This can be for example an in-plane anisotropy related to the demagnetization field in a thin film sample. In the free energy representation, the uniaxial anisotropy leads to two global minima in the easy plane, corresponding to the two purple wells in Fig. B.1 (d). In terms

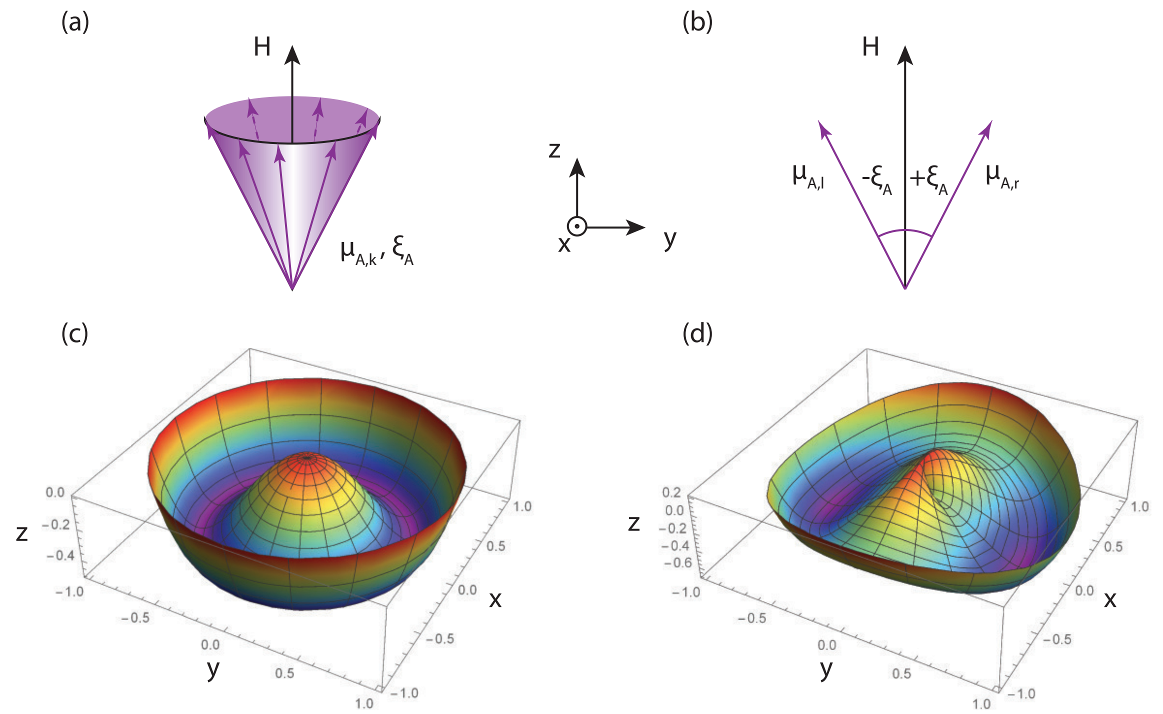

Figure B.1: (a) In the canted magnetic phase of an isotropic system, magnetic moments $\boldsymbol{\mu}_{A,k}$ tilted by a canting angle ξ_A residing on sublattice A can assume any orientation on a cone with opening angle ξ_A (see Sect. 2.3.4). (b) When an easy plane anisotropy is introduced, e.g. a demagnetization field which confines the magnetic moments to **y-z** plane, the cone is reduced to two dominating magnetic moment orientations $\boldsymbol{\mu}_{A,l}$ and $\boldsymbol{\mu}_{A,r}$ with in-plane canting angles $\pm\xi_A$. (c) Qualitative representation of the isotropic free energy landscape, which is radially symmetric with respect to the external magnetic field. The color coding corresponds to the energy scale, i.e. purple and red for the global energy minima and maxima, respectively. The magnetic moments are expected to assume an orientation corresponding to a minimum in the free energy. (d) Free energy landscape with an easy **y-z** plane, giving rise to two distinct global minima in ±**y** direction.

of magnetic moment orientations, there are now two energetically equivalent configurations l and r in the **y-z** plane as sketched in Fig. B.1 (b), which is equivalent to the 2D model discussed in Sect. 2.3.2.

The two global minima are separated by an energy barrier, which is determined by the anisotropy energy. If the thermal energy is larger than this barrier, the moments can in principle fluctuate between the two l and r configurations. Assuming that there is no preferred orientation, one obtains the 50:50 moment distribution discussed in Sect. 2.3.2. If the energy barrier is too large to be overcome by thermal fluctuations, the magnetic moments can be pinned in a specific configuration which depends on the magnetic history of the sample, i.e. previous temperature, magnetic field magnitude or orientation. In

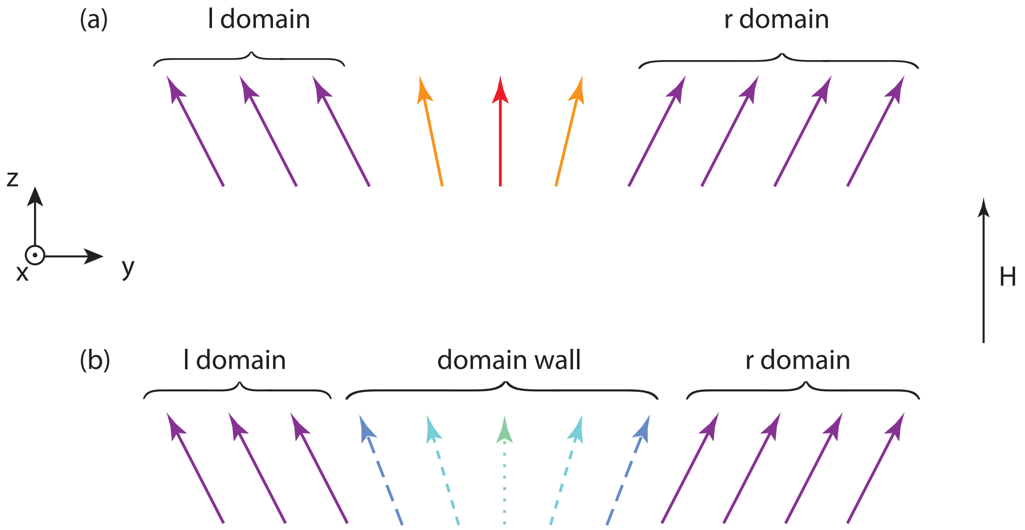

Figure B.2: Schematic representation of domains in the magnetic canting phase, where neighboring moments align parallel due to the intra-sublattice ferromagnetic exchange coupling. (a) A transition from l to r type domains which keeps all moments within the **y**-**z** plane is energetically unfavorable since the red arrow pointing along the external field corresponds to a global energy maximum in Fig. B.1 (b). (b) The energetically more favorable transition between l and r type domains is a domain wall consisting of magnetic moments tilted out of the plane with a component along the **x**-direction, as indicated by the dashed arrows. The arrow colors correspond to the color coding in Fig. B.1.

particular, a hysteretic behavior may arise when the magnetic field is swept in different directions.

Including the ferromagnetic exchange coupling within one magnetic sublattice, neighboring moments tend to align parallel to each other. This can give rise to the formation of domains, i.e. regions of the sample where all magnetic moments are either tilted to the left or right with respect to the magnetic field. In analogy to ferromagnetic domains, the transition region between l and r domains corresponds to a domain wall. The scenario depicted in Fig. B.2 (a) is based on the assumption that all magnetic moments lie in the **y**-**z** plane: the domain wall contains several magnetic moments (orange and red arrows) with in-plane canting angles between $\pm\xi_A$. The color of the arrows corresponds to the color code of the energy scale in Fig. B.1. Such an in-plane domain wall is energetically unfavorable in the canting phase as the orientation of the red arrow corresponds to the local maximum in the center of the energy landscape in Fig. B.1 (d). According to the latter, it is energetically more favorable for the moments in the domain wall to tilt out of the **y**-**z** plane, as represented by the dashed arrows in Fig. B.2 (b), where the light green arrow points along the **x** direction.

Bibliography

[1] S. Zweig, *Decisive Moments in History: Twelve Historical Miniatures, The First Word Across the Ocean* (Ariadne Press, 1999 (first published in 1927)).

[2] J. Bass and W. P. P. Jr, "Spin-diffusion lengths in metals and alloys, and spin-flipping at metal/metal interfaces: an experimentalist's critical review", J. Phys.: Condens. Matter **19**, 183201 (2007).

[3] L. J. Cornelissen, J. Liu, R. A. Duine, J. Ben Youssef, and B. J. van Wees, "Long-distance transport of magnon spin information in a magnetic insulator at room temperature", Nat. Phys. **11**, 1022 (2015).

[4] S. T. B. Goennenwein, R. Schlitz, M. Pernpeintner, K. Ganzhorn, M. Althammer, R. Gross, and H. Huebl, "Non-local magnetoresistance in YIG/Pt nanostructures", Appl. Phys. Lett. **107**, 172405 (2015).

[5] J. E. Hirsch, "Spin Hall Effect", Phys. Rev. Lett. **83**, 1834 (1999).

[6] M. Dyakonov and V. Perel, "Possibility of Orienting Electron Spin with Current", J. Exp. Theo. Phys. **13**, 467 (1971).

[7] O. Smith, "Some possible forms of phonograph", The electrical World p. 116 ff. (1888).

[8] W. Thomson, "On the Electro-Dynamic Qualities of Metals: Effects of Magnetization on the Electric Conductivity of Nickel and of Iron", Proc. R. Soc. Lond. **8**, 546 (1856).

[9] T. McGuire and R. Potter, "Anisotropic magnetoresistance in ferromagnetic 3d alloys", IEEE Trans. Mag. **11**, 1018 (1975).

[10] M. Althammer, S. Meyer, H. Nakayama, M. Schreier, S. Altmannshofer, M. Weiler, H. Huebl, S. Geprägs, M. Opel, R. Gross, D. Meier, C. Klewe, T. Kuschel, J.-M. Schmalhorst, G. Reiss, L. Shen, A. Gupta, Y.-T. Chen, G. E. W. Bauer, E. Saitoh, and S. T. B. Goennenwein, "Quantitative study of the spin Hall magnetoresistance in ferromagnetic insulator/normal metal hybrids", Phys. Rev. B **87**, 224401 (2013).

[11] H. Nakayama, M. Althammer, Y.-T. Chen, K. Uchida, Y. Kajiwara, D. Kikuchi, T. Ohtani, S. Geprägs, M. Opel, S. Takahashi, R. Gross, G. E. W. Bauer, S. T. B. Goennenwein, and E. Saitoh, "Spin Hall Magnetoresistance Induced by a Nonequilibrium Proximity Effect", Phys. Rev. Lett. **110**, 206601 (2013).

[12] Y.-T. Chen, S. Takahashi, H. Nakayama, M. Althammer, S. T. B. Goennenwein, E. Saitoh, and G. E. W. Bauer, "Theory of spin Hall magnetoresistance", Phys. Rev. B **87**, 144411 (2013).

[13] P. Wadley, B. Howells, J. Zelezny, C. Andrews, V. Hills, R. P. Campion, V. Novák, K. Olejník, F. Maccherozzi, S. S. Dhesi, S. Y. Martin, T. Wagner, J. Wunderlich, F. Freimuth, Y. Mokrousov, J. Kuneš, J. S. Chauhan, M. J. Grzybowski, A. W. Rushforth, K. W. Edmonds, B. L. Gallagher, and T. Jungwirth, "Electrical switching of an antiferromagnet", Science **351**, 587 (2016).

[14] D. Kriegner, K. Vyborny, K. Olejnik, H. Reichlova, V. Novak, X. Marti, J. Gazquez, V. Saidl, P. Nemec, V. V. Volobuev, G. Springholz, V. Holy, and T. Jungwirth, "Multiple-stable anisotropic magnetoresistance memory in antiferromagnetic MnTe", Nat. Commun. **7**, 11623 (2016).

[15] G. F. Dionne, *Magnetic Oxides* (Springer, New York, 2009).

[16] S. Mühlbauer, B. Binz, F. Jonietz, C. Pfleiderer, A. Rosch, A. Neubauer, R. Georgii, and P. Böni, "Skyrmion Lattice in a Chiral Magnet", Science **323**, 915 (2009).

[17] S. Seki, X. Z. Yu, S. Ishiwata, and Y. Tokura, "Observation of Skyrmions in a Multiferroic Material", Science **336**, 198 (2012).

[18] E. Ruff, P. Lunkenheimer, A. Loidl, H. Berger, and S. Krohns, "Magnetoelectric effects in the skyrmion host material Cu_2OSeO_3", Sci. Rep. **5**, 15025 (2015).

[19] M. Weiler, A. Aqeel, M. Mostovoy, A. Leonov, S. Geprägs, R. Gross, H. Huebl, T. T. M. Palstra, and S. T. B. Goennenwein, "Helimagnon resonances in an intrinsic chiral magnonic crystal", ArXiv e-prints:1705.02874 (2017).

[20] T. Jungwirth, X. Marti, P. Wadley, and J. Wunderlich, "Antiferromagnetic spintronics", Nat. Nano. **11**, 231 (2016).

[21] S. Loth, S. Baumann, C. P. Lutz, D. M. Eigler, and A. J. Heinrich, "Bistability in Atomic-Scale Antiferromagnets", Science **335**, 196 (2012).

[22] X. Marti, I. Fina, C. Frontera, J. Liu, P. Wadley, Q. He, R. J. Paull, J. D. Clarkson, J. Kudrnovsky, I. Turek, J. Kunes, D. Yi, J.-H. Chu, C. T. Nelson, L. You, E. Arenholz, S. Salahuddin, J. Fontcuberta, T. Jungwirth, and R. Ramesh, "Room-temperature antiferromagnetic memory resistor", Nat. Mater. **13**, 367 (2014).

[23] S. I. Kiselev, J. C. Sankey, I. N. Krivorotov, N. C. Emley, R. J. Schoelkopf, R. A. Buhrman, and D. C. Ralph, “Microwave oscillations of a nanomagnet driven by a spin-polarized current”, Nature **425**, 380 (2003).

[24] I. M. Miron, G. Gaudin, S. Auffret, B. Rodmacq, A. Schuhl, S. Pizzini, J. Vogel, and P. Gambardella, “Current-driven spin torque induced by the Rashba effect in a ferromagnetic metal layer”, Nat. Mater. **9**, 230 (2010).

[25] S. Emori, U. Bauer, S.-M. Ahn, E. Martinez, and G. S. D. Beach, “Current-driven dynamics of chiral ferromagnetic domain walls”, Nat. Mater. **12**, 611 (2013).

[26] C. Hahn, G. de Loubens, O. Klein, M. Viret, V. V. Naletov, and J. Ben Youssef, “Comparative measurements of inverse spin Hall effects and magnetoresistance in YIG/Pt and YIG/Ta”, Phys. Rev. B **87**, 174417 (2013).

[27] N. Vlietstra, J. Shan, V. Castel, B. J. van Wees, and J. Ben Youssef, “Spin-Hall magnetoresistance in platinum on yttrium iron garnet: Dependence on platinum thickness and in-plane/out-of-plane magnetization”, Phys. Rev. B **87**, 184421 (2013).

[28] J. C. Slonczewski, “Current-driven excitation of magnetic multilayers”, J. Magn. Magn. Mater. **159**, L1 (1996).

[29] L. Berger, “Emission of spin waves by a magnetic multilayer traversed by a current”, Phys. Rev. B **54**, 9353 (1996).

[30] K. Ganzhorn, J. Barker, R. Schlitz, B. A. Piot, K. Ollefs, F. Guillou, F. Wilhelm, A. Rogalev, M. Opel, M. Althammer, S. Geprägs, H. Huebl, R. Gross, G. E. W. Bauer, and S. T. B. Goennenwein, “Spin Hall magnetoresistance in a canted ferrimagnet”, Phys. Rev. B **94**, 094401 (2016).

[31] N. F. Mott, “The Electrical Conductivity of Transition Metals”, Proc. R. Soc. Lond. Ser. A **153**, 699 (1936).

[32] M. V. Berry, “Quantal Phase Factors Accompanying Adiabatic Changes”, Proc. R. Soc. Lond. Ser. A **392**, 45 (1984).

[33] N. Nagaosa, J. Sinova, S. Onoda, A. H. MacDonald, and N. P. Ong, “Anomalous Hall effect”, Rev. Mod. Phys. **82**, 1539 (2010).

[34] J. Smit, “The spontaneous hall effect in ferromagnetics II”, Physica **24**, 39 (1958).

[35] J. Smit, “The spontaneous hall effect in ferromagnetics I”, Physica **21**, 877 (1955).

[36] R. Karplus and J. M. Luttinger, “Hall Effect in Ferromagnetics”, Phys. Rev. **95**, 1154 (1954).

[37] L. Berger, “Side-Jump Mechanism for the Hall Effect of Ferromagnets”, Phys. Rev. B **2**, 4559 (1970).

[38] M. Schreier, “Spin transfer torque mediated magnetization dynamics”, Ph.D. thesis, Technische Universität München (2016).

[39] A. Hoffmann, “Spin Hall Effects in Metals”, IEEE Trans. Magn. **49**, 5172 (2013).

[40] S. Meyer, M. Althammer, S. Geprägs, M. Opel, R. Gross, and S. T. B. Goennenwein, “Temperature dependent spin transport properties of platinum inferred from spin Hall magnetoresistance measurements”, Appl. Phys. Lett. **104**, 242411 (2014).

[41] S. R. Marmion, M. Ali, M. McLaren, D. A. Williams, and B. J. Hickey, “Temperature dependence of spin Hall magnetoresistance in thin YIG/Pt films”, Phys. Rev. B **89**, 220404 (2014).

[42] M. Gradhand, D. V. Fedorov, P. Zahn, and I. Mertig, “Spin Hall angle versus spin diffusion length: Tailored by impurities”, Phys. Rev. B **81**, 245109 (2010).

[43] S. Meyer, “Spin Caloritronics in Ferromagnet/Normal Metal Hybrid Structures”, Ph.D. thesis, Technische Universität München (2015).

[44] A. Brataas, Y. V. Nazarov, and G. E. W. Bauer, “Finite-Element Theory of Transport in Ferromagnet–Normal Metal Systems”, Phys. Rev. Lett. **84**, 2481 (2000).

[45] X. Jia, K. Liu, K. Xia, and G. E. W. Bauer, “Spin transfer torque on magnetic insulators”, Europhys. Lett. **96**, 17005 (2011).

[46] Y. M. Lu, J. W. Cai, S. Y. Huang, D. Qu, B. F. Miao, and C. L. Chien, “Hybrid magnetoresistance in the proximity of a ferromagnet”, Phys. Rev. B **87**, 220409 (2013).

[47] S. Geprägs, S. Meyer, S. Altmannshofer, M. Opel, F. Wilhelm, A. Rogalev, R. Gross, and S. T. B. Goennenwein, “Investigation of induced Pt magnetic polarization in Pt/$Y_3Fe_5O_{12}$ bilayers”, Appl. Phys. Lett. **101**, 262407 (2012).

[48] S. Pütter, S. Geprägs, R. Schlitz, M. Althammer, A. Erb, R. Gross, and S. T. B. Goennenwein, “Impact of the interface quality of Pt/YIG(111) hybrids on their spin Hall magnetoresistance”, Appl. Phys. Lett. **110**, 012403 (2017).

[49] M. Isasa, A. Bedoya-Pinto, S. Velez, F. Golmar, F. Sanchez, L. E. Hueso, J. Fontcuberta, and F. Casanova, “Spin Hall magnetoresistance at Pt/$CoFe_2O_4$ interfaces and texture effects”, Appl. Phys. Lett. **105**, 142402 (2014).

[50] N. Miura, I. Oguro, and S. Chikazumi, "Computer simulation of temperature and field dependences of sublattice magnetization and spin-flip transition in Gallium-substituted Yttrium Iron Garnet", J. Phys. Soc. Jap. **45**, 1534 (1978).

[51] T. Aderneuer, "Dependence of the Spin Hall Magnetoresistance on the Interface Magnetic Moment Density in Pt|$Y_3Fe_5O_{12}$ Bilayers", Bachelor's thesis, Technische Universität München (2014).

[52] M. A. Gilleo and S. Geller, "Magnetic and Crystallographic Properties of Substituted Yttrium-Iron Garnet, $3Y_2O_3 \cdot xM_2O_3 \cdot (5-x)Fe_2O_3$", Phys. Rev. **110**, 73 (1958).

[53] S. Geller, "Magnetic Interactions and Distribution of Ions in the Garnets", J. Appl. Phys. **31**, S30 (1960).

[54] R. Gross and A. Marx, *Festkörperphysik* (De Gruyter, 2014).

[55] R. Schlitz, "Spin transport experiments in hypbrid nanostructures", Master's thesis, Technische Universität München (2015).

[56] M. Lammel, "Spin Hall Magnetoresistance in Normal Metal|Compensated Rare Earth Iron Garnet Bilayers", Master's thesis, Technische Universität München (2015).

[57] H. Sakimura, "Investigation of Spin Hall Magnetoresistance in Erbium Iron Garnet/Platinum Systems", Master's thesis, Technische Universität München (2016).

[58] D. Sander, "The correlation between mechanical stress and magnetic anisotropy in ultrathin films", Rep. Prog. Phys. **62**, 809 (1999).

[59] A. Aqeel, N. Vlietstra, A. Roy, M. Mostovoy, B. J. van Wees, and T. T. M. Palstra, "Electrical detection of spiral spin structures in Pt|Cu_2OSeO_3 heterostructures", Phys. Rev. B **94**, 134418 (2016).

[60] R. Metselaar and P. Larsen, "High-temperature electrical properties of yttrium iron garnet under varying oxygen pressures", Solid State Commun. **15**, 291 (1974).

[61] S. Wittekoek, T. J. A. Popma, J. M. Robertson, and P. F. Bongers, "Magneto-optic spectra and the dielectric tensor elements of bismuth-substituted iron garnets at photon energies between 2.2-5.2 eV", Phys. Rev. B **12**, 2777 (1975).

[62] S. Geller and M. Gilleo, "The crystal structure and ferrimagnetism of yttrium-iron garnet, $Y_3Fe_2(FeO_4)_3$", J. Phys. Chem. Solids **3**, 30 (1957).

[63] C. Suchomski, "Strukturelle, optische und magnetische Eigenschaften von Nanokristallinen Metalloxid-Dünnfilmen mit mesoporöser Morphologie", Ph.D. thesis, Justus-Liebig-Universität Giessen (2012).

[64] J. Barker and G. E. W. Bauer, "Thermal Spin Dynamics of Yttrium Iron Garnet", Phys. Rev. Lett. **117**, 217201 (2016).

[65] H. Maier-Flaig, S. Klingler, C. Dubs, O. Surzhenko, R. Gross, M. Weiler, H. Huebl, and S. T. B. Goennenwein, "Temperature-dependent magnetic damping of yttrium iron garnet spheres", Phys. Rev. B **95**, 214423 (2017).

[66] P. Hansen, "Anisotropy and magnetostriction of gallium-substituted yttrium iron garnet", J. Appl. Phys. **45**, 3638 (1974).

[67] S. Altmannshofer, "Epitaxie und Charakterisierung von dünnen Schichten des ferromagnetischen Isolators $Y_3Fe_5O_{12}$", Master's thesis, Technische Universität München (2012).

[68] K. Ganzhorn, "Experimental Study of Spin Currents in Compensated Rear Earth Garnets", Master's thesis, Technische Universität München (2014).

[69] J. Coey, *Magnetism and magnetic materials* (Cambridge University Press, 2009).

[70] P. Röschmann and P. Hansen, "Molecular field coefficients and cation distribution of substituted yttrium iron garnets", J. Appl. Phys. **52**, 6257 (1981).

[71] P. Hansen, G. Winkler, and E. K., *Landolt-Börnstein Group III: Condensed Matter*, vol. 12A (1978).

[72] J. Bernasconi and D. Kuse, "Canted Spin Phase in Gadolinium Iron Garnet", Phys. Rev. B **3**, 811 (1971).

[73] A. E. Clark and E. Callen, "Neel Ferrimagnets in Large Magnetic Fields", J. Appl. Phys. **39**, 5972 (1968).

[74] C. Dubs, O. Surzhenko, R. Linke, A. Danilewsky, U. Brückner, and J. Dellith, "Sub-micrometer yttrium iron garnet LPE films with low ferromagnetic resonance losses", J. Phys. D: Appl. Phys. **50**, 204005 (2017).

[75] S. Klingler, H. Maier-Flaig, C. Dubs, O. Surzhenko, R. Gross, H. Huebl, S. T. B. Goennenwein, and M. Weiler, "Gilbert damping of magnetostatic modes in a yttrium iron garnet sphere", Appl. Phys. Lett. **110**, 092409 (2017).

[76] M. Haertinger, C. H. Back, J. Lotze, M. Weiler, S. Geprägs, H. Huebl, S. T. B. Goennenwein, and G. Woltersdorf, "Spin pumping in YIG/Pt bilayers as a function of layer thickness", Phys. Rev. B **92**, 054437 (2015).

[77] O. d'Allivy Kelly, A. Anane, R. Bernard, J. B. Youssef, C. Hahn, A. H. Molpeceres, C. Carrétéro, E. Jacquet, C. Deranlot, P. Bortolotti, R. Lebourgeois, J.-C. Mage,

G. de Loubens, O. Klein, V. Cros, and A. Fert, "Inverse spin Hall effect in nanometer-thick yttrium iron garnet/Pt system", Appl. Phys. Lett. **103**, 082408 (2013).

[78] A. V. Chumak, A. A. Serga, M. B. Jungfleisch, R. Neb, D. A. Bozhko, V. S. Tiberkevich, and B. Hillebrands, "Direct detection of magnon spin transport by the inverse spin Hall effect", Appl. Phys. Lett. **100**, 082405 (2012).

[79] H. Maier-Flaig, S. Geprägs, Z. Qiu, E. Saitoh, R. Gross, M. Weiler, H. Huebl, and S. T. B. Goennenwein, "Perpendicular magnetic anisotropy in insulating ferrimagnetic gadolinium iron garnet thin films", ArXiv e-prints:1706.08488 (2017).

[80] E. Barati, M. Cinal, D. M. Edwards, and A. Umerski, "Gilbert damping in magnetic layered systems", Phys. Rev. B **90**, 014420 (2014).

[81] K. P. Belov, "Ferrimagnets with a 'weak' magnetic sublattice", Physics-Uspekhi **39**, 623 (1996).

[82] G. F. Dionne, "Molecular Field and Exchange Constants of Gd^{3+} Substituted Ferrimagnetic Garnets", Appl. Phys. Lett. **42**, 2142 (1971).

[83] S. Geprägs, A. Kehlberger, F. D. Coletta, Z. Qiu, E.-J. Guo, T. Schulz, C. Mix, S. Meyer, A. Kamra, M. Althammer, H. Huebl, G. Jakob, Y. Ohnuma, H. Adachi, J. Barker, S. Maekawa, G. E. W. Bauer, E. Saitoh, R. Gross, S. T. B. Goennenwein, and M. Klaui, "Origin of the spin Seebeck effect in compensated ferrimagnets", Nat. Commun. **7**, 10452 (2016).

[84] B. A. Calhoun, J. Overmeyer, and W. V. Smith, "Ferrimagnetic Resonance in Gadolinium Iron Garnet", Phys. Rev. **107**, 993 (1957).

[85] R. Pauthenet, "Spontaneous Magnetization of Some Garnet Ferrites and the Aluminum Substituted Garnet Ferrites", J. Appl. Phys. **29**, 253 (1958).

[86] D. Hinzke and U. Nowak, "Monte Carlo simulation of magnetization switching in a Heisenberg model for small ferromagnetic particles", Comput. Phys. Commun. **121**, 334 (1999).

[87] G. F. Dionne, "Molecular Field Coefficients of Substituted Yttrium Iron Garnets", J. Appl. Phys. **41**, 4874 (1970).

[88] T. Shinohara, S. Takeda, Y. Matsumoto, and Y. Noro, "Magnetic properties of polycrystalline gadolinium calcium vanadium and indium substituted YIG", IEEE Trans. Magn. **11**, 1676 (1975).

[89] J. R. Cunningham and E. E. Anderson, "Effect of Indium Substitution in Yttrium Iron Garnet. High Permeability Garnets", J. Appl. Phys. **32**, S388 (1961).

[90] F. D. Coletta, “Spin Seebeck effect in rare earth iron garnets”, Master’s thesis, Technische Universität München (2015).

[91] S. Frölich, “Thin Film Fabrication for Spin Current and Spin Caloric Experiments”, Bachelor’s thesis, Technische Universität München (2014).

[92] A. Krupp, “Growth and characterization of ferromagneric Heusler compund thin films”, Diploma thesis, Technische Universität München (2010).

[93] K. Uchida, H. Adachi, T. Ota, H. Nakayama, S. Maekawa, and E. Saitoh, “Observation of longitudinal spin-Seebeck effect in magnetic insulators”, Appl. Phys. Lett. **97**, 172505 (2010).

[94] M. Weiler, M. Althammer, F. D. Czeschka, H. Huebl, M. S. Wagner, M. Opel, I.-M. Imort, G. Reiss, A. Thomas, R. Gross, and S. T. B. Goennenwein, “Local Charge and Spin Currents in Magnetothermal Landscapes”, Phys. Rev. Lett. **108**, 106602 (2012).

[95] M. Schreier, N. Roschewsky, E. Dobler, S. Meyer, H. Huebl, R. Gross, and S. T. B. Goennenwein, “Current heating induced spin Seebeck effect”, Appl. Phys. Lett. **103**, 242404 (2013).

[96] S. A. Manuilov, R. Fors, S. I. Khartsev, and A. M. Grishin, “Submicron $Y_3Fe_5O_{12}$ Film Magnetostatic Wave Band Pass Filters”, J. Appl. Phys. **105**, 033917 (2009).

[97] S. Vélez, A. Bedoya-Pinto, W. Yan, L. E. Hueso, and F. Casanova, “Competing effects at Pt/YIG interfaces: Spin Hall magnetoresistance, magnon excitations, and magnetic frustration”, Phys. Rev. B **94**, 174405 (2016).

[98] S. Marmion, “Comparison of the Spin Hall Magnetoresistance Temperature Dependence YIG/Metal Systems”, Ph.D. thesis, University of Leeds (2016).

[99] S. Vélez, V. N. Golovach, A. Bedoya-Pinto, M. Isasa, E. Sagasta, M. Abadia, C. Rogero, L. E. Hueso, F. S. Bergeret, and F. Casanova, “Hanle Magnetoresistance in Thin Metal Films with Strong Spin-Orbit Coupling”, Phys. Rev. Lett. **116**, 016603 (2016).

[100] M. I. Dyakonov, “Magnetoresistance due to Edge Spin Accumulation”, Phys. Rev. Lett. **99**, 126601 (2007).

[101] F. J. Jedema, H. B. Heersche, A. T. Filip, J. J. A. Baselmans, and B. J. van Wees, “Electrical detection of spin precession in a metallic mesoscopic spin valve”, Nature **416**, 713 (2002).

[102] J. Stöhr, "Exploring the microscopic origin of magnetic anisotropies with X-ray magnetic circular dichroism (XMCD) spectroscopy", J. Magn. Magn. Mat. **200**, 470 (1999).

[103] H. Wende, "Recent advances in x-ray absorption spectroscopy", Rep. Prog. Phys. **67**, 2105 (2004).

[104] A. Rogalev and F. Wilhelm, "Magnetic circular dichroism in the hard X-ray range", Phys. Metals Metallogr. **116**, 1285 (2015).

[105] A. Rogalev, J. Goulon, F. Wilhelm, C. Brouder, A. Yaresko, J. B. Youssef, and M. Indenbom, "Element selective X-ray magnetic circular and linear dichroisms in ferrimagnetic yttrium iron garnet films", J. Magn. Magn. Mater. **321**, 3945 (2009).

[106] H. Maruyama and N. Kawamura, "XMCD study of electronic states in rare-earth iron garnet", J. Electron Spectrosc. Relat. Phenom. **136**, 135 (2004).

[107] C. Strohm, T. Roth, C. Detlefs, P. van der Linden, and O. Mathon, "Element-selective magnetometry in ferrimagnetic erbium iron garnet", Phys. Rev. B **86**, 214421 (2012).

[108] Y.-T. Chen, S. Takahashi, H. Nakayama, M. Althammer, S. T. B. Goennenwein, E. Saitoh, and G. E. W. Bauer, "Theory of spin Hall magnetoresistance (SMR) and related phenomena", J. Phys.: Condens. Matter **28**, 103004 (2016).

[109] A. Aqeel, N. Vlietstra, J. A. Heuver, G. E. W. Bauer, B. Noheda, B. J. van Wees, and T. T. M. Palstra, "Spin-Hall magnetoresistance and spin Seebeck effect in spin-spiral and paramagnetic phases of multiferroic $CoCr_2O_4$ films", Phys. Rev. B **92**, 224410 (2015).

[110] A. V. Chumak, A. A. Serga, and B. Hillebrands, "Magnon transistor for all-magnon data processing", Nat. Commun. **5**, 4700 (2014).

[111] K. Vogt, F. Fradin, J. Pearson, T. Sebastian, S. Bader, B. Hillebrands, A. Hoffmann, and H. Schultheiss, "Realization of a spin-wave multiplexer", Nat. Commun. **5**, 3727 (2014).

[112] K. Vogt, H. Schultheiss, S. Jain, J. E. Pearson, A. Hoffmann, S. D. Bader, and B. Hillebrands, "Spin waves turning a corner", Appl. Phys. Lett. **101**, 042410 (2012).

[113] S. S.-L. Zhang and S. Zhang, "Magnon Mediated Electric Current Drag Across a Ferromagnetic Insulator Layer", Phys. Rev. Lett. **109**, 096603 (2012).

[114] S. S.-L. Zhang and S. Zhang, "Spin convertance at magnetic interfaces", Phys. Rev. B **86**, 214424 (2012).

[115] B. L. Giles, Z. Yang, J. S. Jamison, and R. C. Myers, “Long-range pure magnon spin diffusion observed in a nonlocal spin-Seebeck geometry”, Phys. Rev. B **92**, 224415 (2015).

[116] K. Ganzhorn, T. Wimmer, J. Cramer, R. Schlitz, S. Geprägs, G. Jakob, R. Gross, H. Huebl, M. Kläui, and S. T. B. Goennenwein, “Temperature dependence of the non-local spin Seebeck effect in YIG/Pt nanostructures”, AIP Adv. **7**, 085102 (2017).

[117] X. J. Zhou, G. Y. Shi, J. H. Han, Q. H. Yang, Y. H. Rao, H. W. Zhang, L. L. Lang, S. M. Zhou, F. Pan, and C. Song, “Lateral transport properties of thermally excited magnons in yttrium iron garnet films”, Appl. Phys. Lett. **110**, 062407 (2017).

[118] J. Xiao, G. E. W. Bauer, K. Uchida, E. Saitoh, and S. Maekawa, “Theory of magnon-driven spin Seebeck effect”, Phys. Rev. B **81**, 214418 (2010).

[119] T. Kikkawa, K. Uchida, S. Daimon, Z. Qiu, Y. Shiomi, and E. Saitoh, “Critical suppression of spin Seebeck effect by magnetic fields”, Phys. Rev. B **92**, 064413 (2015).

[120] S. R. Boona and J. P. Heremans, “Magnon thermal mean free path in yttrium iron garnet”, Phys. Rev. B **90**, 064421 (2014).

[121] A. Kehlberger, U. Ritzmann, D. Hinzke, E.-J. Guo, J. Cramer, G. Jakob, M. C. Onbasli, D. H. Kim, C. A. Ross, M. B. Jungfleisch, B. Hillebrands, U. Nowak, and M. Kläui, “Length Scale of the Spin Seebeck Effect”, Phys. Rev. Lett. **115**, 096602 (2015).

[122] E.-J. Guo, J. Cramer, A. Kehlberger, C. A. Ferguson, D. A. MacLaren, G. Jakob, and M. Kläui, “Influence of Thickness and Interface on the Low-Temperature Enhancement of the Spin Seebeck Effect in YIG Films”, Phys. Rev. X **6**, 031012 (2016).

[123] K. Ganzhorn, S. Klingler, T. Wimmer, S. Geprägs, R. Gross, H. Huebl, and S. T. B. Goennenwein, “Magnon-based logic in a multi-terminal YIG/Pt nanostructure”, Appl. Phys. Lett. **109**, 022405 (2016).

[124] S. Takahashi, E. Saitoh, and S. Maekawa, “Spin current through a normal-metal/insulating-ferromagnet junction”, Jour. Phys.: Conf. Ser. **200**, 062030 (2010).

[125] S. Zhang and Z. Li, “Roles of Nonequilibrium Conduction Electrons on the Magnetization Dynamics of Ferromagnets”, Phys. Rev. Lett. **93**, 127204 (2004).

[126] L. J. Cornelissen, K. J. H. Peters, G. E. W. Bauer, R. A. Duine, and B. J. van Wees, “Magnon spin transport driven by the magnon chemical potential in a magnetic insulator”, Phys. Rev. B **94**, 014412 (2016).

[127] L. J. Cornelissen and B. J. van Wees, “Magnetic field dependence of the magnon spin diffusion length in the magnetic insulator yttrium iron garnet”, Phys. Rev. B **93**, 020403 (2016).

[128] H. Jin, S. R. Boona, Z. Yang, R. C. Myers, and J. P. Heremans, “Effect of the magnon dispersion on the longitudinal spin Seebeck effect in yttrium iron garnets”, Phys. Rev. B **92**, 054436 (2015).

[129] K. Ganzhorn, T. Wimmer, J. Barker, G. E. W. Bauer, Z. Qiu, E. Saitoh, N. Vlietstra, S. Geprägs, R. Gross, H. Huebl, and S. T. B. Goennenwein, “Non-local magnon transport in the compensated ferrimagnet GdIG”, ArXiv e-prints:1705.02871 (2017).

[130] F. Keffer and C. Kittel, “Theory of Antiferromagnetic Resonance”, Phys. Rev. **85**, 329 (1952).

[131] C. Kittel, “Theory of Ferromagnetic Resonance in Rare Earth Garnets. I. g Values”, Phys. Rev. **115**, 1587 (1959).

[132] A. Gurevich and G. Melkov, *Magnetization Oscillations and Waves* (Taylor & Francis, 1996), ISBN 9780849394607.

[133] Y. Ohnuma, H. Adachi, E. Saitoh, and S. Maekawa, “Spin Seebeck effect in antiferromagnets and compensated ferrimagnets”, Phys. Rev. B **87**, 014423 (2013).

[134] J. Li, Y. Xu, M. Aldosary, C. Tang, Z. Lin, S. Zhang, R. Lake, and J. Shi, “Observation of magnon-mediated current drag in Pt/yttrium iron garnet/Pt(Ta) trilayers”, Nat. Commun. **7**, 10858 (2016).

[135] H. Wu, C. H. Wan, X. Zhang, Z. H. Yuan, Q. T. Zhang, J. Y. Qin, H. X. Wei, X. F. Han, and S. Zhang, “Observation of magnon-mediated electric current drag at room temperature”, Phys. Rev. B **93**, 060403 (2016).

[136] G. P. Rodrigue, H. Meyer, and R. V. Jones, “Resonance Measurements in Magnetic Garnets”, J. Appl. Phys. **31**, S376 (1960).

[137] M. Schreier, A. Kamra, M. Weiler, J. Xiao, G. E. W. Bauer, R. Gross, and S. T. B. Goennenwein, “Magnon, phonon, and electron temperature profiles and the spin Seebeck effect in magnetic insulator/normal metal hybrid structures”, Phys. Rev. B **88**, 094410 (2013).

[138] L. J. Cornelissen, J. Shan, and B. J. van Wees, “Temperature dependence of the magnon spin diffusion length and magnon spin conductivity in the magnetic insulator yttrium iron garnet”, Phys. Rev. B **94**, 180402 (2016).

[139] J. Shan, L. J. Cornelissen, N. Vlietstra, J. Ben Youssef, T. Kuschel, R. A. Duine, and B. J. van Wees, “Influence of yttrium iron garnet thickness and heater opacity on the nonlocal transport of electrically and thermally excited magnons”, Phys. Rev. B **94**, 174437 (2016).

[140] C. D. Rose, “Aufbau eines Messstabes für Magnetotransportmessungen”, Bachelor’s thesis, Technische Universität München (2015).

[141] T. Wimmer, “Spin transport in magnetic nanostructures”, Master’s thesis, Technische Universität München (2016).

[142] J. F. Dillon, “Ferrimagnetic Resonance in Yttrium Iron Garnet”, Phys. Rev. **105**, 759 (1957).

[143] V. Cherepanov, I. Kolokolov, and V. L’vov, “The saga of YIG: Spectra, thermodynamics, interaction and relaxation of magnons in a complex magnet”, Phys. Rep. **229**, 81 (1993).

[144] T. Kasuya and R. C. LeCraw, “Relaxation Mechanisms in Ferromagnetic Resonance”, Phys. Rev. Lett. **6**, 223 (1961).

[145] I. Diniz and A. T. Costa, “Microscopic origin of subthermal magnons and the spin Seebeck effect”, New J. Phys. **18**, 052002 (2016).

[146] M. P. Kostylev, A. A. Serga, T. Schneider, B. Leven, and B. Hillebrands, “Spin-wave logical gates”, Appl. Phys. Lett. **87**, 153501 (2005).

[147] T. Schneider, A. A. Serga, B. Leven, B. Hillebrands, R. L. Stamps, and M. P. Kostylev, “Realization of spin-wave logic gates”, Appl. Phys. Lett. **92**, 22505 (2008).

[148] A. Khitun, M. Bao, and K. L. Wang, “Spin Wave Magnetic NanoFabric: A New Approach to Spin-Based Logic Circuitry”, IEEE Trans. Magn. **44**, 2141 (2008).

[149] K. Wagner, K. Kákay, K. Schultheiss, A. Henschke, T. Sebastian, and H. Schultheiss, “Magnetic domain walls as reconfigurable spin-wave nanochannels”, Nat. Nano. **11** (2016).

[150] S. Klingler, P. Pirro, T. Brächer, B. Leven, B. Hillebrands, and A. V. Chumak, “Design of a spin-wave majority gate employing mode selection”, Appl. Phys. Lett. **105**, 152410 (2014).

[151] S. Klingler, P. Pirro, T. Brächer, B. Leven, B. Hillebrands, and A. V. Chumak, “Spin-wave logic devices based on isotropic forward volume magnetostatic waves”, Appl. Phys. Lett. **106**, 212406 (2015).

[152] T. Fischer, M. Kewenig, D. A. Bozhko, A. A. Serga, I. I. Syvorotka, F. Ciubotaru, C. Adelmann, B. Hillebrands, and A. V. Chumak, “Experimental prototype of a spin-wave majority gate”, Appl. Phys. Lett. **110**, 152401 (2017).

[153] J. Lotze, H. Huebl, R. Gross, and S. T. B. Goennenwein, “Spin Hall magnetoimpedance”, Phys. Rev. B **90**, 174419 (2014).

[154] R. L. Stamps, S. Breitkreutz, J. Akerman, A. V. Chumak, Y. Otani, G. E. W. Bauer, J.-U. Thiele, M. Bowen, S. A. Majetich, M. Kläui, I. L. Prejbeanu, B. Dieny, N. M. Dempsey, and B. Hillebrands, “The 2014 Magnetism Roadmap”, J. Phys. D: Appl. Phys. **47**, 333001 (2014).

[155] A. R. Mellnik, J. S. Lee, A. Richardella, J. L. Grab, P. J. Mintun, M. H. Fischer, A. Vaezi, A. Manchon, E.-A. Kim, N. Samarth, and D. C. Ralph, “Spin-transfer torque generated by a topological insulator”, Nature **511**, 449 (2014).

[156] M. Schreier, G. E. W. Bauer, V. I. Vasyuchka, J. Flipse, K. Uchida, J. Lotze, V. Lauer, A. V. Chumak, A. A. Serga, S. Daimon, T. Kikkawa, E. Saitoh, B. J. van Wees, B. Hillebrands, R. Gross, and S. T. B. Goennenwein, “Sign of inverse spin Hall voltages generated by ferromagnetic resonance and temperature gradients in yttrium iron garnet platinum bilayers”, J. Phys. D: Appl. Phys. **48**, 025001 (2015).

[157] H. Adachi, K. Uchida, E. Saitoh, J. Ohe, S. Takahashi, and S. Maekawa, “Gigantic enhancement of spin Seebeck effect by phonon drag”, Appl. Phys. Lett. **97**, 252506 (2010).

[158] R. Iguchi, K. Uchida, S. Daimon, and E. Saitoh, “Concomitant enhancement of the longitudinal spin Seebeck effect and the thermal conductivity in a Pt/YIG/Pt system at low temperatures”, Phys. Rev. B **95**, 174401 (2017).

[159] J. Cramer, E.-J. Guo, S. Geprägs, A. Kehlberger, Y. P. Ivanov, K. Ganzhorn, F. Della Coletta, M. Althammer, H. Huebl, R. Gross, J. Kosel, M. Kläui, and S. T. B. Goennenwein, “Magnon Mode Selective Spin Transport in Compensated Ferrimagnets”, Nano Lett. **17**, 3334 (2017).

[160] A. Kamra, U. Agrawal, and W. Belzig, “Noninteger-spin magnonic excitations in untextured magnets”, Phys. Rev. B **96**, 020411 (2017).

[161] M. Lambacher, T. Helm, M. Kartsovnik, and A. Erb, “Advances in single crystal growth and annealing treatment of electron-doped HTSC”, Eur. Phys. J. Spec. Top. **188**, 61 (2010).

[162] R. C. LeCraw, J. P. Remeika, and H. Matthews, “Angular Momentum Compensation in Narrow Linewidth Ferrimagnets”, J. Appl. Phys. **36**, 901 (1965).

[163] A. Brandlmaier, “Magnetische Anisotropie in dünnen Schichten aus Magnetit”, Master’s thesis, Technische Universität München (2006).

[164] S. Geschwind and L. R. Walker, “Exchange Resonances in Gadolinium Iron Garnet near the Magnetic Compensation Temperature”, J. Appl. Phys. **30**, S163 (1959).

[165] M. Lahoubi, A. Bouguerra, A. Kihal, and G. Fillion, “Magnetic phase diagrams of dysprosium iron garnet (DyIG) in high dc fields”, J. All. Comp. pp. 598–601 (1998).

[166] G. R. Hoogeboom, A. Aqeel, T. Kuschel, T. T. M. Palstra, and B. J. van Wees, “Negative spin Hall magnetoresistance of Pt on the bulk easy-plane antiferromagnet NiO”, Appl. Phys. Lett. **111**, 052409 (2017).

[167] J. Fischer, O. Gomonay, R. Schlitz, K. Ganzhorn, N. Vlietstra, M. Althammer, H. Huebl, M. Opel, R. Gross, S. T. B. Goennenwein, and S. Geprägs, “Spin Hall magnetoresistance in antiferromagnet/normal metal heterostructures”, ArXiv e-prints:1709.04158 (2017).

[168] S. M. Rezende, R. L. Rodríguez-Suárez, and A. Azevedo, “Theory of the spin Seebeck effect in antiferromagnets”, Phys. Rev. B **93**, 014425 (2016).

[169] S. Seki, T. Ideue, M. Kubota, Y. Kozuka, R. Takagi, M. Nakamura, Y. Kaneko, M. Kawasaki, and Y. Tokura, “Thermal Generation of Spin Current in an Antiferromagnet”, Phys. Rev. Lett. **115**, 266601 (2015).

[170] S. M. Wu, W. Zhang, A. KC, P. Borisov, J. E. Pearson, J. S. Jiang, D. Lederman, A. Hoffmann, and A. Bhattacharya, “Antiferromagnetic Spin Seebeck Effect”, Phys. Rev. Lett. **116**, 097204 (2016).

[171] S. A. Bender, H. Skarsvåg, A. Brataas, and R. A. Duine, “Enhanced Spin Conductance of a Thin-Film Insulating Antiferromagnet”, Phys. Rev. Lett. **119**, 056804 (2017).

List of publications

1. S. T. B. Goennenwein, R. Schlitz, M. Pernpeintner, K. Ganzhorn, M. Althammer, R. Gross, and H. Huebl, “Non-local magnetoresistance in YIG/Pt nanostructures”, Appl. Phys. Lett. **107**, 172405 (2015), doi: 10.1063/1.4935074.

2. K. Ganzhorn, S. Klingler, T. Wimmer, S. Geprägs, R. Gross, H. Huebl, and S. T. B. Goennenwein, “Magnon-based logic in a multi-terminal YIG/Pt nanostructure”, Appl. Phys. Lett. **109**, 022405 (2016), doi: 10.1063/1.4958893.

3. K. Ganzhorn, J. Barker, R. Schlitz, B. A. Piot, K. Ollefs, F. Guillou, F. Wilhelm, A. Rogalev, M. Opel, M. Althammer, S. Geprägs, H. Huebl, R. Gross, G. E. W. Bauer, and S. T. B. Goennenwein, “Spin Hall magnetoresistance in a canted ferrimagnet”, Phys. Rev. B **94**, 094401 (2016), doi: 10.1103/PhysRevB.94.094401.

4. J. Cramer, E.-J. Guo, S. Geprägs, A. Kehlberger, Y. P. Ivanov, K. Ganzhorn, F. Della Coletta, M. Althammer, H. Huebl, R. Gross, J. Kosel, M. Kläui, and S. T. B. Goennenwein, “Magnon mode selective spin transport in compensated ferrimagnets”, Nano Lett. **17**, pp. 3334-3340 (2017), doi: 10.1021/acs.nanolett.6b04522.

5. K. Ganzhorn, T. Wimmer, J. Cramer, R. Schlitz, S. Geprägs, G. Jakob, R. Gross, H. Huebl, M. Kläui, and S. T. B. Goennenwein, “Temperature dependence of the non-local spin Seebeck effect in YIG/Pt nanostructures”, AIP Adv. **7** 085102 (2017), doi: 10.1063/1.4986848.

6. K. Ganzhorn, T. Wimmer, J. Barker, G. E. W. Bauer, Z. Qiu, E. Saitoh, N. Vlietstra, S. Geprägs, R. Gross, H. Huebl, and S. T. B. Goennenwein, “Non-local magnon transport in the compensated ferrimagnet GdIG”, in preparation (2017), arXiv:1705.02871.

7. J. Fischer, O. Gomonay, R. Schlitz, K. Ganzhorn, N. Vlietstra, M. Althammer, H. Huebl, M. Opel, R. Gross, S. T. B. Goennenwein, and S. Geprägs, “Spin Hall magnetoresistance in antiferromagnet/normal metal heterostructures”, submitted (2017), arXiv:1709.04158.

8. B.-W. Dong, J. Cramer, K. Ganzhorn, H. Y. Yuan, E.-J. Guo, S. T. B. Goennenwein, and M. Kläui, “Spin Hall magnetoresistance in a non-collinear ferrimagnet GdIG close to the compensation temperature”, submitted (2017).

9. S. Klingler, S. Geprägs, V. Amin, K. Ganzhorn, H. Maier-Flaig, M. Althammer, H. Huebl, R. Gross, M. D. Stiles, S. T. B. Goennenwein, and M. Weiler, “Spin waves in coupled YIG/Co heterostructures”, in preparation (2017).

Acknowledgments

This thesis would not have been possible without the support of many people. In particular, I would like to thank:

- Prof. Dr. Sebastian T. B. Goennenwein for supervising my thesis, for introducing me to the field of magnetism and spintronics in the first place, for sharing his fascination for science and always coming up with new research ideas. Most importantly I am grateful for numerous fruitful discussions about our experimental data and for his invaluable advice on how to present scientific results and write publications.

- Prof. Dr. Rudolf Gross for enabling me to do my thesis at WMI and for sharing his vast knowledge on various topics concerning solid state physics.

- Dr. Hans Huebl for co-supervising me, lending an open ear even in busy times and offering his help whenever needed. His advice on many topics and his ability to ask the right questions was crucial for improving my understanding of the experimental data. He encouraged me to go beyond my limits while always keeping a smile on my face: “Lächel doch mal!”.

- Dr. Stephan Geprägs for introducing me to thin film fabrication and for several opportunities to accompany him on measurement time to the ESRF in Grenoble. I thank him for being a great mentor, always making time for discussions and contributing to a very relaxed working atmosphere.

- Dr. Matthias Althammer for introducing me to different cryostat setups, for the company during long and monotonous night time measurement shifts at the high field laboratory in Grenoble, for his input on modeling the SMR effect in canted magnets and valuable discussions on how to improve measurement techniques.

- Tobias Wimmer, first as my master student, later as a fellow PhD student, for his help with the non-local measurements and sample fabrication, for countless discussions about the theoretical magnon transport model and many fun times in the lab.

- Claudio De Rose, my bachelor student, for assembling the rotator dipstick allowing for angle dependent measurements in the 17T cryostat.

- Dr. Joe Barker for his theoretical input, for helpful discussions about compensated garnets and for his calculations of the magnetic phase diagram and magnon spectrum of GdIG.
- Dr. Akashdeep Kamra for making complex theoretical models understandable even for experimentalists, for his help with developing a theoretical model for magnon transport in GdIG and for his friendship.
- Prof. Dr. Gerrit Bauer for his theoretical input on SMR and spin transport in compensated ferrimagnets.
- Stephan Altmannshofer, Francesco Della Coletta, Prof. Dr. Andreas Erb, Dr. Sybille Meyer, Dr. Zhiyong Qiu, Dr. Nynke Vlietstra for fabricating some of the samples used throughout this thesis.
- Dr. Benjamin Piot, our local contact at the LNCMI Grenoble, for his valuable help before and during our measurement time at the high field laboratory.
- Dr. Katharina Ollefs, Dr. Francois Guillou, Dr. Fabrice Wilhelm and Dr. Andrei Rogalev at the ESRF beam line ID12, for setting up the XMCD experiments and their help with our measurements.
- Richard Schlitz for his important preliminary work on nanofabrication and providing the mean field simulations of the canting phase in GdIG shown in Chap. 4.
- Stefan Klingler for sharing his knowledge and experience on magnon logic.
- Hannes Maier-Flaig, for being a great office-mate and friend and highlighting many conversations with a matching YouTube video. I also thank him for long (and very helpful) discussions about physics, which typically started with “Wie ist denn das in GdIG...?”. Who could have known that the answers to many of our questions can be found in one single book?!
- My other office-mates Stefan Weichselbaumer and Edwar Xie for the great working atmosphere, as well as the rest of the “coffee gang” Michael Fischer and Daniel Schwienbacher for making me look forward to after-lunch coffee.
- All other members of the magnetism and qubit groups at the WMI, in particular Dr. Matthias Opel, Dr. Matthias Pernpeintner, Dr. Michael Schreier, Dr. Mathias Weiler for sharing their expertise on various topics and for the nice and friendly atmosphere.
- The mechanical workshop team for fabricating the components for the rotator dipstick and helping out with all kinds of smaller issues that required their technical expertise.

- Karen Helm-Knapp and Astrid Habel for preparing the Piranha solution necessary for sample fabrication and their advice on different types of wet etching.
- Thomas Brenninger and Sebastian Kammerer for keeping the thin film fabrication and clean room running.
- The “He-Halle” team for providing liquid He, which is a crucial component for low-temperature measurements.
- Ludwig Ossiander and Emel Dönertas for taking care of all the administrative work.
- Tanja, Simon, Simone and Georg, for their friendship and company since the beginning of our studies.
- My brother and my parents, for supporting me throughout my whole life and encouraging me to follow my own path, even though that means that we do not see each other very often.
- Kai for his constant and unreserved support and encouragement throughout all the ups and downs of the past years.